

University of Warwick institutional repository: <http://go.warwick.ac.uk/wrap>

**A Thesis Submitted for the Degree of PhD at the University of Warwick**

<http://go.warwick.ac.uk/wrap/34627>

This thesis is made available online and is protected by original copyright.

Please scroll down to view the document itself.

Please refer to the repository record for this item for information to help you to cite it. Our policy information is available from the repository home page.

**Excited State Processes of Complexes of W(V) and U(VI)  
by Laser Photolysis and ESR Spectroscopy**

by

**Mark Alexander Shand**

**A thesis submitted to the University of Warwick  
in partial fulfilment of the requirements for the degree of  
Doctor of Philosophy**

**Department of Chemistry  
University of Warwick  
Coventry CV4 7AL**

**January 1987**

**Dedicated to Mum and Dad, my friends and Sue**

## Contents

	<u>Page</u>
Abstract	ii
Abbreviations	ii
Chapter 1 Concepts of Inorganic Photochemistry	
1.1 Photophysical Processes - Energy Levels and Spectra	1
1.2 Spectra of Metal Complexes	1
1.3 Luminescence Spectra of Coordination Compounds	8
1.4 Kinetic Schemes for Primary Processes	12
1.5 Non-Radiative Processes	20
1.6 Quenching Processes and Quenching Mechanisms	
1.6.1 Excited State Electron-Transfer Quenching	23
1.6.2 Quenching of Excited States by Energy Transfer	25
1.7 Photochemical Reactions of Electronically Excited Transition Metal Complexes	28
Chapter 2	
2.1 Electron Spin Resonance	32
2.2 Magnetic Properties of the Electron	
2.2.1 Interaction with a Magnetic Field	34
2.2.2 The Resonance Conditions	34
2.2.3 Relaxation Processes	35
2.2.4 Hyperfine and Fine Structure	37
2.2.5 Nuclear Hyperfine Structure	37
2.3 g-Factors	37

	<u>Page</u>
2.4            Free-Radicals	39
2.5            Nuclear Hyperfine Structure	40
2.5.1        Isotropic and Anisotropic Hyperfine Coupling Constants	40
 Chapter 3    Photophysical and Photochemical Properties of the Uranyl Ion	
3.1           Photophysical Properties of the Uranyl Ion	44
3.2           Quenching of Uranyl Ion Fluorescence	47
3.2.1        Quenching by Metal Ions	47
3.2.2        Quenching by Simple Anions	48
3.2.3        Quenching by Organic Compounds	49
3.2.3.1     Carboxylic Acids	49
3.2.3.2     Alcohols	54
3.2.3.3     Aldehydes	56
3.2.4        Miscellaneous Substrates	57
 Chapter 4	
4.1           Complexation between Uranyl Ion and Amino Acids	58
 Chapter 5	
5.1           Photosensitised Decomposition of Amino Acids by Metal Ions - ESR Investigation	60

	<u>Page</u>
Chapter 6	
6.1 Photochemistry of the Octacyanide Complexes of Tungsten(IV) and (V)	65
Chapter 7 Experimental	
7.1.1 Laser Flash Photolysis	70
7.1.2 Luminescence Intensities and Spectra	73
7.1.3 The Optical Bench	73
7.1.4 Other Instrumentation	75
7.2 Syntheses	76
7.3 Purity of Chemicals	77
7.4 Sample Preparation	77
7.5 Emission and ESA Measurements	78
7.6 Analysis of Results	
7.6.1 Luminescence Studies	80
7.6.2 Emission Lifetime and ESA Measurements	80
Chapter 8 Complexation of Uranyl Ion with Simple Amino Acids	
8.1 Introduction	81
8.2 Spectroscopy	81
8.3 Preparation of $[\text{UO}_2(\text{O}_2\text{CCH}_2\text{NH}_3)_4][\text{NO}_3]_2$	82
8.4 Structure Determination	83
8.5 Determination of Coordination Number using Job's Method	84
8.6 Concluding Remarks	85

	<u>Page</u>
Chapter 9    Interaction of Excited Dioxouranium (VI) Ion with Amino Acids	
9.1            Introduction	86
9.2            Kinetic Measurements	87
9.3            ESR Measurements	88
9.4            Discussion	91
 Chapter 10   Physical and Chemical Quenching of Excited Uranyl Ion by Dialkyl Sulphides	
10.1           Introduction	96
10.2           Concluding Remarks	103
 Chapter 11   A Study of the Photochemistry of Octacyano- tungstate (IV) and (V) Ions	
11.1           Introduction	104
11.2           Quantum Yields of $[\text{W}(\text{CN})_8]^{4-}$ Formation in Aqueous Solution	104
11.3           Discussion	105
11.4           Low Temperature UV-visible Spectra	106
11.5           ESR Studies of the Photolysis of $[\text{W}(\text{CN})_8]^{3-}$ Ion at 77 K	106
11.5.1        ESR Study of Photolysis of $[\text{W}(\text{CN})_8]^{3-}$ Ions at Room Temperature	107
11.5.2        Assignments for Species I-III	108
11.6           Photolysis of $\text{K}_3[\text{W}(\text{CN})_8]$ in KBr Disc and PVA Film	111

	<u>Page</u>
11.6.1      Analysis of Photoproducts using IR Spectroscopy at 293 and 12 K	111
11.6.2      Assignment of IR Changes	112
11.7          Summary	113
11.8          Suggestions for Further Work	114
 References	 115



### Acknowledgements

I would like to express my sincere gratitude to Professor T. J. Kemp for his supervision over the last three years, and for providing me with the opportunity to study for my Ph.D. at the University of Warwick.

I would also like to thank Dr. N. W. Alcock and D. J. Flanders for solving the crystal structure of tetrakis (glycine) dioxouranium (VI) nitrate.

Many thanks to Dr. D. Rehorek for his help and inspiration concerning the photochemistry of  $[\text{W}(\text{CN})_8]^{3-}$  ion in solution.

I would also like to thank everyone in the Department who has provided scientific or technical assistance.

Finally, I wish to thank Kay Pollitt for typing this thesis and the University of Warwick for providing financial support.

Mark A. Shand

January 1987

## Abstract

This thesis deals with the reactions of two high-valent metal complexes,  $[\text{UO}_2]^{2+}$  and  $[\text{W}(\text{CN})_8]^{3-}$  in their excited states in which their one-electron reduction potentials are increased greatly, i.e. sufficiently for them to remove an electron from water.

The studies with uranyl ion cover the following, (i) the ground state interaction with some simple amino acids, (ii) the excited-state interaction with a variety of amino acids including some containing sulphur, which gave results of particular interest and, in following up the latter, (iii) the excited state interaction with some simple organosulphur compounds. These three inter-related topics form Chapters 8, 9 and 10 of this thesis. In more detail, in Chapter 8 we characterise optically, three new complexes of 1:4 stoichiometry between  $[\text{UO}_2]^{2+}$  and glycine and  $\alpha$ - and  $\beta$ -alanine in acidic aqueous solution. The x-ray crystal structure of the glycine complex confirms it as tetrakis (glycine) dioxouranium (VI) nitrate.

Chapter 9 covers the kinetics of luminescence quenching of  $^*[\text{UO}_2]^{2+}$  by amino acids (indicating the level of reactivity) and the quantum yields of  $[\text{U}(\text{IV})]$  which indicate the degree of charge separation from the initial radical-pair configuration, while cryogenic ESR data reveal the nature of the primary ligand-derived radical. Interestingly we find that while much the greatest kinetic reactivity towards  $^*[\text{UO}_2]^{2+}$  is shown by the sulphur-containing amino acids, these show very low yields for  $[\text{U}(\text{IV})]$  production. This pattern is repeated in our study of the photo-oxidation of dialkyl sulphides by excited uranyl ion, in which we believe to have demonstrated that a recent report of high quantum yields in this system and published in Inorganic Chemistry is erroneous.

Our brief study of the aqueous  $[\text{W}(\text{CN})_8]^{3-}$  system confirms the quantum yields for  $[\text{W}(\text{CN})_8]^{4-}$  of Samotus *et al.*, as opposed to the earlier data of Balzani and Carassiti and characterises, using ESR, IR and UV-vis spectroscopy, new W(V)-cyanide complexes obtained during irradiation into the C-T bands of  $[\text{W}(\text{CN})_8]^{4-}$  and  $[\text{W}(\text{CN})_8]^{3-}$  in aqueous solution.

Three publications have resulted hitherto from the above work in the following journals:

- Chapter 8: J. Chem. Soc., Dalton Trans., 1985, 517.
- Chapter 9: Inorg. Chim. Acta, 1986, 114, 215.
- Chapter 10: Inorg. Chem., 1986, 21, 3840.

The results from the final chapter together with data from the photoreduction of  $[\text{W}(\text{CN})_8]^{3-}$  with many organic systems obtained by Dr. D. Rehorek during his visit to the Department, have been compiled and submitted for publication to the Journal of the Chemistry Society, Dalton Transactions (paper 6/2444).

## Abbreviations

AA	amino acid
AM	angular momentum
CT	charge-transfer
CTTL	charge-transfer to ligand
CTTM	charge-transfer to metal
CTTS	charge-transfer to solvent
DPPH	$\alpha$ -diphenyl $\beta$ -picryl hydrazyl
ESA	excited state absorption
ESR	electron spin resonance
IC	internal conversion
ISC	intersystem crossing
LF	ligand field
LMCT	ligand to metal charge-transfer
MLCT	metal to ligand charge-transfer
MO	molecular orbital
SO	spin orbit
T	temperature
UV	ultraviolet
$\epsilon$	extinction coefficient
$\tau$	lifetime
$\phi$	quantum yield
$\lambda$	wavelength

## **Chapter 1**

### **Introduction**

### **Concepts of Inorganic Photochemistry**

## Concepts of Inorganic Photochemistry

### 1.1 Photophysical Processes - Energy Levels and Spectra

Absorption of a photon by a molecular species, A, leads to the production of a short-lived electronically excited species denoted  $A^*$ . This electronic energy can now be dissipated by either chemical or physical processes in a general scheme:



A full understanding of the photochemical primary processes requires an interpretation of the absorption spectrum of the molecule in question and an assessment of the rates of radiative and non-radiative processes occurring within  $A^*$ . These topics are dealt with in the following sections, making particular reference to metal complexes, both as regards their bonding and excited states.

### 1.2 Spectra of Metal Complexes

Absorption of light by a molecular species can induce changes in electronic, vibrational and rotational energies. The total energy,  $E_k$  corresponds to a solution of the Schrödinger equation

$$H\Psi_k = E_k\Psi_k \quad (1.5)$$

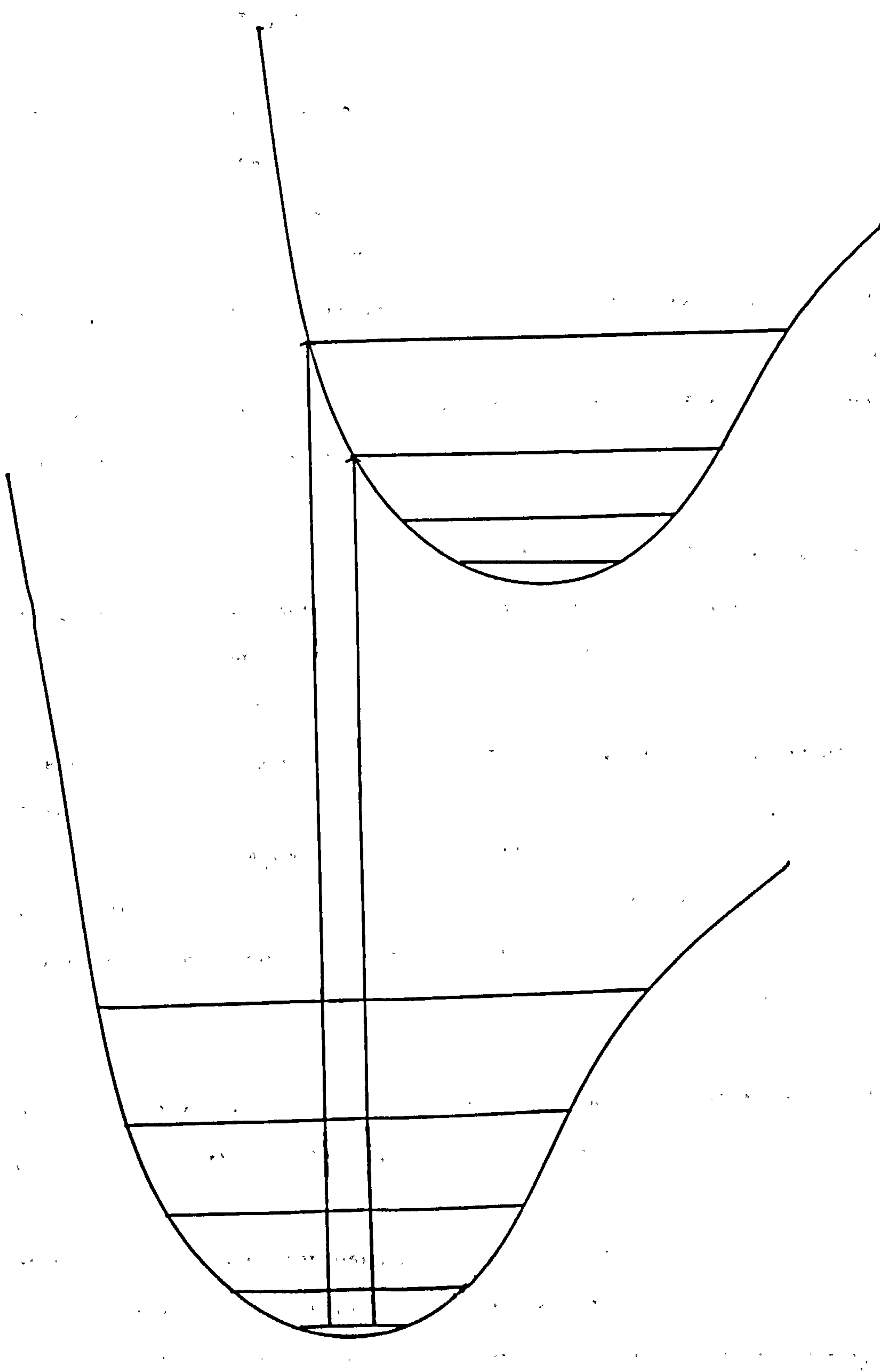
As long as the Born-Oppenheimer approximation is valid, the molecular energy levels can be described by a potential energy diagram (Figure 1.1), in which the vibrational energies are superimposed upon the electronic potential curves. The absorption and emission spectra are therefore represented by a summation of the individual vibronic



**Figure 1.1      Potential energy curves with superimposed vibrational energy levels.**

Energy

Internuclear distance



transitions

$$\Psi_{j\beta} \leftarrow \Psi_{i\alpha} \text{ and } \Psi_{j\beta} \rightarrow \Psi_{i\alpha} \text{ respectively.}$$

In order for a molecule to absorb light of a given frequency, two criteria must be satisfied. First the energy change in the molecule and the frequency of light must relate to the Planck equation

$$h\nu = E_2 - E_1 \quad (1.6)$$

where  $E_2$  and  $E_1$  are the energies of the excited state  $\Psi_2$  and ground state  $\Psi_1$  respectively. The second criterion is that there must be a specific interaction between the electric vector  $E$  of the E.M. wave and the electric dipole of the molecule.

The intensity of light absorption depends upon  $B_{12}$  (Einstein transition probability of absorption) which is given by the relation:

$$B_{12} = \frac{8\pi^3}{3h^2c} g_2 |R_{12}|^2 \quad (1.7)$$

where  $g_2$  is the degeneracy of  $\Psi_2$  and  $R_{12}$  is the transition-moment integral

$$R_{12} = \int \Psi_1 R \Psi_2 d\tau \quad (1.8)$$

which represents the charge displacement during the transition.  $R$  is the dipole-moment operator expressed by

$$R = e \sum_i r_i \quad (1.9)$$

where  $e$  is the electronic charge and  $r_i$  is the vector distance which corresponds to the dipole-moment operator for electron  $i$ .

Spontaneous emission represents a transition from excited state  $\Psi_2$  to ground state  $\Psi_1$  with the emission of a quantum of light. The intensity of the emission depends upon the number of excited states and on  $A_{21}$



(Einstein transition probability for spontaneous emission) which is given by

$$A_{21} = \frac{64\pi^4}{3h} \nu_{21} g_1 |R_{21}|^2 \quad (1.10)$$

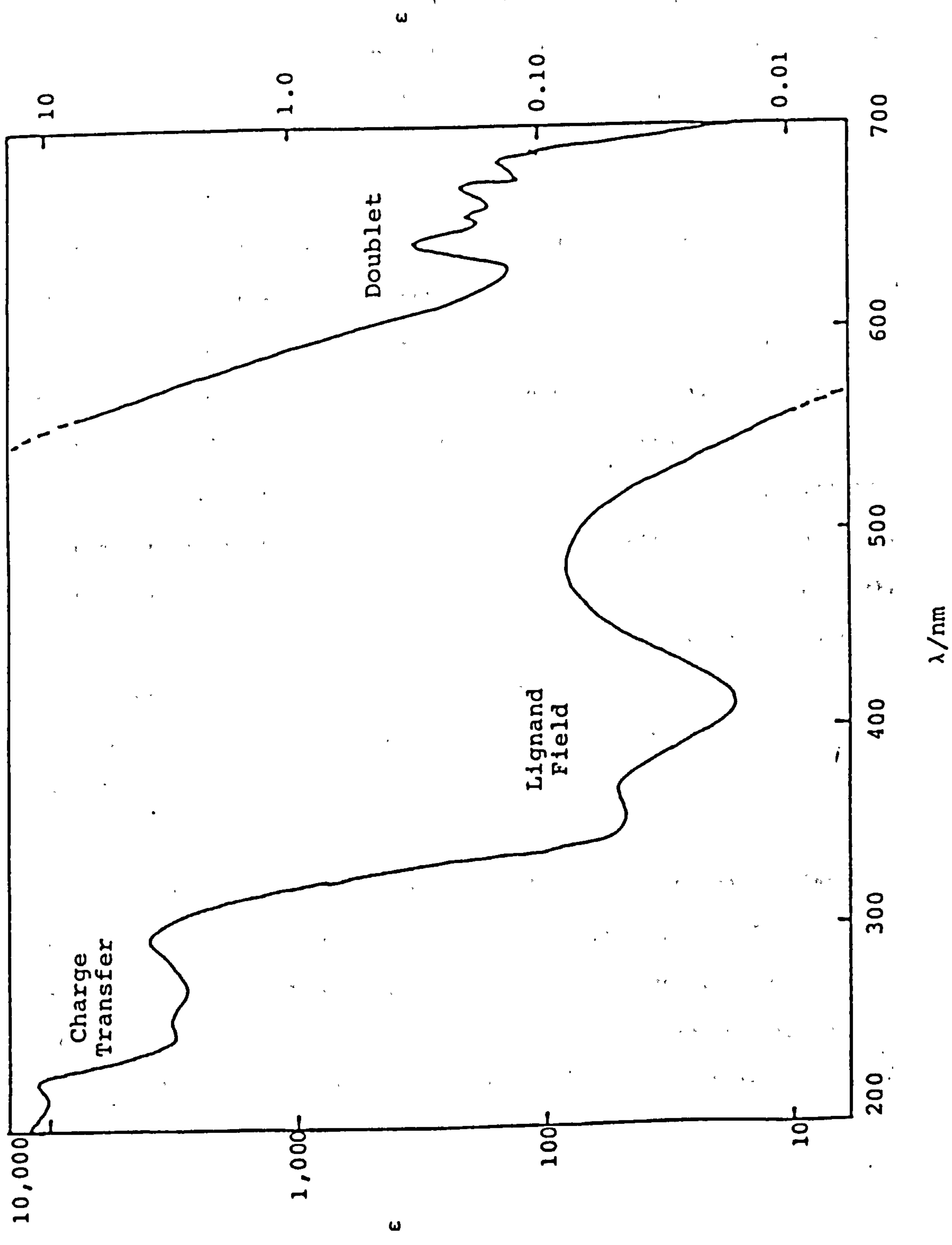
where  $\nu_{21}$  is the wavenumber of the light emitted,  $g_1$  is the degeneracy of  $\Psi_1$  and  $R_{21}$  is the transition moment integral as defined above.

As the rotational energy levels in many molecules are very closely spaced they are not resolved into individual lines and can be ignored. In solution at room temperature the individual vibronic components of a spectrum are also unresolved. A typical absorption spectrum is shown in Figure 1.2.

The most appropriate approach to the electronic structure of coordination compounds is that provided by molecular orbital (MO) theory. Unfortunately, this approach requires much computation effort in order to supply quantitative results. Consequently, other less complete, but more readily applied models are often used in describing bonding in metal complexes, such as the crystal field theory (CFT) and ligand field theory (LFT). In spite of the usefulness of CFT, it is now recognised that a purely electrostatic model is unsatisfactory, and a more realistic approach must take account of the existence of metal-ligand orbital overlap which is featured in LFT.

When an ion is transferred from the gaseous phase to a condensed phase, interaction with the environment alters the energy levels and consequently the transition energies. This environmental perturbation has two components, a symmetric component, the effect of which is to change the separation between free ion terms, and the ligand-field,

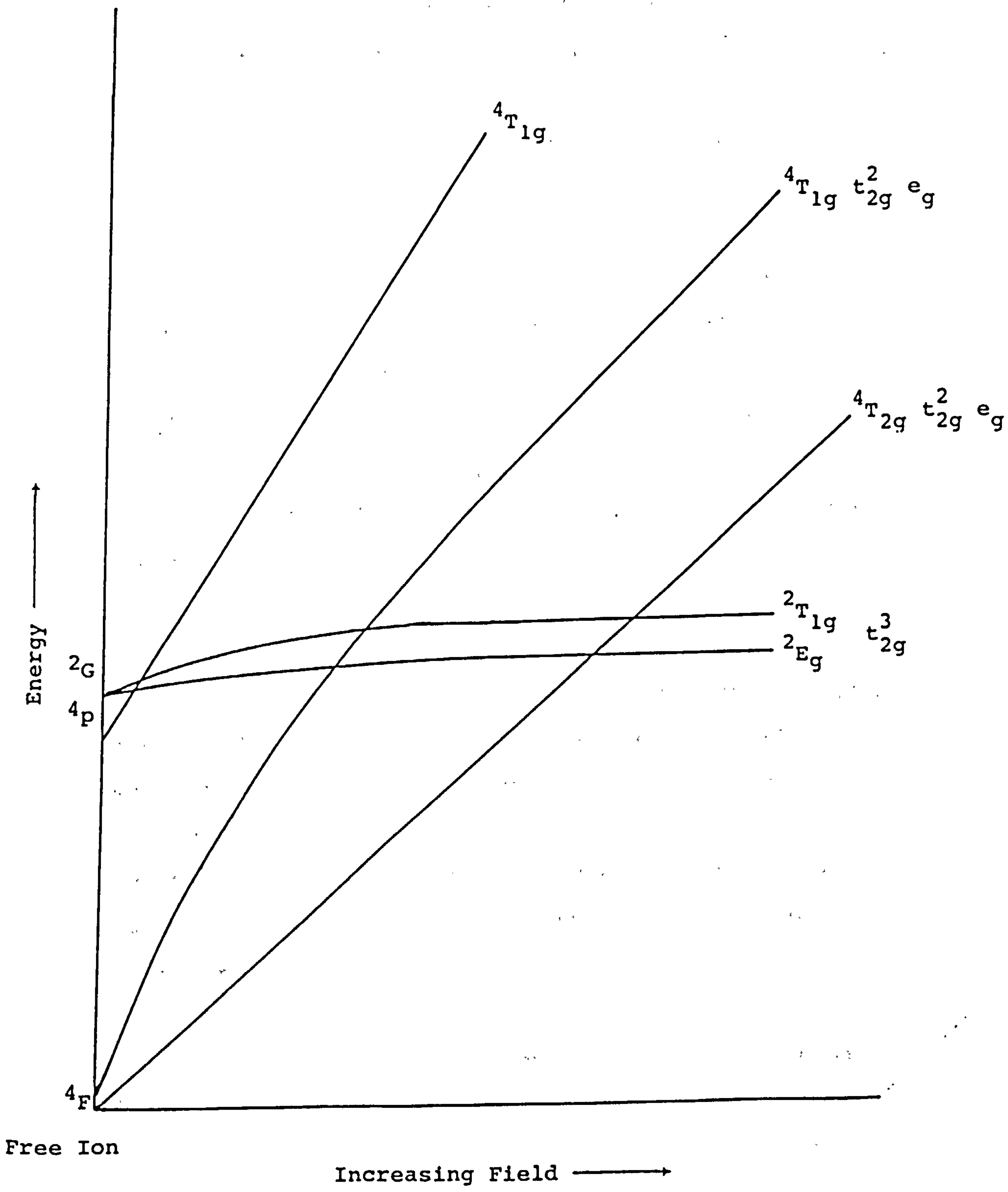
Figure 1.2 Visible and ultraviolet absorption spectrum of aqueous  $[\text{Cr}(\text{NH}_3)_5(\text{NCS})]^{2+}$  (from ref. 15).



perturbation. In octahedral ( $O_h$ ) symmetry the degeneracy of the five d-orbitals is removed resulting in a splitting into two orbital sets; the  $t_2$  orbitals  $d_{xy}$ ,  $d_{xz}$ ,  $d_{yz}$  and the e orbital set  $d_{x^2-y^2}$  and  $d_z^2$ . The ligand-field strength  $Dq$  (or  $\Delta$ ) can be estimated from the spectrochemical series. In determining the term separations produced by ligand fields, two different approaches have been employed, the weak- and strong-ligand field effects. In the weak field effect the ligand field is assumed small compared with d-electron repulsions. The splitting of the terms arising from a free  $d^n$  ion is due to electron repulsions, and the weak field condition means that the ligand-field splitting is small compared to the free-ion separation between the terms. Consequently, analysis is based on free-ion wave functions, the energies of which are modified by the symmetric perturbation (nephelauxetic effect<sup>1</sup>). For the strong-field limit the ligand-field perturbation is greater than the electronic repulsion energy. Analysis in this case is achieved by utilizing the d-orbitals appropriate to the environmental symmetry. The terms corresponding to the configuration are then derived according to group theory. In practice however, neither weak nor the strong-field limits are encountered and intermediate effects prevail.

The ordering of the states can be obtained from Tanabe-Sugano diagrams<sup>2</sup> in which term energies are plotted as a function of  $Dq$ . A Tanabe-Sugano diagram is shown in Figure 1.3, for Cr(III), a  $d^3$  system. In  $O_h$  symmetry Cr(III) has the configuration  $t_{2g}^3$  the associated terms being  $^4A_{2g}$ ,  $^2E_g$ ,  $^2T_{2g}$  and  $^2T_{1g}$ , the ground state from Cr(III) being  $^4A_{2g}$  and the lowest excited state  $^2E_g$ .

**Figure 1.3**      Tanabe-Sugano energy level diagram for a  $d^3$  system in octahedral symmetry.





In equations (1.7) and (1.8) the transitions are said to be "forbidden" when  $R = 0$  and "allowed" when  $R \neq 0$ . The rules defining the conditions in which  $R = 0$  are known as selection rules. These selection rules are obtained by using approximate eigenfunctions of the states so that "forbidden" transitions may in fact occur with low intensity. The total eigenfunction  $\Psi$  is expressed as

$$\Psi = \Psi_{el} \chi$$

where  $\Psi_{el}$  and  $\chi$  are the electronic and vibrational eigenfunctions respectively. The spin portion (S) of  $\Psi_{el}$  is factorised

$$\Psi_{el} = \Psi_{space} S$$

and the spatial electronic eigenfunction is expressed as

$$\Psi_{space} = i^{\pi} \Psi_i$$

Under these approximations, the transition moment integral can be written as

$$R_{12} = \int \Psi_1 R \Psi_2 d\tau_e \int S_1 S_2 d\tau_s \int \chi_1 \chi_2 d\tau_v$$

A transition is called symmetry forbidden when the integral  $\int \Psi_1 R \Psi_2 d\tau_e$  vanishes; this occurs when none of the components of  $R$  belongs to the same symmetry species as the product  $\Psi_1 \Psi_2$ . In centrosymmetric molecules the wavefunctions of which are either symmetric (gerade, g) or anti-symmetric (ungerade, u) with respect to the centre, transition of the same parity (i.e. g→g or u→u) are forbidden (and are referred to as parity- or Laporte-forbidden transitions).

Whenever the two states have different multiplicities the integral  $\int S_1 S_2 d\tau_s$  vanishes and the transitions are said to be spin forbidden. This selection rule is more rigorous than that concerning symmetry. However, molecules containing heavy atoms result in a breakdown of the spin forbidden transitions, which can then occur with low intensity.

In describing the intensity of an electronic transition, the oscillator strength is frequently employed, the quantum-mechanical expression of which is:

$$f_{12} = \frac{8\pi^2 mc \nu_{12}}{3h e^2} g_2 |R_{12}|^2$$

where  $m$  is the electronic mass. The oscillator strength can be related to the experimentally measurable extinction coefficient  $\epsilon$ :

$$f_{12} = 4.32 \times 10^{-9} F \int \epsilon dT$$

where  $F$  constitutes a correction factor related to the refractive index of the medium.

Similarly the radiative lifetime  $\tau_0$  can also be determined using the integrated area of an absorption band, which is given by the Strickler-Berg equation<sup>3</sup>.

$$\frac{1}{\tau_0} = 2.88 \times 10^{-9} n^2 \langle \nu_e^{-3} \rangle_{av} \frac{g_1}{g_2} \int \epsilon d \ln \nu_a$$

in which  $n$  is the refractive index of the medium.

If one is only interested in the order of magnitude of  $\tau_0$  the following approximate expression may be used<sup>4</sup>:

$$\tau_0 \sim 10^{-4} / \epsilon_{\max}$$

Classification of the spectra of organic molecules is achieved according to the "orbital jump" involved, i.e. in  $\pi-\pi^*$ ,  $n-\pi^*$  and  $\sigma-\sigma^*$  transitions. Similarly, it is convenient to describe transition-metal complex spectra in terms of the orbital change concerned. If d-d transitions are involved, it is possible to assign the spectra of metal complexes without introducing MO theory.



However, it is useful to treat the ligands more explicitly by employing the LCAO approach<sup>5</sup>

$$\Psi = a\phi_m + b\phi_l$$

where  $\phi_m$  and  $\phi_l$  represent metal ion and ligand orbitals respectively, and Figure 1.4 represents an MO diagram for  $O_h$  symmetry.

If the interactions between metal ion and ligand orbitals are not too large then classification of electronic transitions can be assigned to the following groups, (1) metal localised, (2) ligand localised and (3) charge transfer.

Metal-localised transitions include d-d and f-f transitions in rare-earth ions. Ligand-localised transitions encompass those of the free ligand, i.e.  $\sigma\text{-}\sigma^*$ ,  $\pi\text{-}\pi^*$  and  $n\text{-}\pi^*$ . Intramolecular charge-transfer transitions can be classified into three types:

- 1) Metal to ligand (CTTL) which involves the promotion of an electron from an orbital largely localised on the metal, to an orbital in which the electron is transferred to the ligand, i.e. a process in which the metal ion is oxidised.
- 2) Ligand to metal, (CTTM) involving a transition from a ligand-localised orbital to a metal-localised orbital resulting in the reduction of the metal-ion.
- 3) Charge-transfer to solvent (CTTS)<sup>6</sup>.

CTTL transitions are likely to happen in complexes with metal centres having low ionisation potentials and ligands with readily available empty  $\pi^*$  orbitals, e.g.  $\text{CN}^-$ ,  $\text{CO}$ ,  $\text{SCN}^-$ . CTTL transitions will be forced when the metal ion is in a low oxidation state. For example, the

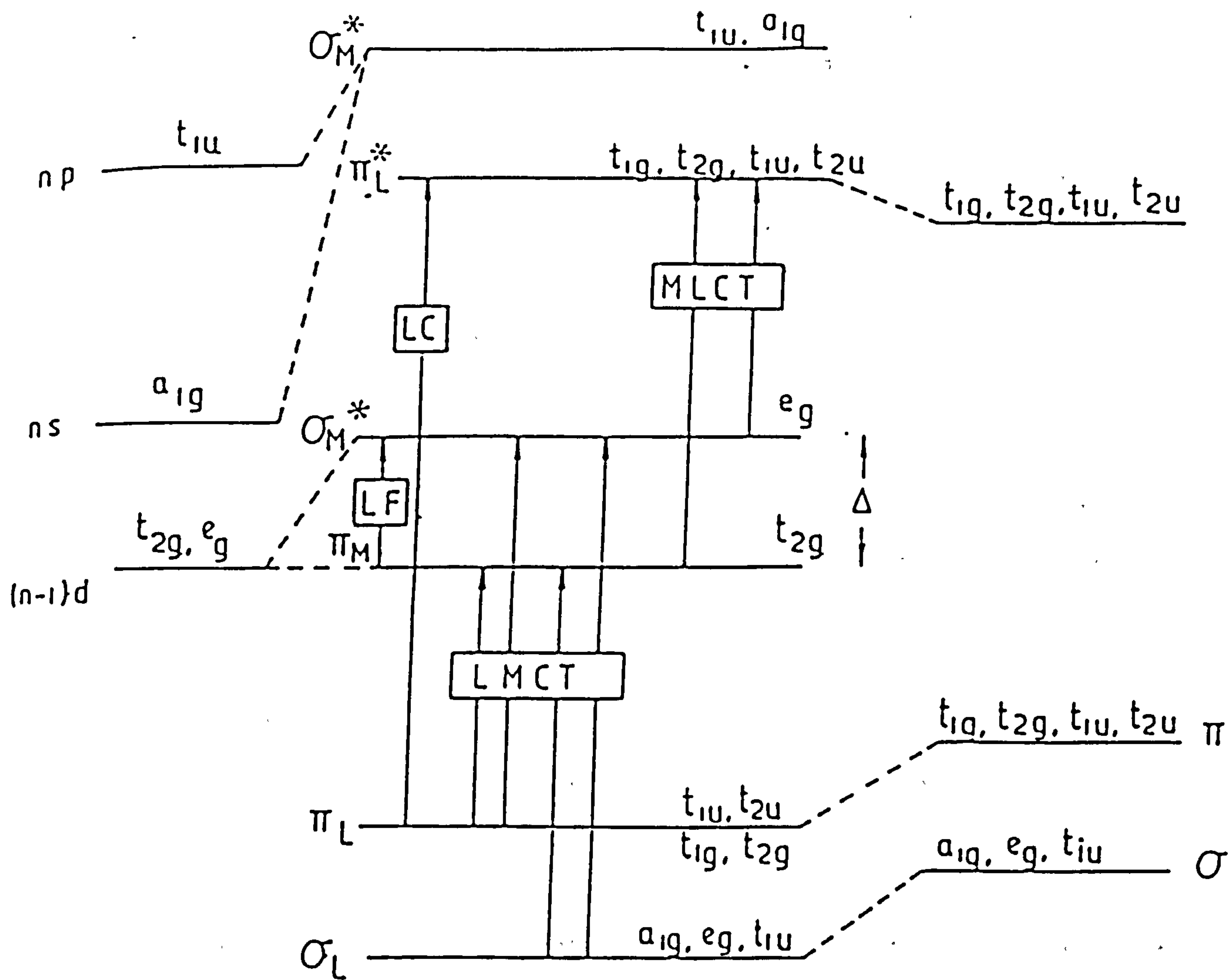
Figure 1.4      Molecular orbital scheme for an octahedral complex:

LF - ligand field transition,

LC - ligand centred transition,

LMCT - ligand to metal charge transfer,

MLCT - metal to ligand charge transfer.



Metal Orbitals

MO's

Ligand Orbitals

visible bands of the low-spin  $[\text{Fe}(\text{phen})_3]^{2+}$  are due to the CTTL while those of low spin  $[\text{Fe}(\text{phen})_3]^{3+}$  are due to CTM transitions<sup>7</sup>.

CTM bands are exhibited in the more UV-visible region by complexes containing highly reducing ligands such as  $\text{I}^-$ ,  $\text{Br}^-$ , and  $\text{Ox}^{2-}$ .

Jørgensen has developed an empirical expression which allows the wave length of CT bands to be predicted<sup>8</sup>

$$\nu = 30 (x_L - x_M) + \Delta$$

where  $x_L$  and  $x_M$  are the optical electro-negativities of the ligand, L, and the metal, M, respectively, and  $\Delta$  is the orbital-energy difference due to ligand field splitting.

CTTS transitions are exhibited by some negative complex ions such as,  $[\text{Fe}(\text{CN})_6]^{4-}$ <sup>9</sup> and hydrated cations in their low oxidation states, for example  $\text{Ce}^{3+}$ <sup>10</sup>.

Charge transfer bands can also occur in the ion-pairs formed between a coordinatively saturated complex and a polarisable anion such as iodide. These ion-pair charge transfer (IPCT) bands, first observed by Linhard and Weigel<sup>11</sup>, are due to intermolecular charge transfer from the anion to the  $e_g$  d-orbitals of the metal ion. These IPCT bands are exhibited by aqueous potassium iodide solutions of  $[\text{Co}(\text{NH}_3)_6]^{3+}$  when the iodide ion concentration is increased.

### 1.3 Luminescence Spectra of Coordinating Compounds

When observable, emission spectra serve two useful purposes to the theoretician: (1) as an aid to locating the  $v=0$  level of the lowest

excited states; and (2) to provide information about the distortion of the lowest excited states relative to the ground state, by means of the Stokes shift.

An empirical rule developed by Kasha, governing the emission from the excited states of a molecule<sup>12</sup> reads as follows:

"The emitting level of a given multiplicity is the lowest excited level of that multiplicity".

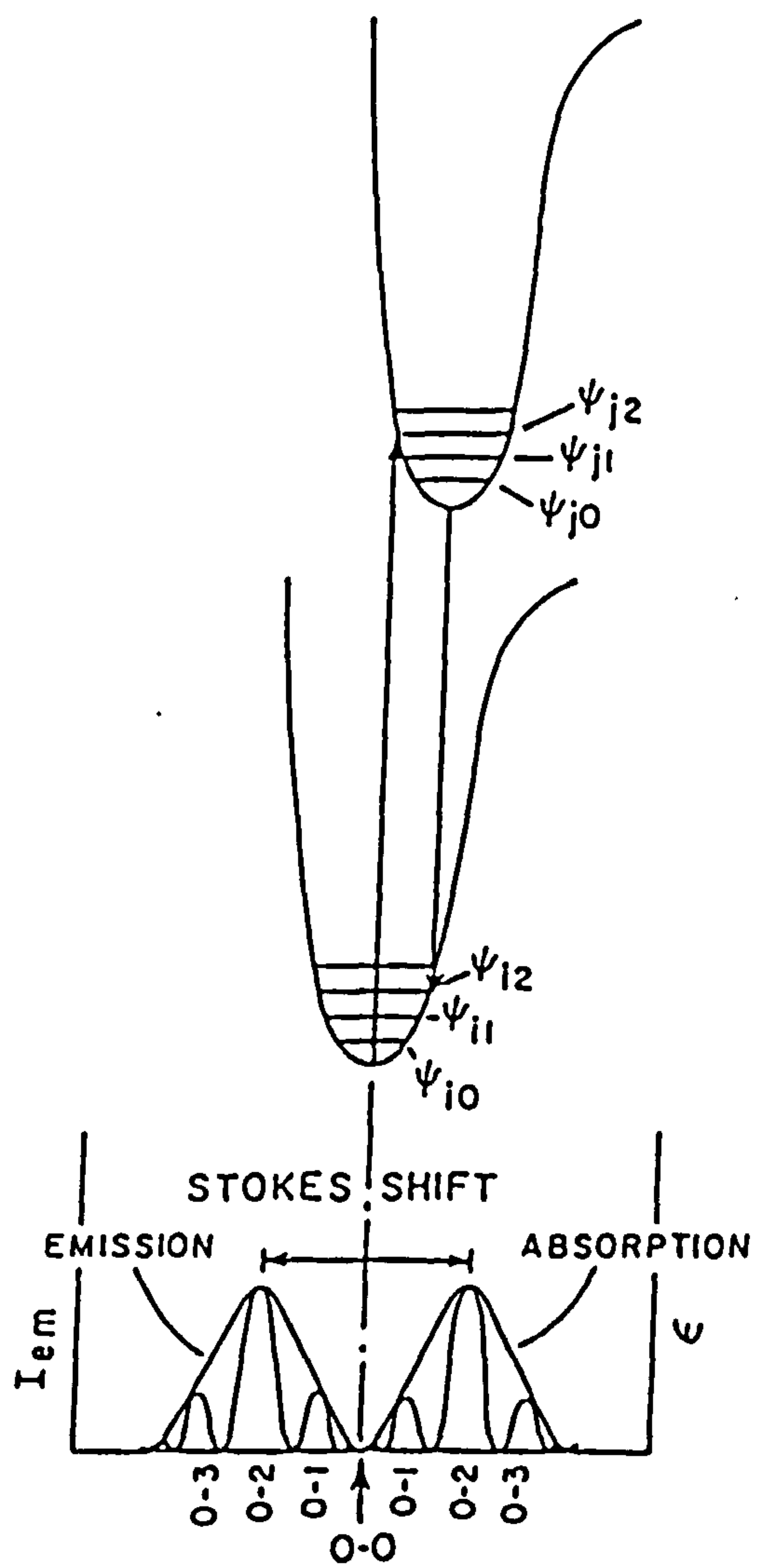
Crosby and Demas<sup>13</sup> modified Kasha's rule to deal with the type of emission observed from transition metal complexes:

"In the absence of photochemistry from upper excited states, emission from a transition metal complex with an unfilled d shell will occur from the lowest electronic state in the molecule or from those states which can achieve a significant Boltzmann population relative to the lowest excited state".

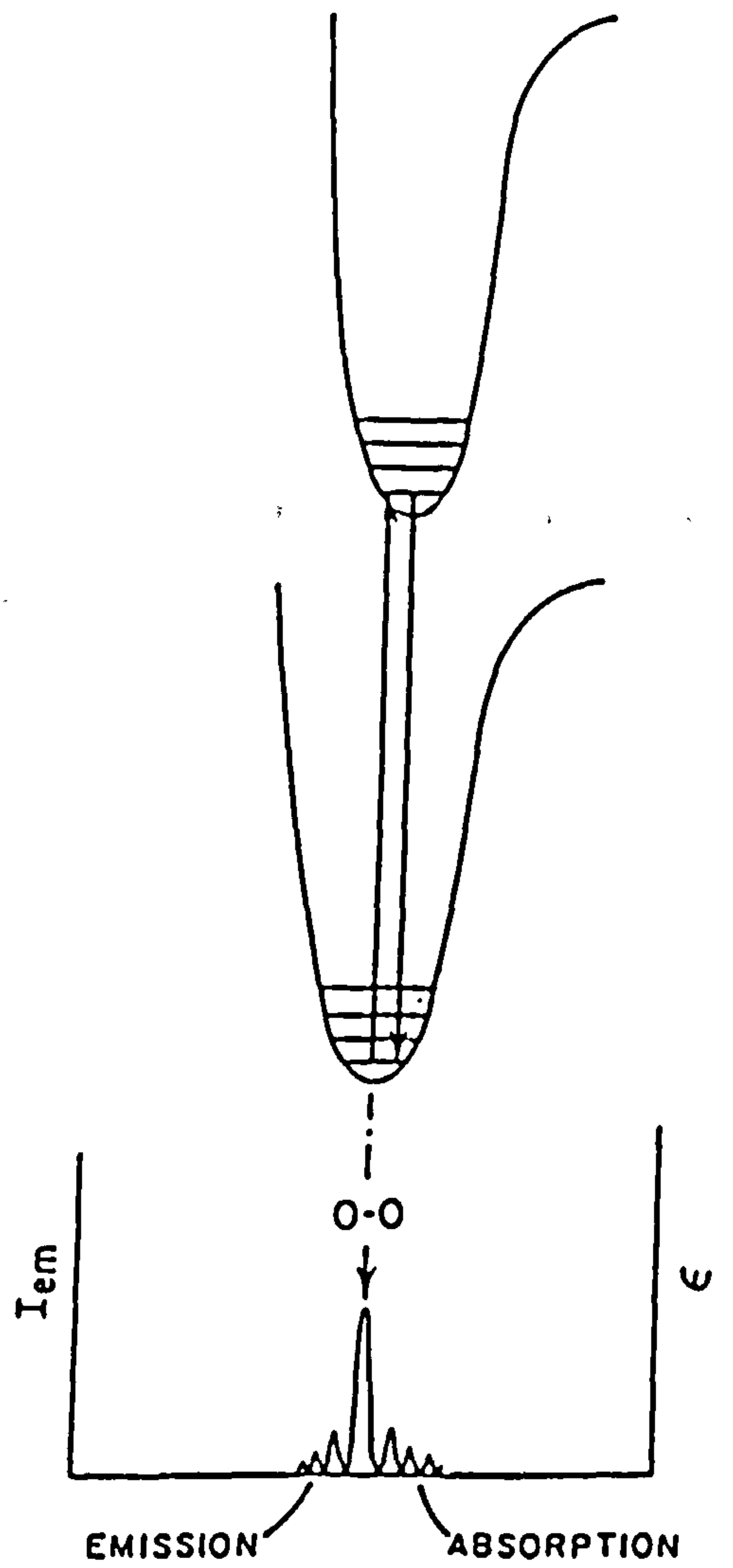
The relation between the absorption and emission spectra for transitions between the two electronic states is shown in Figure 1.5, namely (a) where the ground and excited states are of different geometries resulting in a large Stokes shift and (b) where the ground and excited states are identical and there is no Stokes shift.

When a molecule is embedded in a solid or liquid matrix, the potential curves no longer, strictly speaking, represent intra-molecular energies, but rather the total energy of the molecule plus its environment. In both fluid and rigid solutions absorption is to a configuration corresponding to the ground-state configuration of the solvent molecules (solid curves in Figure 1.6). If the viscosity is small, reorientation

**Figure 1.5**      **Potential curves and corresponding idealised spectra for**  
**(a) different equilibrium geometries in the ground and**  
**excited states, (b) same equilibrium geometries. (from**  
**ref.15).**



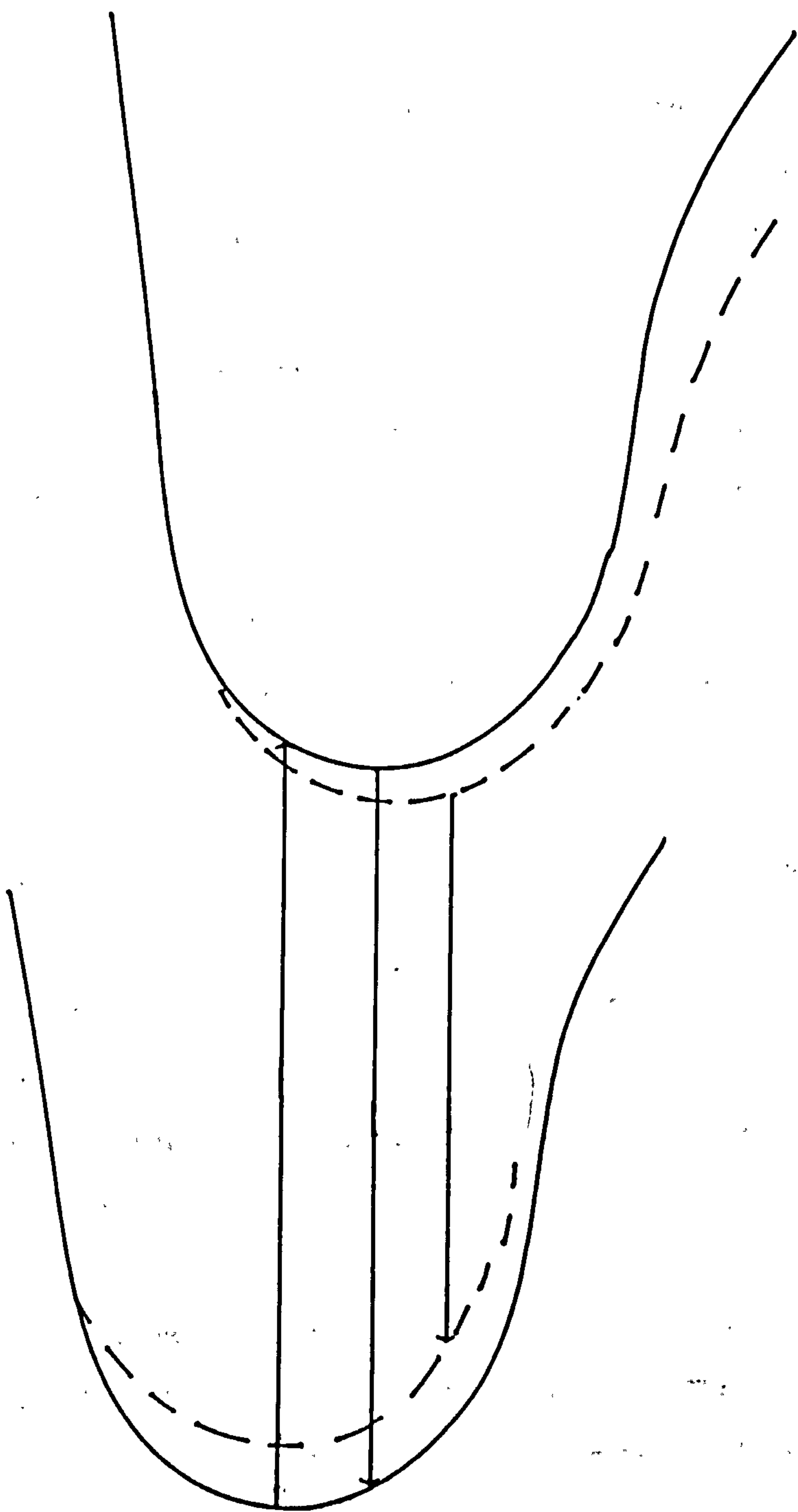
(a)



(b)

**Figure 1.6**      **Potential curves in rigid and fluid media; (-) ground-state solute-solvent orientation; (---) relaxed excited-state solute-solvent orientation.**





of the solvent precedes emission which originates in the relaxed configuration (dashed curves). If, however, the viscosity is high no solvent reorientation can occur, and emission takes place from the (solvent) ground state configuration.

Ligand-localised bands exhibit the same type of solvent dependence as the free ligands, e.g.  $\pi-\pi^*$  transitions are red shifted with increasing solvent polarity, while  $n-\pi^*$  transitions are blue shifted.

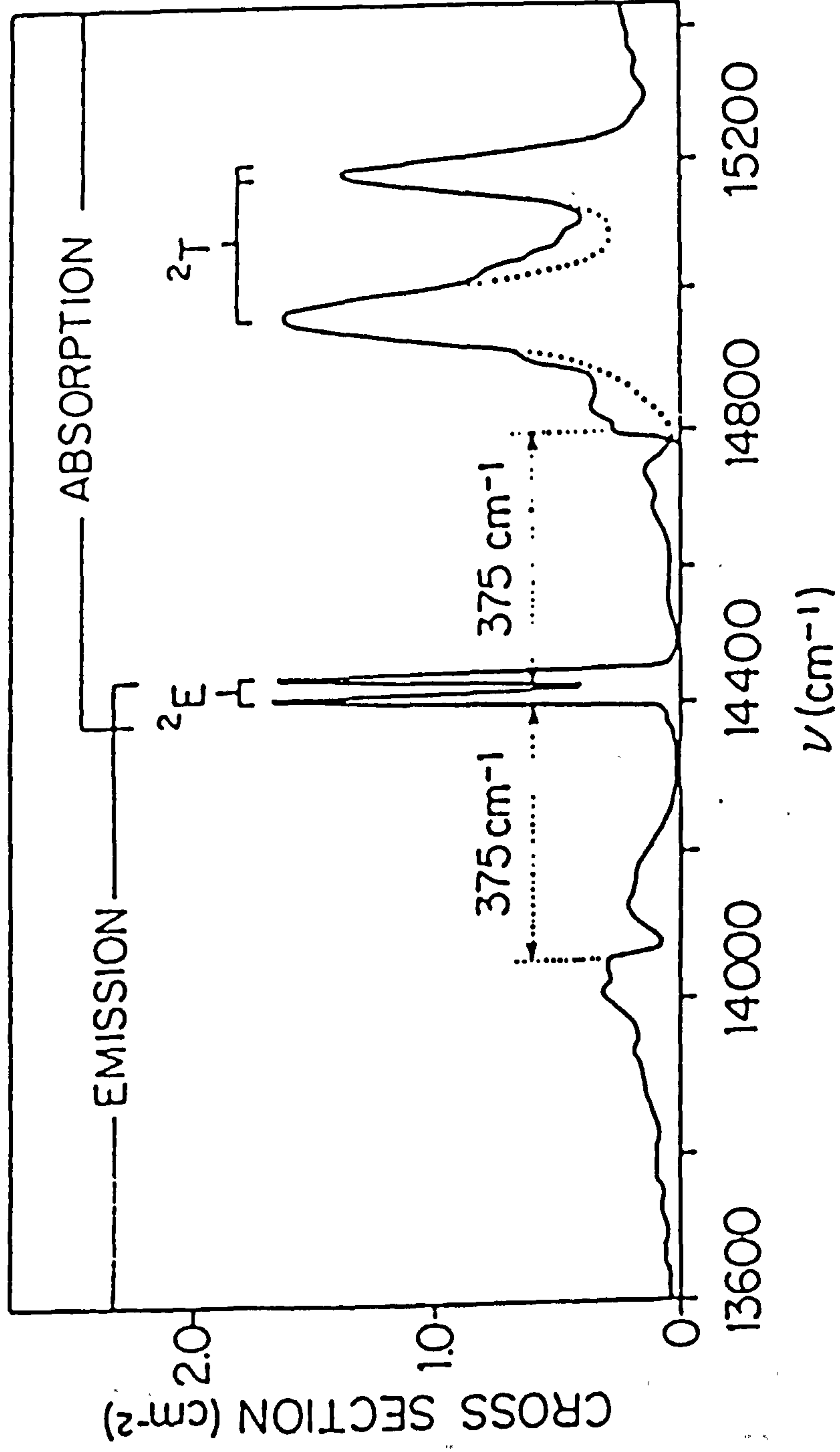
The d-d transition energies are little affected (<12%) by changes in solvent composition, assuming that ligand exchange with solvent does not occur. Intensities, however, may change by as much as 30%<sup>14</sup>.

Certain transition metal coordination compounds with  $d^2$ ,  $d^3$ ,  $d^5$ ,  $d^6$  and  $d^8$  configurations have been reported to be luminescent, and three kinds of emission have been characterised so far<sup>15</sup>:

- 1) Phosphorescence localised on metal-orbitals with a sharp line spectrum.
- 2) Charge-transfer phosphorescence, characterised by a structured spectrum.
- 3) Broad, structureless phosphorescence and fluorescence localised on metal orbitals.

The best known example of sharp lined emission is that of ruby, which consists of about 0.05%  $\text{Cr}^{3+}$  in an  $\text{Al}_2\text{O}_3$  matrix. The R lines of ruby, see Figure 1.7, have been thoroughly investigated<sup>16</sup> in emission and absorption, and in stimulated emission. Emission and absorption are mirror images reflected around the R lines situated at about

Figure 1.7      Absorption and phosphorescence spectra of ruby at 77 K.  
The 'R' lines near  $14000\text{ cm}^{-1}$  are the split origin of  
the  ${}^2\text{E} \leftrightarrow {}^4\text{A}_2$  transition (from ref. 15).



14,400  $\text{cm}^{-1}$ ; however, absorption also involves transitions to states other than the phosphorescent state. The  $d^3$  ions when examined in the appropriate ionic matrix, exhibit a sharp emission when irradiated with UV or visible light. For  $[\text{Cr}(\text{CN})_6]^{3-}$  in DMF solvent, emission is observed at room temperature.

These sharp line spectra arise from the transition:  ${}^2E_g \rightarrow {}^4A_{2g}$  for  $d^3$  ions with  $O_h$  symmetry and are thus both spin- and symmetry forbidden. The lifetime of the phosphorescent state is long as shown by  $[\text{Cr}(\text{en})_3]^{3+}$  which has a radiative lifetime at 77 K of 6 ms<sup>17</sup>.

Fluorescence has only been observed from a few  $d^3$  systems so far. The transition is spin allowed, but Laporte forbidden. The transition  ${}^4T_{2g} \rightarrow {}^4A_{2g}$  has strong field configurations,  $t_{2g}e_g$  and  $t_{2g}$ , respectively.

In a few cases such as  $[\text{CrF}_6]^{3-}$ ,  $[\text{CrCl}_6]^{3-}$  and aquo-fluoro complexes of Cr(III) fluorescence is the only emission observed<sup>18</sup>, but in the case of  $[\text{Cr}(\text{urea})_6]^{3+}$  both fluorescence and phosphorescence are found<sup>19</sup>.

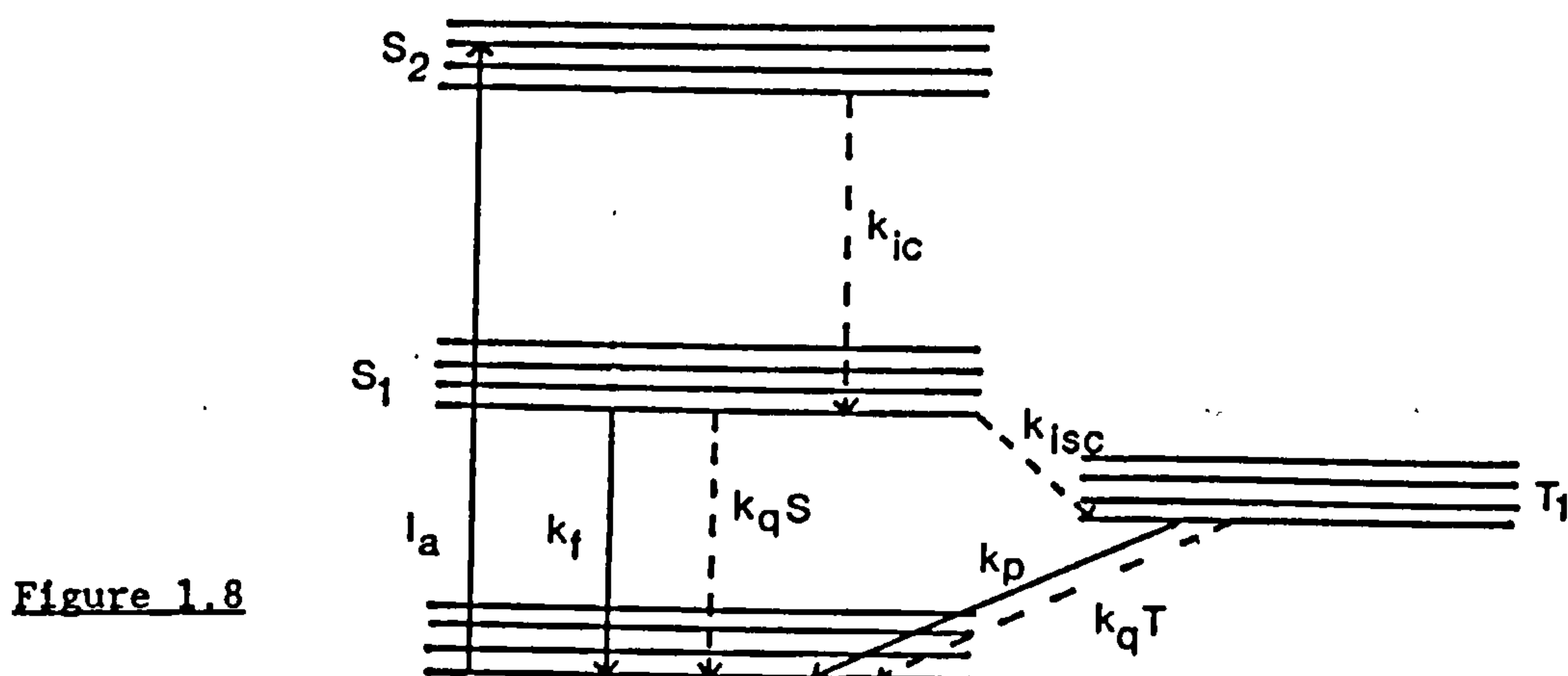
The broad phosphorescence observed in  $d^6$  octahedral complexes originates from an excited state with a strong-field electronic configuration. The transition has been assigned as  ${}^3T_1 \rightarrow {}^1A_1$ <sup>20</sup>, and these states have the electronic configurations  $t_{2g}e_g$  and  $t_{2g}^6$  respectively.

A second type of phosphorescence has also been observed for  $d^6$  complexes which is mutually exclusive with the first type. This phosphorescence exhibits vibrational structure in its spectrum<sup>21</sup> and has so far only been observed with  $d^6$  ions of the second or third transition series with polypyridyl ligands such as 1,10-phenanthroline and 2,2'-bipyridine.

Crosby concluded that the phosphorescence arises from charge-transfer transitions between ligand and metal.

The luminescence observed from a complex such as  $[\text{Rh}(\text{phen})_3]^{3+}$  is very similar to the phosphorescence of the free ligand. The emission of the complex is assigned as a triplet-singlet  $\pi-\pi^*$  intraligand transition. The lifetime of the phosphorescence of the complex is much shorter than of the free ligand, an effect which can be readily accounted for on the basis of enhanced spin-orbit coupling in the case of a complex ion of a heavy metal.

#### 1.4 Kinetic Schemes for Primary Processes



Every electronic state is convertible to another state by one or more radiative or non-radiative processes. The rate equations for the various deactivation processes of an electronically excited state can be derived by the application of the steady-state approximation<sup>22</sup>. Figure 1.8 depicts a general energy level diagram applicable to metal complexes. Assuming that there is no back intersystem crossing, i.e.  $k_4 = 0$ , the kinetic scheme is as follows:

		<u>Rate</u>
$S_0 + h\nu$	$\rightarrow S_2$	$I_a$
$S_2$	$\rightarrow S_1(v=0)$	$k_1 [S_2]$
$S_1$	$\rightarrow S_0 + h\nu_F$	$k_2 [S_1]$
$S_1$	$\rightarrow S_0$	$k_3 [S_1]$
$S_1$	$\rightarrow T_1$	$k_4 [S_1]$
$T_1$	$\rightarrow S_0 + h\nu_p$	$k_5 [T_1]$
$T_1$	$\rightarrow S_0$	$k_6 [T_1]$

The rate of formation of the  $T_1$  state is given by

$$d[T_1]/dt = -(k_5 + k_6)[T_1] + k_4[S_1] \quad (1.9)$$

and that for  $S_1$  is given by

$$d[S_1]/dt = I_a - (k_2 + k_3 + k_4)[S_1] \quad (1.11)$$

Under the assumption of the steady state approximation, i.e.  $d[T_1]/dt = d[S_1]/dt = 0$ , the following expressions are obtained.

$$[S_1] = \frac{I_a}{(k_2 + k_3 + k_4)} \quad (1.12)$$

$$[T_1] = \frac{k_4 I_a}{(k_2 + k_3 + k_4)(k_5 + k_6)} \quad (1.13)$$

By definition

$$\phi_p = \frac{k_5 [T_1]}{I_a} = \frac{k_4 k_5}{(k_2 + k_3 + k_4)(k_5 + k_6)} \quad (1.14)$$



$$\phi_F = \frac{k_2[S_1]}{I_a} = \frac{k_2}{(k_2 + k_3 + k_4)} \quad (1.15)$$

$\phi_{ISC}$  is given by

$$\frac{k_4}{(k_2 + k_3 + k_4)} \quad (1.16)$$

hence

$$\phi_p = \frac{\phi_{ISC} \cdot k_5}{(k_5 + k_6)} \quad (1.17)$$

The fluorescence ( $\tau_F$ ) and phosphorescence lifetimes ( $\tau_p$ ) measured by pulse techniques of negligible duration leads to the modification of equation (1.11)

$$d[S_1]/dt = -(k_2 + k_3 + k_4)[S_1] \quad (1.18)$$

It is assumed that the pulse will excite molecules only from the  $S_0$  state to the  $S_1$  state, and therefore at  $t = 0$ ,  $[T_1] = 0$  and  $[S_1] = [S_1]_0$ . Using this restriction, the following equation is obtained:

$$[T_1] = \frac{k_4[S_1]_0}{k_5 - k_T} [e^{-k_T t} - e^{-k_5 t}] \quad (1.19)$$

where  $k_5 = k_2 + k_3 + k_4$

and  $k_T = k_5 + k_6$ .

The first term of equation (1.19) represents the decay of phosphorescence whilst the second term represents its "grow-in".

Since  $k_5 \gg k_T$  at  $t > 1/k_5$ , equation (1.19) reduces to



$$[T_1] = \frac{k_4[S_1]_0}{k_5} e^{-k_T t} - [T_1]_0 e^{-k_T t} \quad (1.20)$$

where  $[T_1]_0 = \phi_{ISC} [S_1]_0$ . Thus,

$$\tau_p = 1/k_T = 1/(k_5 + k_6) \quad (1.21)$$

while combining equations (1.21) and (1.17) yields

$$\phi_p/\tau_p = \phi_{ISC} \cdot k_5 \quad (1.22)$$

If we introduce back-intersystem crossing ( $k_{-4}$ ) into the rate equations, we now have for continuous illumination

$$d[T_1]/dt = -(k_5+k_6+k_4)[T_1] + k_4[S_1] \quad (1.23)$$

$$d[S_1]/dt = I_a - (k_2+k_3+k_4)[S_1] + k_{-4}[T_1] \quad (1.24)$$

Applying the steady state approximation yields

$$[T_1] = \frac{k_4 I_a}{(k_5+k_6+k_{-4})(k_2+k_3+k_4) - (k_{-4}k_4)} \quad (1.25)$$

$$[S_1] = \frac{(k_5+k_6+k_{-4}) I_a}{(k_5+k_6+k_{-4})(k_2+k_3+k_4) - (k_{-4}k_4)} \quad (1.26)$$

and from these, the luminescence quantum yields can be evaluated:

$$\phi_p = \frac{k_5[T_1]}{I_a} = \frac{k_4 k_5}{(k_5+k_6+k_{-4})(k_2+k_3+k_4) - (k_{-4}k_4)} \quad (1.27)$$

$$\phi_F = \frac{k_2[S_1]}{I_a} = \frac{k_2(k_5+k_6+k_{-4})}{(k_5+k_6+k_{-4})(k_2+k_3+k_4) - (k_{-4}k_4)} \quad (1.28)$$

Under the conditions of a single short photolysis pulse, the rate equations become:

$$d[T_1]/dt = -(k_5+k_6+k_4)[T_1] + k_4[S_1] \quad (1.29)$$

$$d[S_1]/dt = -(k_2+k_3+k_4)[S_1] + k_{-4}[T_1] \quad (1.30)$$

which on differentiation yield

$$d^2[T_1]/dt^2 = -(k_5+k_6+k_{-4})d[T_1]/dt + k_4d[S_1]dt \quad (1.31)$$

$$d^2[S_1]/dt^2 = -(k_2+k_3+k_4)d[S_1]/dt + k_{-4}d[T_1]/dt \quad (1.32)$$

Substitution of equations (1.29) and (1.30) into (1.31) and (1.32) respectively, produces two simultaneous equations which can be solved to yield

$$[T_1] = \frac{k_4[S_1]_0}{\lambda_2 - \lambda_1} [e^{-\lambda_1 t} - e^{-\lambda_2 t}] \quad (1.33)$$

$$[S_1] = \frac{[S_1]_0}{\lambda_2 - \lambda_1} [(\lambda_2 - k_T)e^{-\lambda_1 t} + (k_T - \lambda_1)e^{-\lambda_2 t}] \quad (1.34)$$

$$\text{where } \lambda_{1,2} = 1/2 \{ (k_E + k_T) \pm [(k_T - k_E)^2 + k_{-4}k_4]^{1/2} \} \quad (1.35)$$

$$k_E = k_5 + k_6 + k_{-4}$$

$$k_T = k_2 + k_3 + k_4$$

$$\lambda_{1,2} = (\tau_p)^{-1} = 1/2 \{ (k_E + k_T) \pm [(k_T - k_E)^2 + 4k_4k_{-4}]^{1/2} \} \quad (1.36)$$

Although equation (1.36) appears complex, it can be simplified by considering two limiting cases.

Case (1) - The steady state limit, which is valid for  $S_1$  (after the decay of the exciting pulse), i.e.  $k_4 \gg k_5 + k_6$ . This leads to the assumption  $4k_4k_{-4} \ll (k_T - k_E)^2$ .

In this case equation (1.36) reduces to

$$(\tau_p)^{-1} \approx k_E - \frac{k_4 k_{-4}}{k_T - k_E} \approx k_5 + k_6 + (1 - \phi_{ISC}) k_{-4} \quad (1.37)$$

where  $\phi_{ISC}$  is given by equation (1.16) and  $k_T \gg k_E$ . Combination of equations (1.36) and (1.27) yields

$$\phi_p / \tau_p = \phi_{ISC} k_5 \quad (1.38)$$

This result is the same as that obtained when  $k_{-4}$  is neglected.

Case (ii) - In this situation, it is assumed that the two states are in thermal equilibrium with each other, i.e.  $k_4 \gg k_2 + k_3$ ; then equation (1.36) becomes

$$(\tau_p)^{-1} = \frac{k_5 + k_6 + (k_2 + k_3)(k_{-4}/k_4)}{1 + (k_{-4}/k_4)} \quad (1.39)$$

The inter-state equilibrium constants,  $K$ , is defined as

$$[S_1]/[T_1] = k_{-4}/k_4 \quad (1.40)$$

hence

$$(\tau_p)^{-1} = \frac{k_5 + k_6 + (k_2 + k_3)K}{1 + K} \quad (1.41)$$

Similarly, equation (1.27) simplifies to

$$\phi_p = \frac{k_5}{(k_5 + k_6) + (k_2 + k_3)K} \quad (1.42)$$

and therefore

$$\phi_p / \tau_p = \frac{k_5}{1 + K} \quad (1.43)$$

Comparison of equations (1.43) and (1.38) reveals that  $(1 + K)^{-1}$  is equivalent to an intersystem crossing yield, however,  $K$  is strongly temperature dependent since

$$K = [g(T_1)/g(S_1)] \exp(-\Delta E/kT) \quad (1.44)$$

where  $g(T_1)$  and  $g(S_1)$  represent the degeneracies of the states  $T_1$  and  $S_1$  respectively, and  $\Delta E$  refers to the energy difference between the two states.

Substitution of equation (1.44) into (1.43) gives

$$\phi_p/r_p = \frac{k_5}{1+[g(T_1)/g(S_1) \exp (-\Delta E/kT)]} \quad (1.45)$$

If  $\Delta E > 1000 \text{ cm}^{-1}$ , then at ambient temperatures  $\phi_p/r_p \approx k_5$ . As the equilibrium limit necessitates  $\phi_{ISC} \approx 1$  then at moderate or high values of  $\Delta E$ , equations (1.45) and (1.43) will become indistinguishable.

The measurement of  $r_p$  at a variety of different temperatures allows an estimate of  $\Delta E$  to be obtained.

$r_f$  and  $r_p$  can be measured by pulse techniques<sup>23</sup> for fluorescent or phosphorescent molecules. The excited state lifetime of species that are not luminescent are often obtainable using excited state absorption (ESA) spectroscopy<sup>24</sup>.

In inorganic systems where transitions do not involve a change in multiplicity, values of  $k_{ic}$  are typically of the order  $> 10^{12} \text{ s}^{-1}$  while those of  $k_F$  are of the order  $10^8 \text{ s}^{-1}$ . Where changes in multiplicity are involved, the differences can be substantial. Spin-orbit coupling causes mixing of singlet and triplet states, resulting in a breakdown of selection rules governing changes in multiplicity. For organic molecules intersystem crossing is formally forbidden, however, spin-orbit coupling in inorganic systems results in figures for  $k_{ISC}$  being of

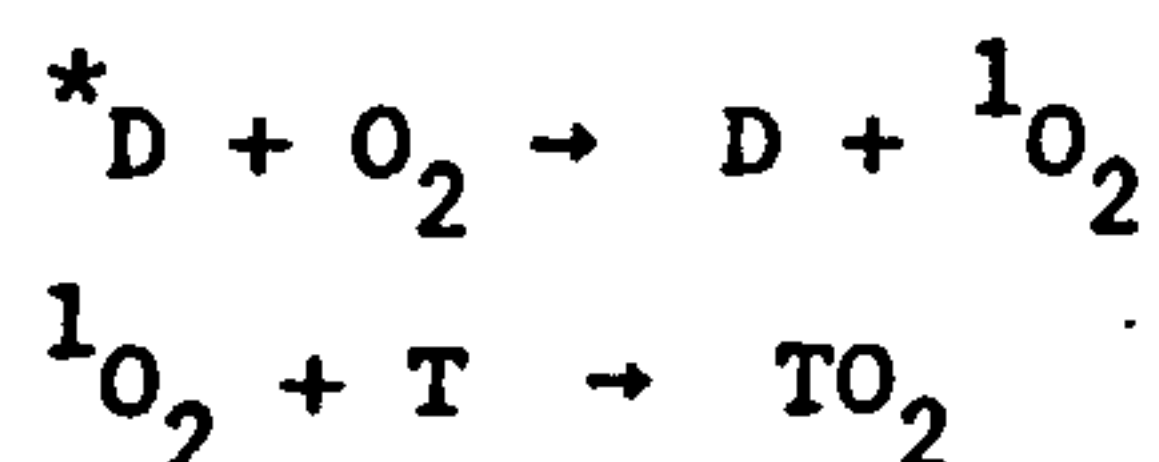
the order of  $10^9$ - $10^{12}$  s<sup>-1</sup>, while those for  $k_p$  generally fall in the range  $10^2$ - $10^5$  s<sup>-1</sup>.

For luminescent materials  $\phi_{IC}$  is readily determined. One merely measures the photon yield with excitation into  $S_1$  and  $S_2$  states, whereupon  $\phi_{IC} = \phi(S_2)/\phi(S_1)$ .

Measurement of  $\phi_{ISC}$  is frequently more difficult. If the  $S_0 \rightarrow T_1$  transition is sufficiently allowed to absorb appreciably then an approach analogous to that for measuring  $\phi_{IC}$  is appropriate. One measures the relative photon yield for exciting into  $S_1$  and  $T_1$ .

$$\phi_{ISC} = \phi_p(S_1)/\phi_p(T_1)$$

An approach for setting lower limits on  $\phi_{ISC}$  is to use photochemical or photophysical scavenging of the  $T_1$  states to 'count' the number of triplets formed per photon absorbed into  $S_1$ . Suitable counting techniques include irreversible chemical reactions<sup>26</sup>, fully reversible reactions, and energy transfer, followed by excited state reactions of the acceptor. Oxygen is a commonly used counter<sup>27</sup>. Singlet oxygen formed by quenching of excited states is scavenged by a suitable trap



The amount of singlet oxygen formed can be determined by monitoring oxygen consumption. Direct measurements of  $k_{ISC}$  and  $k_{IC}$  are possible in principle by exciting the upper excited state and watching the build up of fluorescence or phosphorescence. In practice such measurements are not easily performed because of the extremely high relaxation rates, which would require the use of pico-second lasers.



### 1.5 Non-Radiative Processes

Non-radiative relaxation can occur in two ways namely, via intra-molecular and inter-molecular processes. Inter-molecular relaxation involves quenching of the excited state by a second species, with or without electronic energy transfer. Intra-molecular relaxation can be grouped as:

- 1) Intersystem crossing between states of different multiplicity.
- 2) Vibrational relaxation of an excited state within a given electronic state by collisional interaction with the medium.
- 3) Internal conversion from one electronic state to another state of the same multiplicity.

Processes (1) and (3) occur between isoenergetic vibronic levels of the two states followed by vibrational relaxation.

Most experimental and theoretical work has been applied to aromatic molecules. These treatments have been reviewed by Jortner *et al.*<sup>28</sup> and Henry and Kasha<sup>29</sup>. Many of the approaches are based on the idea that the accessible vibronic levels of the initial state are coupled to a near continuum of isoenergetic levels of the final state.

Engleman and Jortner<sup>30</sup> have developed a unified analysis to describe the theory of non-radiative rate constants. The rate constant of crossing from state  $i$  to state  $j$  is the sum over all levels of the individual transition probabilities  $k_{ij}$ . Each value of  $k_{ij}$  is determined by matrix elements for the coupling of the states, which include both electronic factors,  $C$ , and Frank-Condon factors,  $S_{ij}$ :

$$k_{ij} = \langle \psi_j | V_{ij} | \psi_i \rangle; \quad V_{ij} = CS_{ij}$$

If the two states involved have the same multiplicity, then vibronic coupling largely determines the value of  $C$ . If however, a change in multiplicity is involved, spin-orbit coupling must also be included in its evaluation. The value of  $k_{ij}$  is dependent upon molecular structure and the two quantities,  $\Delta E$ , the difference in the zero-point energies of  $i$  and  $j$ , and  $\Delta Q^\circ$ , the displacement of one potential minimum relative to the other along the coordinate axis describing this dependence. If only one vibration mode couples  $i$  to  $j$ , for example, a symmetric breathing mode<sup>31</sup>, then  $\Delta Q^\circ$  can be represented by a two-dimensional potential diagram. Engleman and Jortner have envisaged two limiting cases: weak coupling, when  $\Delta Q^\circ$  is small, and strong coupling when  $\Delta Q^\circ$  is large. These are illustrated in Figure 1.9 which shows the crossing of two potential surfaces.

The coupling strength can be related to the Stokes shift between absorption and emission,  $E_s$ , which in the strong-coupling case where  $E_s$  is large is given by:

$$E_s \gg 2\langle \nu \rangle \tanh \langle \nu \rangle / 2kT \quad (1.46)$$

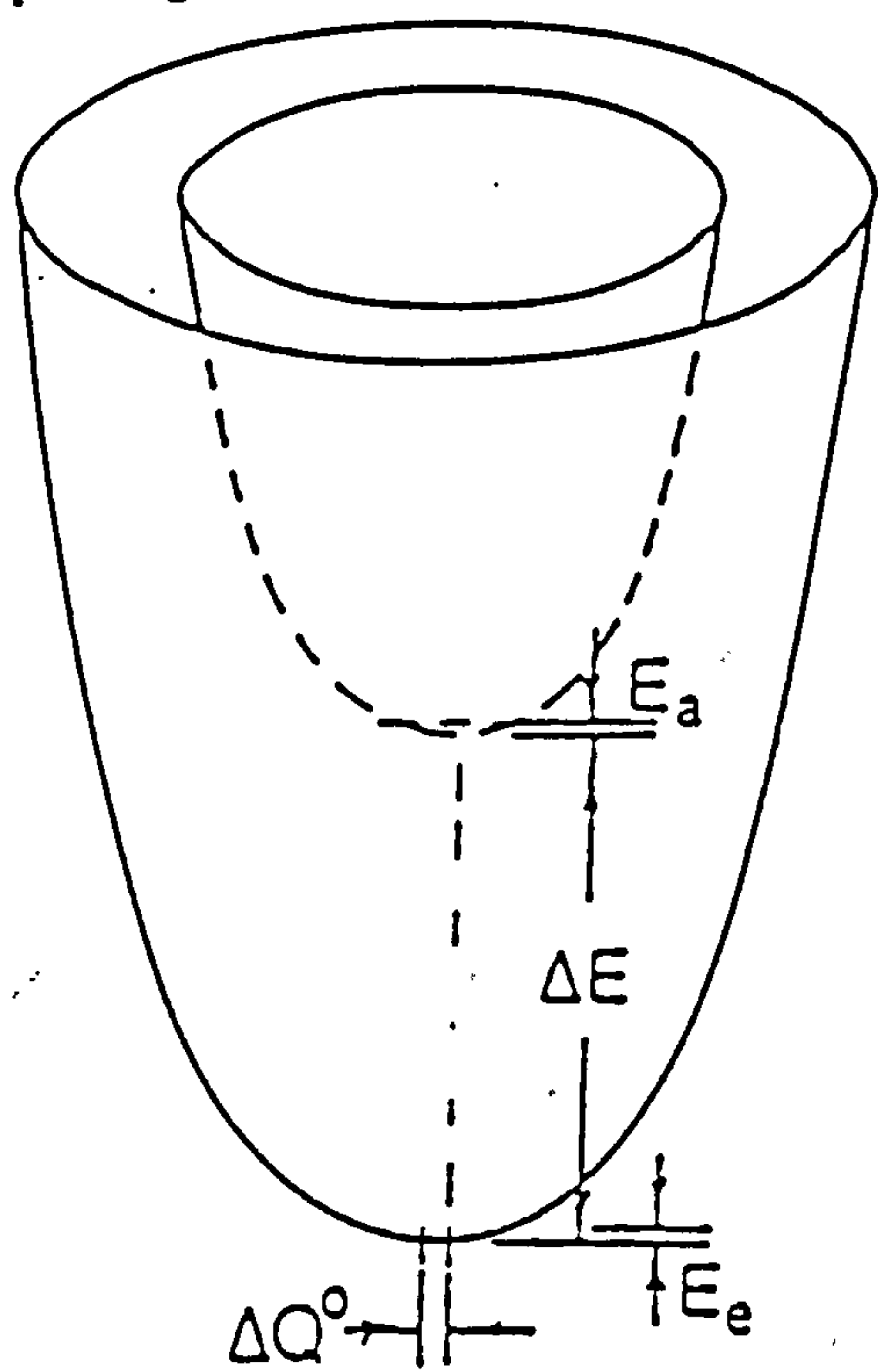
where  $\nu$  is the mean vibrational energy in the molecule. In the weak-coupling limit,  $E_s$  is small:

$$E_s \approx 2\langle \nu \rangle \quad (1.47)$$

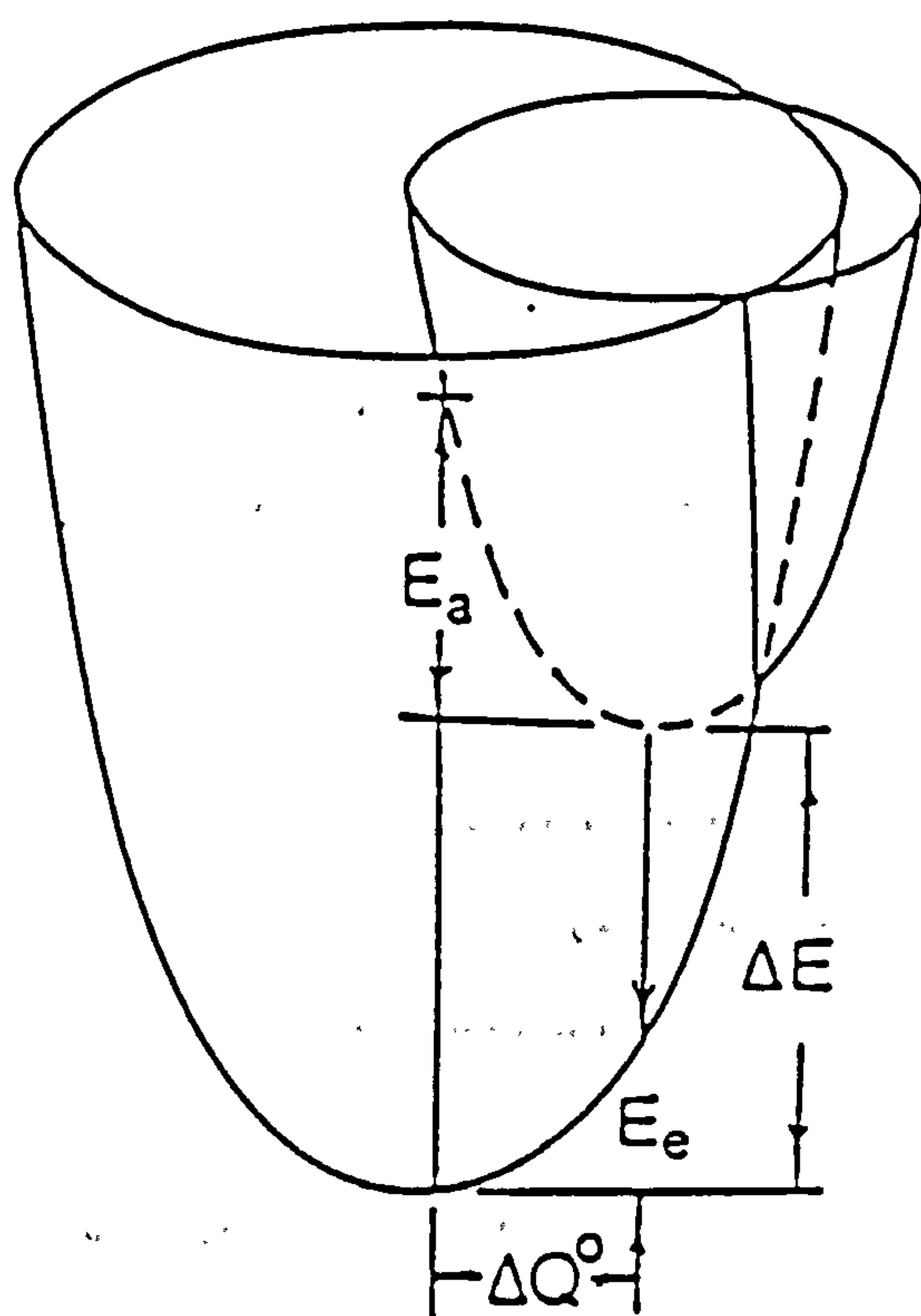
For a strong coupling situation to apply, the Stokes shift would have to exceed  $10,000 \text{ cm}^{-1}$ , and this would apply to relaxation via photochemical rearrangement rather than intersystem crossing. The weak-coupling case, to which the theories of Robinson and Frosch<sup>32</sup> and Ross *et al.*<sup>33</sup> apply, is presumed to be the situation for small configurational changes

Figure 1.9      Schematic potential energy surfaces for (a) strong coupling, and (b) weak coupling. The Stokes shift,  $E_s$ , is represented by the sum  $E_e + E_a$ .  $\Delta Q$  - the displacement of one potential minimum relative to the other along an appropriate coordinate (from ref. 15).





(a)



(b)

involved in internal conversion and intersystem crossing, where  $E_s \approx 4000 \text{ cm}^{-1}$ .

The transition probability for the weak coupling case at low temperatures becomes

$$k_{ij} = \frac{C^2(2\pi)^{1/2}}{h(\nu_m \Delta E)^{1/2}} \exp \frac{-\gamma \Delta E}{\nu_m} \quad (1.48)$$

where  $\nu_m$  is the energy of the highest frequency vibrational modes and

$$\gamma = \log \frac{\Delta E}{\nu_m \Delta \mu^2} - 1 \approx 1 \quad (1.49)$$

where  $\Delta \mu$  is a dimensionless coordinate, corresponding to  $\Delta Q_\mu^\circ$ . Equation (1.48) predicts the absence of any major temperature dependence for the crossing-rate constant.

At higher temperatures however, the expression for  $k_{ij}$  becomes more complex, but there is still only a weak temperature dependence involved. In this treatment,  $C$ , is assumed to be temperature independent.

In the strong-coupling case, there is a temperature dependence other than at very low temperatures.

Experimentally, there is not a great deal of information available about intersystem crossing and internal conversions in transition metal complexes.

For both  $d^3$  <sup>17</sup> and  $d^6$  <sup>34</sup> systems, intersystem crossing has been shown to be competitive with radiative processes. For some systems there is a strong dependence of the lifetime and quantum yields upon the medium and

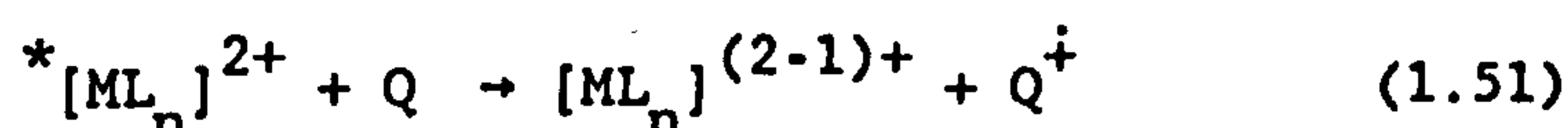
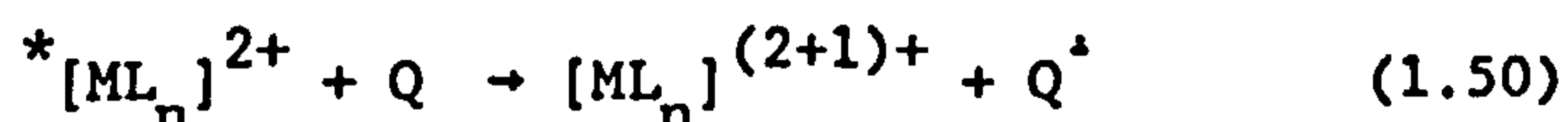
the temperature. This is illustrated by  $[\text{Cr}(\text{CN})_6]^{3-}$  which in a host crystal of  $\text{K}_3[\text{Co}(\text{CN})_6]$  has a phosphorescence lifetime of 0.12 sec at  $T < 50 \text{ K}$  which decreases to 0.05 sec at 300 K<sup>35</sup>. This temperature dependence is that expected for a forbidden but vibronically allowed transition<sup>36</sup>.

## 1.6 Quenching Processes and Quenching Mechanisms

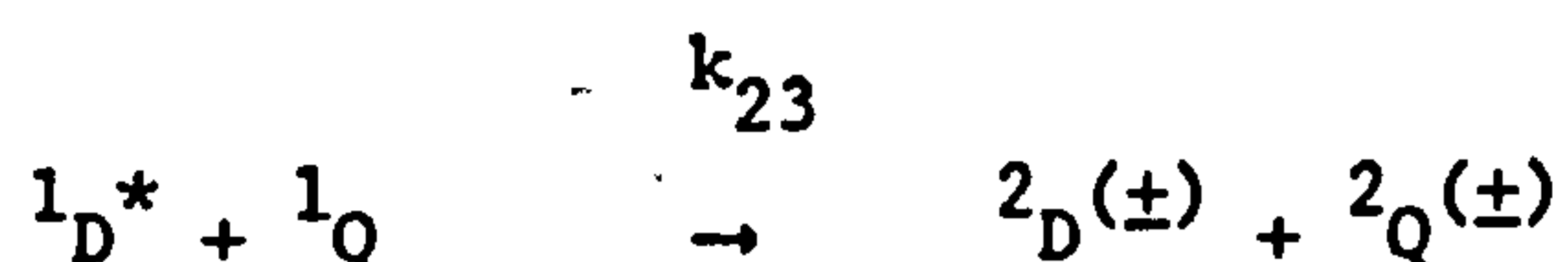
### 1.6.1 Excited State Electron-Transfer Quenching

The investigation of the quenching of luminescent states of transition metal complexes by electron-transfer processes has been a major area of activity throughout the 1970's and has been reviewed in depth recently<sup>37</sup>.

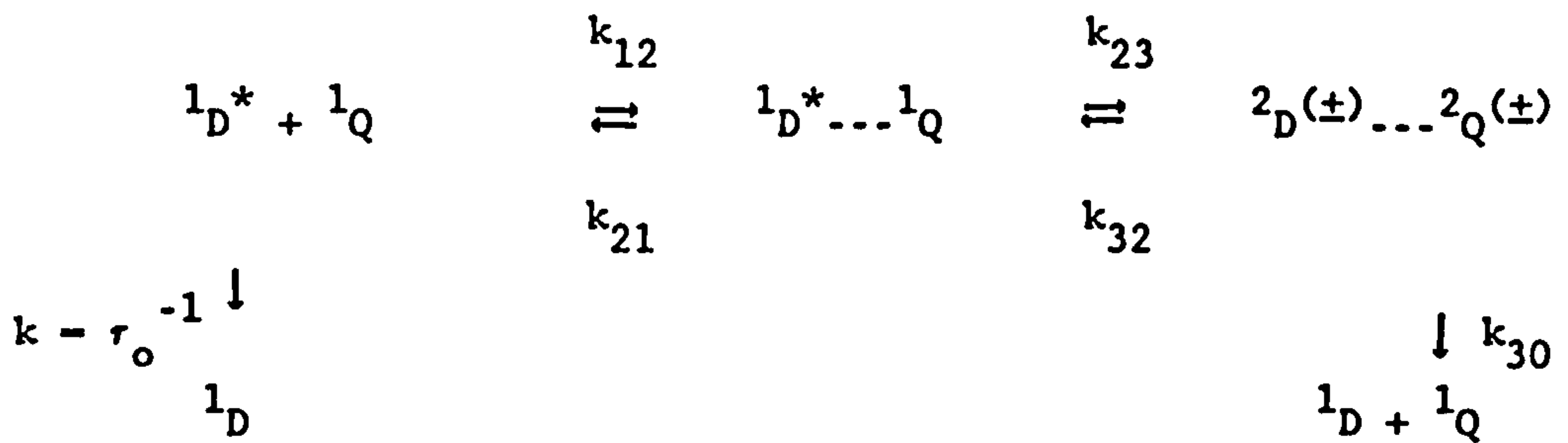
There are two possible directions for the transfer process, namely, oxidative and reductive quenching of the complex shown by equations (1.50) and (1.51) respectively:



The relationship between the rate of the general electron-transfer process



and, inter-alia, the redox potentials  $E^\circ(\text{D}^*/\text{D}^+)$  and  $E^\circ(\text{Q}^-/\text{Q})$  is due to Rehm and Weller<sup>38</sup>, who extended Marcus theory<sup>39,40</sup> for ground-state electron transfer reactions according to the following scheme:



Scheme 1

Application of the steady-state approximation leads to the overall rate of luminescence quenching

$$k_Q = \frac{k_{12}}{1 + \frac{k_{21}}{k_{23}} + \frac{k_{21}}{k_{30}} + \frac{1}{K_{23}}} \quad (1.52)$$

where  $K_{23} = k_{23}/k_{32} = \exp(-\Delta G_{23}^0/RT)$

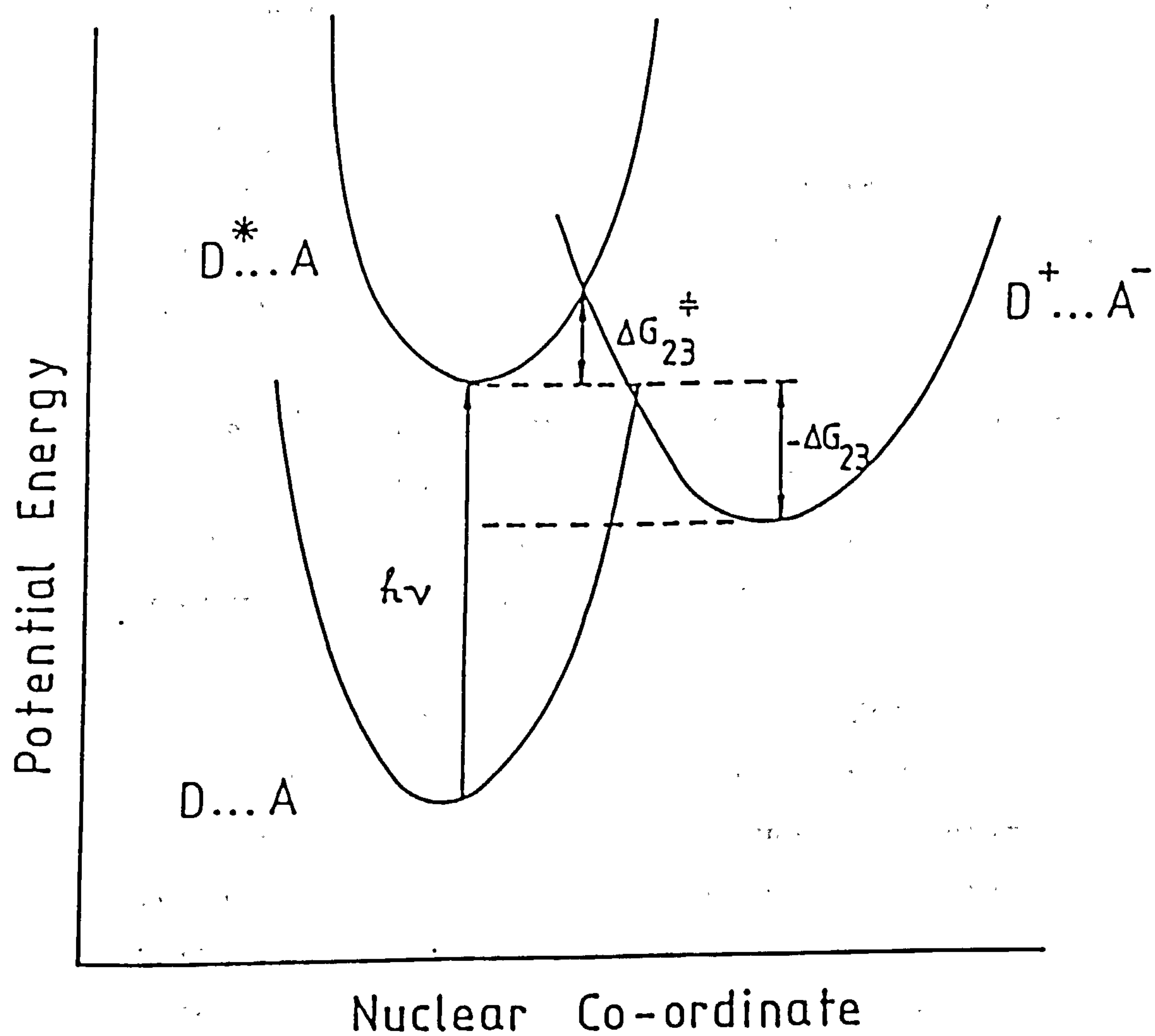
$\Delta G_{23}^0$  is the thermodynamic free energy change for step  $k_{23}$  in the Weller scheme.  $\Delta G_{23}^\ddagger$  is the associated free energy of activation for this step. Figure 1.10 shows a schematic diagram for the energy profiles for an electron transfer process. If it is assumed that  $k_{12}$ ,  $k_{21}$  and  $k_{30}$  are approximately constant for a series of closely related quenchers, then equation (1.52) reduces to equation (1.53)

$$k_Q = \frac{k_{12}}{1 + \frac{k_{12}}{K_{12}k_{30}} [\exp(\Delta G_{23}^\ddagger/RT) + \exp(\Delta G_{23}^0/RT)]} \quad (1.53)$$

When  $\Delta G_{23}^0$  is large and negative, equation (1.53) reduces to equation (1.54)

$$k_Q(1t \Delta G_{23}^0 \ll 0) = \frac{k_{12}K_{12}k_{30}}{K_{12}k_{30} + k_{12} \exp(\Delta G^\ddagger/RT)} \quad (1.54)$$

**Figure 1.10**      **Schematic diagram of the energy profiles for an electron transfer process.**



This equation indicates that when  $\Delta G_{23}^\ddagger$  is zero or very small, then  $k_Q$  achieves a constant value, i.e.  $k_Q$  reaches a plateau region. When  $\Delta G_{23}$  is large and positive, then  $\Delta G_{23} \approx \Delta G_{23}^\ddagger$  and equation (1.53) reduces to equation (1.55).

$$k_Q \text{ (lt } \Delta G_{23} \gg 0) = (K_{12}k_{30}/2) \exp (-\Delta G_{23}/RT) \quad (1.55)$$

$\Delta G_{23}$  can also be written in terms of the redox couples involved in the electron transfer step. For an excited donor species we can write

$$\Delta G_{23} = E^\circ(D^+/D^*) - E^\circ(Q/Q^-) + w_p - w_r \quad (1.56)$$

where  $w_p$  and  $w_r$  represent the electrostatic energies involved in forming the 'ion-pair' and 'encounter complex' respectively. From equations (1.54), (1.55) and (1.56) two important limiting cases can be predicted, i.e.

- (1) at low  $E^\circ(Q/Q^-)$ , a plot of  $\log k_Q$  versus  $E(Q/Q^-)$  for a given donor should be linear with a slope  $(-1/2.303 RT)$ ;
- (2) at high  $E^\circ(Q/Q^-)$ , this plot should reach a limiting value.

The predictions are borne out in Figure 1.11.

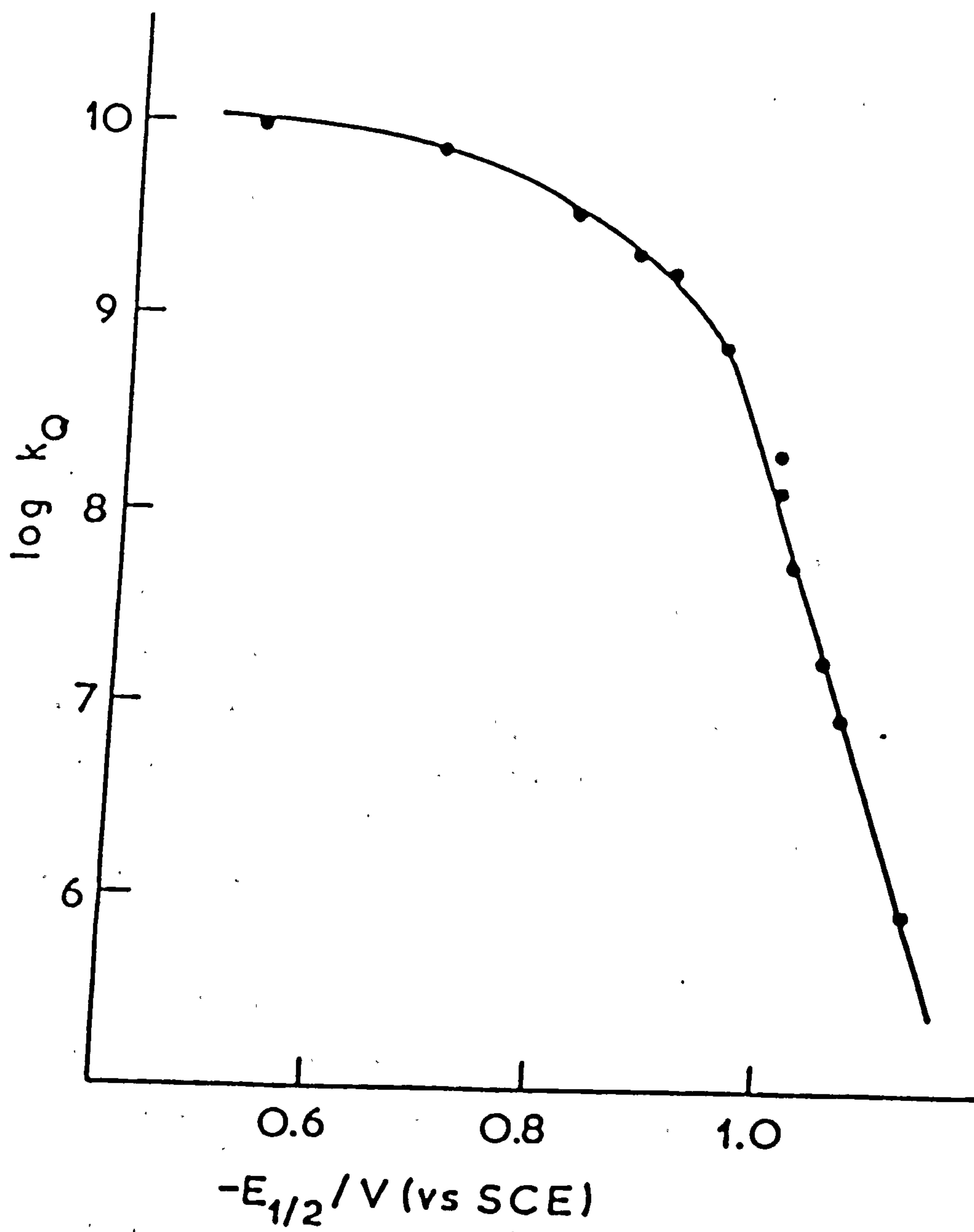
### 1.6.2 Quenching of Excited States by Energy Transfer

In this process, an excited donor molecule collapses to its ground state with the simultaneous transfer of its electronic excitation energy to an acceptor molecule which is thereby promoted to an excited state.

Neglecting the radiative intermolecular process, whereby the emission of one molecule is absorbed by another, there are otherwise two principal mechanisms of energy transfer: long-range resonance transfer and collisional energy transfer.



Figure 1.11      Plot of  $\log k_q$  versus half-wave reduction potential of a series of nitroaromatic quenchers in the quenching of  $^*[Ru(bipy)_3]^{2+}$  (from ref.22).



Collisional energy transfer is the most important for transition metal complexes. The energy transfer is the process by which one excited molecule donor, D, is quenched and simultaneously excites another, the acceptor, A, is raised to an excited state.



Collisional-energy transfer involves a bimolecular encounter between the donor and acceptor molecules. It is often found that every collision results in energy transfer. The diffusion controlled rate constant is then given by a modified version of the Stokes-Einstein equation.

$$k_d = \frac{8kT}{3000\eta}$$

The energy transfer is therefore an inverse function of the viscosity,  $\eta$ . For a solvent of relatively low viscosity such as water at room temperature,  $k_d$  is approximately  $5 \times 10^9 \text{ dm}^{-1} \text{ mol}^{-1} \text{ s}^{-1}$ , while  $k_d$  for a viscous solvent like glycerine is about  $5 \times 10^6 \text{ dm}^{-1} \text{ mol}^{-1} \text{ s}^{-1}$ . The energy transfer rate constant  $k_{et}$  may be controlled by other factors, for example if the donor excited state level lies below that of the acceptor then a normal Boltzmann factor will influence the energy-transfer constant<sup>41</sup>.

Long-range energy transfer is generally recognised by the fact that it occurs in a rigid medium at dilutions such that donor and acceptor may be an average distance of some 50 to 100 Å apart.

If an interaction occurs between  $D^*$  and A, no matter how small, it can be described by a perturbation Hamiltonian operator  $H'$ . The system ( $D^* + A$ ) is no longer a 'stationary' state of the total Hamiltonian

$(H_D^* + H_A + H')$ . If an isoenergetic system  $(D + A^*)$  exists, then time-dependent perturbation theory reveals that the effect of the interaction  $H'$  is to cause the system  $(D^* + A)$  to evolve into the system  $(D + A^*)$  and vice versa, with a probability given by<sup>42</sup>

$$P \propto \rho \langle \Psi_i / H' / \Psi_F \rangle^2$$

where  $\rho$  is the density of isoenergetic states,  $\Psi_i$  describes the initial system  $(D^* + A)$ , and  $\Psi_F$  describes the final system  $(D + A^*)$ .

The perturbation therefore induces coupled radiationless transitions in both D and A so that the excitation energy is shuttled back and forth between D and A and the rate of energy transfer ( $k_{et}$ ) is determined by the strength of the interaction  $H'$ . The state density factor  $\rho$  is a measure of the number of coupled isoenergetic donor and acceptor transitions.

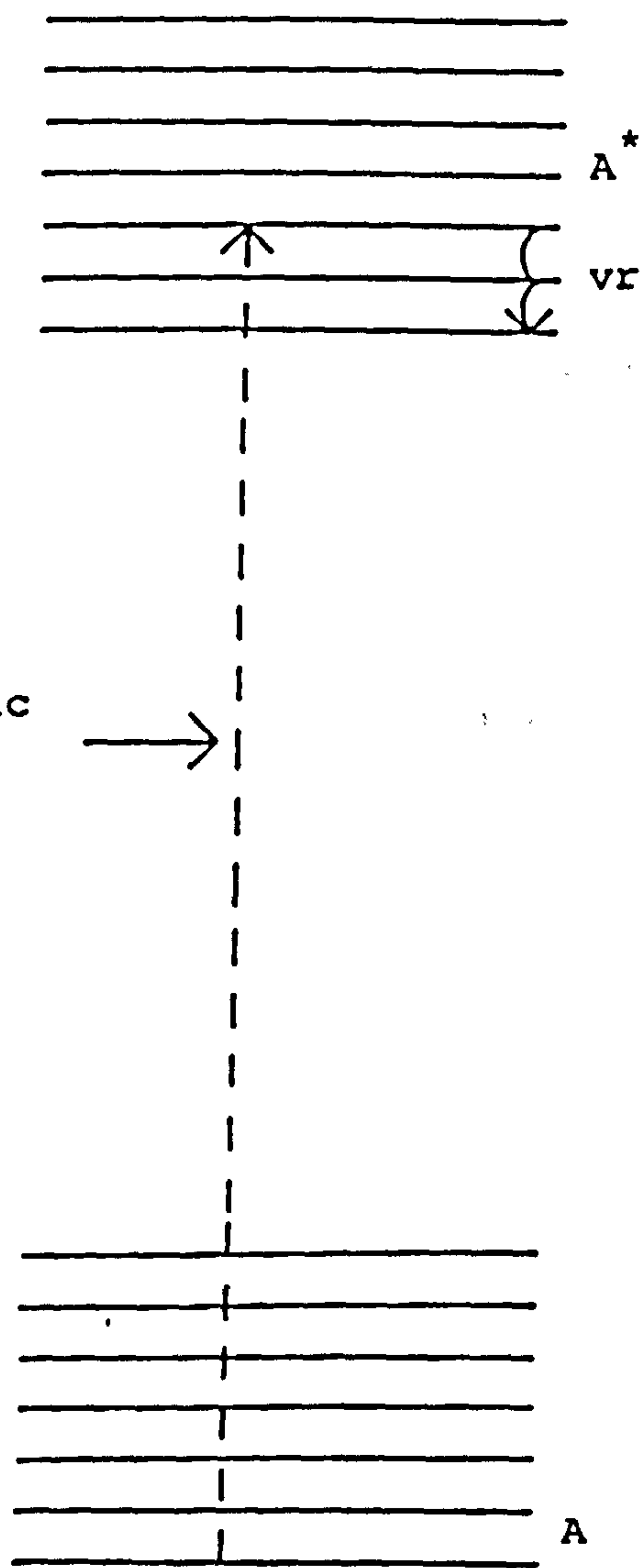
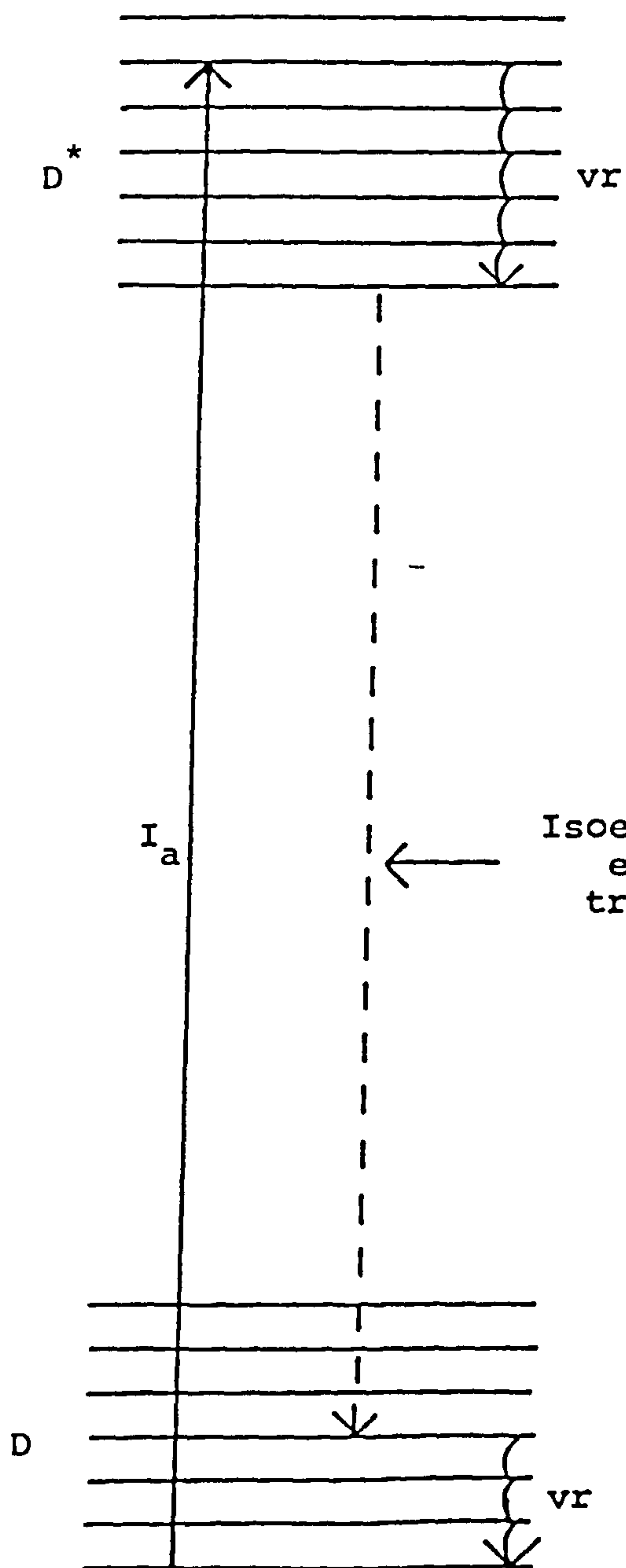
Where  $H'$  is sufficiently small and  $k_{et} < k_{vr}$  the rate constant for vibrational relaxation under these circumstances (i)  $D^*$  will undergo energy transfer from its bottom vibrational level; (ii)  $A^*$ , when formed, will promptly collapse to its lowest vibrational level, making the energy transfer unidirectional. The coupling of isoenergetic donor and acceptor transitions is shown in Figure 1.12.

The perturbation  $H'$  contains several terms such as Coulombic and electron exchange interactions.

The Colombic interaction has been treated by Förster

$$k_{et} = 1.25 \times 10^7 \frac{\phi_E}{\eta^4 r_D r^6} \int F_D(\nu) \epsilon_A(\nu) \frac{d\nu}{\nu^4}$$

Figure 1.12      Schematic representation for nonradiative energy transfer, 'vr' indicates vibrational relaxation.



Isoenergetic  
energy  
transfer

where  $\phi_E$  is the quantum yield for donor emission,  $\tau_D$  is the lifetime of the emission,  $n$  is the refractive index of the solvent and  $r$  is the distance between  $D^*$  and A.  $F_D(\nu)$  is the emission spectrum of the donor expressed in wavenumbers and  $\epsilon_A(\nu)$  is the extinction coefficient of A at the wavenumber  $\nu$ .

The electron-exchange Hamiltonian  $H'$  is given by

$$k_{et} \propto e^{-2R/L} \int F_D(\nu) \epsilon_A(\nu) d\nu$$

where  $R$  is the distance between  $D^*$  and A and  $L$  is a constant.

## 1.7 Photochemical Reactions of Electronically Excited Transition Metal Complexes

Most transition metal excited states can be classified as "ligand field" or "charge transfer" electronic states. This depends on whether the ground-state electronic orbitals have predominantly metal-d-orbital character (i.e. LF-states) or differ in the amount of metal and ligand contribution (CT-states) in the electronic wave function. The chemistry observed is a function of the excited state electronic configuration and the possibilities are as follows:

- A) Unimolecular processes originating in LF-states
  - i) Substitutional processes ( $S$  = solvent,  $L$  = ligand)
 
$$^*ML_6 + S \rightarrow ML_5S + L$$
  - ii) Isomerisation processes ( $LL$  = bidentate or two monodentate ligands)
 
$$(cis \text{ or } trans)-^*M(LL)_2XY \rightarrow (trans \text{ or } cis)-M(LL)_2XY$$



iii) Deactivation processes



iv) Radiative processes



B) Unimolecular processes originating from CT states

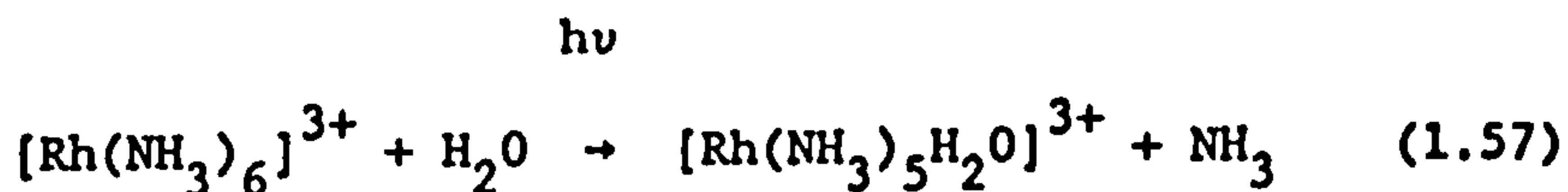
i) Oxidation-reduction processes



ii) As in (i)-(iv) above

Substitutional, isomerisation and electron transfer reactions will be dealt with briefly here. For a more comprehensive review of these and other reactions of excited state transition metal complexes see references 3, 15 and 43.

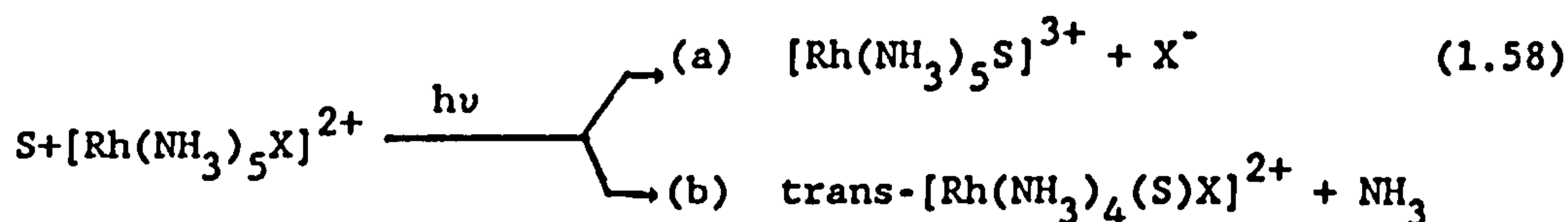
The photoreactions of Rh(III) ammine complexes can serve as a prototype for the excited-state chemistry of other complexes having the important  $d^6$  configuration, including complexes of Ir(III), Co(III), Fe(II), Os(II) and Pt(IV) as well as the extensively studied complexes of Ru(II)<sup>44</sup>. The ground state complexes of Rh(III) have low-spin configurations and are slow in their thermal substitution reactions. A typical photo-reaction is illustrated in equation (1.57):



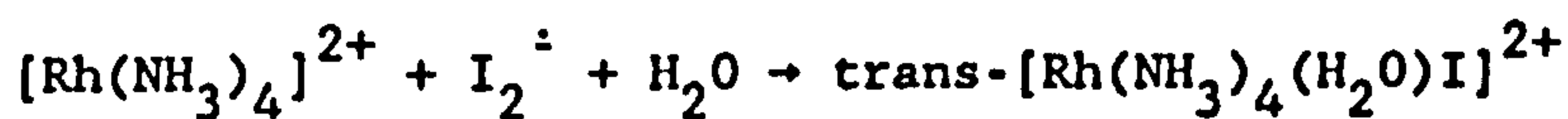
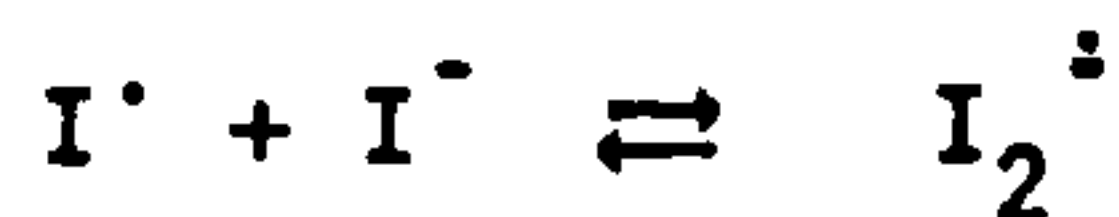
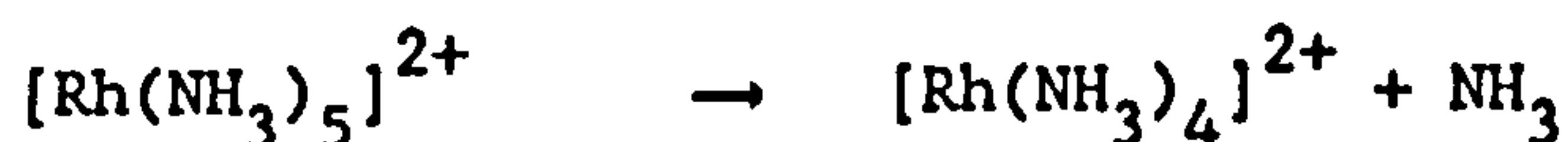
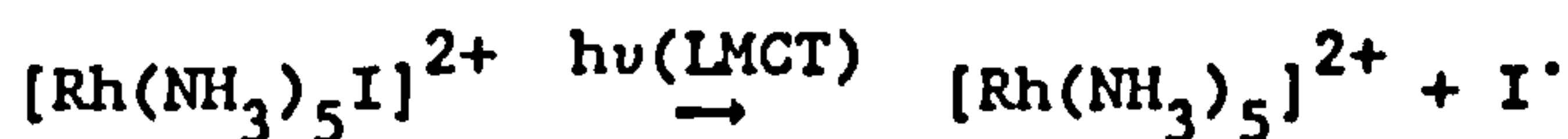
The ammine complexes are of particular interest since both the lower energy absorption bands (in the near UV) and the excited state luminescence involve electronic transitions between the ground state and ligand field excited states (i.e. d-d). The lowest energy absorption

bands in  $[\text{Rh}(\text{NH}_3)_6]^{3+}$ ,  $[\text{Rh}(\text{NH}_3)_5\text{Cl}]^{2+}$  and  $[\text{Rh}(\text{NH}_3)_5\text{py}]^{3+}$  (py - pyridine) correspond to the spin-allowed singlet to singlet LF transitions,  ${}^1\text{T}_{1g} \leftarrow {}^1\text{A}_{1g}$  and  ${}^1\text{T}_{2g} \leftarrow {}^1\text{A}_{1g}$ . The emission originates from the LF triplet  ${}^3\text{T}_{1g}$  and it is generally concluded that the large majority of singlet excited states undergo efficient ISC to the lower energy triplet LF state.

The halopentaamminerhodium(III) complexes in solution undergo photo-substitution both of halide and ammine ligands, processes which are dependent upon the nature of the excited species.

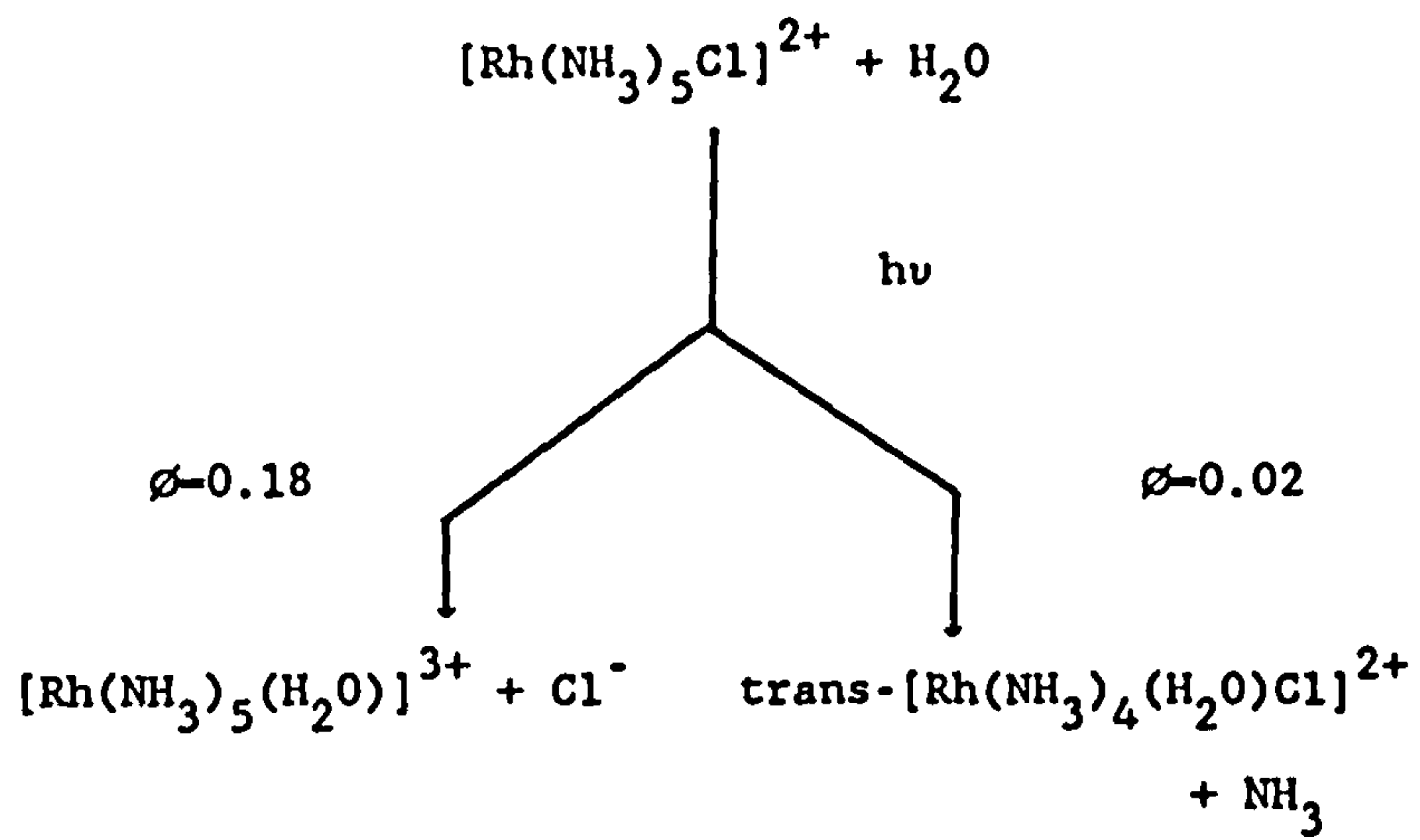


For  $\text{X} = \text{I}^-$ , the LMCT band is seen in the UV spectrum. When aqueous solutions of  $[\text{Rh}(\text{NH}_3)_5\text{I}]^{2+}$  with traces of  $\text{I}^-$  were flash photolysed,  $\text{I}_2^\cdot$  was detected. Thus although the net photoreaction is substitution of  $\text{NH}_3$  to give  $\text{trans-}[\text{Rh}(\text{NH}_3)_4(\text{H}_2\text{O})\text{I}]^{2+}$ , the primary mechanism involves a photoredox process.



For  $[\text{Rh}(\text{NH}_3)_5\text{Cl}]^{2+}$  in aqueous solution at  $25^\circ\text{C}$ , the main reaction is aquation of  $\text{Cl}^-$  although modest aquation of  $\text{NH}_3$  is also detected.

No evidence of a redox process is observed in this case.



## **Chapter 2**

### **Introduction**

### **Electron Spin Resonance**

## 2.1 Electron Spin Resonance

ESR is the phenomenon whereby the orientation of the spin angular momentum of a species containing one or more unpaired electrons with respect to an external magnetic field, intensity  $B_0$ , is reversed on application of a suitable source of radiation, normally in the microwave region. The frequency  $\nu_0$  of the electromagnetic radiation which causes the ESR transition, is related to the magnetic field  $B_0$ , in which the sample is placed, by the equation

$$h\nu_0 = g\beta B_0 \quad (2.1)$$

where  $h$  is Planck's constant,  $\beta$  is the Bohr magneton, and  $g$  is a numerical factor which is close to two when no significant orbital contribution is involved, as in most organic molecules.

In order to give a more precise meaning to the energy levels involved in the observed transitions, we must first examine the way in which the magnetic properties of the electron follow from its spin and orbital motions. We can then formulate the conditions under which resonant absorption occurs.

## 2.2 Magnetic Properties of the Electron

### 2.2.1 Interaction with a Magnetic Field

An electron interacts with a magnetic field such as to align itself with its magnetic moment vector along the field direction.

The energy of a magnetic dipole of moment  $\mu$  in a field  $B_0$  is given by

$$E = -\mu B_0 \cos\theta \quad (2.2)$$

where  $\theta$  is the angle between the axis of the dipole and the field direction. Thus different orientations of the magnetic moment vector with respect to  $B_0$  correspond to different energies. However, quantisation restricts the number of possible orientations. For an atom with total AM  $J\hbar/2\pi$ , there are  $2J + 1$  possible orientations, where  $M_J = J, J-1, J-2, \dots -J$ . The length of the vector is given by  $[J(J+1)]^{1/2}\hbar/2\pi$ . This means that the vector is never aligned exactly along the field direction but precesses about the axis of the field at a constant angle  $\theta$ , see Figure 2.1. The angular frequency  $\omega_0$  is called the Larmor frequency and is related to the applied field  $B_0$  by the equation

$$\omega_0 = \gamma B_0 \quad (2.3)$$

where  $\gamma$  is the magnetogyric ratio of the dipole.

If the magnetic moment of an atom is derived only from its spin angular momentum, i.e.  $L = 0$ , then the energy levels are given by

$$E_{MS} = 2\beta M_S B_0 \quad (2.4)$$

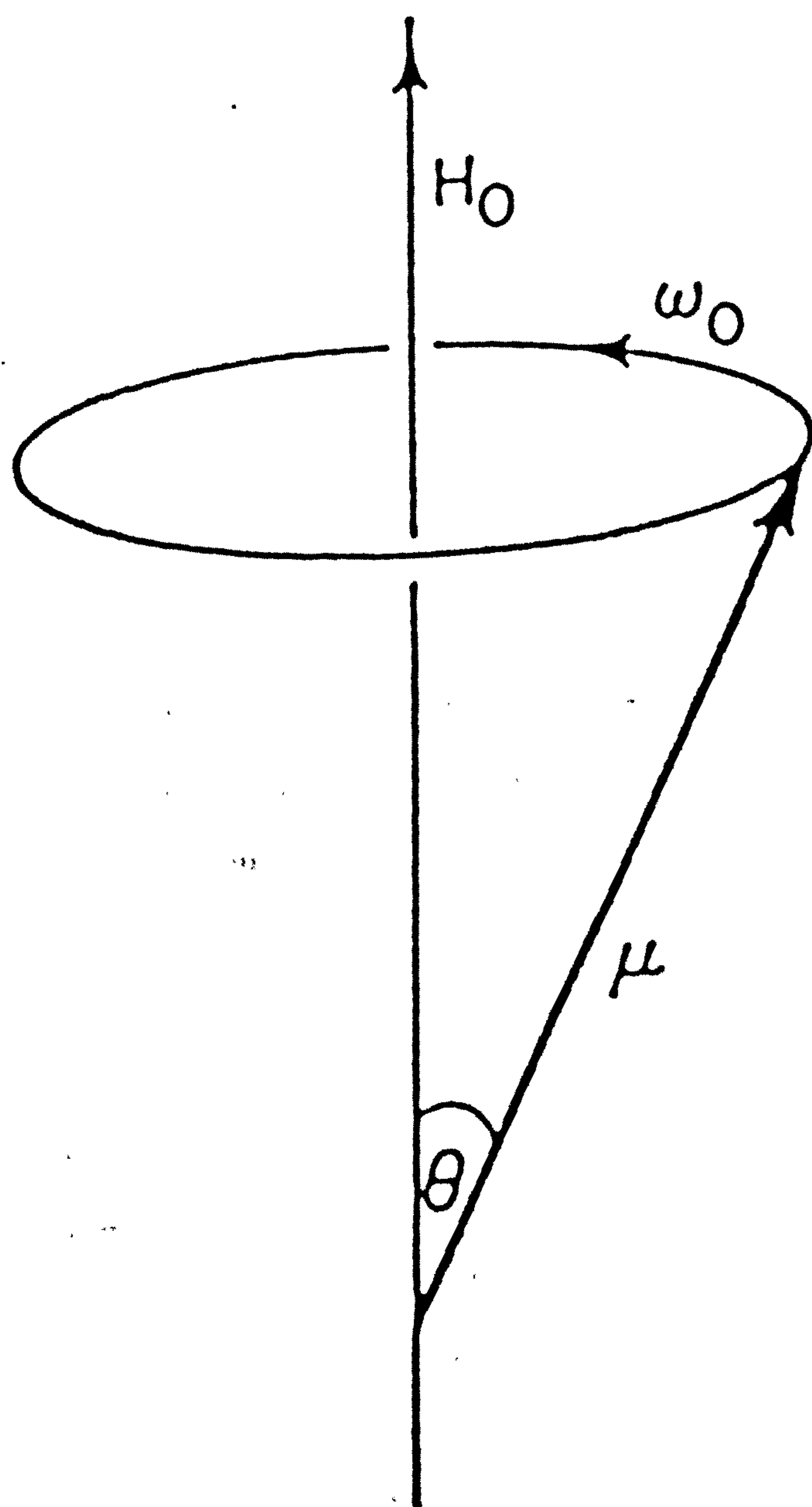
where  $M_S = S, S-1, \dots -S$ . Thus in a magnetic field each energy level corresponding to a given value of  $S$  (or  $J$ ) is split into  $2S+1$  sub-levels with equal separation of  $2\beta B_0$ . If on the other hand only the orbital angular momentum is involved, i.e.  $S=0$ , the the energy levels are given by

$$E_{ML} = \beta M_L B_0 \quad (2.5)$$

with an energy separation of  $\beta B_0$ .

Figure 2.1      The precession of a magnetic dipole about the axis of an external magnetic field  $B_0$ . The angular velocity of precession is  $\omega_0$ .





When  $L$  and  $S$  are strongly coupled to give a resultant momentum  $J$ , the energy levels are given by equation (2.6), where  $g_J$  is a rational number depending on the values of  $L$ ,  $S$  and  $J$ .  $g_J$  is called the Landé splitting factor and takes the values given in equation (2.7)

$$E_{MJ} = g_J \beta M_J B_0 \quad (2.6)$$

$$g_J = \frac{1 + S(S+1) + J(J+1) - L(L+1)}{2J(J+1)} \quad (2.7)$$

While the  $g$ -factor can be calculated precisely for atoms with Russell-Saunders coupling the general  $g$ -factor used in equation (2.1) is an experimental parameter and cannot be calculated a priori.

Equations (2.5) and (2.6) show the energies for the magnetic or Zeeman levels for atoms in singlet states, i.e.  $S = 0$ , and in multiplet states, i.e.  $S \neq 0$ , respectively. The selection rule for magnetic transitions in atomic emission spectra is  $\Delta M_J = \pm 1$  or  $0$ . The Zeeman energy levels are shown in Figure 2.2.

### 2.2.2 The Resonance Conditions

Application of a magnetic field removes the degeneracy of the magnetic energy levels. The  $g$ -factor represents the rate of divergence of the magnetic energy levels with the field. In the simplest case, namely that of a free spin with  $M_J = M_S = \pm 1/2$ , only two energy levels are possible, and if  $g$  is constant, then the divergence of the Zeeman levels will be linear with the field. This is illustrated in Figure 2.3. The corresponding energy levels in a field  $B_0$  are given by equation (2.8) and the energy difference by equation (2.9).

Figure 2.2      Zeeman energy levels and transitions for an atom with  $J = 2$  or  $1$ : the spectrum consists of three equally spaced lines.

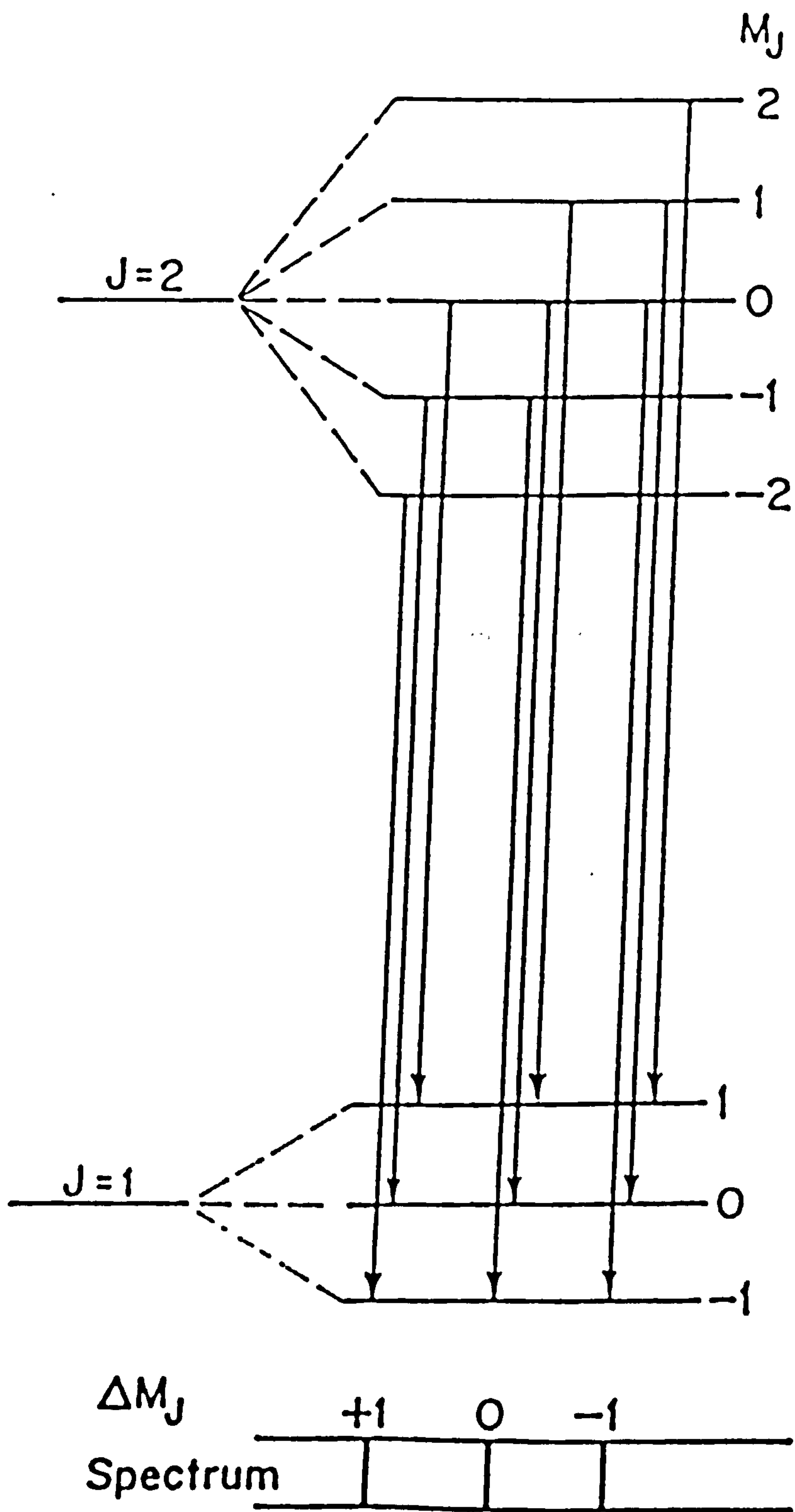
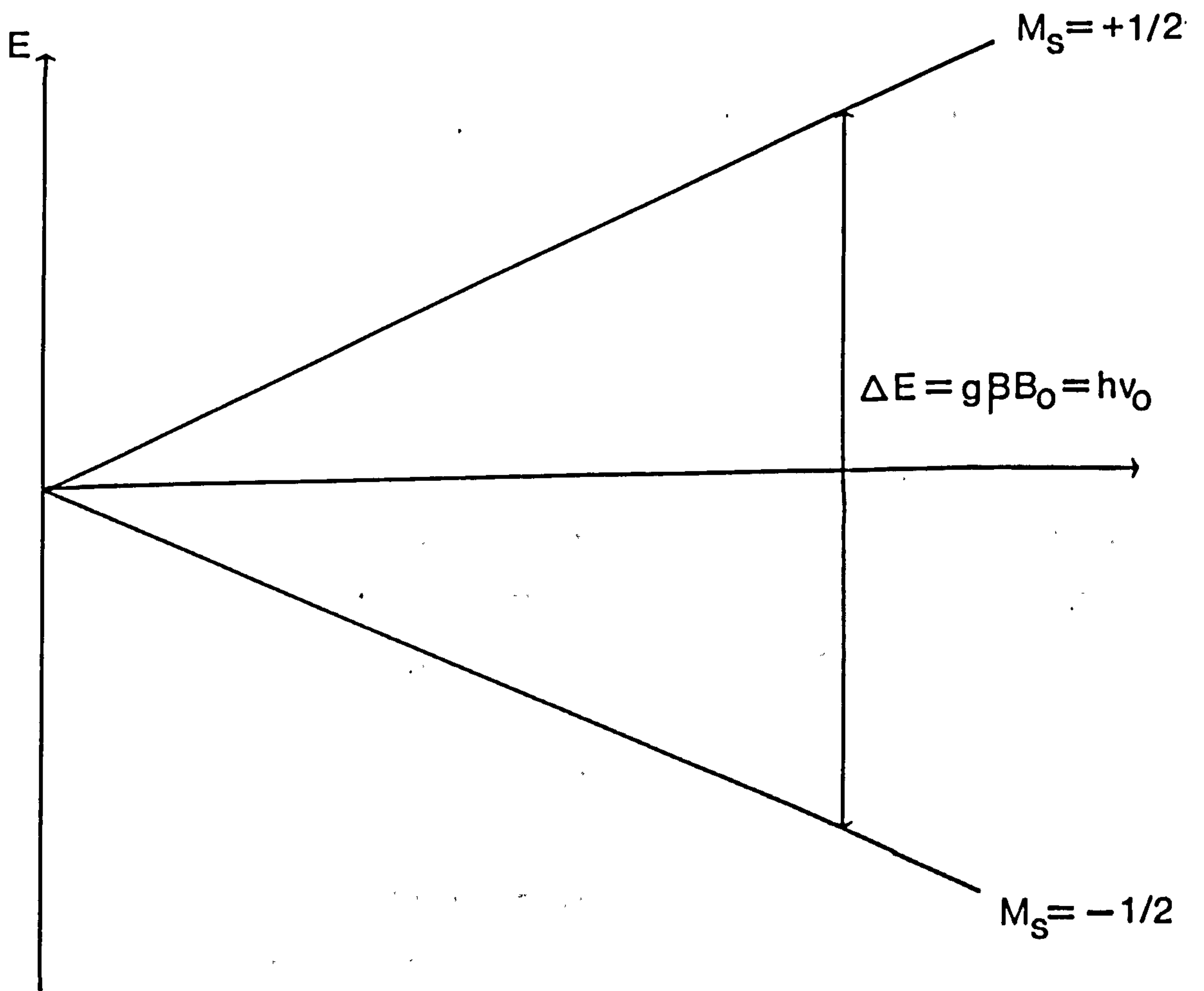


**Figure 2.3**      **Zeeman energy levels for a single unpaired electron as a function of magnetic field.**



$$E_{+1/2} = +1/2 g\beta B_0, \quad E_{-1/2} = -1/2 g\beta B_0 \quad (2.8)$$

$$\Delta E = g\beta B_0 = h\nu_0 \quad (2.9)$$

Transitions between these levels can be induced by the interaction of EM radiation of frequency  $\Delta E = h\nu_0$ , or in other words when the applied field is of the same frequency as  $\omega_0$ , the Larmor frequency.

Substituting into equation (2.9) reasonable values for  $B_0$  of 3500 G and with  $g = 2.00232$  as for a free electron, we find that  $\nu_0$  is of the order of 9000 to 10000 MHz corresponding to the microwave X-band region with a wavelength of about 3 cm.

### 2.2.3 Relaxation Processes

The difference in population between the lower ( $M_S = -1/2$ ) and the upper ( $M_S = +1/2$ ) states is very small. The population difference can be estimated from the Boltzmann distribution law, provided that the system is in thermal equilibrium, which is given by equation (2.10)

$$n_{(+1/2)}/n_{(-1/2)} = \exp (-g\beta B_0/kT) \quad (2.10)$$

where  $T$  is the absolute temperature. At a temperature of 300 K, and for a species with  $g = 2$  and with  $B_0 = 3000$  G, the ratio  $n_{+1/2}/n_{-1/2}$  is 0.9986. Thus the excess population in the ground state is only about 0.07%. However, the whole phenomenon of ESR absorption depends on this difference. The probability of upward transitions equals that for transitions downward. This means that the two levels would quickly become equally populated, resulting in a decrease of absorption in a process known as saturation. The processes which dissipate the energy



stored in the upper state, permitting a return to the ground state are known as relaxation processes. Spin-lattice relaxation involves interaction between the paramagnetic species and the surrounding medium. This interaction provides a pathway whereby excess spin energy finds its way into low energy 'lattice' or vibrational modes of the surrounding molecules.

The spin-lattice relaxation is characterised by a relaxation time  $T_1$ , which is the time for the spin-system to lose  $1/e$  parts of its excess energy. Slow spin-lattice relaxation causes saturation of the spin system, resulting in a decrease of energy absorbed. Extremely efficient operation of spin-lattice relaxation may result in line broadening because of the operation of Heisenberg's uncertainty principle, whereby reduction of  $T_1$  causes a corresponding uncertainty in the energy content.

Another important relaxation process is spin-spin relaxation which is characterised by the relaxation time  $T_2$ . Since any dipole, electronic or nuclear, produces a magnetic field at each of its neighbours, the total magnetic field experienced by a particular spin will include contributions from all of its neighbours which will differ from the applied field. This has the effect of producing transitions which will occur over a wide range of frequencies, resulting in line broadening.

Two types of line shapes are commonly encountered in ESR. When spin-spin broadening predominates the line shape is approximately Gaussian. On the other hand spin-lattice broadening results in a Lorentzian line shape.

#### 2.2.4 Hyperfine and Fine Structure

Many of the transition metal ions have a total spin  $S > 1/2$ . In such cases application of a magnetic field splits this energy level into  $2S+1$  magnetic energy levels. In the absence of any external fields, the transition frequencies will have the same energy and a single line will be observed. In general, however powerful electrostatic fields are present in crystalline matrices which remove the degeneracy (i.e. split the spin levels) even in the absence of any external field, giving rise to a zero-field splitting. This situation is illustrated in Figure 2.4 for an ion with  $S=3/2$ . Such multiple transitions are called fine structure, resulting in lines of unequal intensities and spacings.

#### 2.2.5 Nuclear Hyperfine Structure

A nucleus possessing a resultant angular momentum will also have a magnetic moment which will interact with the field, and the electronic magnetic moment to produce hyperfine structure. For a nucleus of spin  $I$ , there are  $2I+1$  observable values, where  $M_I = I, I-1, I-2, \dots -I$ , in the field direction. In a strong magnetic field the nuclear and angular momenta are decoupled, i.e. are quantised separately, and each electronic level is split into  $2I+1$  nuclear sub-levels. For the simplest case, a hydrogen atom with  $S=1/2$ ,  $I=1/2$  and  $L=0$ , the two electronic levels ( $M_S = +1/2$  and  $-1/2$ ) are further split into two nuclear levels ( $M_I = +1/2$  and  $-1/2$ ), see Figure 2.5.

#### 2.3 g-Factors

The local environment of a paramagnetic ion has a profound effect on the g-factor. The orbital motion of the electron is distorted by electric fields of neighbouring species, i.e. ligands, and this effect will react

Figure 2.4      Energy levels for a system with spin  $S = 3/2$  with zero-field splitting  $\Delta h\nu$ .

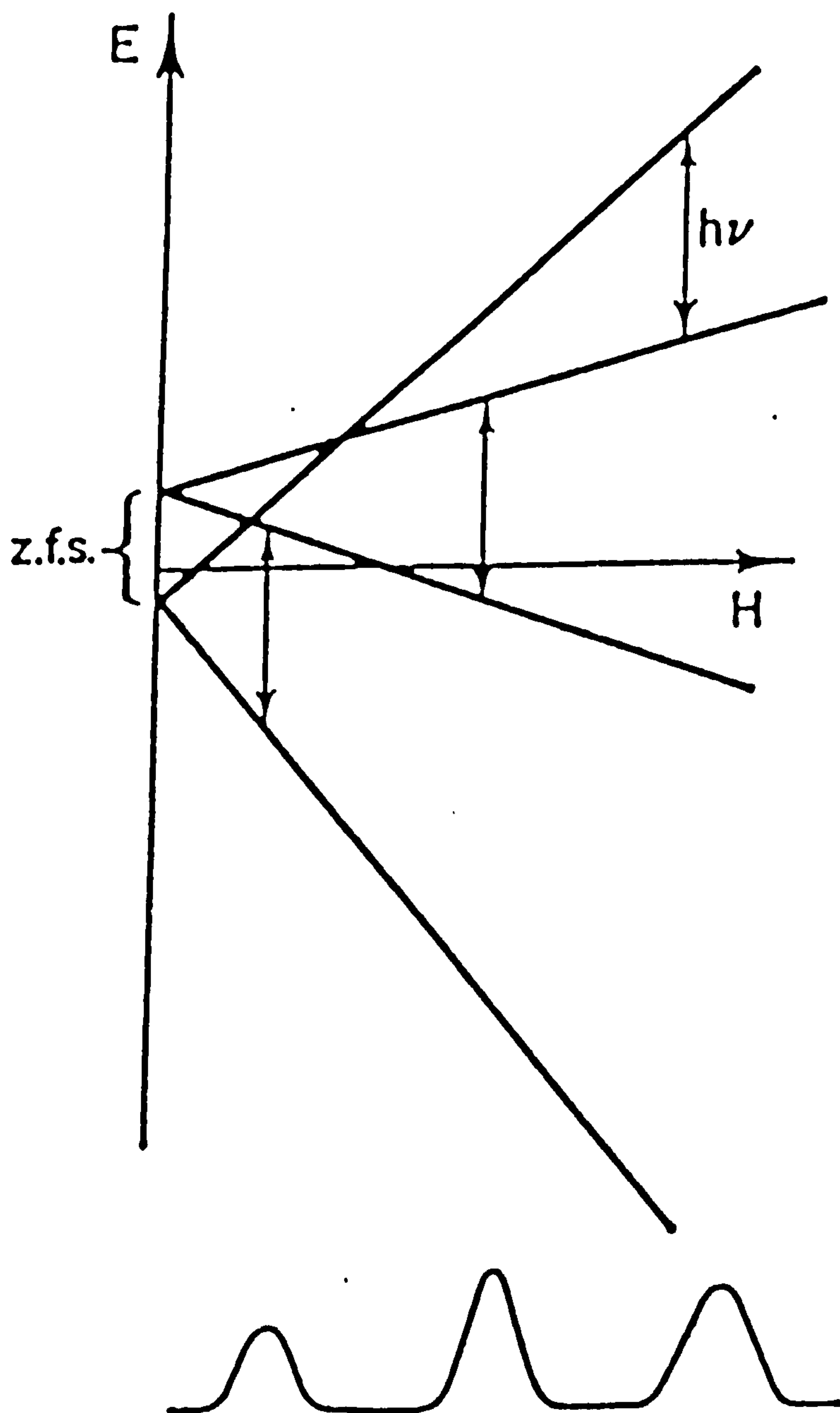
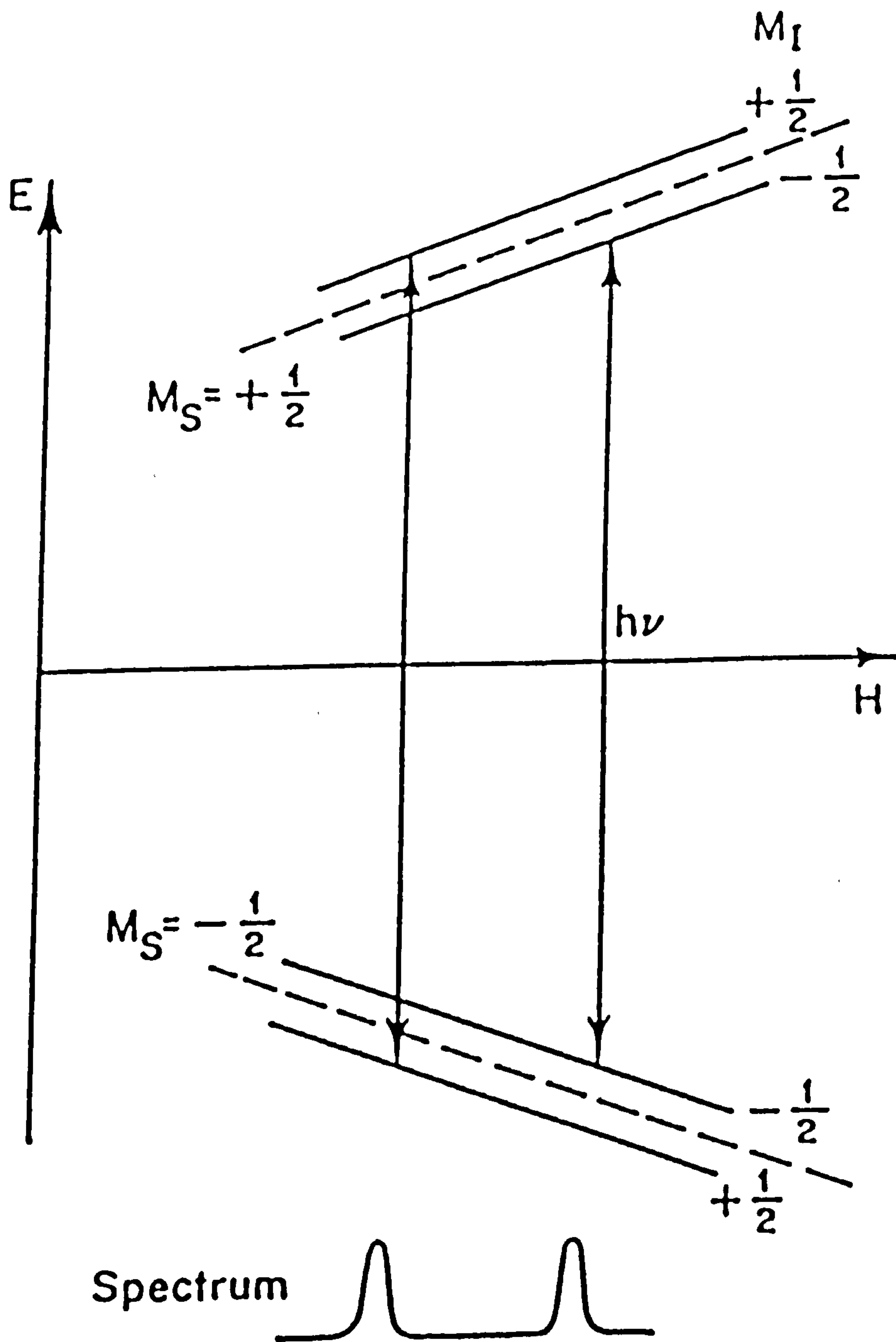


Figure 2.5      Energy levels for a system with electron spin  $S = \frac{1}{2}$  and nuclear spin  $I = \frac{1}{2}$ , as a function of magnetic field.



upon the spin through the coupling between orbital and spin angular momenta. A general simplified Hamiltonian for an ion in a crystalline environment can be written

$$H = H_{LS} + H_V + H_{SH} + H_{IH} \quad (2.11)$$

$H_{LS}$  represents S-O coupling and may be expressed as follows

$$H_{LS} = \lambda L \cdot S \quad (2.12)$$

where  $\lambda$  is an interaction constant and  $L$  and  $S$  are free-ion values derived from the ground state.

$H_V$  describes the effect of a crystal field and may be written

$$H_V = \sum_i e_i V(r_i) \quad (2.13)$$

in which  $V(r_i)$  is the electrostatic potential at the ion with which each electron interacts.  $H_{SH}$  and  $H_{IH}$  represent the interaction of the angular momenta of the electrons and nuclei respectively with the field

$$H_{SH} = \beta(L + g_e S) \cdot H_o \quad (2.14)$$

$$H_{IH} = \frac{h}{2\pi} \sum_i \gamma_i I_i \cdot H_o \quad (2.15)$$

It can be seen from equation (2.14) that variations in g-factor are caused by different relative contributions of  $L$  and  $S$  to the ground state of the ion in its particular environment.



Three levels of interaction of the crystal field with metal ions are recognised:

(i) Small effect - as in rare earth ions.

Electrostatic interactions are weak due to the partially shielded 4f electrons. L and S remain coupled and therefore  $M_J$  is a good quantum number and in calculating energy levels one first considers S-O coupling ( $H_{LS}$ ) and then applies the crystal field term ( $H_V$ ) as a perturbation.

(ii) Moderate effect - as in the iron group.

In these cases the crystal field is usually strong enough to decouple L and S so  $M_L$  and  $M_S$  are proper quantum numbers.

(iii) Strong effect - as in covalent complexes

Hence chemical bonding means overlap of electronic orbitals and one must employ MO theory.

The calculation of g-factors for transition metal ions is extremely complex, and outside the realms of this discussion.

## 2.4 Free-Radicals

Most organic radicals have the unpaired electron in a p-orbital, i.e.  $L = 1$ . The weak fields commonly encountered in organic matrices are enough to lift p-orbital degeneracy to such an extent that orbital angular momentum is almost completely quenched, and therefore g-factors correspond closely to the free spin value, i.e. 2.00232. Large deviations from this figure occur when the unpaired electron is on an atom for which S-O coupling is strong, or when low lying excited states

can interact with the ground state, reintroducing orbital angular momentum.

The g-factors of a paramagnetic ion or radical, after taking into account crystal field and S-O coupling, have the same symmetry as that obtained by combining the crystal field and Jahn-Teller distortion. Thus for an axially symmetric system, the values of  $g_{11}$  and  $g_{\perp}$  are found to correspond to application of the magnetic field parallel or perpendicular to the axis of distortion. If no symmetry exists, the g-factor must be expressed in terms of  $g_x \neq g_y \neq g_z$ .

## 2.5 Nuclear Hyperfine Structure

Hyperfine structure results from interaction of the magnetic moment of the unpaired electron and that of any magnetic nuclei within its orbital. The interaction between the unpaired electron and nucleus arises in two distinct ways. Anisotropic hyperfine interaction results from the combined spin and orbital angular momenta of the electron setting up a field at the nucleus which depends on the shape of the orbital and distance from the nucleus. Isotropic interaction depends upon a finite spin density being present at the nucleus, and hence only electrons in s orbitals need to be considered. Isotropic interactions are independent of the orientation of the magnetic field. Anisotropic interactions which are orientation dependent may be averaged to zero if the paramagnetic species is tumbling rapidly in a fluid medium.

### 2.5.1 Isotropic and Anisotropic Hyperfine Coupling Constants

The isotropic coupling constant,  $a$ , is a linear function of the unpaired spin density at the nucleus. In atoms in which the unpaired electron

resides in a p-orbital no isotropic splitting should be observed. When isotropic splitting is observed in such systems, it must be concluded that the ground state wave function contains small contributions from s-orbitals. These contributions may be expressed by means of equation (2.16)

$$a = A_o \cdot C_{ns}^2 \quad (2.16)$$

where  $A_o$  represents the theoretical isotropic hyperfine splitting for an atom with a single unpaired electron in a ns-orbital<sup>45,46</sup>.  $C_{ns}^2$  is a coefficient which expresses the proportion of unpaired spin residing in the ns orbital.

The isotropic hyperfine interactions observable in the spectra of both aromatic<sup>47</sup> and aliphatic  $\pi$ -radicals are due to spin polarization in the C-H bond. Thus in Figure 2.6 the unpaired electron in the  $2p_z$ -orbital of the carbon causes spin polarization in the  $sp^2$ -bonding orbital<sup>48,49</sup>. This results in a net positive spin density in the carbon orbital and a net negative spin density in the hydrogen 1s-orbital. The isotropic proton hyperfine interaction ( $a^H$ ) is proportional to the spin density on the central carbon atom ( $\rho$ ) according to equation (2.17)

$$a^H = Q_{CH}^H \cdot \rho_c \quad (2.17)$$

where  $Q_{CH}^H$  is a constant estimated to be about  $-28 \text{ G}^{50}$ .

$\beta$ -Proton coupling in fragments of the type  $\text{C-CH}_3$  arises from the fact that the methyl protons lie in a plane parallel to the axis of the  $2p_z$  orbital of the unpaired electron, and perpendicular to the C-C bond, see Figure 2.7. The orbitals are in a position such that they can overlap

and some unpaired spin can find its way to the hydrogen 1s orbitals by a hyperconjugative mechanism<sup>51,52</sup>. The coupling constant for a  $\beta$  proton is given by

$$a^H = Q_{CCH}^H \rho_C \cos^2 \theta \quad (2.18)$$

where  $Q_{CCH}^H$  is a constant characteristic of the C-C-H system,  $\theta$  is the angle between the axis of the  $2p_z$  orbital and the projection of the C-H bond in the plane passing through this axis, see Figure 2.8.

For anisotropic interactions the energy levels are given by

$$E_{M_I, M_S} = g\beta M_S B_0 + g_I \beta_I M_I B_0 + ha' M_I M_S \quad (2.19)$$

where the orientation dependent coupling constant  $a'$  is given by

$$a' = g_e g_{\pm} \beta \beta_I \langle (1-3 \cos^2 \theta)/r^3 \rangle_{av} \quad (2.20)$$

Consequently, when  $g$  is isotropic and  $M_S = \pm 1/2$ , the hyperfine spectrum consists of  $2I+1$  equally spaced and equally intense lines symmetrically distributed about  $B_0$ . Now, however, the line separations are dependent on the relative orientation of the orbital of the unpaired electron and the applied field. Transitions occur at fields given by

$$B_{MI} = B_0 + M_I a' / g\beta \quad (2.21)$$

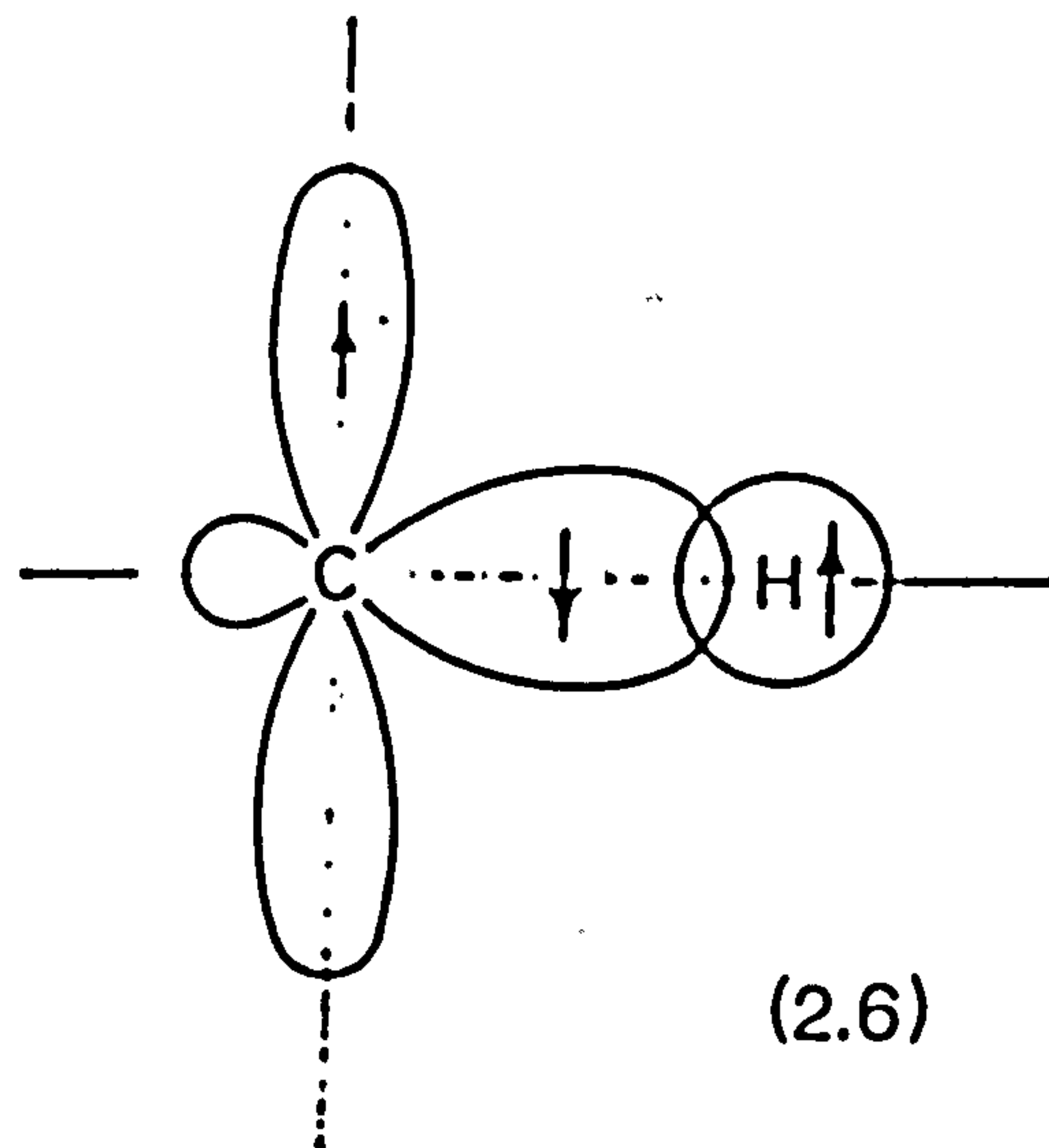
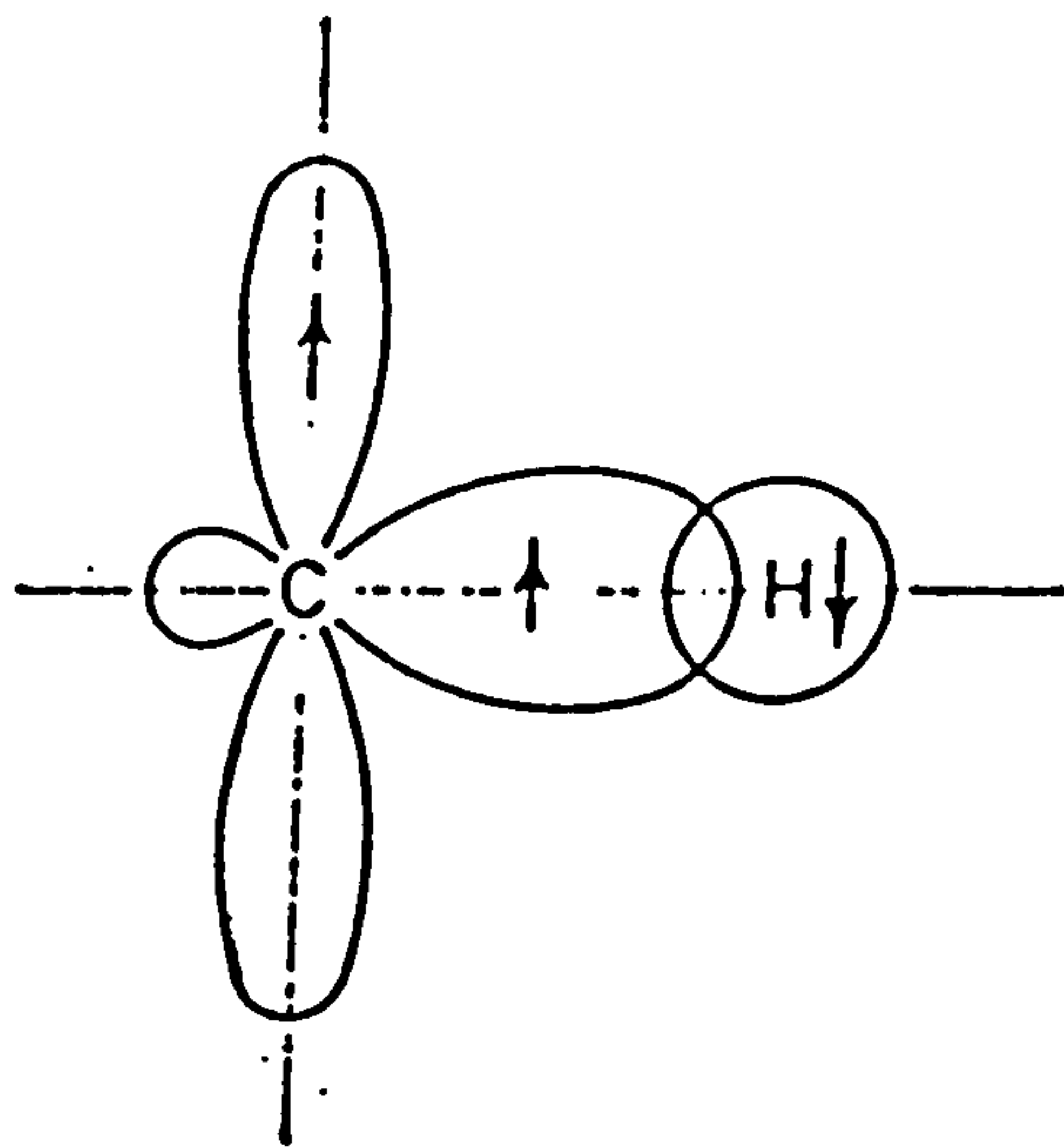
When both isotropic and anisotropic interactions contribute to the hyperfine spectra, they are added together to give the total hyperfine coupling constant  $A$ . Therefore, for the nucleus  $i$ , we can write

Figure 2.6      Schematic representation of the origin of negative spin density at  $\alpha$ -protons.

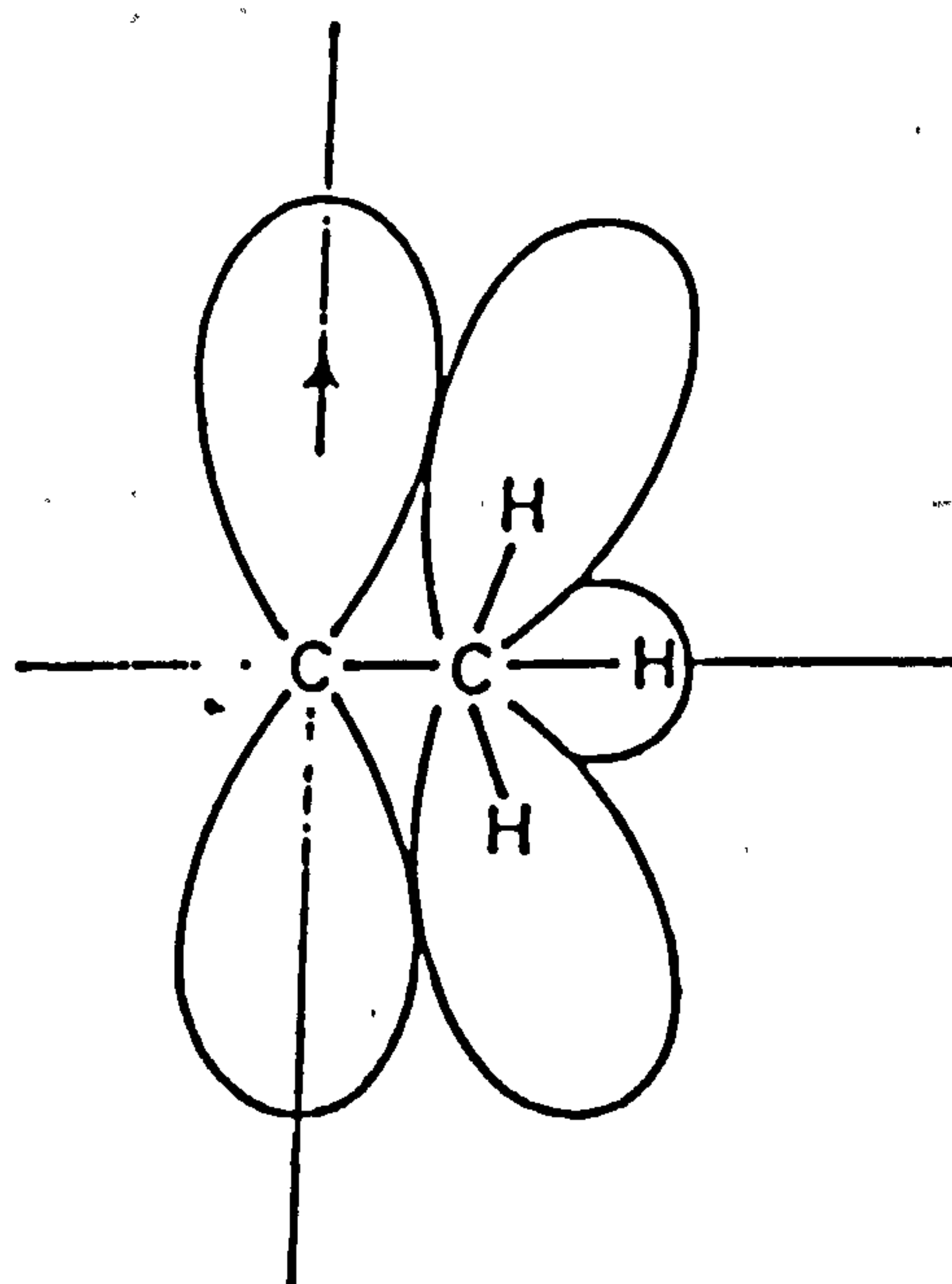
Figure 2.7      Overlap of electronic orbitals in a C-CH<sub>3</sub> fragment.

Figure 2.8      The effect of dihedral angle  $\theta$  on overlap of electronic orbitals in a C-CH<sub>3</sub> fragment.

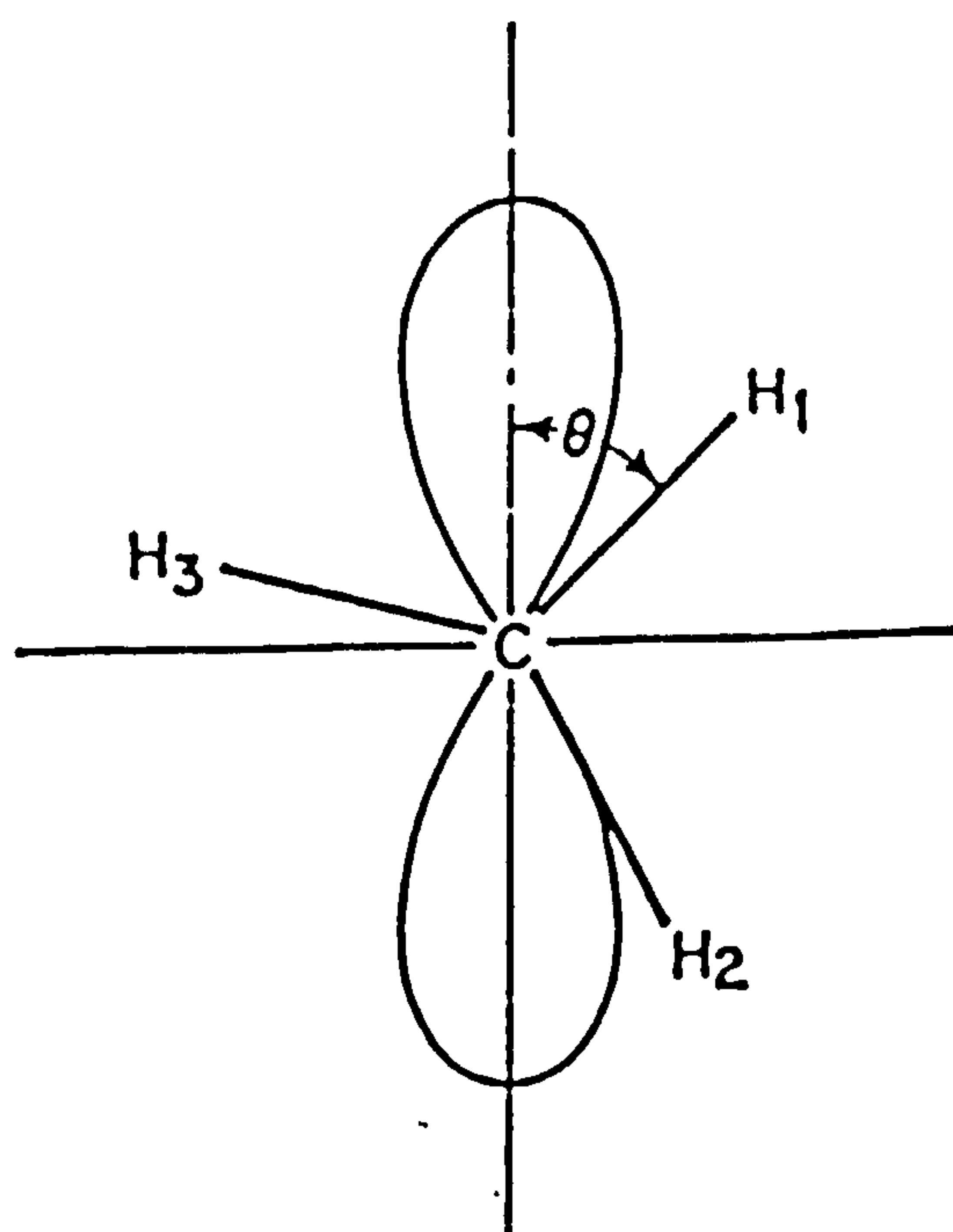




(2.6)



(2.7)



(2.8)

$$A_i = a_i + a'_i \quad (2.22)$$

If  $A_i$  is measured along the x, y and z axis it is possible to separate isotropic and anisotropic components since  $(A_x)_i = a_i + (a'_i)_x$  etc. Hence

$$a_i = 1/3 (A_x + A_y + A_z)_i \quad (2.23)$$

or  $1/3 (A_{11} + 2A_{\perp})_i$  in cases of axial symmetry.

The function  $\langle (1-3 \cos^2 \theta) r^3 \rangle_{av}$  can be calculated from the wave functions of s-, p- and d-orbitals so that  $a'$  can be calculated from equation (2.20). When the magnetic field is applied along the x or y axes for a species with an unpaired electron in an np-orbital then  $a'_{\perp} = B_0$ ; but when it is applied along the z axis then  $a'_{11} = -2B_0$ .

An estimate of the p-orbital contribution to the observed anisotropic hyperfine interaction can be made from the following equations

$$a'_{\perp} = B_0 \cdot C_{np}^2 \quad \text{or} \quad a'_{11} = -2B_0 \cdot C_{np}^2 \quad (2.24)$$

where  $C_{np}$  is the coefficient of  $\psi_{np}$  in the overall wavefunction.



## **Chapter 3**

### **Introduction**

# **Photophysical and Photochemical Properties of the Uranyl Ion**

### 3.1 Photophysical Properties of the Uranyl Ion

The  $[\text{UO}_2]^{2+}$  ion occurs in many uranium compounds and is known to be linear both in solution<sup>53</sup> and in the solid state<sup>54</sup>. The U-O bond lengths within the  $[\text{UO}_2]^{2+}$  unit lie between 1.50 Å and 2.08 Å with a mean value of approximately 1.77 Å. Around the uranyl ion can be coordinated a further 4, 5 or 6 ligands, with no substantial change in the U-O bond lengths.

The outer shell electronic configuration<sup>53</sup> of U is  $5f^3 6d^1 7s^2$ . The 6d orbitals of uranium are thought to be involved in both  $\sigma$ - and  $\pi$ -bonding with the 2p-orbitals of the O atoms<sup>53,55-57</sup>.

Calculations have shown only limited 5f-orbital involvement, but Coulson and Lester<sup>58</sup> have shown that 6f orbitals may be involved in the bonding to other ligands. McGlynn and Smith<sup>53</sup> have proposed that the energies of the filled valence orbitals lie in the order  $\sigma_u < \sigma_g < \pi_u < \pi_g$ , with a singlet ground state  $^1\Sigma_g$ . Ab initio calculations on the uranyl ion have revealed a variety of orderings of the MO's. A non-relativistic model<sup>59</sup> gives the order of energy of the highest filled MO as  $\sigma_g < \pi_u < \sigma_u < \pi_g$ , while a relativistic version<sup>52</sup> of the same method gives the order  $\sigma_u < \sigma_g < \pi_u < \pi_g$ , which is in agreement with McGlynn and Smith.

Uranyl compounds absorb light up to ca. 500 nm. The absorption spectrum in solution and the solid state shows a structured band system with equidistant spacing down to 340 nm, below which transitions take place into a continuum. The assignment of the electronic states involved in the absorption spectrum of the uranyl ion is controversial. McGlynn and Smith<sup>53</sup> suggest that the lowest energy absorption between 20,500 and 30,000  $\text{cm}^{-1}$  results from a triplet  $\leftarrow$  singlet transition to either a  $^3\pi_u$

or  ${}^3\Delta_u$  states ( $\epsilon_{\max}$  101 l mol<sup>-1</sup> cm<sup>-1</sup>). These bands can be divided into three groups with origins at 22,050, 24,125 and 27,000 cm<sup>-1</sup>. Support for the assignment of the lowest excited state to a triplet have come from magnetic circular dichroism studies on (Bu<sub>4</sub>N)UO<sub>2</sub>(NO<sub>3</sub>)<sub>3</sub> in a polymer matrix at 10 K<sup>65</sup>. A detailed study by Bell and Biggers<sup>61,64,65</sup> using a non-linear least squares computer program resolved the absorption spectrum into a series of 24 Gaussian bands in 7 groups. They assigned the first 13 bands to the triplet state  ${}^3\pi_u$  at 21,329, 24,107 and 22,731 cm<sup>-1</sup>.

Alternative suggestions have been made as to the nature of the low-energy absorptions. Volod'ko et al.<sup>66</sup> investigated the absorption spectrum of uranyl solutions and crystals at low temperatures. They concluded that the absorption spectrum has four series of lines in the region 330-500 nm which arise from four singlet  $\leftarrow$  singlet transitions. Görrler-Walrand and Vanquickenborne<sup>67,68</sup> have also interpreted the absorption spectrum in terms of singlet  $\leftarrow$  singlet transitions.

Bell and Biggers have made a comprehensive analysis of the absorption spectrum of uranyl perchlorate, the absorption and emission spectra of which are shown in Figure 3.1. They assign the state at 31,367 cm<sup>-1</sup> to the second triplet state with the remainder of the UV spectrum resolved into a further five excited states of almost equal spacing,  $6015 \pm 39$  cm<sup>-1</sup>. Figure 3.2 shows an energy level diagram based on their assignments.

The presence of strongly complexing species greatly alters the absorption spectrum in both intensity and band width<sup>68</sup> with little change in the energy location. These changes have been interpreted in

Figure 3.1

(a) Absorption spectrum of uranyl perchlorate (0.1 M)  
in 0.1 M perchloric acid

(b) Emission spectrum of uranyl perchlorate (0.1 M) in  
perchloric acid

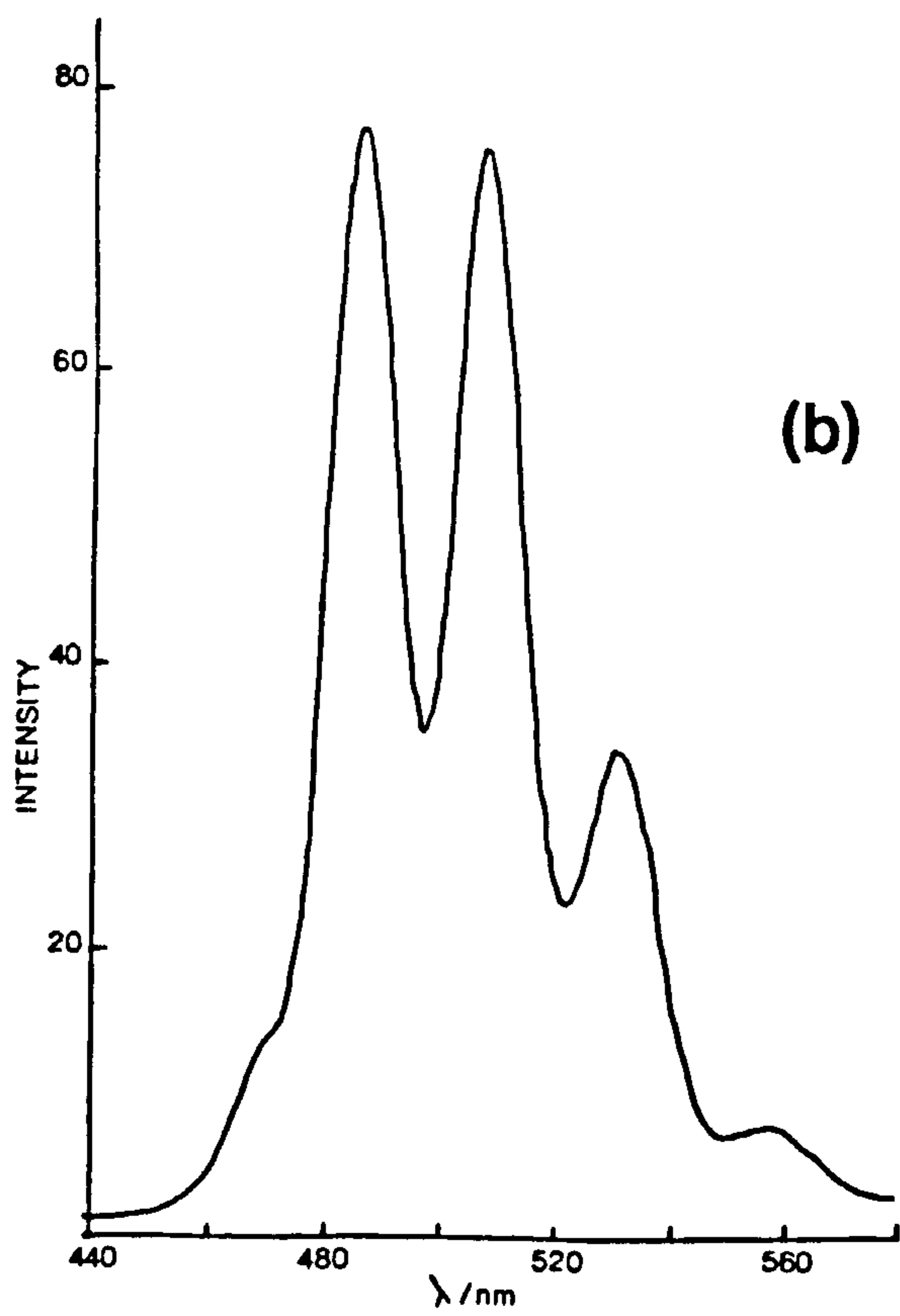
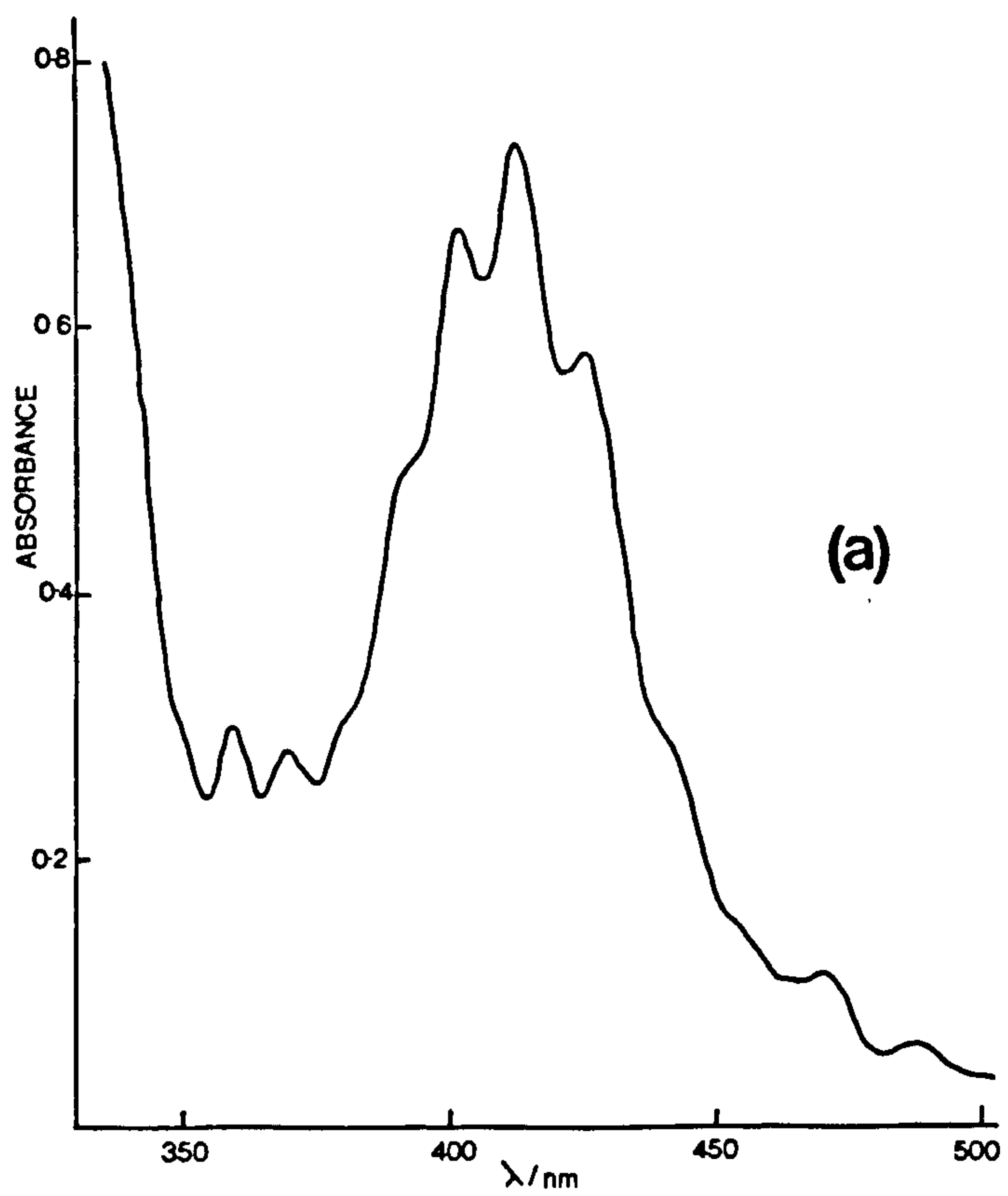
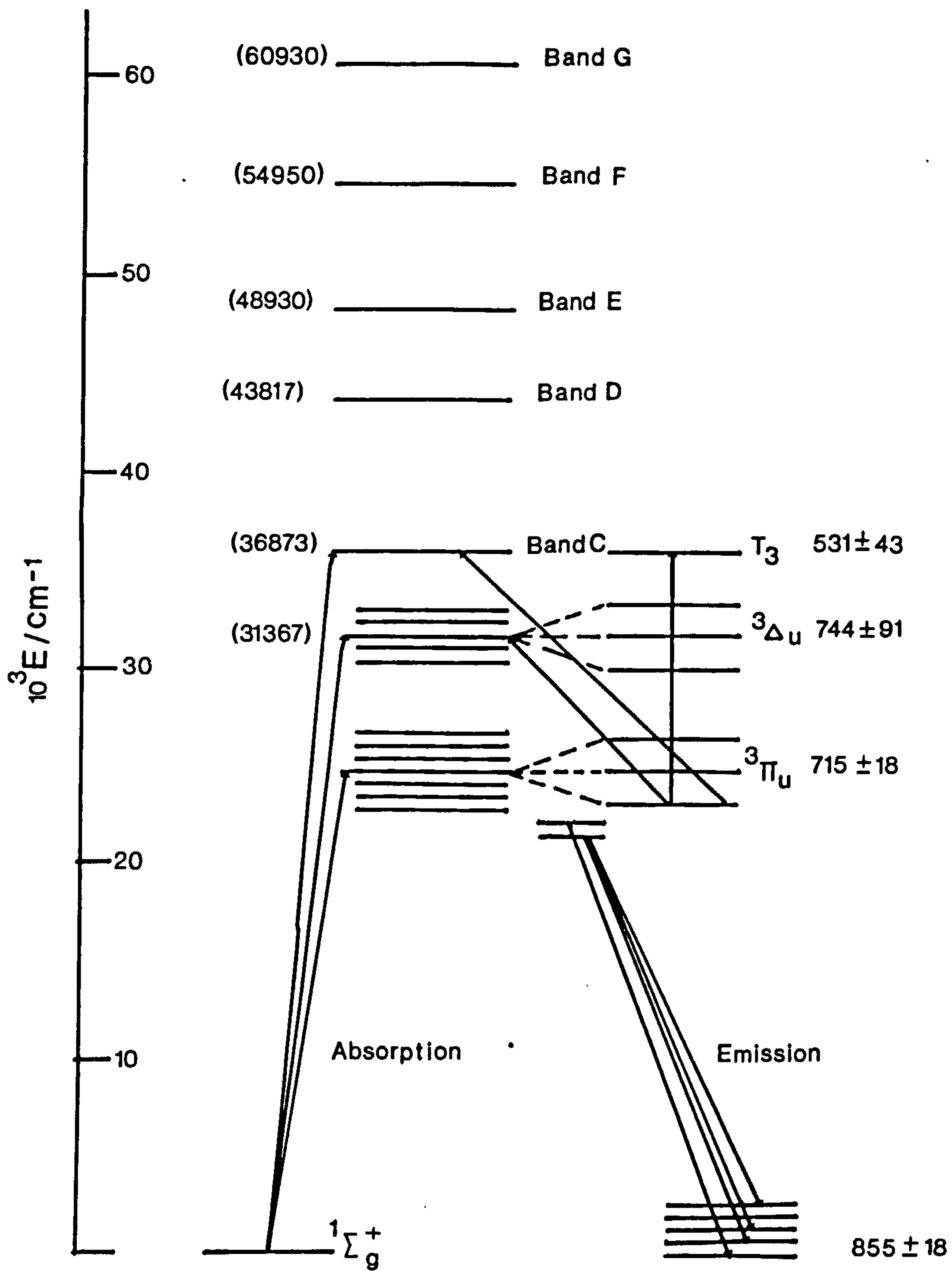


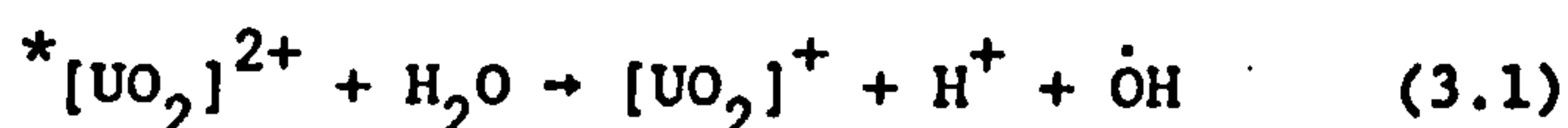
Figure 3.2      Energy level diagram for  $[\text{UO}_2]^{2+}$  ion





terms of a variation in the symmetry of the uranyl centre<sup>69,70</sup>. Uranyl complexes of the type  $[\text{UO}_2 (\text{H}_2\text{O})_{n-1} \text{X}]^+$  (where  $\text{X} = \text{Br}^-$ ,  $\text{NCS}^-$  and  $\text{S}_2\text{O}_3^{2-}$ ) display weak charge transfer transitions in the region 200 to 330 nm<sup>71</sup>. Charge transfer bands have also been seen in the absorption spectrum of  $[\text{UO}_2]^{2+}$  complexed with organic ligands<sup>72,73</sup>.

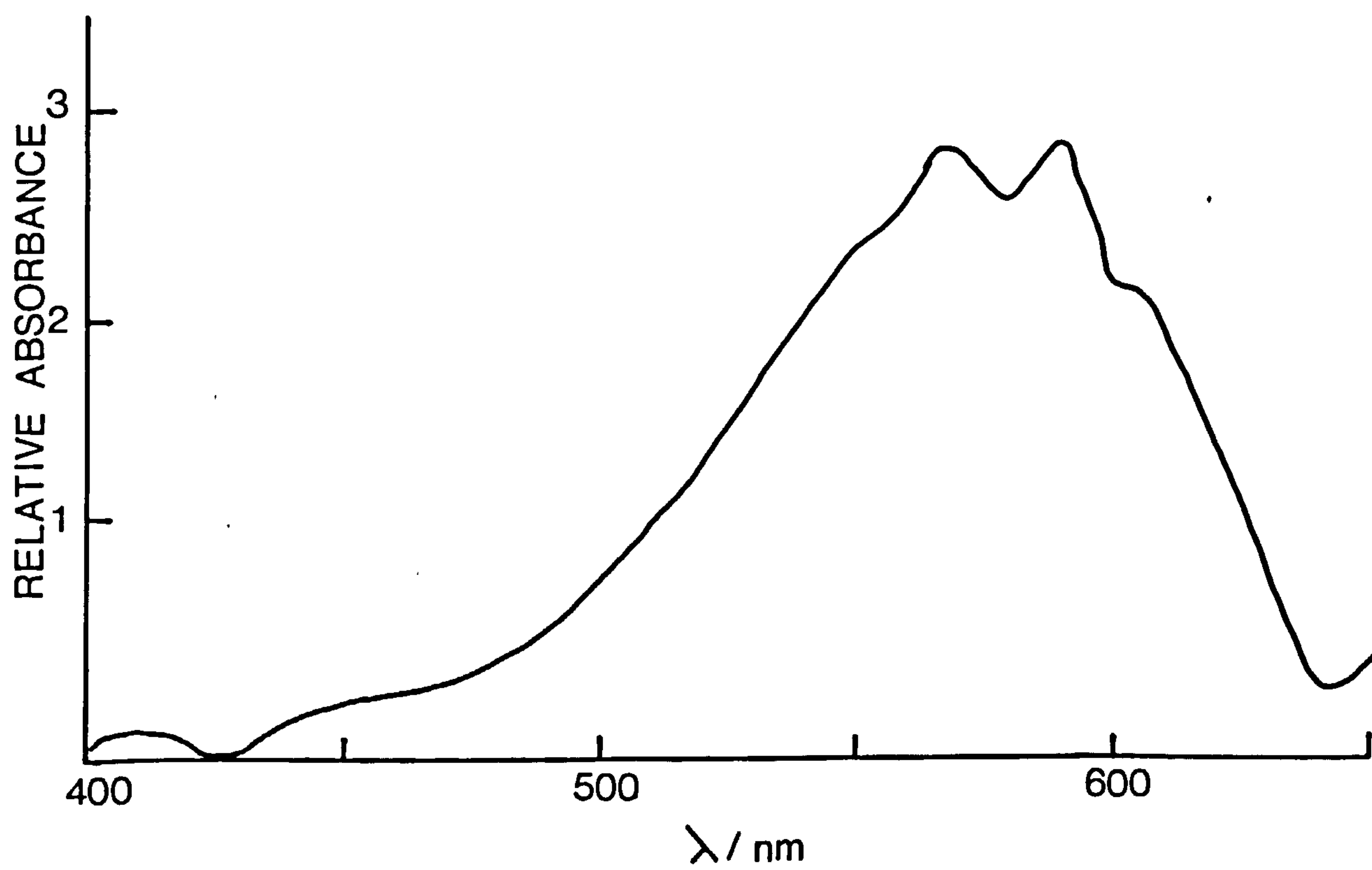
The lifetime of  $^*[\text{UO}_2]^{2+}$  in solution is of the order of  $10^{-6}\text{s}$ <sup>74</sup>, which is strongly dependent on the solvent, pH, and the ionic strength of the medium<sup>75,76</sup>. Flash photolysis of aqueous solutions of uranyl can allow direct observation of absorption by  $^*[\text{UO}_2]^{2+}$  with  $\lambda_{\text{max}}$  590 nm<sup>74,77</sup>, see Figure 3.3. The luminescence lifetime shows a strong temperature dependence between 77 and 300 K<sup>78</sup>. Between room temperature and 357 K the decay constant of  $^*[\text{UO}_2]^{2+}$  shows an Arrhenius dependence with an activation energy  $E_a = 41.2 \text{ kJ/mol}$ . This is a high activation energy for a purely photophysical process and has been attributed to the chemical quenching of  $^*[\text{UO}_2]^{2+}$  by water<sup>75</sup>



Uranyl compounds display a characteristic green luminescence in the region 450-650 nm which is independent of excitation wavelength, see Figure 3.1(b). As in absorption, the band shape and intensity are determined by the environment of the uranyl ion. The luminescence spectrum shows vibrational structure with an average band spacing of ca.  $850 \text{ cm}^{-1}$  in solution and  $700 \text{ cm}^{-1}$  in glasses<sup>79</sup>.

The luminescence of the uranyl ion has been assigned to the lowest  $^3\pi_u$  state and should therefore strictly be designated phosphorescence although the majority of workers still use the term fluorescence.

Figure 3.3      Excited state absorption spectrum of uranyl perchlorate  
in water.



The luminescence quantum yield ( $\phi_f$ ), in suitable cases, approaches unity in the solid state, but in solution  $\phi_f$  decreases markedly.

The deuteration of the ligands affects both the luminescence intensity and the lifetime of  $[\text{UO}_2]^{2+}$  both in solution and the solid state. Thus the luminescence yield and lifetime of  $[\text{UO}_2]^{2+}$  in  $\text{D}_2\text{O}$  is 1.7-2 times greater than in  $\text{H}_2\text{O}$ <sup>74,80</sup>.

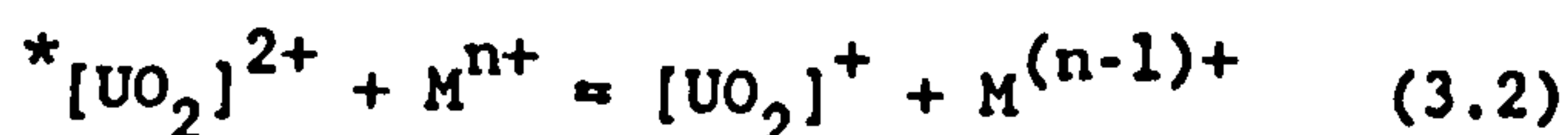
### 3.2 Quenching of Uranyl Ion Fluorescence

The lowest excited electronic state of the  $[\text{UO}_2]^{2+}$  ion has a lifetime in the  $\mu\text{s}^-$  region, which means that chemical reactions readily compete with fluorescence. The bimolecular quenching reaction of excited uranyl ion with ground state molecules in solution can in theory utilize electronic excitation energy in three ways: (a) through energy transfer; (b) through chemical reactions, and (c) through physical quenching.

#### 3.2.1 Quenching by Metal Ions

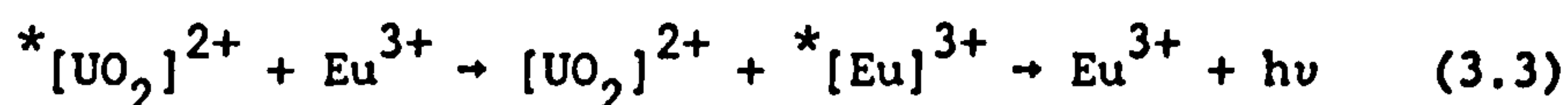
The quenching of uranyl fluorescence by metal ions has been thoroughly investigated.

Fluorescence quenching takes place without chemical change of the uranyl compound or the quencher, indicating that either physical or reversible chemical quenching is occurring. The latter possibility is borne out by the observed variation of  $\log k_q$  with ionisation potential of the quenching metal ions<sup>81</sup>, and reversible electron transfer mechanism for the fluorescence quenching has been proposed<sup>82</sup>



Evidence that quenching by metal ions occurs via exciplex formation has been proposed for the quenching of  $[\text{UO}_2]^{2+}$  fluorescence by  $\text{Tl}^{+83,84}$ . Complete electron transfer occurs in the quenching of  $^*[\text{UO}_2]^{2+}$  by  $\text{Fe}^{2+}$  and  $\text{Ce}^{3+}$  with  $k_q$  close to diffusion control<sup>85,86</sup>. Electron transfer quenching of  $^*[\text{UO}_2]^{2+}$  also occurs with Fe, Ru and Os d<sup>6</sup>-metallocenes<sup>87,88</sup>, as well as metal carbonyls<sup>89</sup>. Cyano complexes such as  $[\text{Mo}(\text{CN})_8]^{3-}$  and  $[\text{Co}(\text{CN})_6]^{3-}$  also quench uranyl fluorescence in 0.01 M nitric acid<sup>90</sup>.

The quenching of  $^*[\text{UO}_2]^{2+}$  by  $\text{Eu}^{3+}$  occurs by electronic energy transfer<sup>91,92</sup>



as does the quenching by transition metal and lanthanide ions, such as  $[\text{MnO}_4]^-$ ,  $[\text{Cr}_2\text{O}_7]^{2-}$  and  $\text{Ce}^{4+}$ <sup>86</sup>.

Uranyl fluorescence is also quenched by  $\text{UCl}_4$  in frozen aqueous solutions at 77 K. Short-lived  $[\text{UO}_2]^+$  formed by reduction of  $[\text{UO}_2]^{2+}$  in aqueous solution is also an effective quencher of uranyl fluorescence with  $k_q$  close to diffusion control<sup>93</sup>.

### 3.2.2 Quenching by Simple Anions

Quantitative experiments on the quenching of uranyl fluorescence by halide and pseudohalide ions have shown that the quenching rate constant increases with decreasing oxidation potential<sup>81</sup>, with  $k_q$  for  $\text{I}^-$  and  $\text{SCN}^-$  ca.  $3.5 \times 10^9 \text{ dm}^3 \text{ mol}^{-1} \text{ s}^{-1}$ . The quenching of  $^*[\text{UO}_2]^{2+}$  fluorescence by halide and other anions is thought to occur by an electron transfer mechanism<sup>82</sup>.

Flash photolysis studies of aqueous uranyl solutions with the anions  $\text{I}^-$ ,  $\text{CNS}^-$  and  $\text{Br}^-$  have revealed the short-lived radical ion  $\text{X}_2^{\cdot -}$  formed through single electron transfer<sup>94</sup>.

### 3.2.3. Quenching by Organic Compounds

The redox potential ( $E(^*\text{[UO}_2\text{]}^{2+})/[\text{UO}_2]^{2+} = 2.6 \text{ eV}$ )<sup>204</sup> of the excited uranyl ion makes it a most powerful oxidising agent, similar to OH or a free fluorine atom. Many classes of organic compound such as aliphatic alcohols and carboxylic acids chemically quench the excited state of the  $[\text{UO}_2]^{2+}$  ion leading in many cases to the production of free radicals which can be detected by ESR.

The important processes in the photochemistry of uranyl systems are:

(i) oxidation of ligands or other species in solution, including solvent. This usually, but not invariably, leads to reduction to  $[\text{U(IV)}]$ , and

(ii) in the presence of oxygen, sensitised oxidations which depend on regeneration of  $[\text{U(VI)}]$  by autoxidation of  $[\text{U(V)}]$ .

Rabinowitch and Belford<sup>97</sup> classified the oxidations into two types, i.e.

(i) those occurring via complexes between  $[\text{UO}_2]^{2+}$  and the reducing species, and (ii) those involving a kinetic encounter between free  $^*\text{[UO}_2\text{]}^{2+}$  and the substrate.

#### 3.2.3.1 Carboxylic Acids

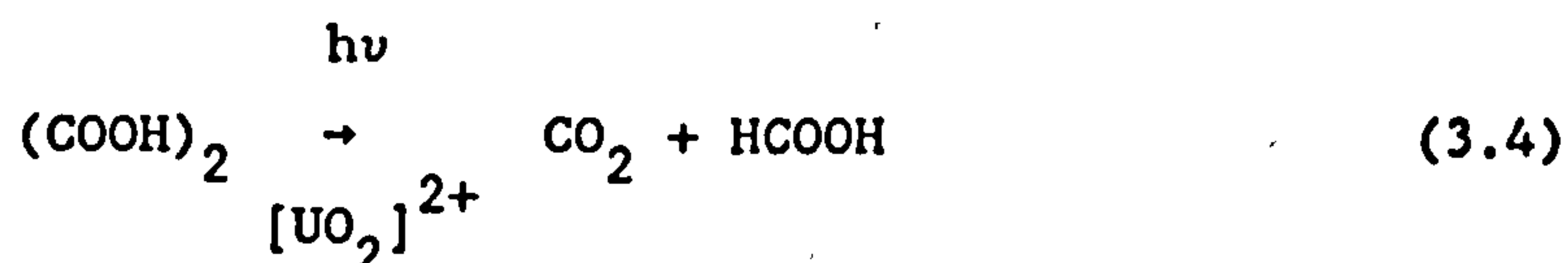
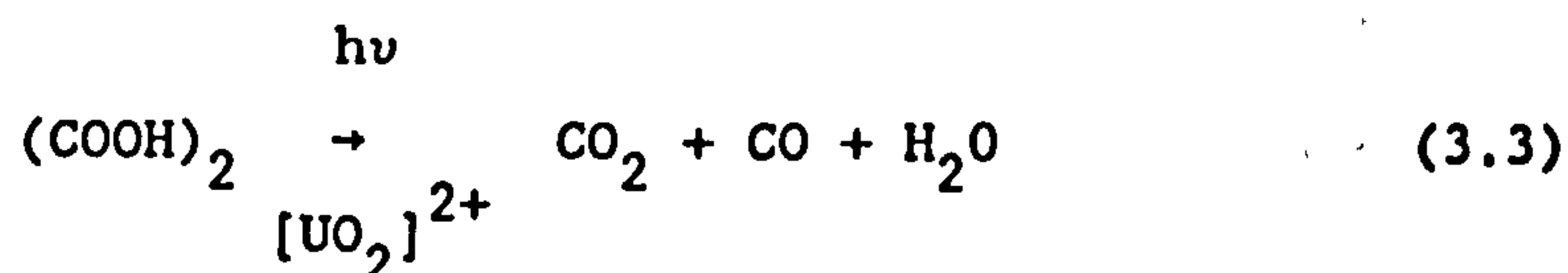
The uranyl ion forms complexes with carboxylic acids as evident from changes in the shape and extinction of the absorption spectra<sup>70</sup>.

Photolysis of these complexes leads to decomposition of the ligands

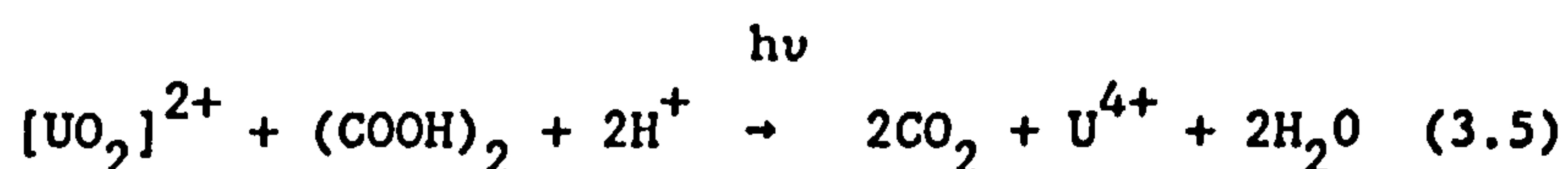


generally via decarboxylation.

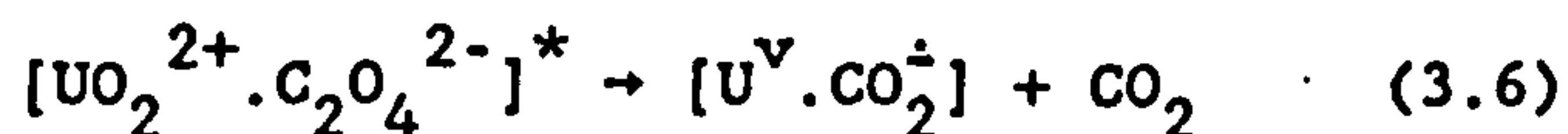
The uranyl-carboxylic acid system most extensively investigated is that involving oxalic acid. The primary reaction is the uranyl-sensitised decomposition of oxalic acid:



At pH = 0, ca 96% of the decomposition of oxalic acid takes place according to equation (3.3). However, at pH 3 and pH 7 the ratio of reaction (3.3) to (3.4) shifts from 25% to zero respectively. A minor pH dependent redox reaction has been reported by several authors<sup>72,98,99</sup>:



The majority of authors assume that the sensitised decomposition occurs from a uranyl-oxalate complex, since mono and bis-oxalato complexes of the uranyl ion have been established in the pH range 1 to 7<sup>72,97</sup>. The proposed mechanism is:





The complexed  $\text{CO}_2$  radical thus serves as a source of formic acid formed in reaction (3.4).

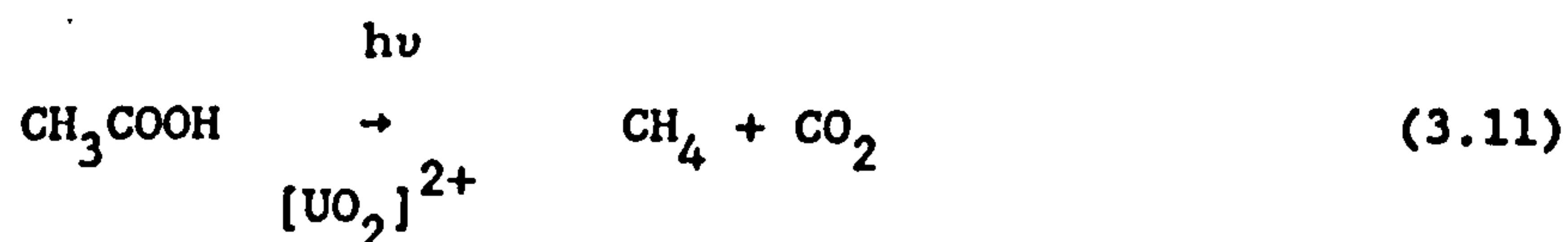
Malonic acid forms as a 1:1 complex of the dianion with uranyl ion, which undergoes photosensitised decomposition to form  $\text{CO}_2$  and acetic acid<sup>100</sup>. The  $[\text{UO}_2]^{2+}$  photosensitised decomposition of glutaric acid occurs via a 2:1 complex of the monoanion with  $[\text{UO}_2]^{2+}$ , with the formation of  $\text{CO}_2$  and n-butyric acid<sup>101</sup>.

The photodecomposition of formic acid also occurs via a complex,  $[\text{UO}_2(\text{HCOO})]^+$ <sup>97,101</sup>. In the proposed mechanism an electron transfer takes place in the complex on irradiation:

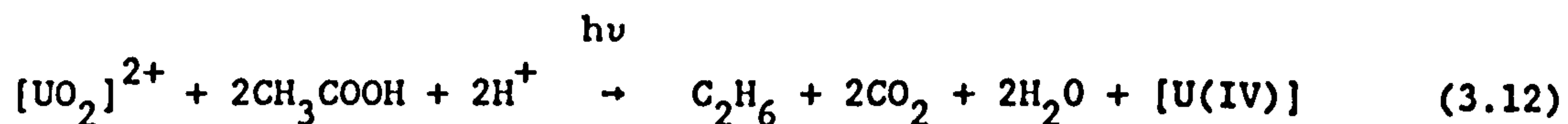


Both the  $\text{HCOO}^\cdot$  radical and a  $[\text{U(V)}]$  intermediate have been identified by ESR<sup>102</sup>.

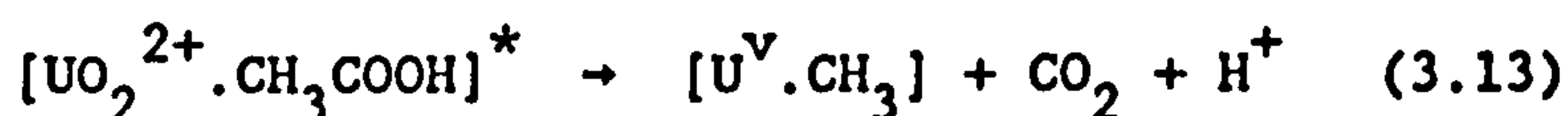
The sensitised decarboxylation of acetic acid proceeds via the primary reaction.



A minor photo-oxidation occurs as a side reaction

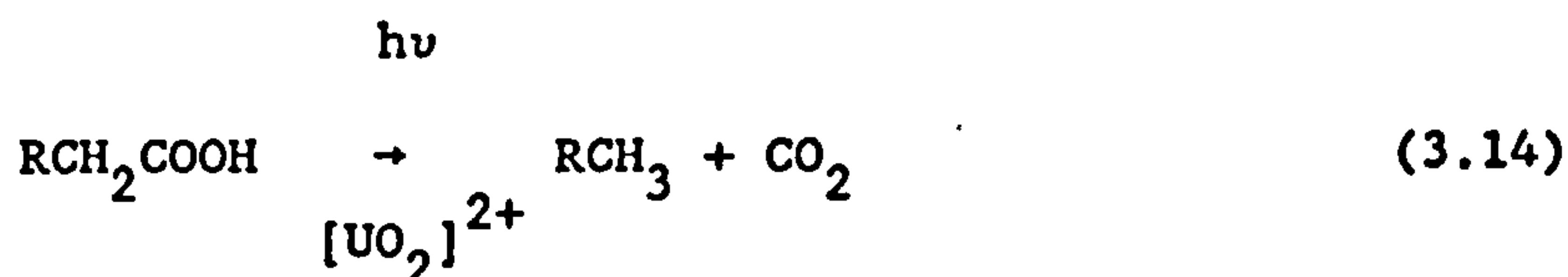


Reaction (3.12) is thought to occur via an electronically excited  $[\text{UO}_2]^{2+}$ -acetic acid complex.

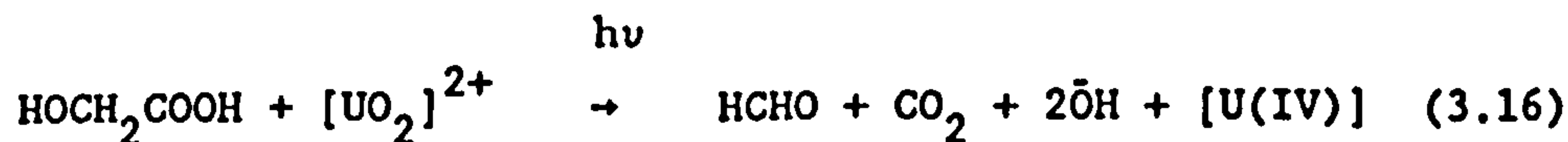
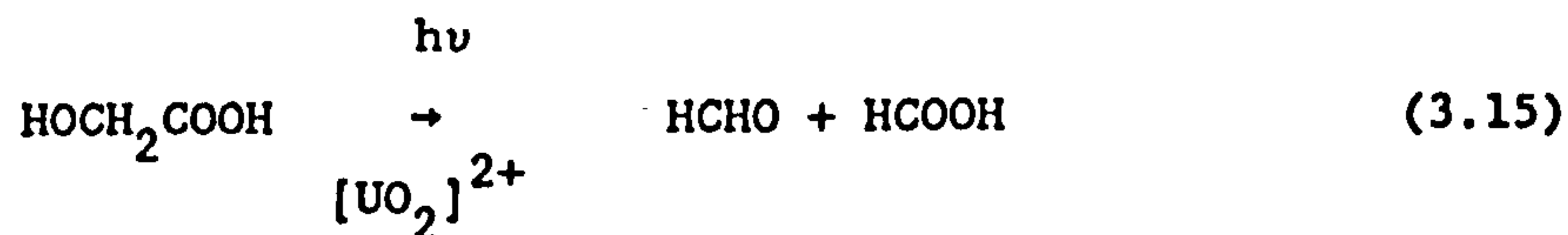


ESR studies at 77 K and at room temperature yield well-resolved spectra of the  $\text{CH}_2\text{COOH}$  radical<sup>103,104</sup>. At high acetic acid concentrations,  $\alpha$ -hydrogen atom abstraction occurs, while in more dilute solutions decarboxylation becomes the dominant reaction.

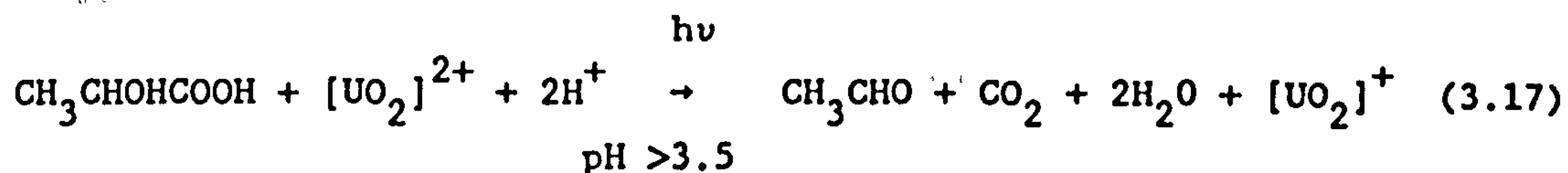
With the higher monocarboxylic acids, such as, propionic, butyric and valeric acid<sup>97</sup>, decomposition takes place with  $\text{CO}_2$  evolution and the generation of the associated alkane<sup>101</sup>.



Photolysis of glycolic acid in the presence of uranyl ion produces both a sensitised decomposition to yield formaldehyde and formic acid, equation (3.15) and a redox reduction, equation (3.16)<sup>97,105</sup>.



The photolysis of lactic acid in the presence of uranyl salts has also been thoroughly investigated. Recent studies have shown that at high pH, the photolysis yields both acetaldehyde and CO<sub>2</sub>:

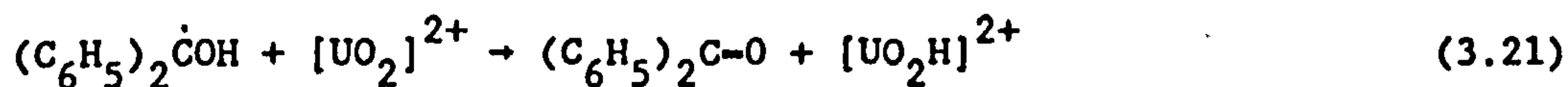
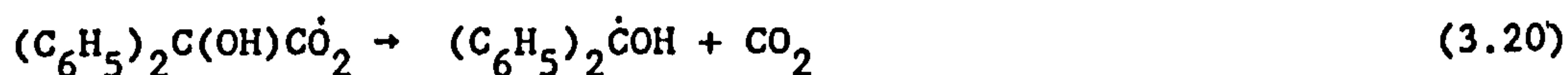
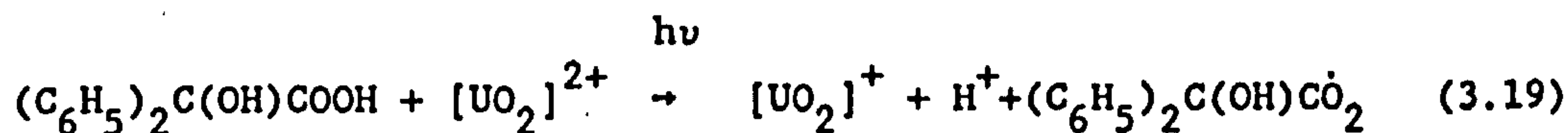


while at low pH pyruvic acid is produced<sup>106</sup>



ESR investigations at 77 K and pH 7 have shown that CH<sub>3</sub>CHOH radical is first formed by decarboxylation of lactic acid which is then oxidised to acetaldehyde. However, at pH 1 the CH<sub>3</sub>C(OH)COOH radical formed by hydrogen atom abstraction by <sup>\*</sup>[UO<sub>2</sub>]<sup>2+</sup>, is then further oxidised to pyruvic acid<sup>103</sup>.

Photolysis of benzilic acid in the presence of uranyl perchlorate produces benzophenone as the sole product. ESR investigations have confirmed the presence of the diphenylketyl radical<sup>107,108</sup>, equation (3.20) which is then oxidised to benzophenone, equation (3.21)



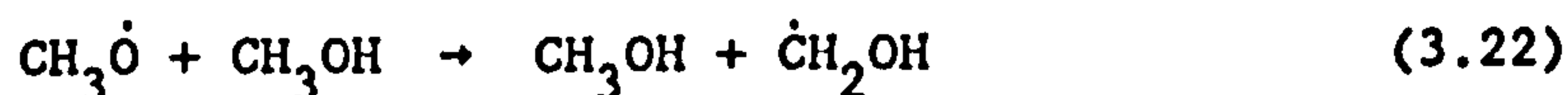
The halogenation of organic acids results in a range of varying effects

on the quenching rate of  $^*[UO_2]^{2+}$ . The replacement of a methyl hydrogen atom of acetic acid by a chlorine does not significantly affect the quenching rate constant  $k_q$ , but substitution by an iodine atom dramatically increases<sup>134</sup>. Replacement of all three methyl hydrogens by fluorine or chlorine results in a three-fold enhancement of the luminescent intensity indicating that the complexes formed are much more luminescent than the  $^*[UO_2]^{2+}$  ion. However, the introduction of chlorine or bromine atoms at either the 2 or 3 position of propionic acid, results in a large increase in  $k_q$ .

### 3.2.3.2 Alcohols

Photolysis of uranyl salts in the presence of alcohols results in the oxidation of the alcohol to the corresponding aldehyde<sup>97</sup>. The rate of photoreduction of  $[UO_2]^{2+}$  by alcohols increases in the order t-butyl < methyl < ethyl < isobutyl = n-butyl < isopropyl<sup>109</sup>.

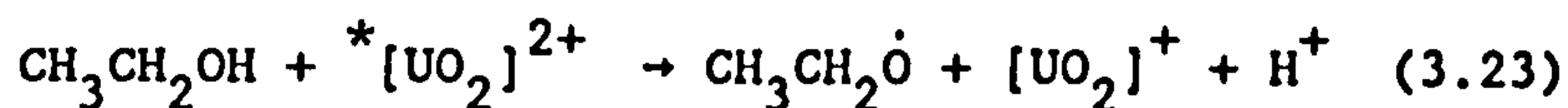
The RCHOH radical has been identified by ESR during the photolysis of methanol, ethanol, n-propanol and n-butanol in the presence of uranyl salts, both at room temperature and 77 K<sup>104,107,118</sup>. However, in the case of liquid methanol,  $CH_3\dot{O}$  is the primary radical. The  $\dot{C}H_2OH$  radical arises through abstraction by the methoxy radical of an  $\alpha$ -hydrogen atom from a second methanol molecule.



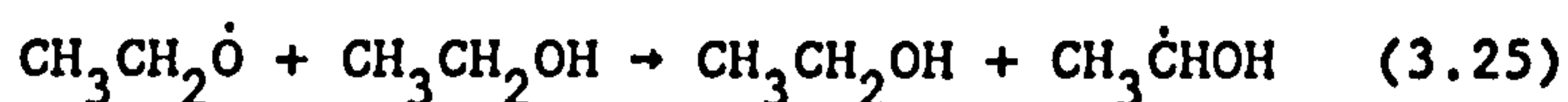
According to previous experiments on the photolysis of uranyl ions in ethanol solution as a rigid matrix at 77 K<sup>103</sup> only the  $CH_3\dot{C}HOH$  radical was observed. However, recent experiments<sup>118</sup> have shown the presence of methyl radicals in the ESR spectrum at high  $[UO_2]^{2+}$  concentrations



(>1 M). The formation of methyl radicals is explained in terms of a charge transfer mechanism followed by C-C cleavage:



Fukutomi *et al.*<sup>118</sup> propose that the formation of  $\text{CH}_3\dot{\text{C}}\text{HOH}$  at low uranyl (<0.1 M) concentrations arises through abstraction by ethoxyl radicals of an  $\alpha$ -hydrogen atom from another ethanol molecule.



The absence of  $\text{CH}_3\text{CH}_2\dot{\text{O}}$  radicals in the ESR spectrum is attributed to their high reactivity. With an increase of  $[\text{UO}_2]^{2+}$  concentration the concentration of uncoordinated ethanol available to participate in equation (3.25) is concomitantly reduced, and reaction (3.24) becomes more prominent than reaction (3.25).

Ethanol (0.2 M) is oxidised to acetaldehyde by uranyl salts when, photolysed at 366, 406 and 436 nm, using high quantum fluxes<sup>110-112</sup>. The photoreduction of  $[\text{UO}_2]^{2+}$  by ethanol in  $\text{H}_2\text{SO}_4$  solution at 441.6 nm with a Cd-He laser has a reported quantum yield of 0.69<sup>113</sup>. A similar quantum yield of 0.6 has been reported for  $[\text{U(IV)}]$  formation in a  $\text{H}_2\text{SO}_4$ -ethanol system irradiated with an argon laser<sup>114</sup>. The quantum yield in pure ethanol is reported to be 1.0<sup>115</sup>.

Secondary alcohols, by contrast, undergo C-C bond cleavage to yield  $\text{R}\dot{\text{C}}\text{HOH}$  radicals which have been spin-trapped using *t*-nitrosobutane<sup>116</sup>.

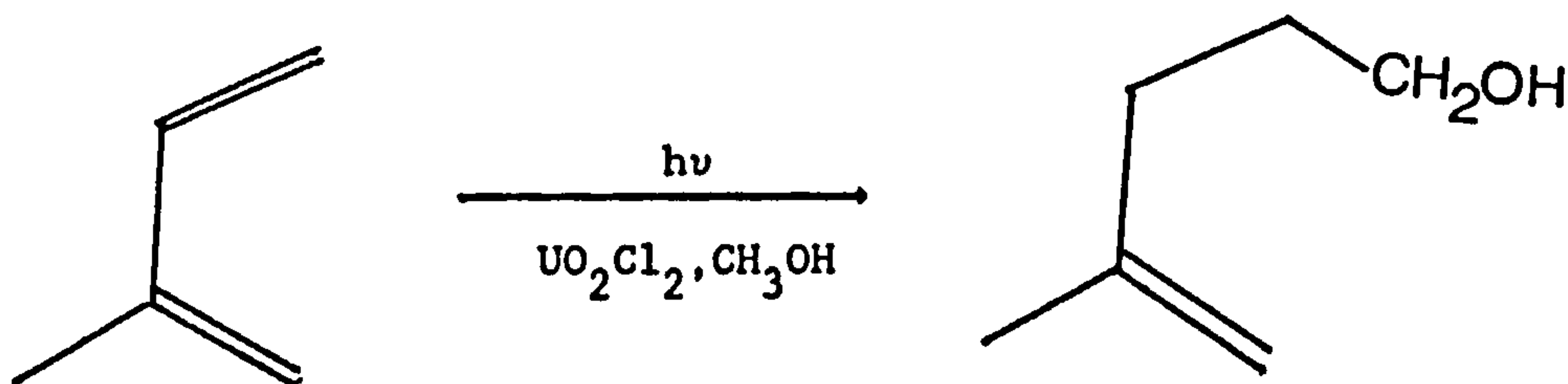
Photolysis of  $[\text{UO}_2]^{2+}$  in glassy t-butanol yields the ESR spectrum of the methyl radical<sup>117</sup>.

### 3.2.3.3 Aldehydes

The uranyl-sensitised oxidation of acidic solutions of formaldehyde<sup>127</sup> and acetaldehyde<sup>128</sup> produces  $[\text{U(IV)}]$  plus formic and acetic acids respectively. The quantum yield for  $[\text{U(IV)}]$  formation is dependent upon pH, and has been measured at 365, 405 and 436 nm as 0.79, 0.76 and 0.50 for formaldehyde and 0.93, 0.79 and 0.37 for acetaldehyde respectively<sup>129</sup>.

Illumination of vinyl monomer in the presence of  $[\text{UO}_2]^{2+}$  causes polymerisation, the rate of which is dependent upon light intensity, pH and temperature<sup>130,131</sup>.

Illumination of  $\alpha,\beta$ -unsaturated carbonyl compounds in alcohol solutions in the presence of uranyl chloride, causes a 1,4-addition of the alcohol at the  $\alpha, \beta$ -unsaturated bond<sup>132</sup>.



Alkenes are also highly effective quenchers of  $^*[\text{UO}_2]^{2+}$  but the quantum yield values for  $[\text{U(IV)}]$  formation are extremely small. The suggested quenching mechanism is one of physical quenching by radiationless deactivation of an exciplex formed from  $^*[\text{UO}_2]^{2+}$  and quencher of the type proposed by Matsushima for aromatics<sup>133</sup>.

#### 3.2.4 Miscellaneous Substrates

Sandhu and Brar<sup>119</sup> have studied the photochemical reduction of uranyl ion with a series of nitriles, and they report that only acetonitrile and propionitrile photoreduce the uranyl ion.

In another series of photochemical reductions of the uranyl ion with triphenylphosphine<sup>120</sup>, tri-p-tolylphosphine<sup>121</sup>, triphenylarsine<sup>122</sup>, triphenylantimony<sup>123</sup> and triphenylbismuth<sup>124</sup>, the supposed major products are [U(IV)] and the oxides of the substrate, such as triphenylphosphine oxide.

The photo-oxidation of hydrazine in  $\text{HNO}_3$  and  $\text{HClO}_4$  media has been studied as a possible approach to the reprocessing of nuclear fuel. The potential of this method, despite the efficient photoreduction of uranyl by hydrazine, is limited by the production of ammonia as a photoproduct<sup>125</sup>.

Strong quenching of the fluorescence of excited uranyl ion has been found on addition of the molecules  $\text{RHal}$  ( $\text{Hal} = \text{Br}, \text{I}$ ),  $\text{R}_2\text{S}$  and  $\text{R}_4\text{M}$  ( $\text{M} = \text{Si}, \text{Ge}, \text{Sn}, \text{Pb}$ )<sup>126</sup>. The second order rate constants  $k_2$  for the quenching process fall in the region  $10^7 - 6 \times 10^9 \text{ dm}^3 \text{ mol}^{-1} \text{ s}^{-1}$ . ESR examination of the photoreduction of  $[\text{UO}_2]^{2+}$  in the presence of  $\text{R}_2\text{S}$ , yields the radical species  $(\text{R}_2\text{S})_2^{+\cdot}$ . It has been proposed that the quenching mechanism for the above species occurs via a fast reversible electron transfer within an exciplex.



## **Chapter 4**

### **Introduction**

### **Complexation Between Uranyl Ion and Amino Acids**

#### 4.1 Complexation Between Uranyl Ion and Amino Acids

The interaction of the dioxouranium (VI) (or uranyl) ion with  $\alpha$ -,  $\beta$ -, and  $\gamma$ -amino acids has attracted a large number of investigations, with particular reference to the site and extent of coordination of these ambidentate ligands. The simplest amino acid, glycine, has alone attracted over 20 investigations. One of the aims of these investigations was to establish a model for the interaction between toxic or radioactive metal ions<sup>157</sup> and proteins. There seems however to be much disagreement in the literature concerning the maximum number of ligands that may be coordinated to the  $[\text{UO}_2]^{2+}$  ion, the values of the stability constants and the exact role of the amino and carboxylate groups in co-ordination. While the majority of authors favour coordination to the uranyl ion via the carboxylate group, a small number suggest the participation of the amino group<sup>141,146-148</sup>.

Solution studies of the complexation of amino acids with  $[\text{UO}_2]^{2+}$  have been carried out using a wide variety of techniques, namely polarography, potentiometry, paper electrophoresis and calorimetry. A summary of this solution work is given in Table 4.1.

Recent work has established the existence of the complexes,  $[\text{UO}_2(\text{OH})\text{L}](\text{ClO}_4) \cdot 3\text{H}_2\text{O}$  and  $[\text{UO}_2(\text{L}')_3](\text{ClO}_4)_2$  in the solid state (where L = glycine,  $\beta$ -alanine and L' = 2-aminobutanoic acid). The amino acids in all of these complexes exist in the zwitterionic form, binding to  $[\text{UO}_2]^{2+}$  through the ionised carboxyl group. The structure of  $[\text{UO}_2(\text{L}')_3](\text{ClO}_4)_2$  has been determined by x-ray crystallography<sup>135</sup>. In this complex the uranyl group is equatorially bonded to the bidentate carboxylate moieties of the three ligands forming a distorted hexagonal bipyramidal coordination geometry around the metal.

The reaction of glycine with uranyl sulphate has been found to form the complex  $[\text{UO}_2(\text{SO}_4)(\text{Gly})_3]$ , which has been characterised by thermogravimetric and elemental analysis<sup>144</sup>. Sergeev and Korshunov have reported the synthesis of  $[\text{UO}_2(\text{OH})\text{Gly}]\cdot 2\text{H}_2\text{O}$  as an amorphous solid<sup>145</sup>, and an infra-red examination of this compound is reported to reveal the interaction of both the carboxylate and amino groups of glycine which forms a chelate ring with the central atom in contrast to a similar complex reported above. They also report the isolation of 1:1 complexes of aspartic and glutamic acids with  $[\text{UO}_2]^{2+}$ , in which the amino acids exist in the form of protonated ions ( $\text{HAsp}^+$  and  $\text{HGlu}^+$ ).

The action of proline on uranyl nitrate leads to the replacement of the coordinated water molecules with proline. The ligand coordinates to  $[\text{UO}_2]^{2+}$  as the unidentate zwitterion through the carboxyl oxygen atom to form  $[\text{UO}_2(\text{NO}_3)_2(\text{Pro})_2]$ , the structure of which has been confirmed by x-ray crystallography<sup>151</sup>. Shchelokov *et al.*<sup>151</sup> have also synthesised uranyl-proline complexes of the type  $[\text{UO}_2(\text{NCS})_2(\text{Pro})_3]\cdot 3\text{H}_2\text{O}$  and  $[\text{UO}_2(\text{C}_2\text{O}_4)(\text{Pro})]\cdot \text{H}_2\text{O}$ , the suggested formulation of these compounds being determined by I.R. and elemental analysis.

Table 4.1

Summary Detailing the Complexation of  $[UO_2]^{2+}$  with  
Amino Acids in Solution

Amino Acid	$[UO_2]^{2+}$ : Amino Acid Stoichiometry	Formation Constants	Ref.
Glycine $(^-\text{O}_2\text{CCH}_2\overset{+}{\text{NH}}_3)$	1:1, 1:2	$\log K_1 = 1.16,$ $\log K_2 = 1.04$	137
	1:1, 1:2	$\log \beta_2 = 2.14$	138
	1:1, 1:3	$\log K_1 = 7.88,$ $\log k_3 = 18.93$	139
	1:1, 1:2	$\log \beta_1 = 1.34$ $\log \beta_2 = 2.72$	140
	1:1	$\log K = 7.34$	141
	1:1	$\log K = 8.65$	143
	1:1	$k_f = 28$	142
$\alpha$ -Alanine $(^-\text{O}_2\text{CCH}(\overset{+}{\text{NH}}_3)\text{CH}_3)$	1:1, 1:2	$\log \beta_1 = 7.33,$ $\log \beta_2 = 14.97$	146
	1:1, 1:2 and 1:4	$\log \beta_1 = 2.04,$ $\log \beta_2 = 2.08,$ $\log \beta_4 = 3.85$	140
	1:1, 1:2	$\log \beta_2 = 2.15$	138
	1:1	$\log K = 7.00$	141
	1:1	$\log K = 9.00$	143

(contd.)

Table 4.1 (contd.)

Amino Acid	[UO <sub>2</sub> ] <sup>2+</sup> : Amino Acid Stoichiometry	Formation Constants	Ref.
β-Alanine	1:1	log β <sub>1</sub> = 3.41	140
( <sup>-</sup> O <sub>2</sub> CCH <sub>2</sub> CH <sub>2</sub> NH <sub>3</sub> <sup>+</sup> )	1:1, 1:2	log β <sub>2</sub> = 3.49	138
	1:1	log K = 7.86	142
	1:1	log K <sub>1</sub> = 9.90	143
	1:1	log K <sub>1</sub> = 9.20	147
	1:1, 1:2	log β <sub>1</sub> = 1.93	136
	and 1:3	log β <sub>2</sub> = 3.44	
		log β <sub>3</sub> = 4.82	
Serine	1:1	log K = 6.04	141
( <sup>-</sup> O <sub>2</sub> CCH(NH <sub>3</sub> <sup>+</sup> )CH <sub>2</sub> OH)	1:1	log K = 6.90	143
	1:1, 1:2	log β <sub>1</sub> = 8.66	146
		log β <sub>2</sub> = 14.66	
Threonine	1:1	log K = 6.00	141
( <sup>-</sup> O <sub>2</sub> CCH(NH <sub>3</sub> <sup>+</sup> )CH(OH)CH <sub>3</sub> )	1:1, 1:2	log β <sub>1</sub> = 6.65	146
		log β <sub>2</sub> = 12.08	

(contd.)

Table 4.1 (contd.)

Amino Acid	$[\text{UO}_2]^{2+}$ : Amino Acid Stoichiometry	Formation Constants	Ref.
Aspartic Acid	1:1	$\log K = 8.40$	141
$(^-\text{O}_2\text{CCH}_2\text{CH}(\text{NH}_3^+)\text{CO}_2^-)$	1:1	$\log K_1 = 2.61$	148
	1:1		149
Glutamic Acid	1:1	$\log K = 8.11$	141
$(^-\text{O}_2\text{C}(\text{CH}_2)_2\text{CH}(\text{NH}_3^+)\text{CO}_2^-)$	1:1	$\log K = 2.66$	148
Asparagine	1:1, 1:2		149
$(^-\text{O}_2\text{CCH}(\text{NH}_3^+)\text{CH}_2\text{CONH}_2)$	1:1	$\log K = 6.85$	143
Proline	1:1	$\log K = 10.45$	143
$(^-\text{O}_2\text{C}.\text{CH}.\text{CH}_2.\text{CH}_2.\text{CH}_2\text{NH})$	1:1	$\log K = 7.54$	141
	$[\text{UO}_2(\text{Pro})^+], [\text{UO}_2(\text{Pro})_2]$		153
Hydroxyproline	1:1	$\log K_c = 1.50$	153
$(^-\text{O}_2\text{C}.\text{CH}.\text{CH}_2.\text{CH}(\text{OH}).\text{CH}_2.\text{NH})$	1:1	$\log K = 6.52$	141

(contd.)



Table 4.1 (contd.)

Amino Acid	$[\text{UO}_2]^{2+}$ :	Formation Constants	Ref.
	Amino Acid		
	Stoichiometry		
Valine	1:1	$\log K_{\text{ML}} = 7.97$	153
$(^-\text{O}_2\text{CCH}(\text{NH}_3^+)\text{CH}(\text{CH}_3)_2)$	1:1	$\log K = 8.60$	143
	1:1, 1:2	$\log \beta_1 = 7.10$	146
		$\log \beta_2 = 14.72$	
Leucine	1:1, 1:2	$\log \beta_1 = 7.13,$	146
$(^-\text{O}_2\text{CCH}(\text{NH}_3^+)\text{CH}_2\text{CH}(\text{CH}_3)_2)$		$\log \beta_2 = 14.36$	
	1:1	$\log K = 8.60$	143
Isoleucine	1:1, 1:2	$\log \beta_1 = 7.02$	146
$(^-\text{O}_2\text{CCH}(\text{NH}_3^+)\text{CH}(\text{CH}_3)\text{CH}_2\text{CH}_3)$		$\log \beta_2 = 14.66$	
Arginine	$\text{UO}_2\text{L} \times n\text{H}_2\text{O}$		155
$(^-\text{O}_2\text{CCH}(\text{NH}_3^+)(\text{CH}_2)_3\text{NHC}(\text{NH}_2^+)\text{NH}_2)$			
	L = Arginine, X = $\text{NO}_3^-$		
	$\text{AcO}^-$ , or $\text{ClO}_4^-$		
	n = 2 or 3		

(contd.)



Table 4.1 (contd.)

Amino Acid	[UO <sub>2</sub> ] <sup>2+</sup> : Amino Acid Stoichiometry	Formation Constants	Ref.
Cysteine	1:1	log K <sub>1</sub> = 9.04	147
( <sup>-</sup> O <sub>2</sub> CCH(NH <sub>3</sub> <sup>+</sup> )CH <sub>2</sub> SH)	1:1, 1:2	log β <sub>1</sub> = 5.84 log β <sub>2</sub> = 11.85	146
Methionine	1:1, 1:2	log K <sub>1</sub> = 7.65	147
( <sup>-</sup> O <sub>2</sub> CCH(NH <sub>3</sub> <sup>+</sup> )(CH <sub>2</sub> ) <sub>2</sub> SCH <sub>3</sub> )		log K <sub>2</sub> = 6.30	
	1:1, 1:2	log β <sub>1</sub> = 6.41 log β <sub>2</sub> = 13.38	146
Histidine	1:1	log β <sub>1</sub> = 1.45	140
( <sup>-</sup> O <sub>2</sub> CCH(NH <sub>3</sub> <sup>+</sup> )CH <sub>2</sub> . <u>C.CH.NH<sup>+</sup>.CH.NH</u> )			
Tryptophan	1:1, 1:2	log K <sub>1</sub> = 14.37	156
Phenylalanine	1:1, 1:2	log β <sub>1</sub> = 6.77	146
( <sup>-</sup> O <sub>2</sub> CCH(NH <sub>3</sub> <sup>+</sup> )CH <sub>2</sub> C <sub>6</sub> H <sub>5</sub> )		log β <sub>2</sub> = 13.91	
	1:1	log K = 6.49	141

## **Chapter 5**

### **Introduction**

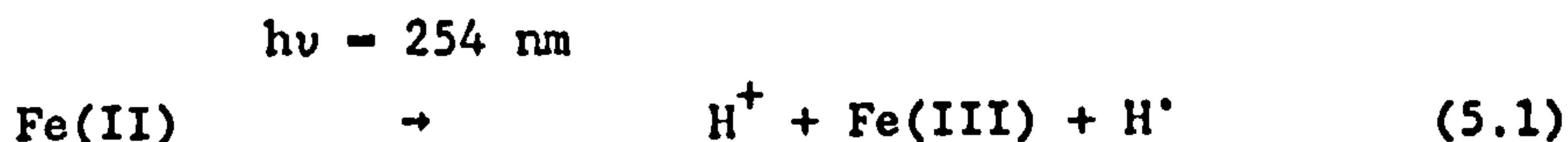
#### **Photosensitised Decomposition of Amino Acids by Metal Ion-ESR Investigations**

## 5.1 Photosensitised Decomposition of Amino Acids by Metal Ions-ESR Investigations

The photolysis of amino acids and peptides leads to the generation of free radicals, which can be produced either by direct irradiation of the amino acid with UV light, or ionising radiation, or through use of photosensitisers such as ketones or dyes. These radicals usually result from a homolytic cleavage of the alpha C-H bond to yield radicals of the type  $\text{H}_3\text{N}^+-\dot{\text{C}}\text{RCOO}^-$  and  $\dot{\text{C}}\text{HRCOO}^-$ . Other methods for the generation of free radicals from amino acids or peptides involve the interaction of the amino acid with  $\dot{\text{O}}\text{H}$  radicals generated by the  $\text{Ti}^{3+}-\text{H}_2\text{O}_2$  system<sup>158</sup> in acidic, neutral or slightly alkaline media. Free radicals of this type have been extensively studied by electron spin resonance (ESR).

Free radicals have also been identified following the photolysis of amino acids in the presence of a number of oxidising or reducing metal ions in frozen solutions at 77 K.

Hydrogen atoms produced by the photolysis of Fe(II) in aqueous sulphuric acid glasses at 77 K,

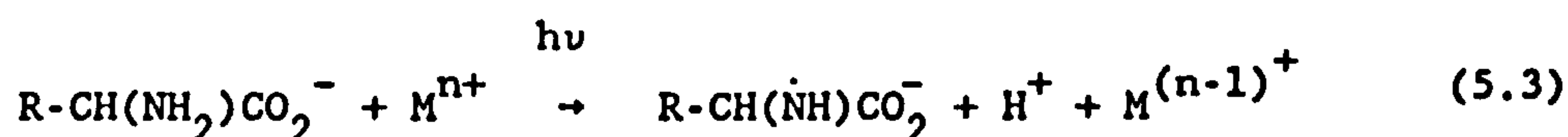


abstract from C-H bonds of amino acids to yield  $\text{NH}_3^+-\dot{\text{C}}\text{RCOO}^-$  radicals<sup>159</sup>. Poznyak et al.<sup>160</sup> have identified radicals of the type  $\text{R}\dot{\text{C}}\text{H}\text{NH}_3^+$  using ESR following the UV photolysis at 77 K of frozen solutions of amino acids containing  $\text{NH}_4\text{Fe}(\text{SO}_4)_2 \cdot 12\text{H}_2\text{O}$  (pH of medium 2-3),  $[\text{CsCo}(\text{SO}_4)_2] \cdot 12\text{H}_2\text{O}$  (6 M  $\text{H}_2\text{SO}_4$ ) or  $[\text{K}_3\text{Fe}(\text{CN})_6]$  (pH from 0 to 8)<sup>160</sup>.

The rate of accumulation of the decarboxylated glycine radical,  $\dot{\text{C}}\text{H}_2\text{NH}_3$  was found to be dependent upon the pH of the medium. It was found that the rate of accumulation increases with a rise in pH reaching a maximum at pH 8.0 and falling to zero at pH 12.0. They concluded from this that only the zwitterion form  $\text{R}\dot{\text{C}}\text{H}(\text{NH}_3^+)\text{COO}^-$  and possibly  $\text{R}\dot{\text{C}}\text{H}(\text{NH}_3^+)\text{COOH}$  are responsible for the formation of the radicals. In a later paper Poznyak et al.<sup>161</sup> investigated the photolysis of amino acids in the presence of hexacyanide and trisphenanthroline complexes of Fe(III). They observed that for  $\beta$ -alanine, decarboxylation occurred irrespective of the pH. The decomposition reaction of the  $\alpha$ -amino acids are however sensitive to the pH of the environment. In acidic or neutral media decarboxylation of the amino acid occurred,



However, in an alkaline medium of pH 13 hydrogen atom abstraction from the deprotonated amino group took place in addition to decarboxylation.



They concluded that when the amino group is protonated, decarboxylation of the amino acid occurs. When the amino and carboxyl groups are far removed, as in  $\beta$ -alanine, the state of the amino group does not influence the character of the oxidative breakdown.

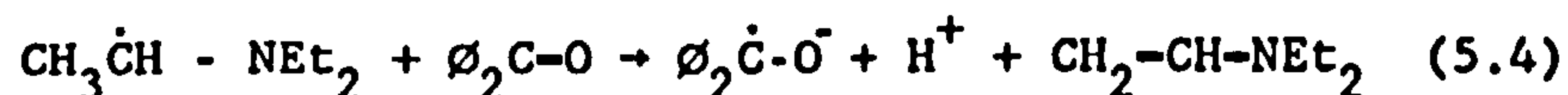
Poupko et al.<sup>162</sup> have conducted an ESR investigation of the radicals produced by UV irradiation of amino acids in the presence of  $\text{K}_3[\text{Fe}(\text{CN})_6]$  at low temperatures. For the monocarboxylic amino acids, the photosensitised irradiation resulted in loss of carbon dioxide, leading

to the formation of free radicals of the type  $\text{H}_3\dot{\text{N}}\text{CR}_1\text{R}_2$ . With the dicarboxylic amino acids, e.g. aspartic acid, decarboxylation took place at the position more remote from the amino group.

Uranyl-sensitised photochemical reactions of some amino acids have been studied by I.R. spectroscopy using a medium of pressed KBr pellets at room temperature<sup>163</sup>. However, the results from these experiments are inconclusive as to the nature of the photoproducts.

The photoreduction of benzophenone by amino acids, aminopolycarboxylic acids and their Fe(II), Co(II) and Ni(II) complexes has been investigated by Das *et al.*<sup>164</sup> using laser flash photolysis. The efficiency of the photoreduction was measured in terms of the yield of ketyl radical  $\phi_2\dot{\text{C}}\text{OH}$  or radical anion  $\phi_2\dot{\text{C}}\text{O}^-$ . At neutral pH it was found that the amino and aminopolycarboxylic acids were better quenchers when complexed with the metal ions. Among a series of metal complexes with a given acid, the triplet quenching rate constants ( $k_q$ ) and yields ( $\delta$ ) of ketyl radical increased in the order:  $\text{Ni(II)} \leq \text{Co(II)} < \text{Fe(II)}$ . This was attributed to the increasing exothermicity for charge-transfer interaction with the ketone triplet (for  $k_q$ ) and for back-electron transfer in the photogenerated radical pair.

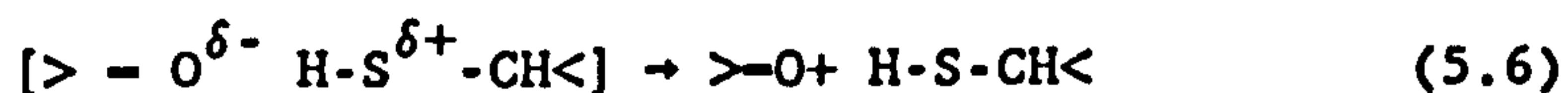
Under basic conditions, the formation of  $\phi_2\dot{\text{C}}\text{O}^-$  was observed to be a slow process with a time scale longer than that associated with triplet quenching. This secondary reduction has been ascribed to electron transfer from an amino-alkyl radical to the ground state of the ketone, typically shown by triethylamine:





The bimolecular quenching constants for triplet benzophenone using glycine gave  $k_q < 5 \times 10^5 \text{ dm}^3 \text{ mol}^{-1} \text{ s}^{-1}$ . The aromatic-containing amino acids tryptophan and tyrosine have  $k_q$  ca.  $2 \times 10^9 \text{ dm}^3 \text{ mol}^{-1} \text{ s}^{-1}$ ; the sulphur-containing amino acid methionine has  $k_q = 2.4 \times 10^9 \text{ dm}^3 \text{ mol}^{-1} \text{ s}^{-1}$ . Complexation with metal ions increases  $k_q$  for glycine ca. 1000 times while little effect is seen with the other amino acids.

A similar study on the quenching of triplet benzophenone by sulphur-containing amino acids and peptides has been carried out by Lissi *et al.*<sup>165</sup>. The values of  $k_q$  for the sulphur-containing compounds are ca.  $10^8$ - $10^9 \text{ dm}^3 \text{ mol}^{-1} \text{ s}^{-1}$ . The quenching of triplet benzophenone by thiols is thought to proceed via a charge-transfer complex followed by hydrogen atom abstraction from the S-H bond and/or the  $\alpha$  carbon atom.



This mechanism is supported by the dependence of  $k_q$  on solvent polarity.  $\phi_{\text{ketyl}}$  for cysteine  $\ll 1.0$ , which implies that reaction (5.6) contributes significantly to decay of the C-T complex, and that hydrogen atom abstraction is only a minor process. Also the fact that photoreduction quantum yields are smaller than  $\phi_{\text{ketyl}}$  indicates that back-transfer of a hydrogen atom from the ketyl radical is one of the main reaction paths for the primary radical.

The quenching of triplet benzophenone by cysteine in water occurs with significant formation of ketyl radicals. This result indicates that at

least in polar solvents a significant contribution from a mechanism involving formation of an exciplex with C-T character is occurring.



## **Chapter 6**

### **Introduction**

**Photochemistry of the Octacyanide Complexes of Tungsten(IV) and (V)**

## 6.1 Photochemistry of the Octacyanide Complexes of Tungsten(IV) and (V)

The photochemistry of the octacyano metalates,  $[M(CN)_8]^{n-}$ , (where M = W or Mo and n = 3 or 4) has been actively investigated for the past 25 years.

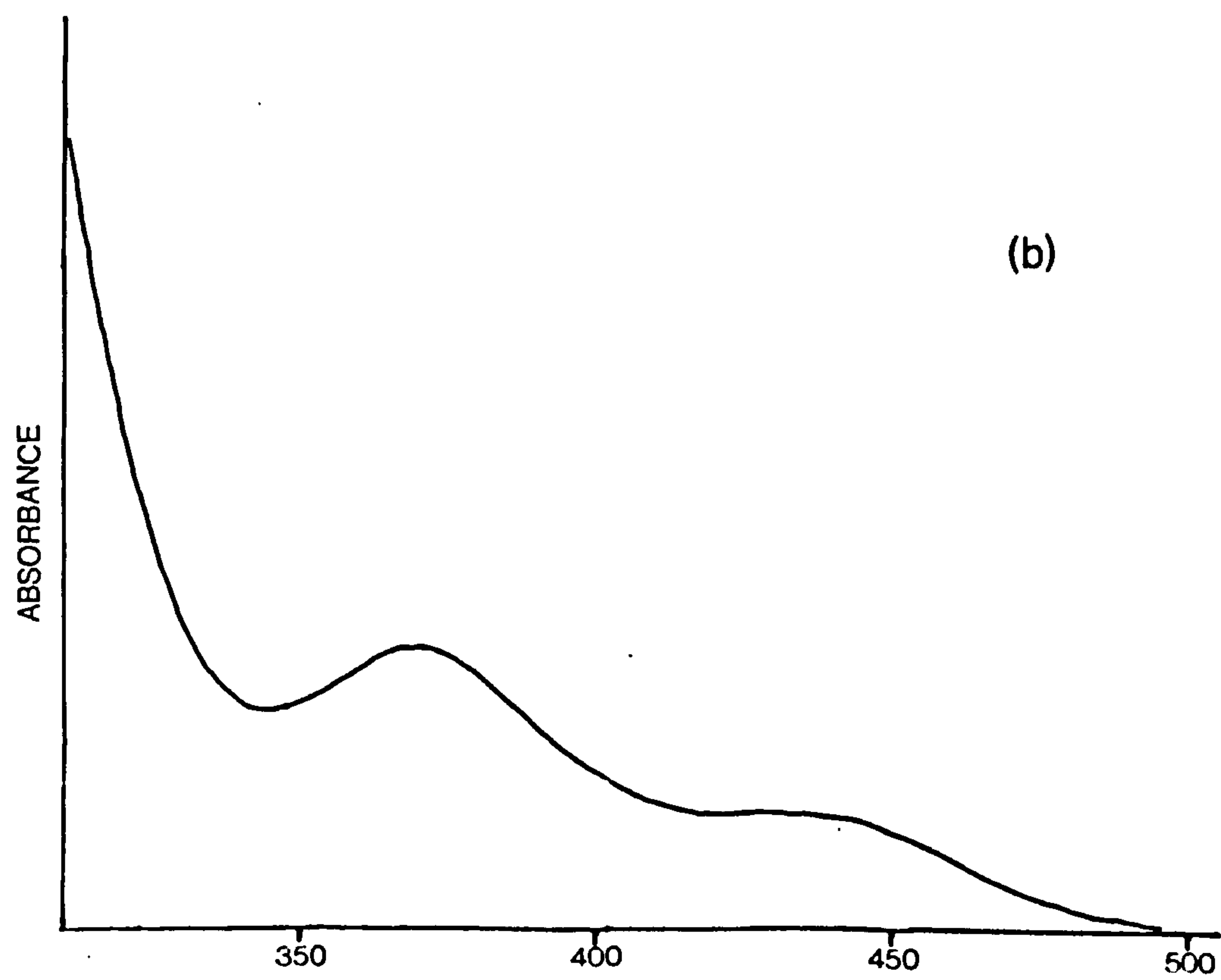
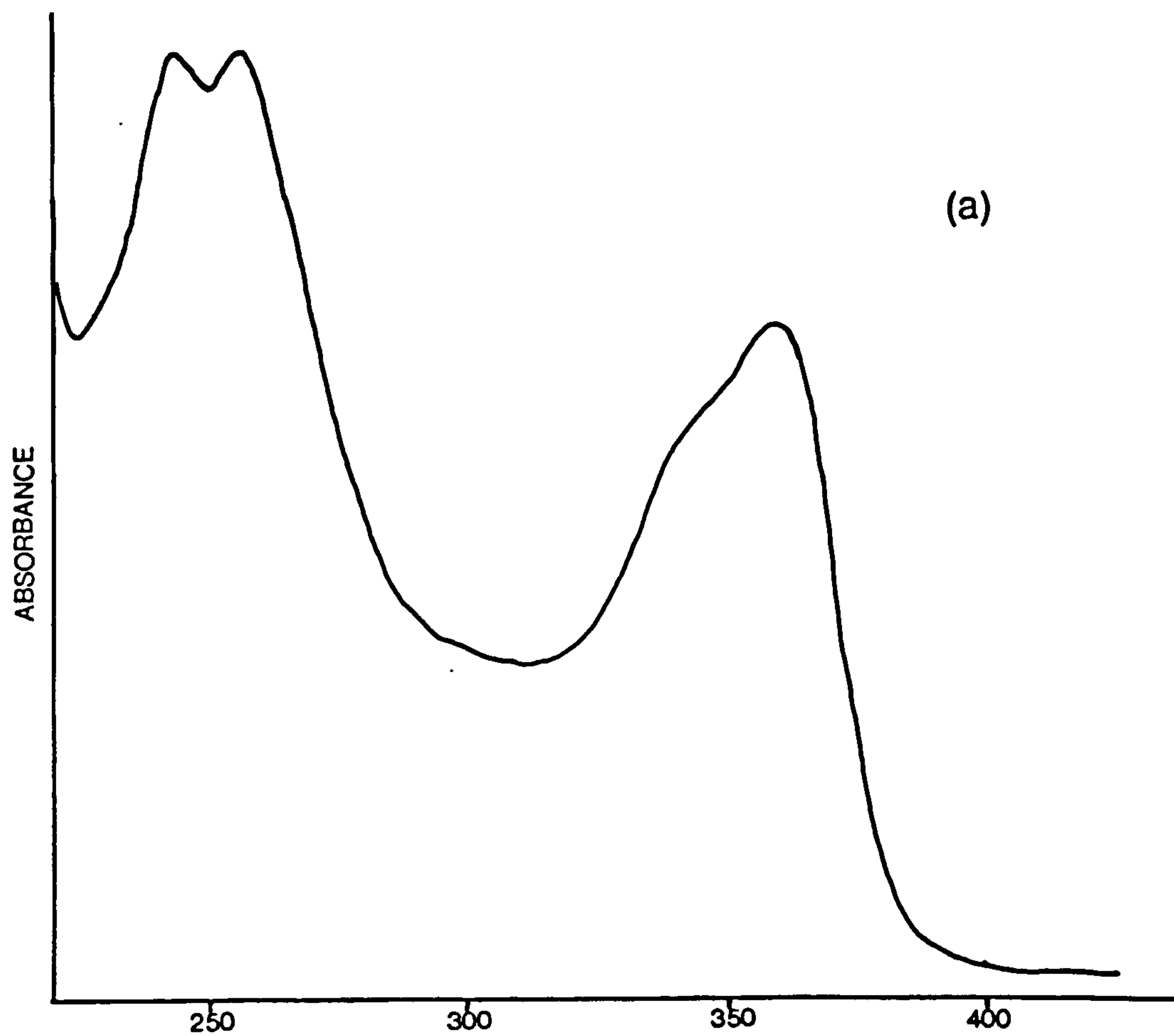
W(IV) is a  $d^2$  system and the electronic absorption spectrum of  $K_4[W(CN)_8]$  in water is shown in Figure 6.1(a). The absorption bands occurring at 671, 570, 431, 368 and 280 nm have been assigned as d-d transitions, while a charge-transfer band occurs at 248 nm<sup>166</sup>. An aqueous solution of  $[W(CN)_8]^{4-}$  is inert towards dilute acid and alkali in the absence of light. Exchange of labelled cyanide with  $[W(CN)_8]^{4-}$  is also very slow in the dark<sup>157</sup>. Electron transfer between  $[W(CN)_8]^{4-}$  and  $[W(CN)_8]^{3-}$  is extremely fast as are the other electron exchange reactions between  $[W(CN)_8]^{4-}$  and  $[IrCl_6]^{2-}$ ,  $[Fe(CN)_6]^{3-}$  and  $[Mo(CN)_8]^{3-}$ , the rate constants for these processes being in good agreement with those calculated from Marcus' theory<sup>168</sup>.

The standard potential for the system  $[W(CN)_8]^{3-} + e^- \rightleftharpoons [W(CN)_8]^{4-}$  is +0.57 V in KCl solution<sup>169</sup>, therefore, strong oxidising agents such as chlorine,  $[MnO_4]^-$  or Ce(IV) are required to oxidise  $[W(CN)_8]^{4-}$  to the corresponding W(V) octacyanide.

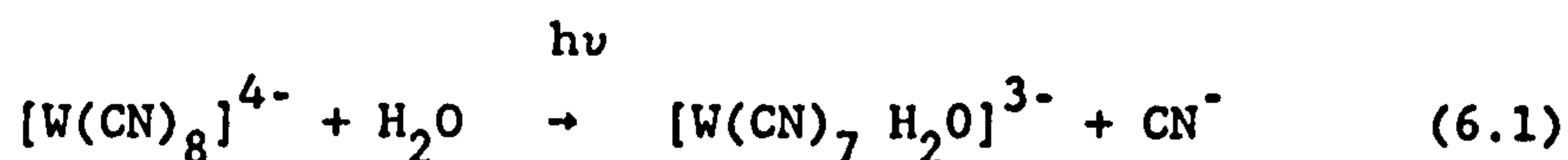
The electronic spectrum of the  $[W(CN)_8]^{3-}$  ion in aqueous solution is shown in Figure 6.1(b), and four ligand field (LF) transitions have been assigned at 357, 297, 259 and 239 nm<sup>170</sup>.

The early work of Carassiti and Balzani<sup>171,172</sup> on the photochemistry of the  $[W(CN)_8]^{3-}$  and  $[W(CN)_8]^{4-}$  ions in aqueous solution, established that

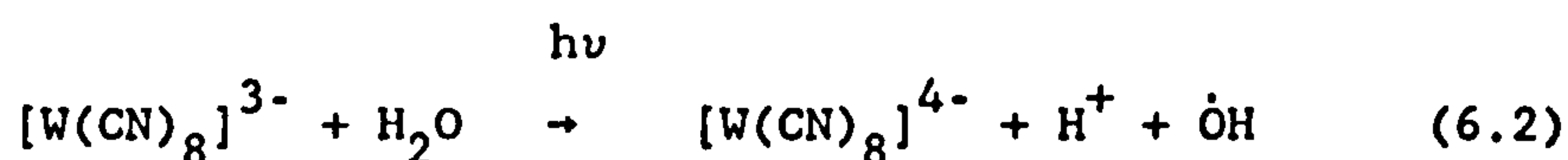
Figure 6.1      Electronic absorption spectrum of (a)  $[\text{W}(\text{CN})_8]^{3-}$  ion,  
and (b)  $[\text{W}(\text{CN})_8]^{4-}$ , both in aqueous solution.



these complexes are photosensitive to d-d irradiation. The  $[\text{Mo}(\text{CN})_8]^{4-}$  and  $[\text{W}(\text{CN})_8]^{4-}$  complexes were found to undergo photoaquation:

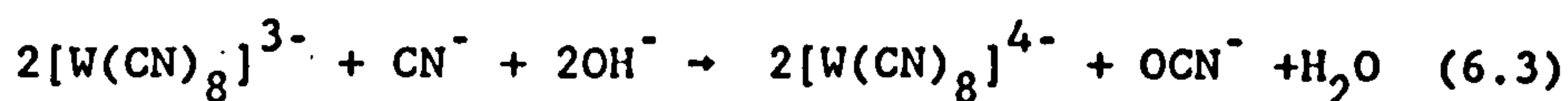


while  $[\text{M}(\text{CN})_8]^{3-}$  (M = Mo or W) were found to undergo photoreduction via an intramolecular redox process:



Additional evidence for the operation of a free-radical mechanism involving OH radicals has come from spin-trapping experiments<sup>173,174</sup>.

Measurements of the quantum yields of  $[\text{W}(\text{CN})_8]^{4-}$  formation from the photoreduction of  $[\text{W}(\text{CN})_8]^{3-}$ , see equation (6.2), in aqueous solution are in disarray. Balzani et al. report a quantum yield of 1.6 for the 365 nm photoysis of  $[\text{W}(\text{CN})_8]^{3-}$  in aqueous solution at pH = 5.5<sup>172</sup>. Samotus et al. obtained  $\phi = 0.8$  for the photolysis of  $\text{H}_3[\text{W}(\text{CN})_8]$ <sup>175</sup>, i.e. half the value found by Balzani. In a later paper, Samotus et al.<sup>176</sup> found that the initial quantum yield,  $\phi_o$ , remained practically constant over the pH range 1.02-12.78 and equal to  $0.81 \pm 0.05$  mole/Einstein. The final quantum yields,  $\phi_f$ , for neutral and alkaline solutions were found to be approximately constant, with  $\phi_f = 3.42 \pm 0.25$  in the 7-12 pH range. They attribute the large value of  $\phi_f$  to the secondary alkaline photolysis of  $[\text{W}(\text{CN})_8]^{4-}$  and the dark reaction of  $[\text{W}(\text{CN})_8]^{3-}$  with  $\text{CN}^-$ :



Excitation of LF transitions of  $[\text{W}(\text{CN})_8]^{4-}$ , equation (6.1), leads to the formation of a mixed aquocyano complex,  $[\text{W}(\text{CN})_7\text{H}_2\text{O}]^{3-}$  which has been observed spectroscopically as a red species ( $\lambda_{\text{max}}$  520 nm)<sup>177</sup>. A fast thermal reaction of  $[\text{W}(\text{CN})_7\text{H}_2\text{O}]^{3-}$  with  $\dot{\text{O}}\text{H}$  radicals results in the formation of  $[\text{W}(\text{CN})_7\text{H}_2\text{O}]^{2-}$  which has also been observed spectroscopically as a red species with  $\lambda_{\text{max}}$  535 nm<sup>175</sup>.

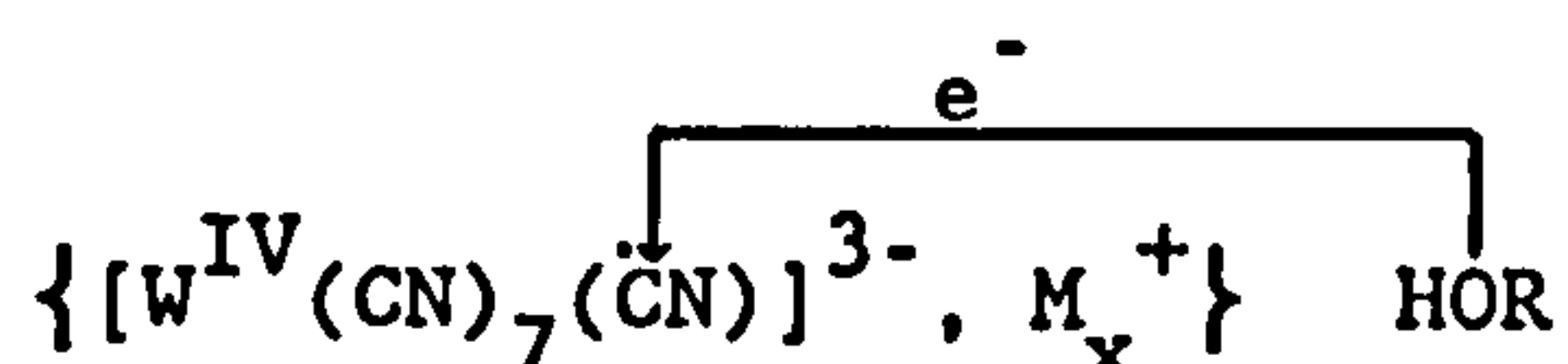


High intensity photolysis of  $[\text{W}(\text{CN})_8]^{3-}$  in aqueous or aqueous-methanol solutions results in the reported formation of the dioxygen complexes,  $[(\text{CN})_7\text{WO}_2]^{3-}$  (I) and  $[(\text{CN})_7\text{WO}_2\text{W}(\text{CN})_7]^{6-}$  (II). As irradiation of  $[\text{W}(\text{CN})_8]^{3-}$  ( $\lambda > 305$  nm) proceeds the solution changes from colourless to red with a new band appearing at 535 nm (species I). Under alkaline conditions the red solution turned violet (species II) with  $\lambda_{\text{max}}$  560 nm. The formation of complex (II) was found to be facilitated by using solvents of low polarity<sup>174</sup>.

Laser flash photolysis (at 249 nm) of  $[\text{W}(\text{CN})_8]^{3-}$  in water and methanol produces an intense ESA ( $\lambda_{\text{max}} \approx 410$  nm) which decays by first-order kinetics with a lifetime of 5 ms. The rate constant of the W-intermediate was found to be dependent upon the solvent used, the presence of oxygen, which increases  $k_{\text{obs}}$ , and pH. The addition of electrolytes was also found to dramatically increase  $k_{\text{obs}}$ , a cation effect operating specifically. The effect of the cation was attributed to a close-contact ion-pair between the W-intermediate and the cation,  $\{^*[\text{W}(\text{CN})_8]^{3-}, \text{M}_x^+\}$ . The formation of  $[\text{W}(\text{CN})_8]^{4-}$  and  $\dot{\text{O}}\text{H}$  radical is



thought to stem from a process in which an electron-deficient cyanide removes an electron from an adjacent solvent molecule with the cations acting as conducting bridges<sup>178</sup>.



Flash photolysis of deaerated solutions of  $[W(CN)_8]^{4-}$  gives rise to  $e^-$  (aq) with a photoelectron yield of 0.34 as measured by scavenging<sup>179</sup> by  $N_2O$  to give  $N_2$ . Similarly the photolysis of the alkylammonium salt of  $[W(CN)_8]^{4-}$  at 282 nm in  $CHCl_3$  results in its oxidation to  $[W(CN)_8]^{3-}$ , the  $CHCl_3$  acting as an electron scavenger:



The quantum yield for the conversion is measured as 0.37<sup>180</sup>.

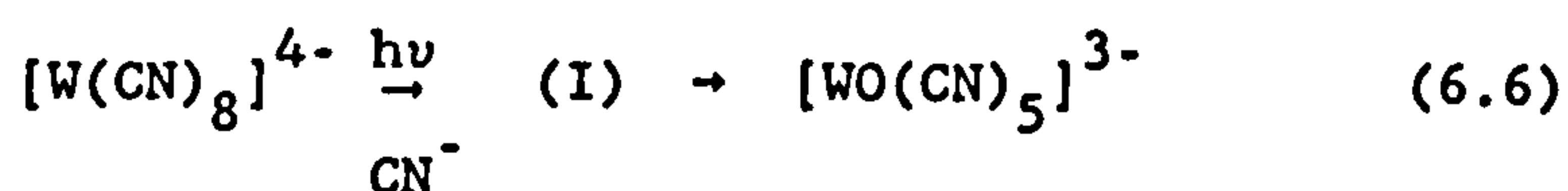
Photolysis of  $[W(CN)_8]^{4-}$  in  $CHCl_3:ROH$  (3:1) mixtures ( $R = Me, Et, Pr, Bu$ ) in the presence of phenanthroline results in the formation of stable  $[W(OR)_4(phen)]$  complexes<sup>181</sup>.

The photochemistry of aqueous solutions of  $[W(CN)_8]^{4-}$  depends to a great extent on the excitation wavelength, the concentration of the reactant, temperature and pH of the medium. Under LF excitation,  $[W(CN)_8]^{4-}$  undergoes efficient photoaquation as shown by equation (6.1). The red product of this initial photolysis has been isolated as  $Ag_3[W(CN)_7H_2O]$ <sup>182,183</sup>.

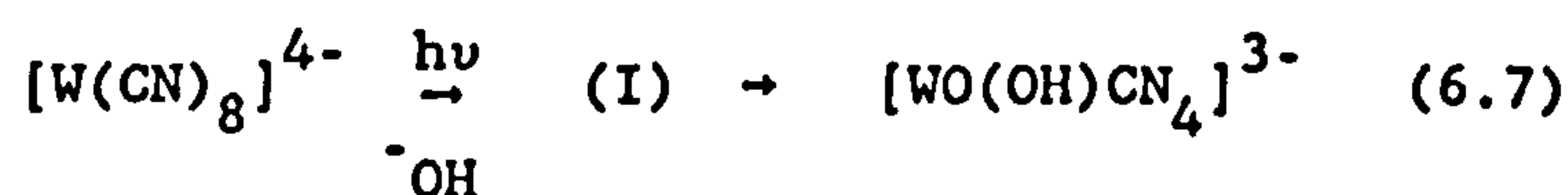


$[\text{W}(\text{CN})_8]^{4-}$  has been irradiated at 365 nm and at various pH, to give three primary photoproducts  $[\text{HW}(\text{CN})_7\text{H}_2\text{O}]^{2-}$ ,  $[\text{W}(\text{CN})_7\text{H}_2\text{O}]^{3-}$  and  $[\text{W}(\text{CN})_7\text{OH}]^{4-}$  in acid-base equilibria, characterised by  $\lambda_{\text{max}}$  at 520, 520 and 490 nm respectively<sup>184,185</sup>.

Ligand field photolysis of aqueous alkaline solutions of  $\text{K}_4[\text{W}(\text{CN})_8]$  containing KCN produces  $[\text{WO}(\text{CN})_5]^{3-}$  species, equation (6.6)



The oxopentacyanotungstate (IV),  $[\text{WO}(\text{CN})_5]^{3-}$  is green with  $\lambda_{\text{max}}$  615 nm. However, in aqueous alkaline media photolysis of  $[\text{W}(\text{CN})_8]^{4-}$  has been found to result in the formation, through intermediate (I), of oxohydroxotetracyanotungstates (IV) with  $\lambda_{\text{max}}$  540 nm<sup>186</sup>.



The photochemistry of other transition metal cyanide complexes has been investigated, including those of Cr, Mn, Fe, Ru and Co<sup>172,187</sup>.

Photoaquation is often observed and quantum yields are in the range 0.01 to 0.40<sup>188</sup>. Photolysis of aqueous  $[\text{Fe}(\text{CN})_6]^{4-}$  at 218 nm leads to photoelectron production<sup>188</sup>, and the yields for photoelectron production are in the order of increasing oxidising potential<sup>183</sup>  $[\text{Fe}(\text{CN})_6]^{4-} > [\text{W}(\text{CN})_8]^{4-} > [\text{Mo}(\text{CN})_8]^{4-}$ . Irradiation of  $[\text{Cr}(\text{CN})_6]^{3-}$  in acetonitrile at 366 nm leads to photosolvolysis yielding  $[\text{Cr}(\text{CN})_5\text{MeCN}]^{2-}$ , with a quantum yield of 0.043<sup>189</sup>.

## **Chapter 7**

### **Experimental**

### 7.1.1 Laser Flash Photolysis

In 1949 Norrish and Porter<sup>190</sup> demonstrated that a very intense flash of light could be used to initiate a large number of reactions. The technique of flash photolysis involves the generation of a non-equilibrium concentration of electronically excited molecules. If the excited species are luminescent, the fluorescence or phosphorescence can be recorded as time-dependent kinetics at a pre-set monitoring wavelength. This involves the use of a monochromator fitted with a photomultiplier which is in turn coupled to an oscilloscope. However, if the excited species is non-luminescent, an excited state absorption spectrum (ESA) can sometimes be obtained by the use of an analysing beam of light. The ESA can also be recorded as time-dependent kinetics.

The limitations of flash photolysis employing conventional electric discharge lamps is the duration of the lamp pulse, which is at best a few microseconds at reasonable intensities. However, with the advent of the laser, reactions in the nano-second time scale could be studied. The continuing development of lasers has now extended laser flash photolysis into the pico- and subpicosecond time domain.

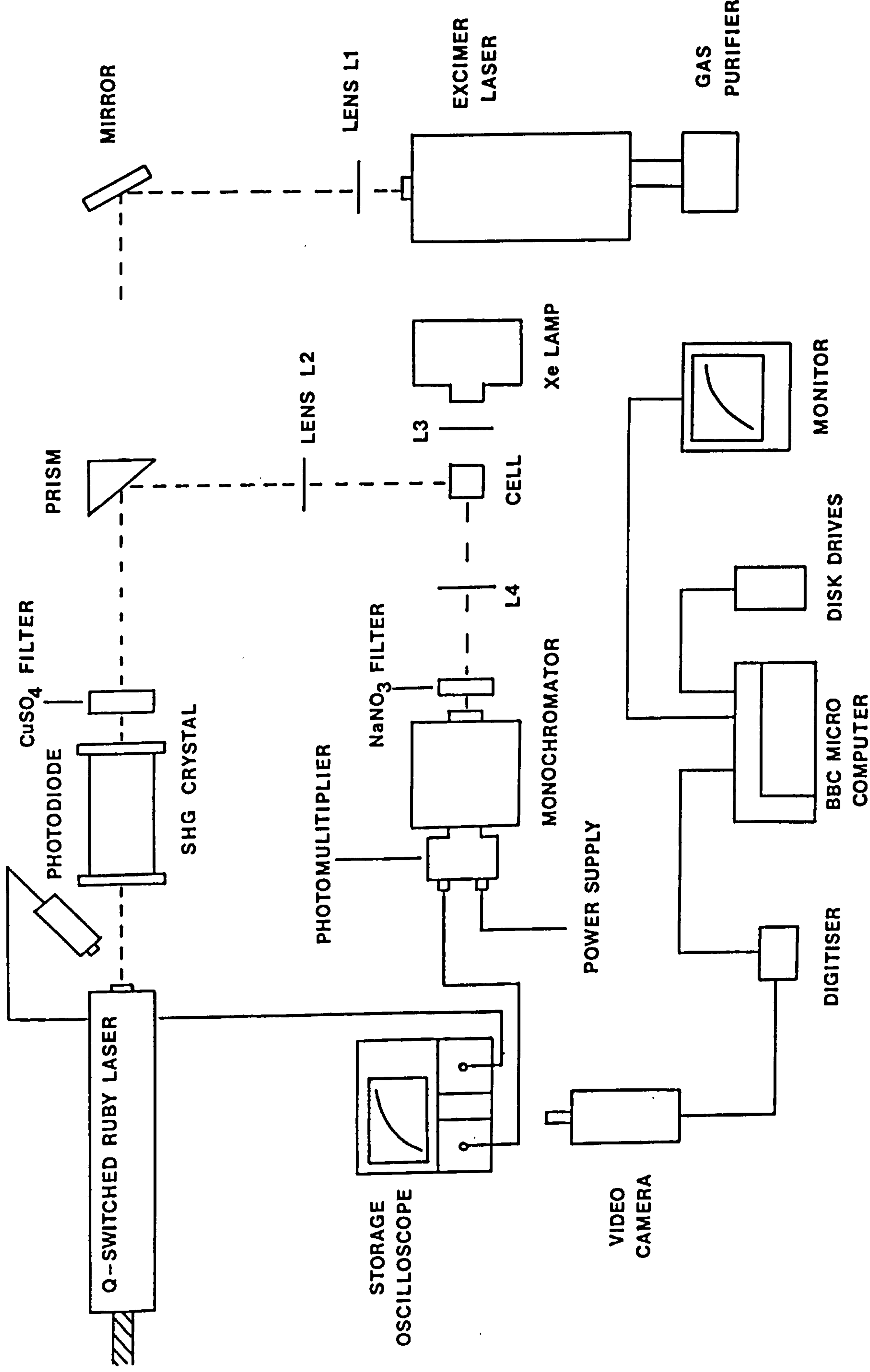
Two types of lasers have been employed in the present work, i.e. a solid state Q-switched ruby laser (Applied Photophysics Ltd., London) and a rare gas halide laser (Oxford Lasers Ltd.).

The work on the uranyl ion was carried out using both the ruby and excimer lasers, while in the study of the tungsten octacyanides the excimer laser was used exclusively.

The Q-switched ruby laser assembly is depicted in Figure 7.1, Q-switching being achieved using a solution of vanadyl phthalocyanine in nitrobenzene with an OD ca. 0.3 at 694 nm. The fundamental frequency output (694 nm, 1 J/pulse of 50 ns duration) is frequency doubled to 347 nm using a rubidium dihydrogen arsenate crystal (thermostatted at 323 K) to yield a 100 mJ pulse. The pulse then passes through an acidic copper sulphate solution (OD = 2.0 at 694 nm) to remove any remaining 694 nm radiation, which is then focused onto the sample cell. For ESA studies the laser beam is focused onto the sample cell coincident with and at  $90^\circ$  to the analysing beam from a water-cooled xenon high-pressure lamp (250 W). Absorption of the laser pulse by the sample produces a large yield of molecules in their excited state which in turn partly absorb the analysing light which results in a time-resolvable transient change in beam intensity, corresponding to the lifetime of the excited state. This intensity change is monitored at a preset wavelength by a high radiance monochromator and photomultiplier (either a model RCA IP28 or Hamamatsu 666) after it has passed through a sodium nitrite solution to remove any stray 347 nm laser radiation.

The oscilloscope used in this work was a Tektronix 7623 storage oscilloscope fitted with 7A15A(Y) and 7B50(X) amplifiers. Triggering of the oscilloscope is achieved by the use of a photodiode placed near to the front of the laser head. The signal from the photodiode is divided between the Tektronix oscilloscope and a second oscilloscope (Iwatsu model DMS-510) which displays a profile of the structure and intensity of the laser pulse, giving warning of any multiple laser pulsing. Two methods were employed to analyse the stored trace on the Tektronix oscilloscope. The first method involves photographing the trace onto Polaroid Type 46L film employing a Telford Type A oscilloscope camera.

**Figure 7.1**      **Ruby laser and a rare gas halide excimer laser flash  
photolysis assembly.**

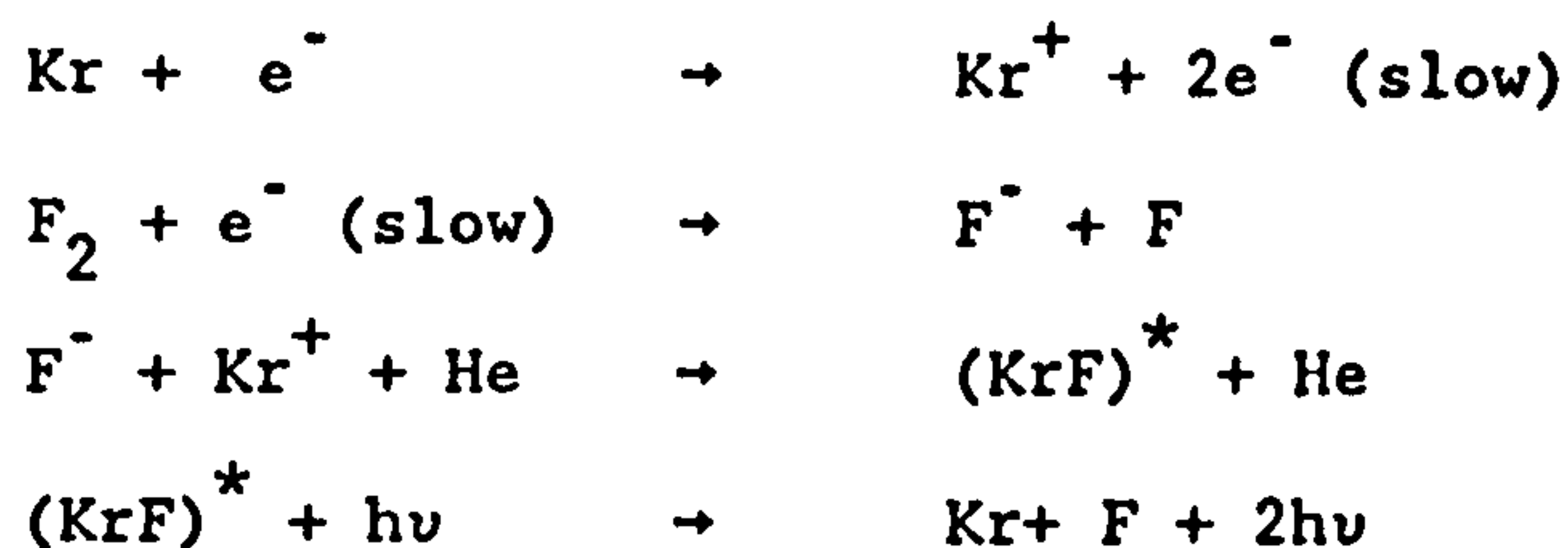




The transparencies are then fixed using a Polaroid dippit. The negatives are then enlarged (x2) onto graph paper and the transient curves digitised by hand ready for analysis by computer. The second method involves capturing the oscilloscope trace using a Rediffusion video camera. The resultant video image is then transferred via an interface (Data Harvest Ltd.) into a BBC Model B microcomputer which is in turn connected to a dual disk drive, monitor and Epson dot-matrix printer. The captured oscilloscope trace is now displayed on the computer monitor, from which, after scaling, data points can be selected using a moving cursor. After ca. 15 points have been selected from the trace, the computer performs the required kinetic least squares analysis, the results of which are presented on the monitor and output to the printer. For a more comprehensive review of the operation of the data analysis system, the reader is referred to reference 193.

To allow the focusing of the rare gas halide excimer laser beam onto the sample cell, an adjustable mounted prism is employed as depicted in Figure 7.1. The gas mixtures used in the excimer laser were, (i) 100 mbar of 10% fluorine in helium, 125 mbar of krypton and 1 bar of helium which provides the 249 nm output, and (ii) 25 mbar of xenon and 100 mbar of 10% fluorine which provides the 353 nm output. The laser cavity is connected to a gas purifier kept at 106 K for Kr/F<sub>2</sub> mixture and 127 K for Xe/F<sub>2</sub> mixture, which removes unwanted products formed by the lasing action. Lasing is achieved by discharging a high voltage ( 35 kV) across a spark gap. The excitation mechanism of rare gas halide lasers are complex and not fully understood. However, the following reactions for the KrF laser are thought to be the most important:





High overall efficiency results from the fact that  $\text{Kr}^+$  is formed very efficiently in a high current glow discharge, and of the energy stored in  $\text{Kr}^+$  approximately 30% reappears in the emitted photon. The ultraviolet output at 249 nm has a pulse energy of 250 mJ and 15 ns duration. Triggering of the oscilloscope is made internally rather than by the use of a photodiode.

#### 7.1.2 Luminescence Intensities and Spectra

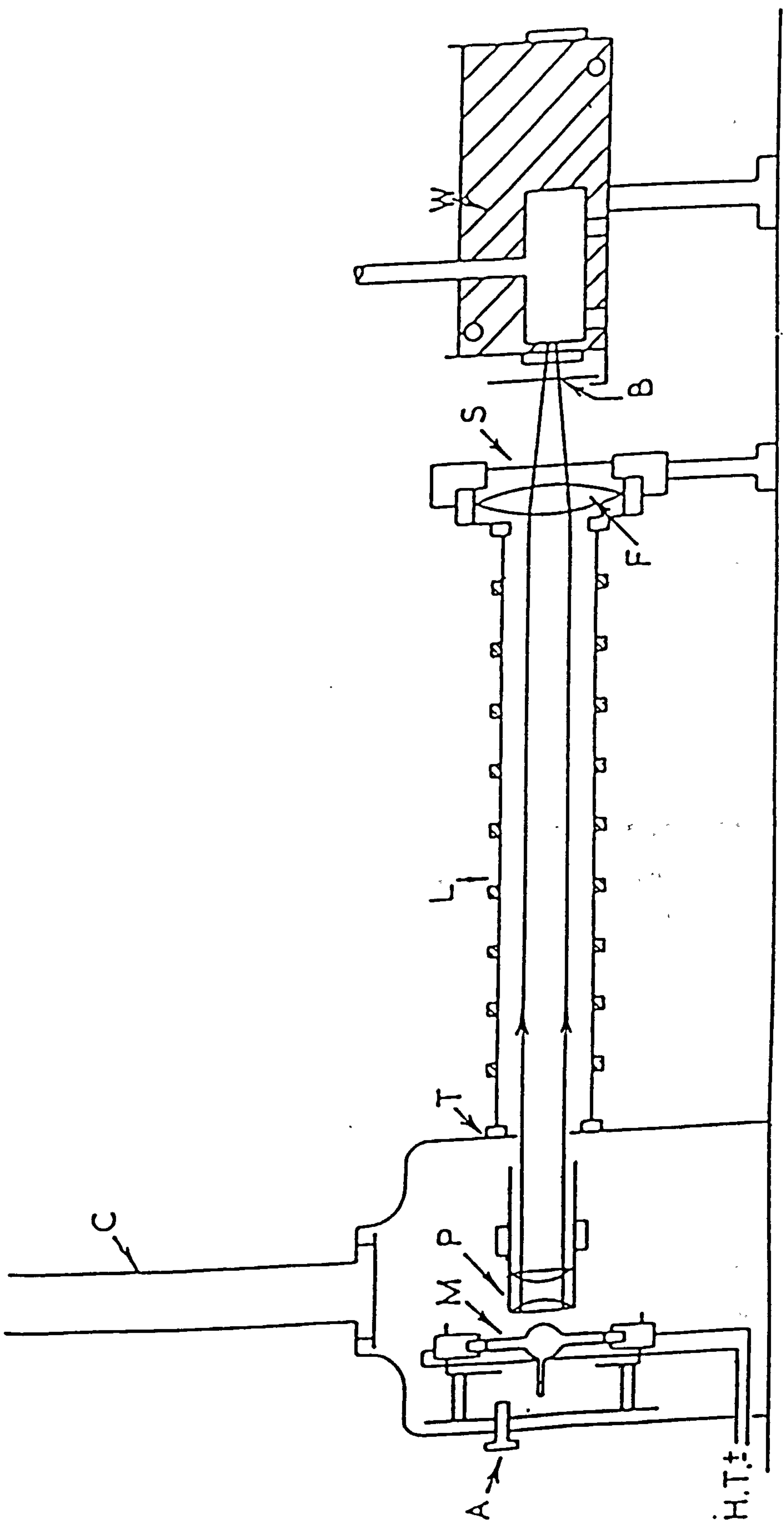
Luminescence studies were carried out using both Perkin Elmer MPF-3 and LS5 double beam spectrofluorimeters. Both instruments use right-angle illumination, which reduces effects from scattered light, sample cell luminescence and the portion of the excitation beam which is transmitted. The fact that both models are double-beam instruments means that the spectra are automatically connected up for lamp intensity fluctuations.

#### 7.1.3 The Optical Bench

The optical bench depicted in Figure 7.2 was used for all quantum yield experiments. The mercury vapour lamp, Wotan type HBO 200 W, is connected to a power supply which produces a stabilised current to within  $\pm 0.1\%$ . The transmitted beam passes through two quartz plano-convex lenses yielding a parallel beam which is focused using a third quartz lens onto the sample cell. Narrow band Balzer metal interference filters can be introduced into the light beam to obtain monochromatic

**Figure 7.2      The optical bench**

- A   Adjustment screws (for aligning lamp)**
- M   Mercury vapour lamp**
- P   Quartz plano - convex lenses**
- C   Cooling tower**
- T   Teflon seals**
- L   Light shield**
- F   Quartz focusing lenses**
- S   Shutter**
- B   Balzer filter**
- W   Water bath**



light of the required wavelength. The photolysis cell consists of a quartz cylinder, 5 cm in length and 2.5 cm in diameter. A glass sidearm is connected to the cell which terminates with a Teflon tap, allowing the solution to be argon-bubbled to remove dissolved oxygen prior to photolysis and isolated from the atmosphere.

Quantum yields can be expressed in terms of either product appearance or reactant loss.

$$\phi_{\text{product}} = \frac{\text{number of molecules of product formed}}{\text{number of Einsteins of radiation absorbed}} \quad (7.1)$$

$$= \frac{\text{rate of formation of product}}{\text{rate of absorption of radiation}} \quad (7.2)$$

If the number of molecules  $N$ , undergoing a particular process is known, the quantum yield can be determined from equation (7.3):

$$\phi = \frac{N_{\text{prod}}}{I_0 t (1 - 10^{-OD})} \quad (7.3)$$

$I_0$  - intensity of the incident light (quanta per second)

$t$  - irradiation time in seconds

$(1 - 10^{-OD})$  - Fraction of light absorbed by the reactant (assuming only one absorbing species at the irradiation wavelength).

$N_{\text{prod}}$  - number of molecules of product formed during the photolysis for a period sufficiently short to leave the net absorbance virtually unchanged.

Actinometry was performed according to the method of Hatchard and Parker employing the potassium trisoxalatoferrate (III) actinometer<sup>191</sup>. This procedure is based upon the photochemical reduction of the iron(III) complex to produce Fe(II) ions. The concentration of Fe(II) is determined by conversion to the 1,10-phenanthroline complex, the concentration of which can be determined spectrophotometrically. The number of Fe(II) ions produced on photolysis can be calculated from equation (7.4):

$$N_{\text{Fe}}^{2+} = \frac{6.023 \times 10^{20} \times V_1 V_3 \times \text{OD}}{V_2 l \epsilon} \quad (7.4)$$

where

$V_1$  - Volume of actinometer solution irradiated ( $\text{cm}^3$ )

$V_2$  - Volume of aliquot taken for analysis ( $\text{cm}^3$ )

$V_3$  - Final volume to which the aliquot  $V_2$  is diluted ( $\text{cm}^3$ )

OD - The measured OD of the solution at 510 nm after addition of 0.1% 1,10-phenanthroline and buffer solution.

$\epsilon$  - Experimental value of the molar extinction coefficient of the Fe (II) complex ( $1.09 \times 10^4 \text{ dm}^3 \text{ mol}^{-1} \text{ cm}^{-1}$ ).

#### 7.1.4 Other Instrumentation

Ultraviolet and visible spectra were recorded using either Perkin Elmer 552 or Shimadzu UV365 recording spectrophotometers. A Pye Unicam SP500 spectrophotometer was also used for the determination of uranium (IV) in quantum yield experiments.

Infra-red spectra were recorded using a Perkin Elmer 580B spectrophotometer. Fourier transform infra-red experiments at 12 K were recorded using a Nicolet 7000 series spectrophotometer at Southampton University.



Low temperature (77 K) IR and UV-vis spectra of photolysed polyvinylalcohol (PVA) films containing  $K_3[W(CN)_8]$  or  $K_4[W(CN)_8]$  were conducted in the apparatus depicted in Figure 7.3(a). In the case of 12 M LiCl (aq) or aqueous glycerol glasses (1:1), UV-vis spectra of the photolysed samples were recorded at 77 K in the apparatus shown in Figure 7.3(b).

Mass spectra were recorded on a Kratos Model MS80 spectrometer. ESR experiments were performed using a Bruker Model ER 200 tt spectrometer. Irradiation of samples for ESR study was carried out with a 900 W Xe/Hg point source, the output of which was filtered through both Schott UG5 and Pyrex filters, i.e.  $\lambda_{irr} = 330-410$  nm. Measurements of pH were made with a Pye Unicam Model PW9410 digital pH meter.

## 7.2 Syntheses

Co(III) (A.A)<sub>3</sub> was prepared from  $Na[Co(CO_3)_2] \cdot 3H_2O$  and the associated amino acid according to that reported previously<sup>194,195</sup>.

$Na[Co(CDTA)] \cdot 2H_2O$  was prepared according to the method of Mellor et al.<sup>196</sup>.

Potassium octacyanotungstate (IV) was prepared by the method of Leipoldt et al.<sup>192</sup>.

Oxidation to  $K_3[W(CN)_8] \cdot 1.5H_2O$  was achieved using aqueous acidic potassium permanganate<sup>197</sup>.

The purity of  $K_4[W(CN)_8] \cdot 2H_2O$  and  $K_3[W(CN)_8] \cdot 1.5H_2O$  was checked using UV-vis, IR and elemental analysis, the results of which are shown below:

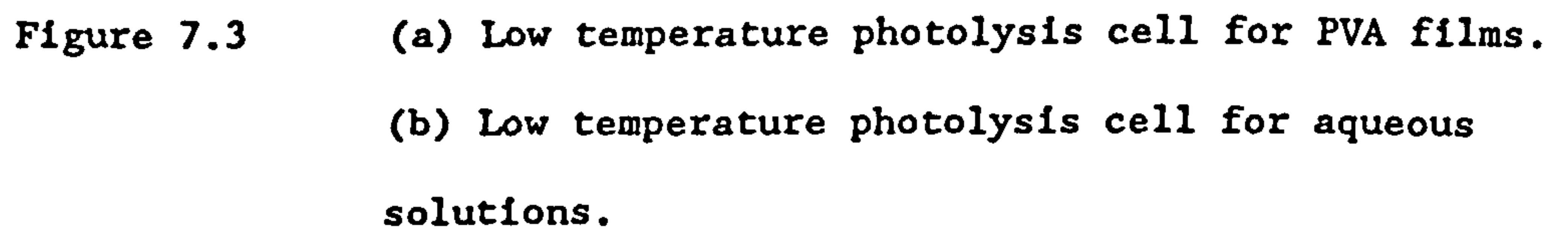
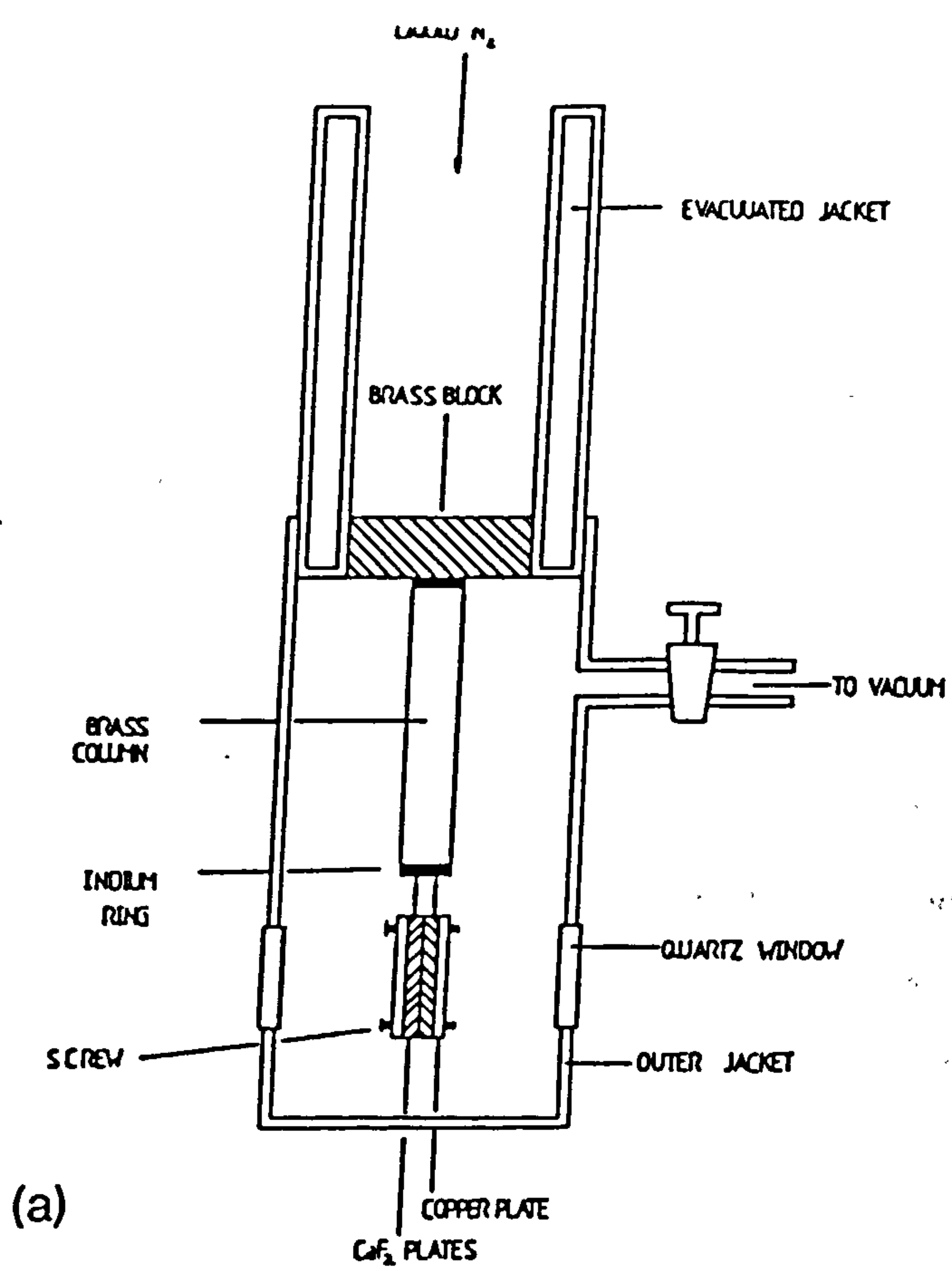
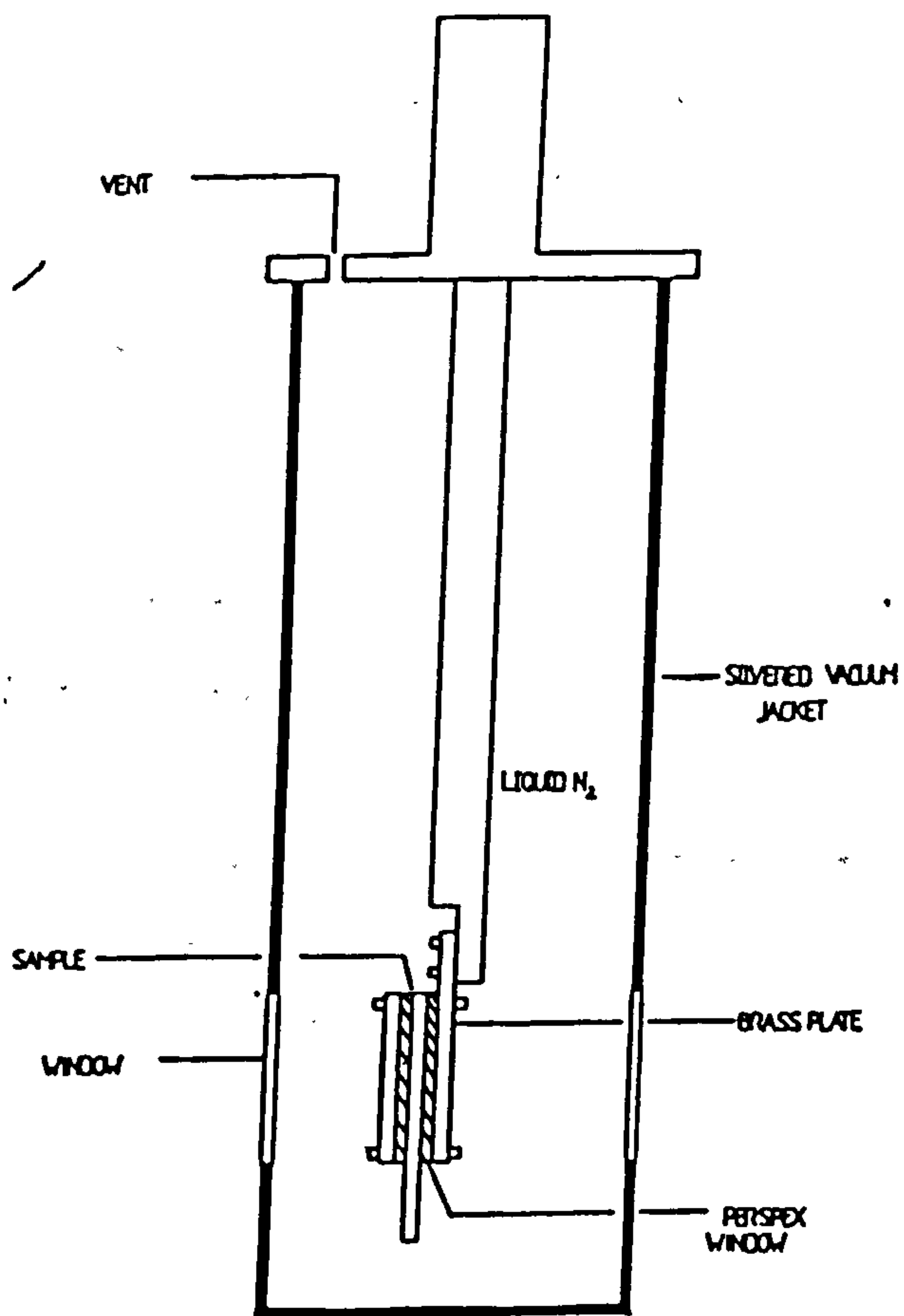


**Figure 7.3**      **(a) Low temperature photolysis cell for PVA films.**  
**(b) Low temperature photolysis cell for aqueous**  
**solutions.**





(a)



(b)

<u>Compound</u>	<u>Calculated %</u>			<u>Found %</u>		
	C	H	N	C	H	N
$K_4[W(CN)_8] \cdot 2H_2O$	16.44	0.69	19.16	16.55	0.53	19.45
$K_3[W(CN)_8] \cdot 1.5H_2O$	18.22	0.38	21.24	18.03	0.29	21.21

### 7.3 Purity of Chemicals

Purified water was obtained by refluxing doubly distilled water over alkaline permanganate for 48 hours and again doubly distilling. All organic solvents were either of spectroscopic or AnalaR grade and were used without further purification. All reagents used were of either AnalaR grade or the purest grade commercially available.

### 7.4 Sample Preparation

To ensure reproducible results for luminescence studies, quantum yield determinations and laser flash photolysis studies, all glassware used was frequently cleaned in a chromic acid solution to remove any traces of organic impurities.

In ESA studies the OD of the solution (1 cm cell) was adjusted to be between 2.0-2.5 at the laser wavelength thus ensuring that most of the laser pulse is absorbed near to the front of the cell. An OD of between 0.5-1.0 was employed for emission studies. Samples that were sensitive to either quenching or oxidation by oxygen were bubbled with high purity argon (BOC 99.999%) prior to use. Samples for ESR measurements were degassed, prior to photolysis, using the freeze-pump-thaw method (x3).

## 7.5 Emission and ESA Measurements

The sample cell for emission and ESA measurements was a quartz fluorimeter cell fitted with a Teflon tap to enable the sample to be degassed and isolated from the atmosphere.

ESA spectra were recorded by measuring the initial intensity of the transient as a function of monitoring wavelength. At each wavelength three readings were taken to allow for fluctuations in the intensity of the laser pulse. Measurements of weakly absorbing transients can be made more easily by the use of an 'offset box'. The transient intensity is a constant percentage of  $I_0$  (initial intensity of the analysing light) for a given time, and therefore by increasing  $I_0$  a larger transient signal can be obtained. The zero light level is off-set off the 'top' of the oscilloscope screen, which means that the 'light-off' trace no longer appears on the screen, i.e.  $I_0$  cannot be detected visually. The 'off-set box' overcomes this problem as it gives a precalibrated output voltage which when applied to the Y amplifier of the oscilloscope, in place of the photomultiplier output, allows the 'light off' level to be brought back onto the screen. This value can now be used to give the 'apparent'  $I_0$  value and by addition of the applied voltage from the 'off set box' the true value of  $I_0$  in mV can be calculated. The circuit diagram of the 'off set box' is shown in Figure 7.4.

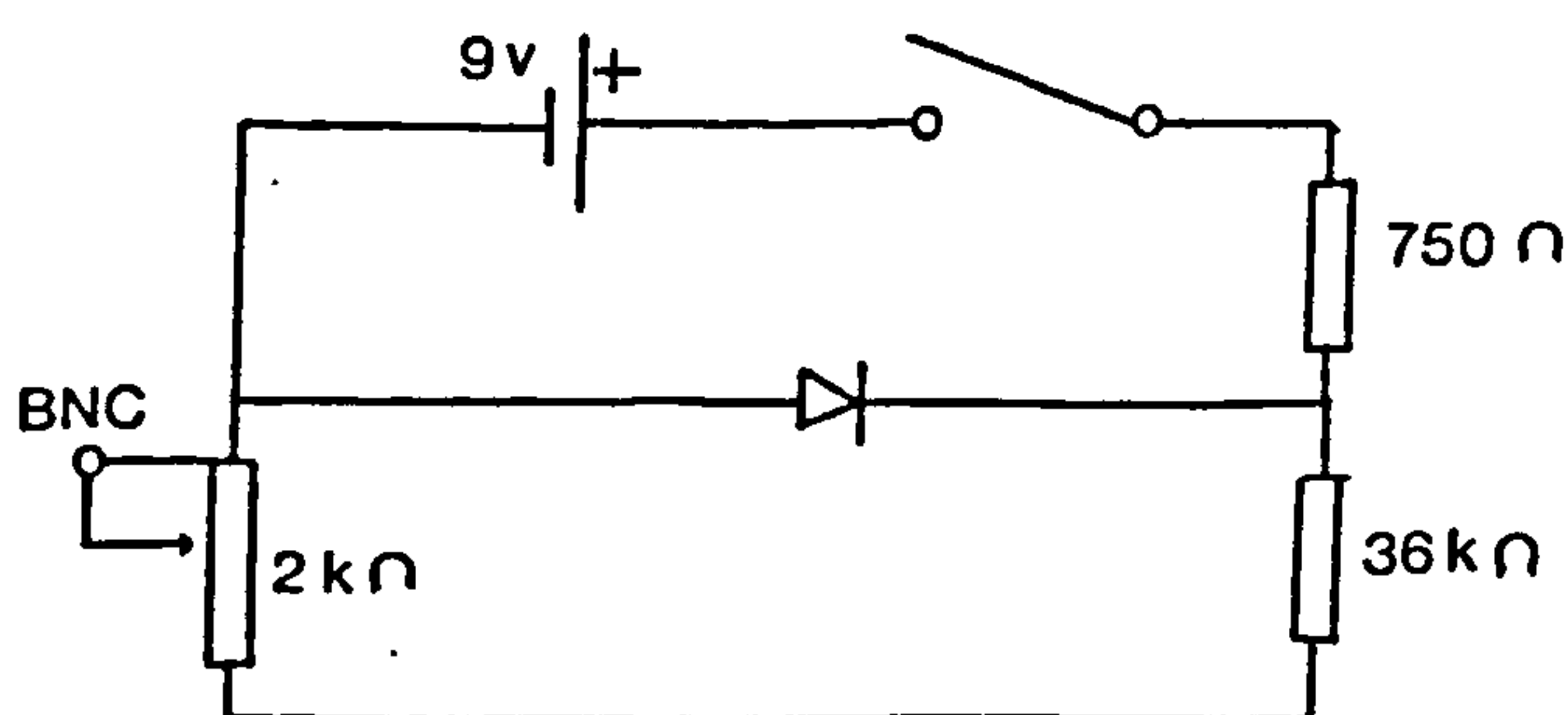


Figure 7.4 Off set box.

A transient absorption decay curve is shown in Figure 7.5.

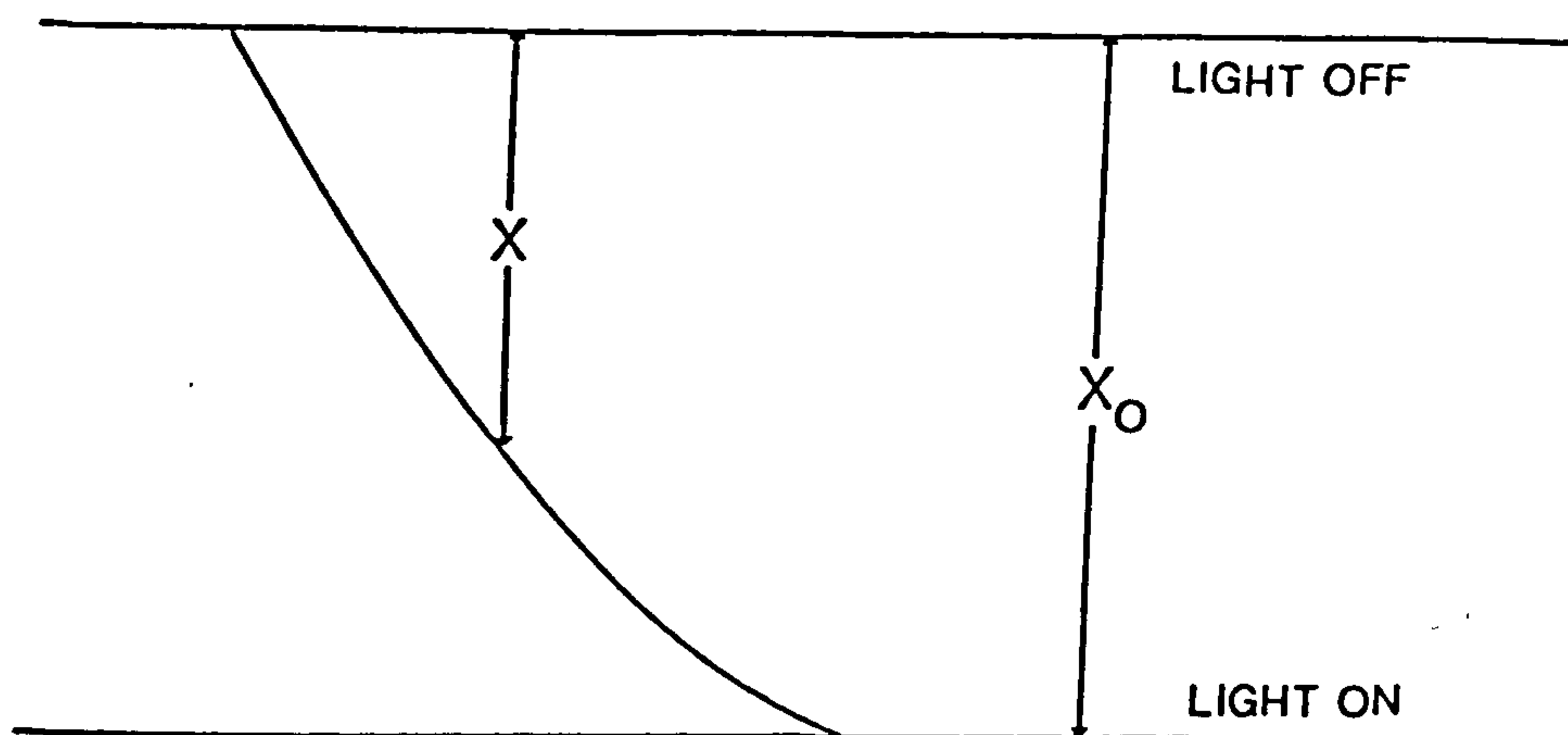


Figure 7.5 Transient Absorption Decay

Assuming that Beer's Law is obeyed, at any instant  $t$ , the OD can be calculated from

$$OD = \log I_0/I_t = \log X_0/X = \epsilon_{\lambda} C_t l \quad (7.5)$$

so that relative or absolute concentrations can be determined as a function of time, and the order and rate of the reactions of the transient calculated.

In equation (7.5),  $I_0$  and  $I_t$  are related to the oscilloscope deflections by

$$I_0 = k(\text{'light-on' deflection} - \text{'light off' deflection}) = kX_0$$

$$I_t = k(\text{'transient' deflection} - \text{'light off' deflection}) = kX_t$$

where  $k$  is a constant which depends on the detection sensitivity and which need not be evaluated.

## 7.6 Analysis of Results

### 7.6.1 Luminescence Studies

The results from luminescence quenching studies were analysed in terms of the Stern-Volmer equation (7.6)

$$I_{fo}/I_f = 1 + K^{sv} [Q] \quad (7.6)$$

where

$I_{fo}$  - the intensity of fluorescence without any added quencher.

$I_f$  - the intensity of fluorescence at quencher concentration  $[Q]$ .

$K^{sv}$  - the Stern-Volmer constant  $K^{sv}$  which can be factorised as  $k_q \tau$

where,

$k_q$  is the quenching rate constant and  $\tau$  is the lifetime of the luminescent species in the absence of quencher.

$[Q]$  - concentration of quencher.

Values of  $K^{sv}$  were obtained using a linear least squares programme.

### 7.6.2 Emission Lifetime and ESA Measurements

For emission lifetime measurements the linear relationship between the logarithm of  $I_f$  and the time  $t$  (in seconds) which gives a slope of  $-k_{obs}$  (first order rate constant  $s^{-1}$ ) was analysed using a linear least squares programme. The second-order quenching rate constant was obtained from the linear plot of  $-k_{obs}$  against  $[Q]$ , also using a linear least squares programme.

Normal first-order kinetics for ESA measurements were analysed according to the equation (7.7)

$$I_t = I_o \exp (-k_{obs} t) \quad (7.7)$$

using computer techniques.

## **Chapter 8**

### **Results**

#### **Complexation of Uranyl Ion with Simple Amino Acids**



## 8.1 Introduction

Our investigation of the interaction of the three most structurally basic amino acids glycine,  $\alpha$ -alanine and  $\beta$ -alanine with the ground-state uranyl ion is described in this chapter. Although a large number of investigations have been conducted on the complexation of  $[\text{UO}_2]^{2+}$  with the naturally occurring amino acids, discrepancies still exist as to the donor site and maximum coordination number of these ambidentate ligands. Solution studies have so far indicated a maximum coordination number of three, but debate still continues as to whether the amino group is involved in bonding to the uranyl ion. This chapter reports on several new uranyl ion-amino acid complexes, including an x-ray crystal structure of a novel 1:4 uranyl ion:glycine complex.

## 8.2 Spectroscopy

Absorption and emission spectra were recorded for uranyl nitrate and the corresponding uranyl-amino acid complex. The vibronic components of the absorption and emission spectra are shown in Tables 8.1 and 8.2 respectively. The addition of these amino acids to aqueous acidic uranyl nitrate induces a marked bathochromic-hyperchromic effect on the visible absorption bands, and both a red shift in the luminescence bands and an increase in luminescence intensity. Such changes in the intensities and band widths of the absorption spectrum have been interpreted in terms of a variation of the symmetry of the uranyl centre<sup>69,70</sup>, and a good correlation has been observed between the intensity and splitting of vibronic fine structure and the overall geometry of the coordination to the  $[\text{UO}_2]^{2+}$  centre.



Table 8.1      Absorption spectra for Uranyl Nitrate and 1:4 uranyl-amino  
acid Complexes

nm			
<sup>a</sup> [UO <sub>2</sub> ] <sup>2+</sup>	<sup>b</sup> [UO <sub>2</sub> (O <sub>2</sub> CCH <sub>2</sub> NH <sub>3</sub> ) <sub>4</sub> ] <sup>2+</sup>	<sup>a</sup> [UO <sub>2</sub> (O <sub>2</sub> CC(CH <sub>3</sub> )NH <sub>3</sub> ) <sub>4</sub> ] <sup>2+</sup>	<sup>a</sup> [UO <sub>2</sub> (O <sub>2</sub> CCH <sub>2</sub> CH <sub>2</sub> NH <sub>3</sub> ) <sub>4</sub> ] <sup>2+</sup>
485.0	488.0	487.0	488.0
467.0	470.0	470.0	470.0
449.0 (sh)	453.0 (sh)	451.0	454.0 (sh)
436.5 (sh)	438.0 (sh)	440.0 (sh)	440.0 (sh)
424.5	422.5 (sh)	424.0 (sh)	425.0 (sh)
412.5	416.5 <sup>d</sup>	416.0 <sup>d</sup>	418.0 <sup>d</sup>
401.5	409.0 (sh)	409.0	411.0
392.0 (sh)			
381.0 (sh)			
368.0	365.0 (sh)	370.0	
358.0		360.0	358.0 (sh)

<sup>a</sup>concentration = 0.10 M

<sup>b</sup>[UO<sub>2</sub>(O<sub>2</sub>CCH<sub>2</sub>NH<sub>3</sub>)<sub>4</sub>]<sup>2+</sup> = 0.019 M

<sup>c</sup>λ<sub>max</sub>

[HClO<sub>4</sub>] = 0.2 M,      T = 293 K

Table 8.2      Emission spectra for uranyl nitrate and 1:4 uranyl-amino  
acid Complexes

	$\lambda$ excitation/nm	$\lambda$ emission/nm
<sup>a</sup> $[\text{UO}_2]^{2+}$	412	490.0, 510.0 <sup>c</sup> , 531.5, 557.0
<sup>b</sup> $[\text{UO}_2(\text{O}_2\text{CCH}_2\text{NH}_3)_4]^{2+}$	416.5	495.0 <sup>c</sup> , 516.0, 537.5, 561.0
<sup>a</sup> $[\text{UO}_2(\text{O}_2\text{C}(\text{CH}_3)\text{NH}_3)_4]^{2+}$	416	493.0, 513.5 <sup>c</sup> , 536.5, 563.0
<sup>a</sup> $[\text{UO}_2(\text{O}_2\text{CCH}_2\text{CH}_2\text{NH}_3)_4]^{2+}$	418	495.0, 516.0 <sup>c</sup> , 538.0, 564.0

<sup>a</sup> concentration = 0.1 M

<sup>b</sup>  $[\text{UO}_2(\text{O}_2\text{CCH}_2\text{NH}_3)_4]^{2+}$  = 0.019 M

<sup>c</sup>  $\lambda_{\text{max}}$

$[\text{HClO}_4]$  = 0.20 M,      T = 293 K

The effect of addition of glycine to the luminescence lifetime of aqueous acidic uranyl nitrate, shown in Figure 8.1, indicates that complexation increases as the ligand concentration is increased, giving longer lived states (similar to the effects observed with phosphate and fluoride ions<sup>198</sup>), until at the highest glycine concentrations a plateau region is reached.

In the uranyl- $\alpha$ -alanine system, Figure 8.2, there seems to be an initial decrease in the lifetime, followed by a general trend of increasing lifetime with ligand concentrations of up to four times that of uranyl ion itself. The  $\beta$ -alanine system, shown in Figure 8.3, indicates that an initial decrease in  $\tau$  is experienced with increasing ligand concentration up to a four-fold excess of  $\beta$ -alanine, which is then followed by a slow further increase in luminescence lifetime.

### 8.3 Preparation of $[\text{UO}_2(\text{O}_2\text{CCH}_2\text{NH}_3)_4][\text{NO}_3]_2$

Equal aliquots of uranyl nitrate (1 M) and glycine (4 M), both in aqueous nitric acid (0.01 M), were mixed together. The water was allowed to evaporate slowly to leave a bright yellow amorphous solid. This was redissolved in the minimum amount of water and a quantity placed in an NMR tube (diameter 5 mm); acetonitrile was layered on top and the two-layer system left for 2-3 days where upon small crystals grew at the interface. The liquid layers were withdrawn to leave yellow, lath-shaped crystals which were washed with acetonitrile and allowed to dry in a desiccator. An elemental analysis of the crystals confirmed the 1:4 uranyl ion-glycine formulation.

Figure 8.1      Dependence of lifetime ( $\tau$ ) of excited  $[\text{UO}_2]^{2+}$  upon  
glycine concentration.

$[\text{UO}_2]^{2+} = 0.1 \text{ M}, \quad [\text{HClO}_4] = 0.2 \text{ M}.$

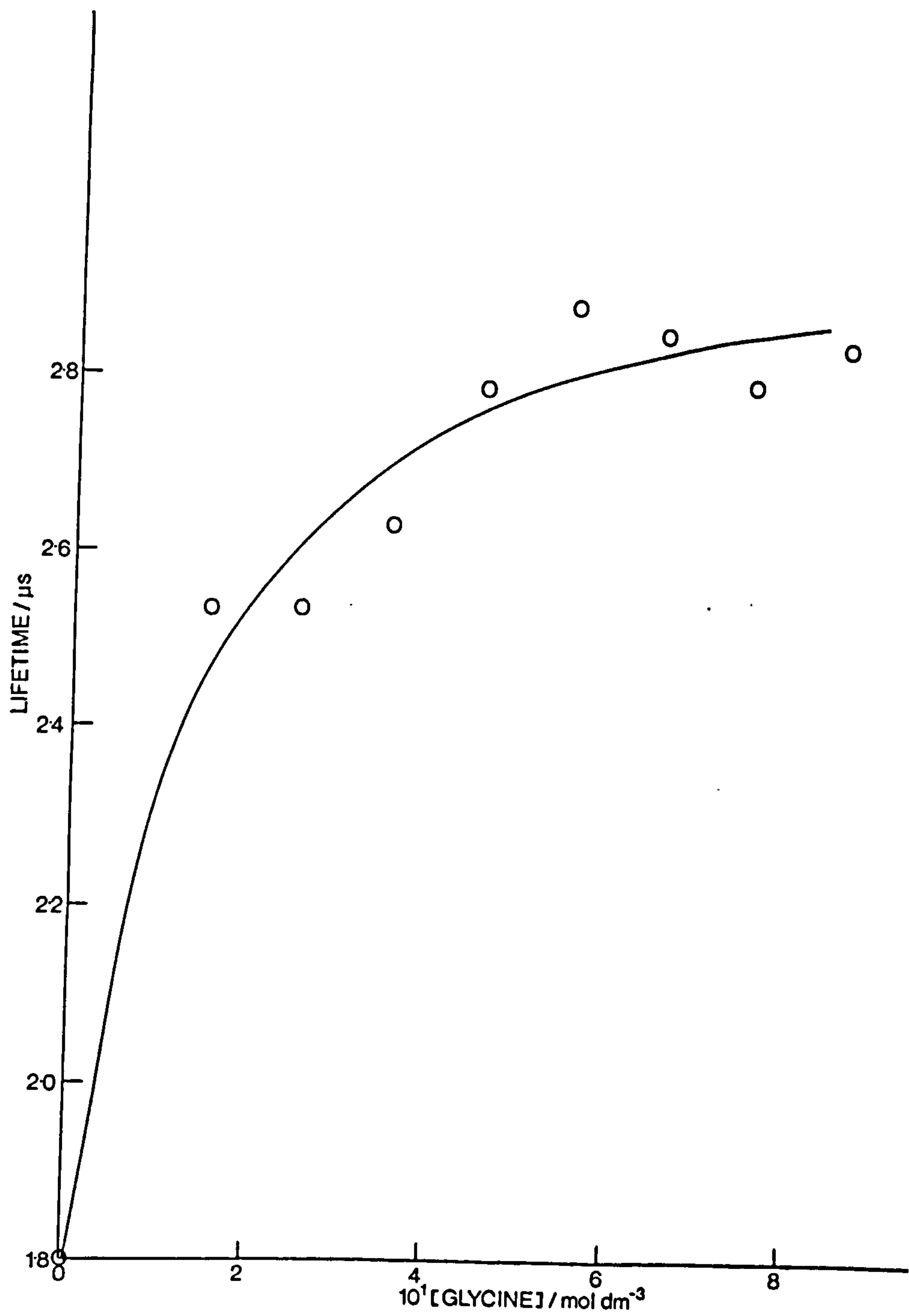


Figure 8.2      Dependence of lifetime ( $\tau$ ) of excited  $[\text{UO}_2]^{2+}$  upon  $\alpha$ -alanine concentration.

$[\text{UO}_2]^{2+} = 0.1 \text{ M}, \quad [\text{HClO}_4] = 0.2 \text{ M}.$



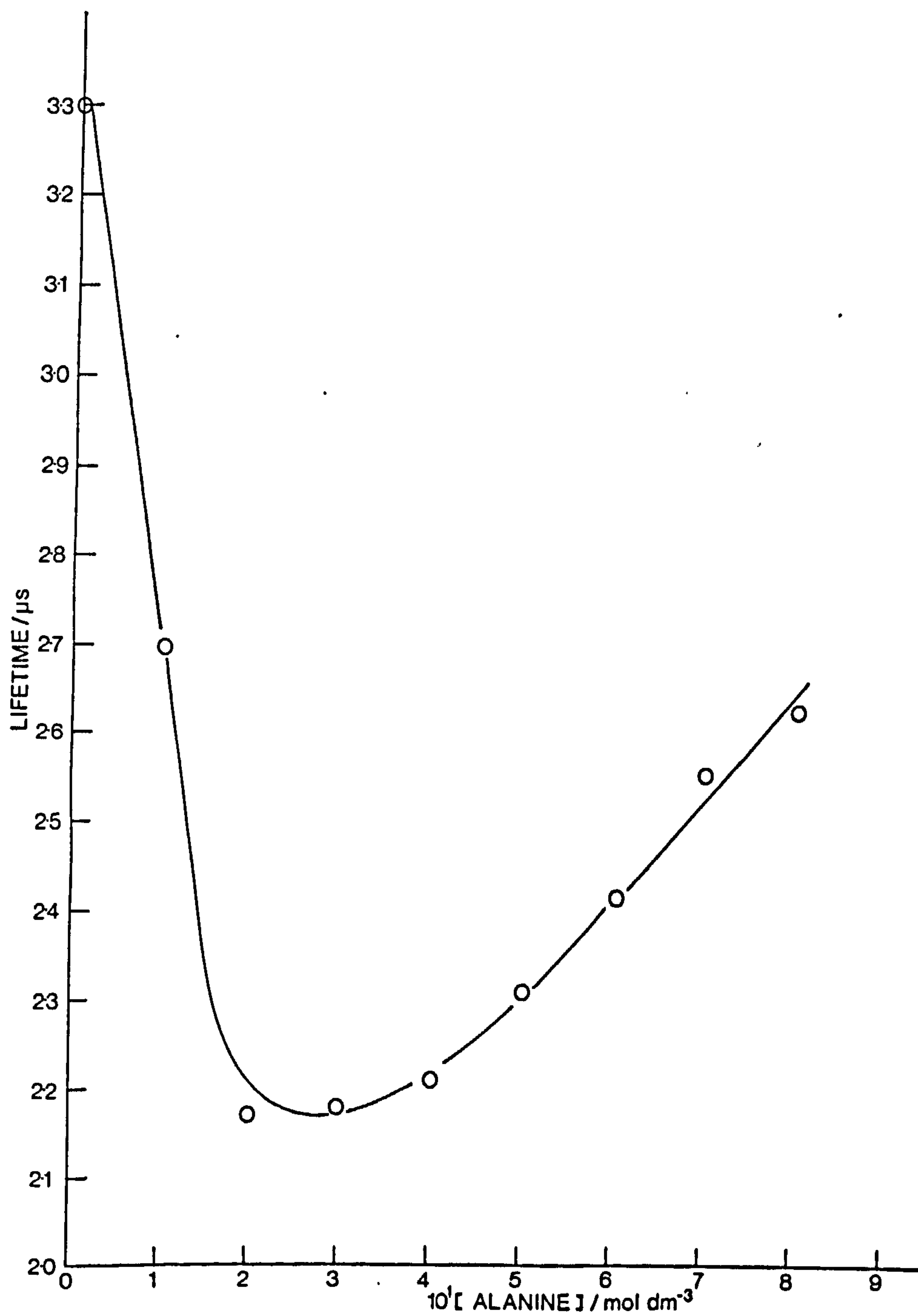
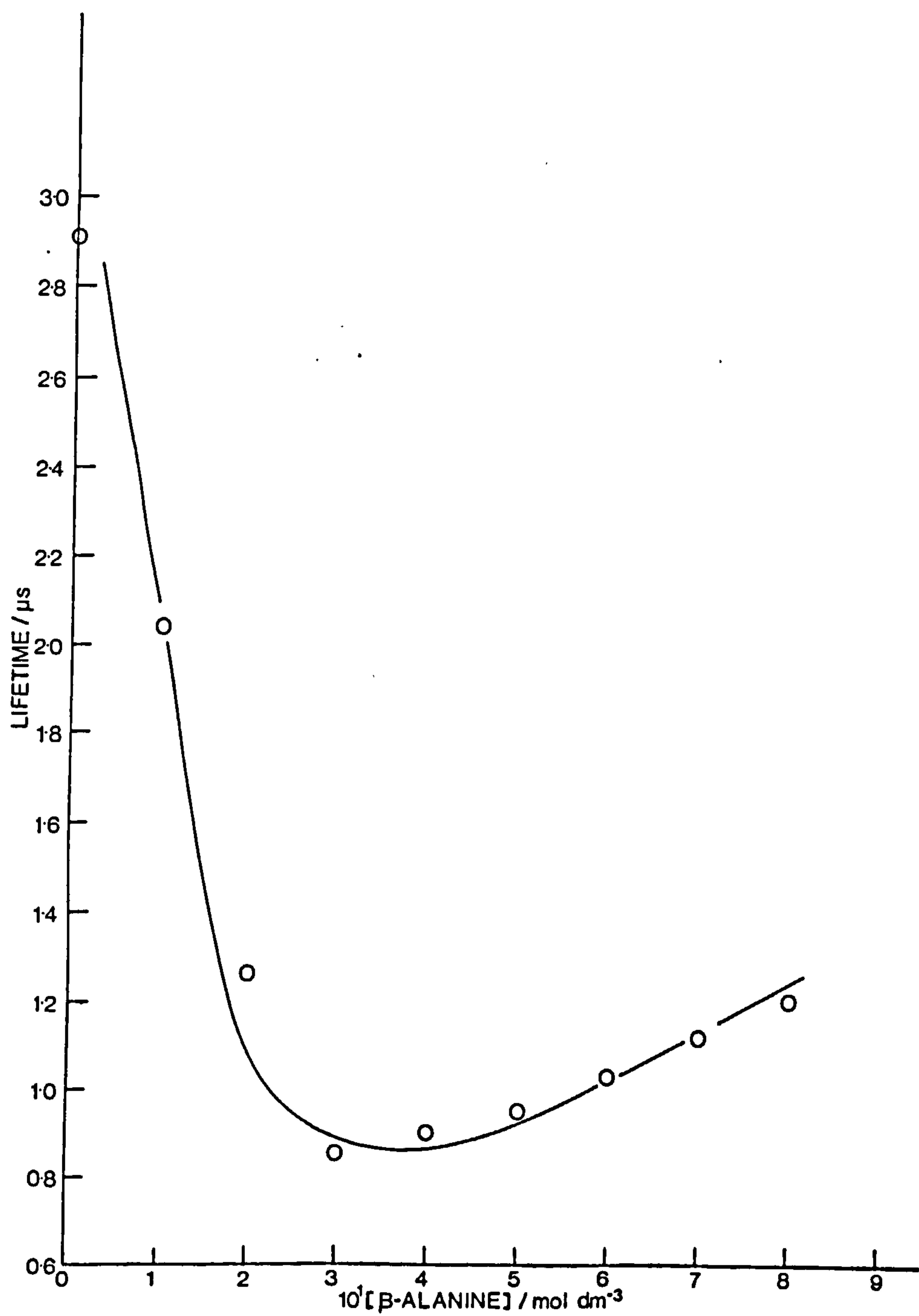


Figure 8.3      Dependence of lifetime ( $\tau$ ) of excited  $[\text{UO}_2]^{2+}$  upon  $\beta$ -alanine concentration.

$[\text{UO}_2]^{2+} = 0.1 \text{ M}, \quad [\text{HClO}_4] = 0.2 \text{ M}.$



	<u>% C</u>	<u>% H</u>	<u>% N</u>
Expected	13.83	2.90	12.10
Found	13.85	2.86	12.36

The IR spectrum of the recrystallised complex (KBr disc) showed that  $\bar{\nu}(\text{asym}) (\text{CO}_2^-)$  increased from 1590 (free glycine) to 1640  $\text{cm}^{-1}$ , while  $\bar{\nu}(\text{sym}) (\text{CO}_2^-)$  decreased from 1415 to 1385  $\text{cm}^{-1}$ . The N-H stretching frequencies were unchanged on complexation to  $[\text{UO}_2]^{2+}$ , indicating a lack of involvement in ligation.

#### 8.4 Structure Determination

The solution data indicate that, at least at the acidity and glycine concentrations employed, the coordination of glycine involves four ligands. This was confirmed unequivocally by an x-ray structure determination. A view of the cation  $[\text{UO}_2(\text{O}_2\text{CCH}_2\text{NH}_3)_4]^{2+}$  is shown in Figure 8.4 together with the atomic numbering, bond lengths and angles which are shown in Table 8.3, while hydrogen bond distances and angles are shown in Table 8.4. The coordination about the uranium atom is seen to be hexagonal bipyramidal with four glycine molecules coordinated in the equatorial plane, all via their carboxylate oxygen atoms. Two of the glycine molecules are monodentate and two are bidentate. The two cations found in the unit cell (cations 1 and 2) (Figure 8.5) are very similar, each having asymmetric coordination to the bidentate glycine molecules with one longer and one shorter distance: U(1)-O(12) and U(1)-O(13) are 2.562(5) and 2.489(6) Å respectively, while U(2)-O(22) is 2.502(6) Å and U(2)-O(23) is 2.561(5) Å. The U-O distances of the unidentate glycine are shorter, namely 2.436(4) and 2.438(4) Å.

Figure 8.4      The  $[\text{UO}_2(\text{O}_2\text{CCH}_2\text{NH}_3)_4]^{2+}$  cation 1, showing the atomic numbering.

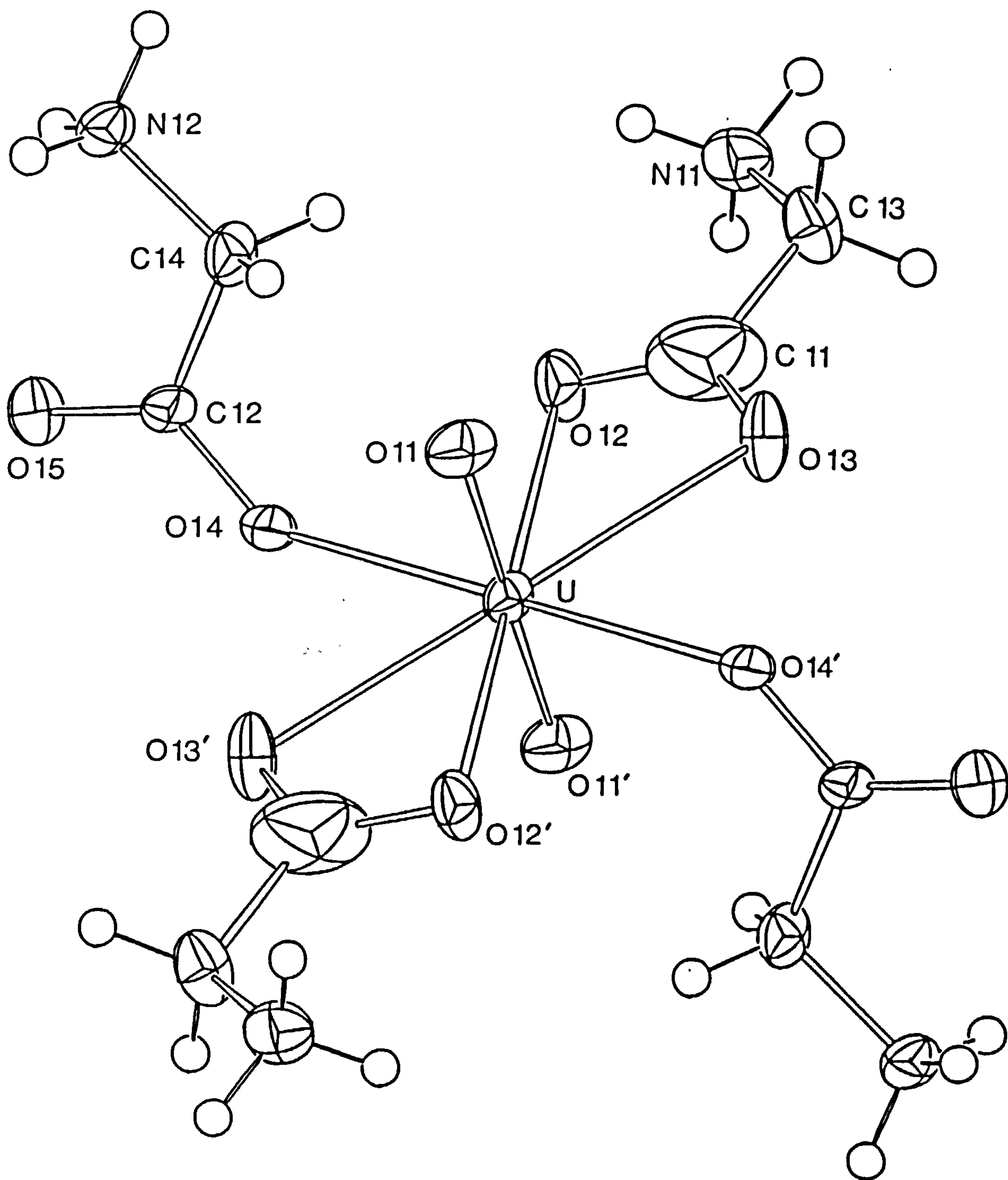




**Figure 8.5**      **View of the unit cell down a showing the hydrogen bonds  
as broken lines.**

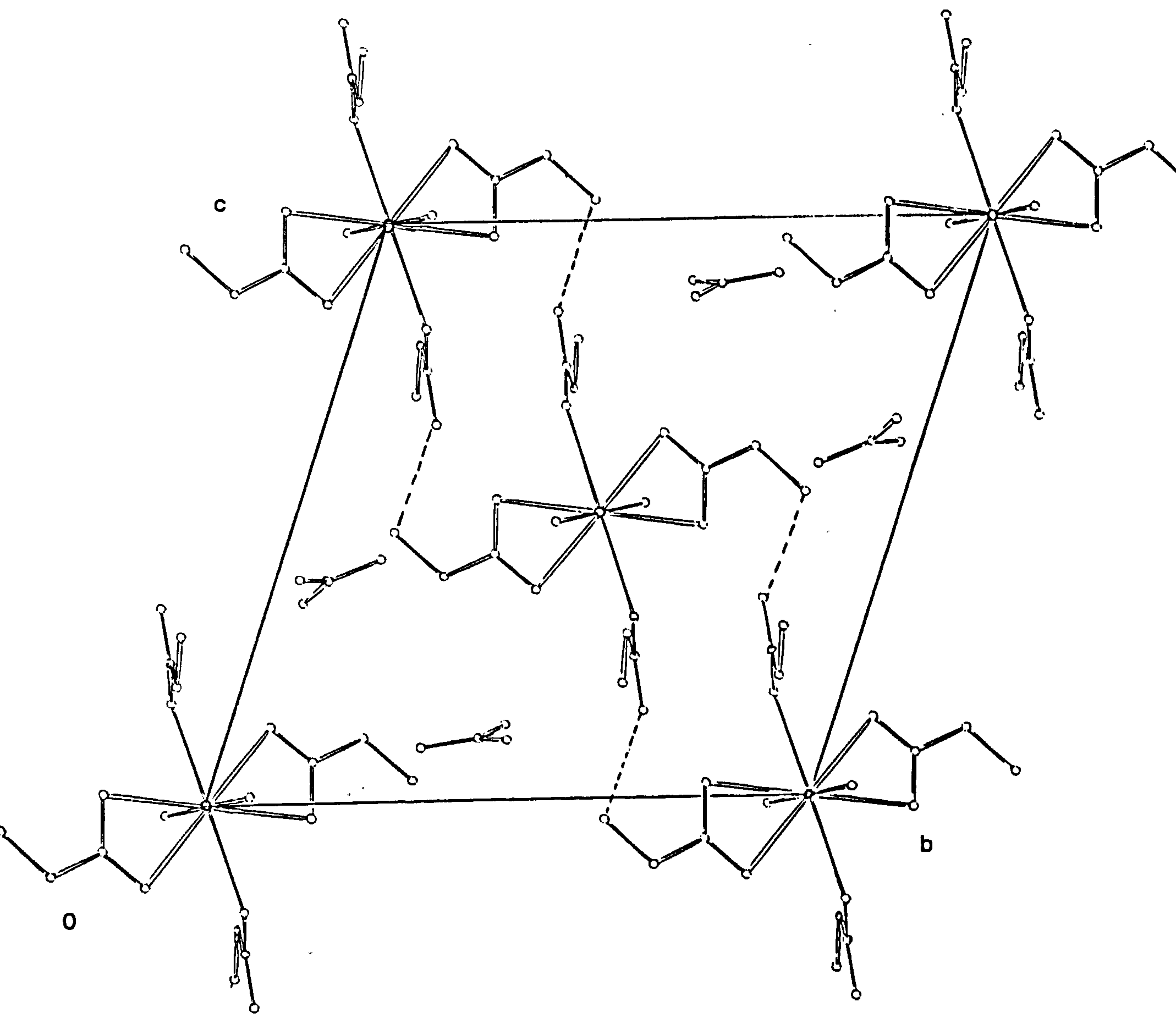


Table 8.3      Significant Bond Lengths (Å) and Angles (°) with  
Estimated Standard Deviations in Parentheses for  
 $[\text{UO}_2(\text{O}_2\text{CCH}_2\text{NH}_3)_4][\text{NO}_3]_2$

	<u>Molecule 1</u> (n = 1)	<u>Molecule 2</u> (n = 2)
U-O(n1)	1.765(5)	1.777(2)
U-O(n2)	2.562(5)	2.502(6)
U-O(n3)	2.489(6)	2.561(5)
U-O(n4)	2.436(4)	2.438(4)
O(n2)-C(n1)	1.275(10)	1.263(8)
O(n3)-C(n1)	1.263(9)	1.256(9)
C(n1)-C(n3)	1.524(13)	1.498(11)
C(n3)-N(n1)	1.464(9)	1.481(8)
O(n4)-C(n2)	1.285(8)	1.269(8)
O(n5)-C(n2)	1.224(8)	1.228(8)
C(n2)-C(n4)	1.509(10)	1.493(9)
C(n4)-N(n2)	1.469(9)	1.474(9)
N(n0)-O(n01)	1.246(12)	1.245(10)
N(n0)-O(n02)	1.246(10)	1.251(10)
N(n0)-O(n03)	1.238(11)	1.243(12)
O(n1)-U-O(n1)	180.0	180.0
O(n1)-U-O(n2)	92.7(2)	92.3(2)
O(n1)-U-O(n3)	87.1(2)	86.4(2)
O(n1)-U-O(n4)	90.4(2)	89.6(2)
O(n2)-U-O(n3)	51.9(2)	51.0(2)
O(n2)-U-O(n4)	64.4(2)	64.3(2)
O(n3)-U-O(n4)	116.0(2)	114.9(2)
U-O(n2)-C(n1)	91.5(4)	95.7(5)
U-O(n2)-C(n1)	95.3(5)	93.1(7)
O(n2)-C(n1)-O(n3)	121.2(8)	120.1(7)
O(n2)-C(n1)-C(n3)	120.8(6)	118.6(7)
O(n3)-C(n1)-C(n3)	117.8(7)	121.2(6)
C(n1)-C(n3)-N(n1)	111.4(6)	112.2(6)
U-O(n4)-C(n2)	135.7(4)	135.7(4)
O(n4)-C(n2)-O(n5)	124.8(6)	124.4(6)
O(n4)-C(n2)-C(n4)	115.5(6)	116.6(6)
O(n5)-C(n2)-C(n4)	119.6(6)	118.9(6)
C(n2)-C(n4)-N(n2)	112.3(6)	113.0(6)
O(n01)-N(n0)-O(n02)	119.9(8)	120.3(8)
O(n01)-N(n0)-O(n03)	119.5(8)	120.3(8)
O(n02)-N(n0)-O(n03)	120.5(8)	119.4(7)

Table 8.4      Hydrogen Bonds: Distances (Å) and Angles (°)

(a)      N(11) - H(113) ... O(25)

N(11) - H(113)	0.91 <sup>a</sup>
H(113) ... O(25)	1.913(9)
N(11) ... O(25)	2.810(9)

(b)      N(21)-H(212) ...O(15)

N(21)-H(212)	0.91 <sup>a</sup>
H(212) ... O(15)	1.946(9)
N(21) ... O(15)	2.788(9)

<sup>a</sup>Bond length fixed; H atoms held in rigid tetrahedral geometry, with freedom for the NH<sub>3</sub> unit to move.

### 8.5 Determination of Coordination Number Using Job's Method

Job's method<sup>199</sup> is based on the assumption that the optical density of a solution is proportional to the concentration of the complex  $ML_n$ . The optical density is measured for a series of solutions in which  $(M_t + L_t)$  is held constant, ( $M_t$  = total amount of metal ion present,  $L_t$  = total amount of ligand present), whilst varying the ratio of  $M_t/L_t$ . If a single complex  $ML_n$  is present, the optical density reaches a maximum value when  $L_t/M_t = n$ ,  $n$  being the coordination number.

Stock solutions of uranyl nitrate (1 M) and amino acid (1 M) both in aqueous perchloric acid (0.6 M), were maintained. Two sets of solutions were then prepared. The first set had  $(M_t + L_t)$  maintained at 1 M but varying the ratio of  $M_t/L_t$ ; the second set had the corresponding concentrations of uranyl ion as in the first set but without any added amino acid. The nitrate (as  $Na^+$  salt) and acid concentrations in both sets of solutions were maintained at 2 M and 0.6 M respectively. The optical densities of both sets of solutions were measured at 468 nm in 5 mm pathlength quartz cells.

The differences in optical densities between uranyl-amino acid and uranyl solutions were plotted against the mole fraction of uranyl ion present in solution. Job plots for uranyl ion-glycine,  $\alpha$ -alanine and  $\beta$ -alanine systems are shown in Figure 8.6; all have the absorption maximum  $L_t/M_t$  corresponding to a coordination number of four.

Attempts to produce crystals of analogous complexes to  $[UO_2(O_2CCH_2NH_3)_4][NO_3]_2$ , using  $\beta$ -alanine and serine by a variety of methods, resulted in the complexes separating from solution either as an oil or a precipitate. However, a 1:4 uranyl: $\alpha$ -alanine complex has been

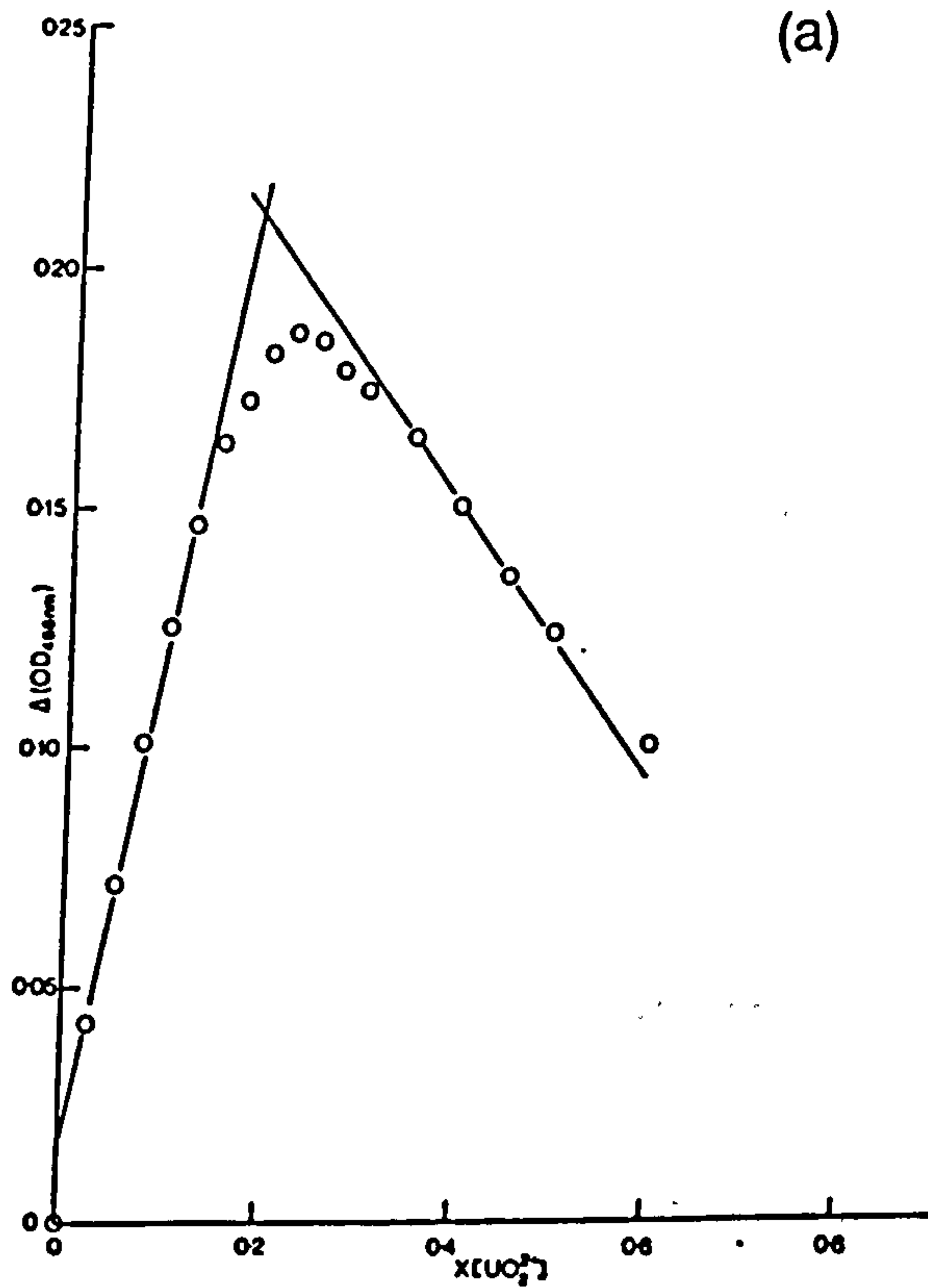
Figure 8.6      Job plots for complexation of glycine (a),  $\alpha$ -alanine (b), and  $\beta$ -alanine (c), with uranyl ion (x = mole fraction).

$[\text{UO}_2]^{2+} + [\text{AA}] = 1.0 \text{ M}$ ;  $[\text{HClO}_4] = 0.6 \text{ M}$ ;  $[\text{NO}_3] = 2.0 \text{ M}$   
(as  $\text{Na}^+$  salt);  $\lambda = 468 \text{ nm}$ , cell pathlength  $0.5 \text{ cm}$ .

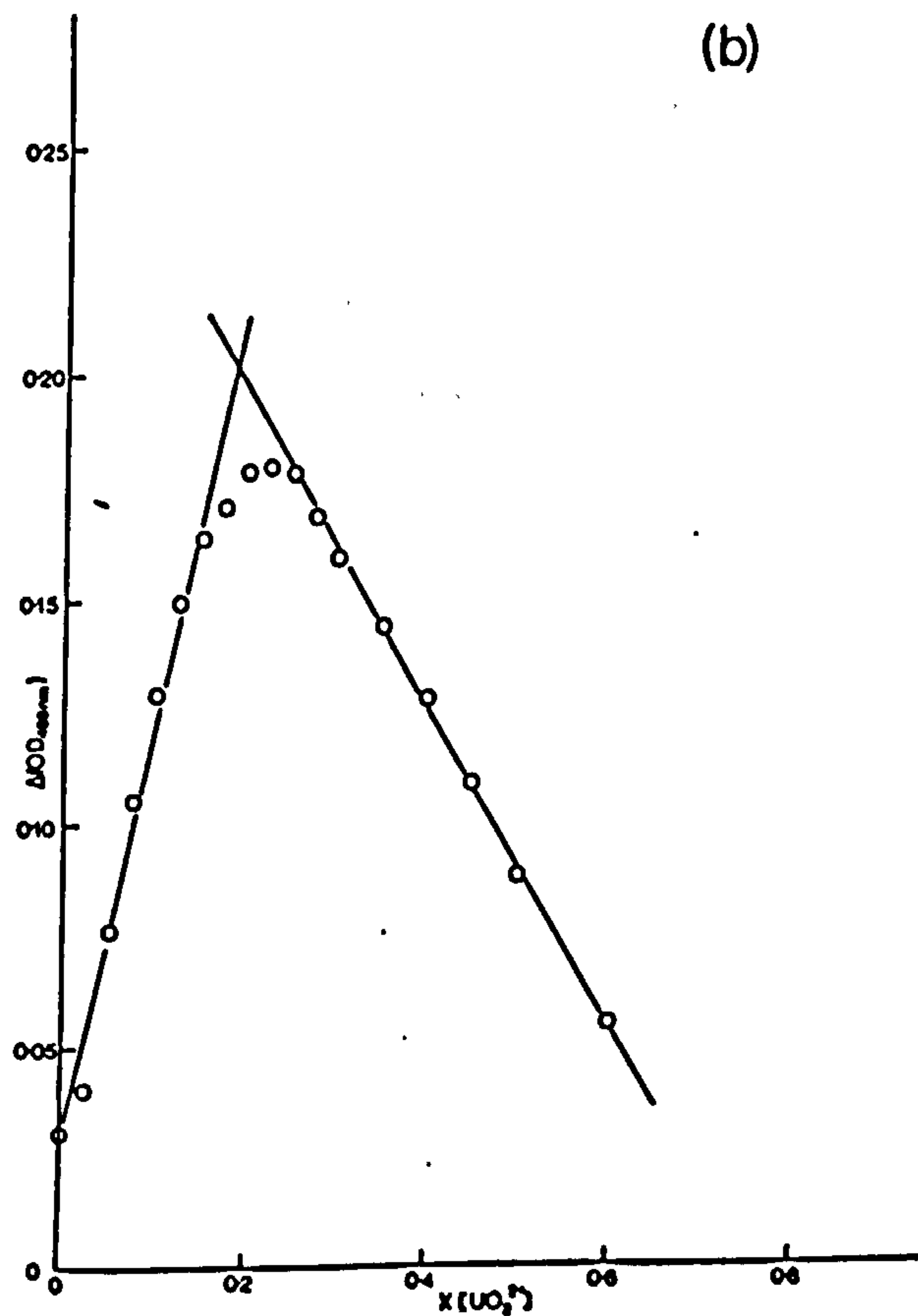
Uranyl salt as the dinitrate hexahydrate.



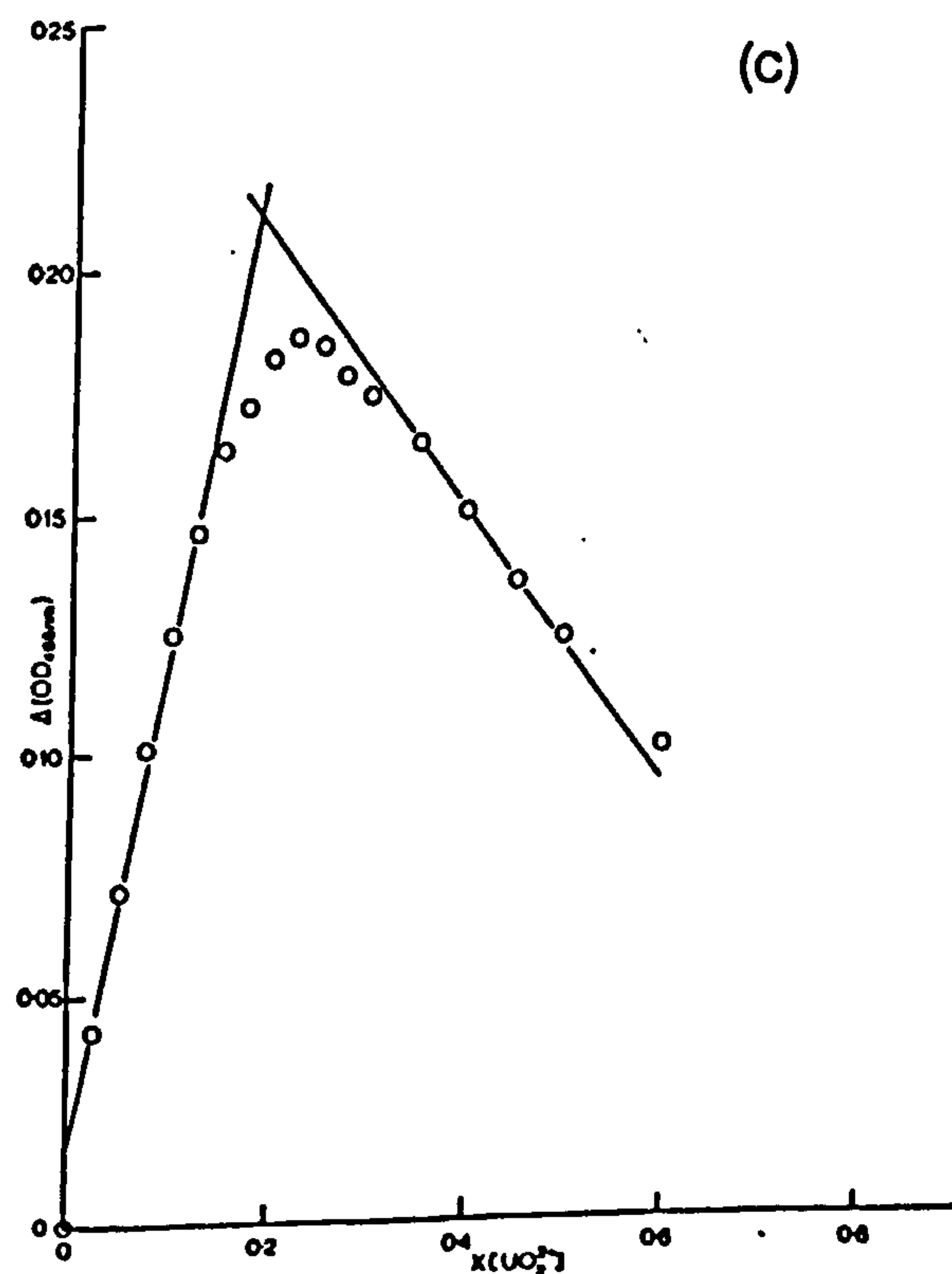
(a)



(b)



(c)



isolated in the crystalline state and an x-ray diffraction structure is being conducted at the present.

#### 8.6 Concluding Remarks

The results from the solution studies and x-ray crystal structure have shown that the maximum possible coordination number, at least with glycine, and  $\alpha$ - and  $\beta$ -alanine, around the  $[\text{UO}_2]^{2+}$  centre is four.

The x-ray crystal structure of the 1:4 uranyl:glycine complex unambiguously proves that ligation to  $[\text{UO}_2]^{2+}$  occurs via the ionised carboxyl groups, with no involvement of the amino function as was previously thought by several research groups<sup>141,146-148</sup>.

## **Chapter 9**

### **Results**

#### **Interaction of Excited Dioxouranium(VI) Ion with Amino Acids**

## 9.1 Introduction

It has been proposed that the natural concentration of uranium in sea water (ca.  $10^{-8}$  M), complexed as uranyl carbonate, contributes to the photochemical degradation of dissolved organic material. Calculations have shown that approximately  $3 \times 10^{-3}$  Einstein  $\text{cm}^{-2}$  day of luminous energy above the threshold required to excite  $[\text{UO}_2]^{2+}$  is incident upon sea water. If the average penetration of the incident light is 30 m, and taking  $\epsilon$  is ca. 10 for uranyl carbonate, then  $2 \times 10^{-6}$  Einstein  $\text{cm}^{-2}$  day is absorbed by U(VI) in sea water. If the concentration of reactive organic molecules is ca.  $10^{-5}$  to  $10^{-4}$  M, then 0.02 mole of organic material is activated per  $\text{m}^2$  of sea surface each day. This has the effect of reducing the 'lifetime' of reasonably reactive organic molecules to a few months by this process<sup>200</sup>.

As amino acids are the immediate breakdown products of proteins, of which every living (and dead) creature is composed, it is of ecological interest to determine the level of reactivity of these organic 'waste' products, which are present in sea water in high concentrations, towards the electronically excited uranyl ion. The results in this chapter detail the interaction of  $*[\text{UO}_2]^{2+}$  towards the naturally occurring amino acids, amino polycarboxylic acids and their metal ion complexes.

Kinetic results obtained by laser flash photolysis indicate the level of reactivity of the substrate, quantum yields of U(IV) indicate the degree of charge-separation from the initial radical pair configuration, and ESR data reveal the structure of the primary ligand-derived radical.

## 9.2 Kinetic Measurement

The kinetics of interaction between  $^*[UO_2]^{2+}$  and the amino acids were initially investigated by measuring the luminescence yields of uranyl solutions in both the absence and presence of quencher. This approach yields conventional Stern-Volmer plots, with slopes  $K^{SV} = k_2\tau_0$ , as shown in Figure 9.1. The Stern-Volmer constants,  $K^{SV}$ , are collated in Table 9.1.

The lifetime of  $^*[UO_2]^{2+}$ , determined at its emission maximum of 508 nm in acidic solution, was systematically reduced on addition of the various amino acids. Pseudo-first-order rate constants,  $k_1$ , were determined at ten different concentrations of each quencher to give the second-order quenching rate constant,  $k_2$ , exemplified in Figure 9.2 and collated in Table 9.2.

Quantum yield measurements were determined in the form of appearance of U(IV) at its wavelength maximum of 648 nm, with  $\epsilon_{\max} = 50.0 \text{ dm}^3 \text{ mol}^{-1} \text{ cm}^{-1}$  for a nitrate medium<sup>201</sup>. A typical growth plot is illustrated in Figure 9.3. The solutions were bubbled with high purity argon prior to photolysis and the cell sealed from the atmosphere. The growth plots obtained were linear from zero time and the U(VI) concentrations employed were sufficiently high to absorb all the monochromatic light incident upon the cell. Photolysis times were kept to a minimum, usually below 1% total reaction, in order to minimise secondary reactions. Quantum yields for the photoreduction of  $[UO_2]^{2+}$  by amino acids are presented in Table 9.3.

ESR samples were prepared by dissolving the amino acid in a solution of uranyl perchlorate in aqueous  $HClO_4$ . Where heavy water was used as a

Table 9.1      Stern-Volmer Constants for the Quenching of  $^{*}[UO_2]^{2+}$   
by Amino Acids and Aminopolycarboxylates<sup>a</sup>

Substrate	$K_{sv}$ 410nm <sup>b</sup>
Glycine	Enhancement
$\alpha$ -Alanine	Enhancement
$\beta$ -Alanine	Enhancement
Serine	4.56
Valine	2.68
Leucine	13.60
Threonine	10.21
Asparagine	5.82
Glutamine	59.00
Isoleucine	11.40
Histidine	423.23
Proline	0.15
Aspartic acid	2.05
Glutamic acid	Very little quenching
Tyrosine	$3.95 \times 10^3$
Tryptophan	$7.08 \times 10^3$
Phenylalanine	$1.90 \times 10^3$
Methionine	$3.32 \times 10^3$
Cystine	$1.50 \times 10^3$
Cysteine	$1.95 \times 10^3$
CDTA	$1.53 \times 10^3$
EDTA	$1.14 \times 10^3$
MeN(CH <sub>2</sub> CO <sub>2</sub> H) <sub>2</sub>	1.40
HN(CH <sub>2</sub> CO <sub>2</sub> H) <sub>2</sub>	Enhancement
Na[Co(CDTA)]	$1.34 \times 10^3$
Co(Gly) <sub>3</sub>	188.00
Co(Ala) <sub>3</sub>	186.50
Co(Leu) <sub>3</sub>	121.0
Na[Eu(CDTA)]	$2.00 \times 10^3$

<sup>a</sup>[UO<sub>2</sub>(NO<sub>3</sub>)<sub>2</sub>] = 0.05 M,    [HClO<sub>4</sub>] = 0.2 M

<sup>b</sup>Excitation wavelength



Table 9.2      Absolute Rate Constants for the Quenching of  $*[UO_2]^{2+}$   
by Amino Acids and Aminopolycarboxylates<sup>a</sup>

Substrate	$k_2$ (dm <sup>3</sup> mol <sup>-1</sup> s <sup>-1</sup> )
Glycine	Enhancement
$\alpha$ -Alanine	Enhancement
$\beta$ -Alanine	Enhancement
Serine	$(1.92 \pm 0.42) \times 10^6$
Valine	$(1.13 \pm 0.29) \times 10^6$
Leucine	$(5.71 \pm 0.25) \times 10^6$
Threonine	$(4.29 \pm 0.22) \times 10^6$
Asparagine	$(2.45 \pm 0.31) \times 10^6$
Glutamine	$(2.48 \pm 0.21) \times 10^6$
Isoleucine	$(4.78 \pm 0.22) \times 10^6$
Histidine	$(1.78 \pm 0.08) \times 10^8$
Proline	$(6.43 \pm 0.12) \times 10^4$
Aspartic acid	$(8.70 \pm 0.09) \times 10^5$
Glutamic acid	No significant quenching
Tyrosine	$(1.66 \pm 0.10) \times 10^9$
Tryptophan	$(2.97 \pm 0.09) \times 10^9$
Phenylalanine	$(7.92 \pm 0.16) \times 10^8$
Methionine	$(1.28 \pm 0.06) \times 10^9$
Cystine	$(5.67 \pm 0.01) \times 10^8$
Cysteine	$(7.48 \pm 0.04) \times 10^8$
CDTA	$(6.15 \pm 0.51) \times 10^8$
EDTA	$(4.77 \pm 0.49) \times 10^8$
MeN(CH <sub>2</sub> CO <sub>2</sub> H) <sub>2</sub>	$(5.40 \pm 0.22) \times 10^5$
HN(CH <sub>2</sub> CO <sub>2</sub> H) <sub>2</sub>	Enhancement
Na[Co(CDTA)]	$(5.71 \pm 0.11) \times 10^8$
Co <sup>III</sup> (Gly) <sub>3</sub>	$(7.90 \pm 0.13) \times 10^7$
Co <sup>III</sup> (Ala) <sub>3</sub>	$(7.83 \pm 0.10) \times 10^7$
Co <sup>III</sup> (Leu) <sub>3</sub>	$(5.08 \pm 0.09) \times 10^7$
Na[Eu(CDTA)]	$(8.36 \pm 0.07) \times 10^8$

[UO<sub>2</sub>(NO<sub>3</sub>)<sub>2</sub>] - 0.1 M,      [HClO<sub>4</sub>] - 0.2 M  
Medium: water

Table 9.3

Quantum Yields for U(IV) Formation<sup>a</sup>

Substrate	$\phi_{\text{U(IV)}}$
Glycine	<0.017
$\alpha$ -Alanine	0.094
$\beta$ -Alanine	<0.005
Serine	0.084
Valine	0.145
Leucine	0.120
Threonine	0.191
Asparagine	0.018
Glutamine	0.128
Isoleucine	0.143
Histidine	<0.005
Proline	<0.005
Aspartic acid	0.03
Glutamic acid	<0.005
Tyrosine	<0.005
Tryptophan	<0.005
Phenylalanine	<0.005
Methionine	0.017
Cystine	0.002
Cysteine	0.007
CDTA	0.191
EDTA	0.194
$\text{MeN}(\text{CH}_2\text{CO}_2\text{H})_2$	0.020
$\text{HN}(\text{CH}_2\text{CO}_2\text{H})_2$	0.079

<sup>a</sup> $[\text{UO}_2(\text{NO}_3)_2] = 0.08 \text{ M}$ ,  $[\text{HClO}_4] = 0.2 \text{ M}$

Medium: water

Figure 9.1 Stern-Volmer plot for the quenching of uranyl ion luminescence intensity ( $I_f$ ) by added threonine.

$[\text{UO}_2(\text{NO}_3)_2] = 0.05 \text{ M}; [\text{HClO}_4] = 0.2 \text{ M}; \lambda_{\text{em}} = 510 \text{ nm};$   
 $\lambda_{\text{ex}} = 410 \text{ nm}.$

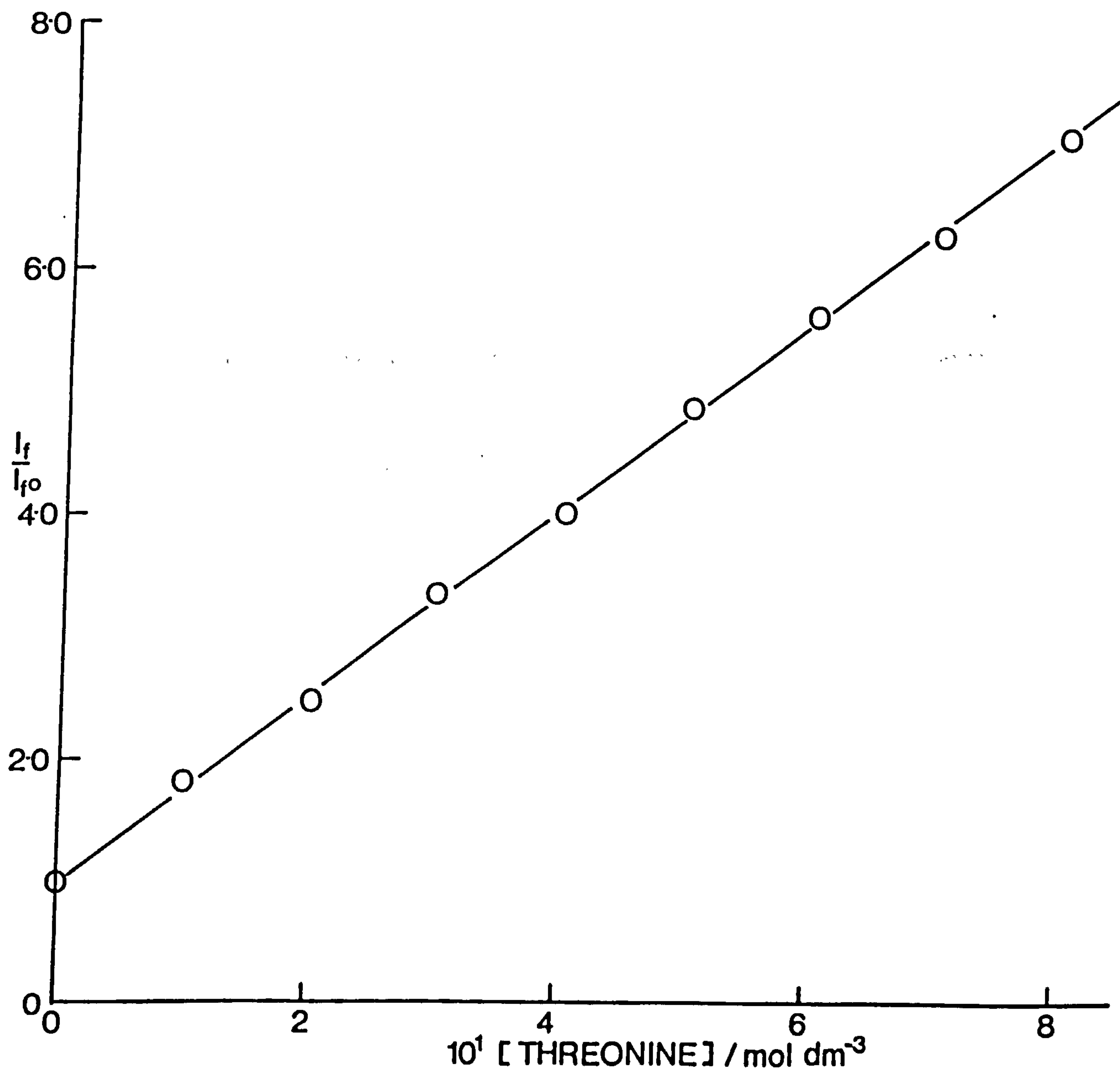


Figure 9.2      Quenching of excited uranyl ion by L-phenylalanine

$[\text{UO}_2(\text{NO}_3)_2] = 0.2 \text{ M}; \quad [\text{HClO}_4] = 0.2 \text{ M}.$

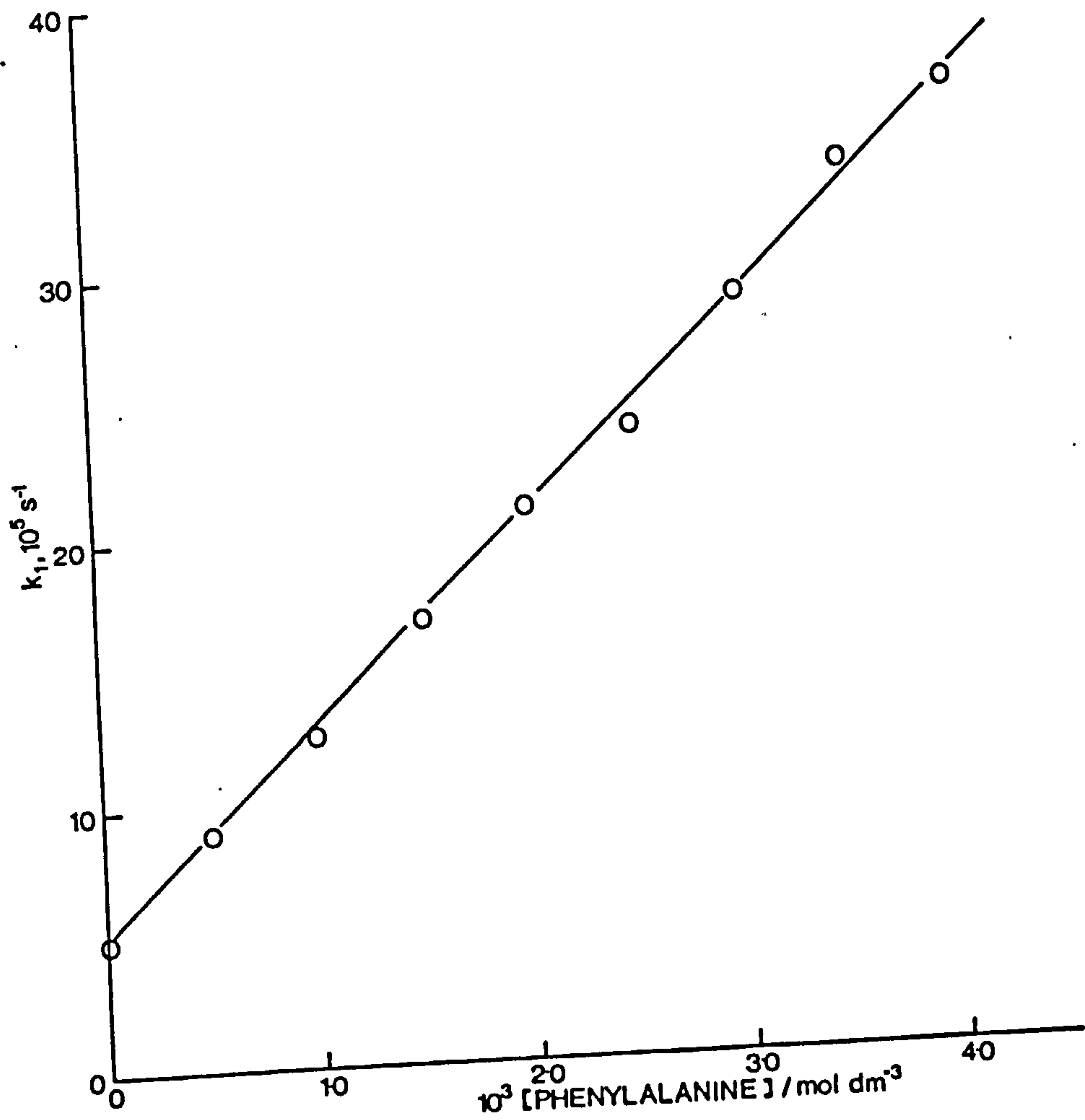
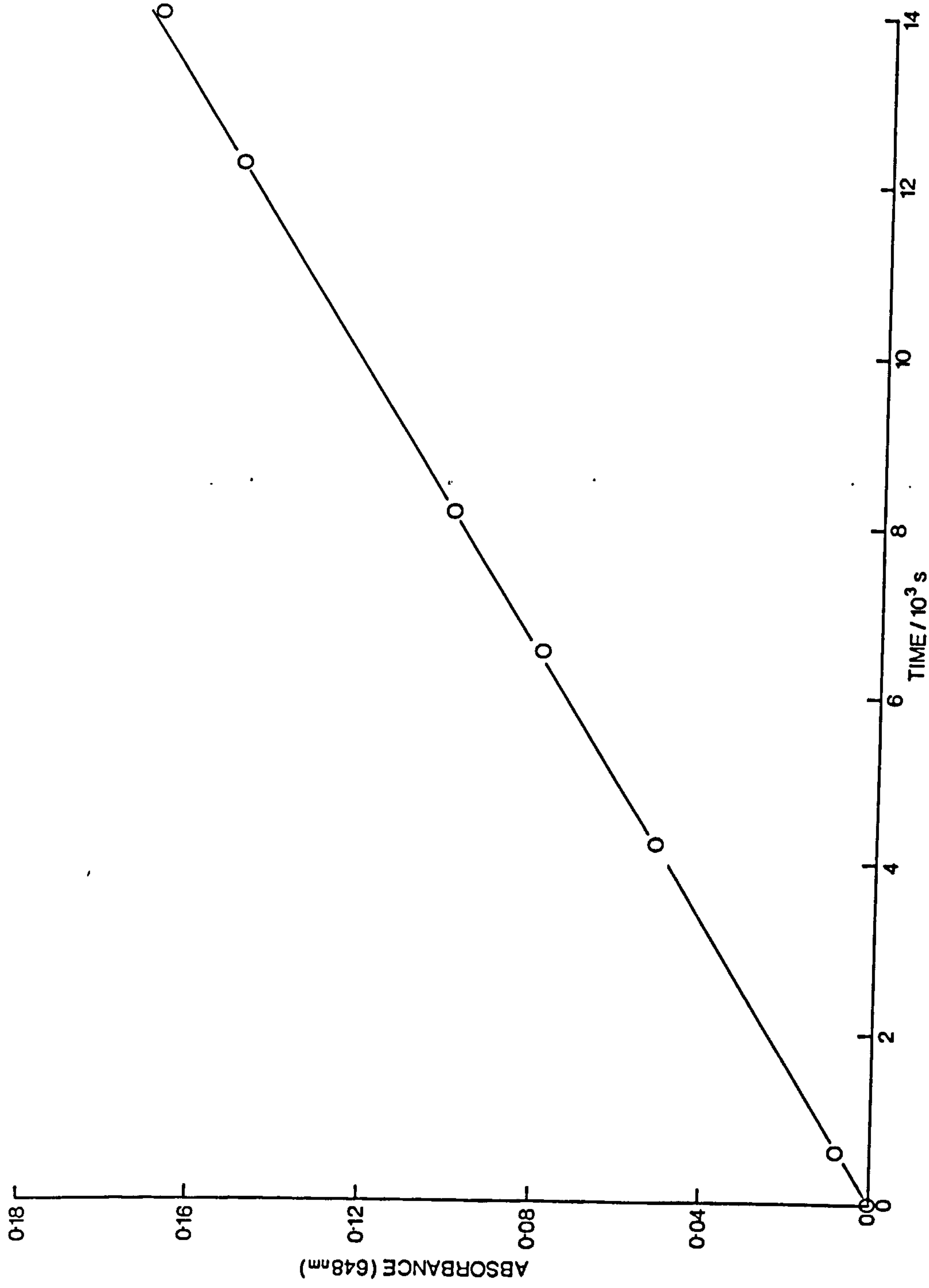




Figure 9.3      Development of absorbance of U(IV) at 649 nm during 401 nm photolysis of EDTA ( $4.75 \times 10^{-3}$  M) and uranyl nitrate in aqueous  $\text{HClO}_4$  (0.2 M).



solvent the final isotopic composition was at least 99.8%  $^2\text{H}$ . Samples were then frozen to 77 K prior to photolysis for 1-4 h. ESR spectra are given in terms of the individual amino acids below, and are collated in Table 9.4.

### 9.3 ESR Measurements

#### Glycine

A six-line spectrum of approximately binomial distribution was obtained in  $\text{H}_2\text{O}$  with  $a(\text{H})_{\text{av}} = 30.0$  G and  $g = 2.00243$ , see Figure 9.4(a), which was reduced to a 1:2:1 triplet in  $\text{D}_2\text{O}$  with  $a(\text{H})_{\text{av}} = 23.5$  G, as shown in Figure 9.4(b). The radicals responsible are respectively,  $\dot{\text{C}}\text{H}_2\text{NH}_3^+$  and  $\dot{\text{C}}\text{H}_2\text{ND}_3^+$ . A six-line spectrum was also observed using  $\text{Ce(IV)}$  in  $\text{H}_2\text{O}$ , having  $a(\text{H})_{\text{av}} = 26$  G and  $g = 2.00244$  corresponding to the same radical as that observed using  $[\text{UO}_2]^{2+}$ .

#### $\alpha$ -Alanine

An intense, complex spectrum is produced in  $\text{H}_2\text{O}$ , while in  $\text{D}_2\text{O}$  this reduces to a five-line spectrum in a binomial intensity distribution with  $a(\text{H})_{\text{av}} = 28$  G,  $g = 2.0024$ . The radicals responsible are considered to be  $\text{Me}\dot{\text{C}}\text{HNH}_3^+$  and  $\text{Me}\dot{\text{C}}\text{HND}_3^+$  in agreement with Poupko *et al.*<sup>162</sup> who obtained a similar spectrum using  $\text{K}_3[\text{Fe(CN)}_6]$  as photo-oxidant. The spectra of the radicals obtained in  $\text{H}_2\text{O}$  and  $\text{D}_2\text{O}$  are shown in Figure 9.5. Irradiation of  $\alpha$ -alanine in  $\text{H}_2\text{O}$  using  $\text{Ce(ClO}_4)_4$  as the photo-oxidant, produced a seven-line spectrum with  $a(\text{H})_{\text{av}} = 27$  G and  $g = 2.0031$ , as shown in Figure 9.5(c). This is very similar to the spectrum obtained using  $[\text{UO}_2]^{2+}$ , and we can conclude that identical radical species are produced.

Figure 9.4      ESR spectra produced at 77 K on photolysis of glycine in  
(a)  $\text{H}_2\text{O}$  and (b)  $\text{D}_2\text{O}$ .

Arrow refers to DPPH standard.

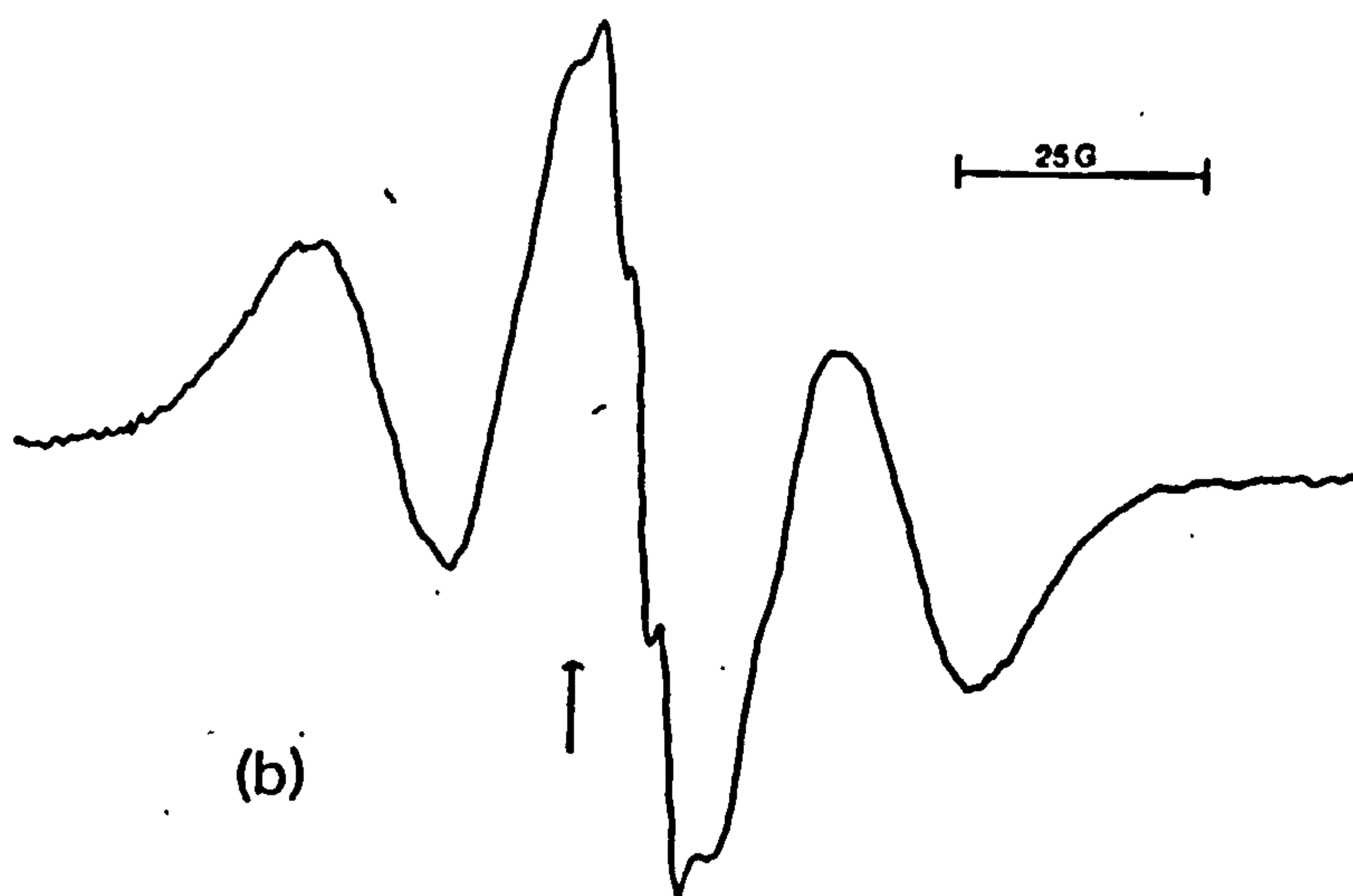
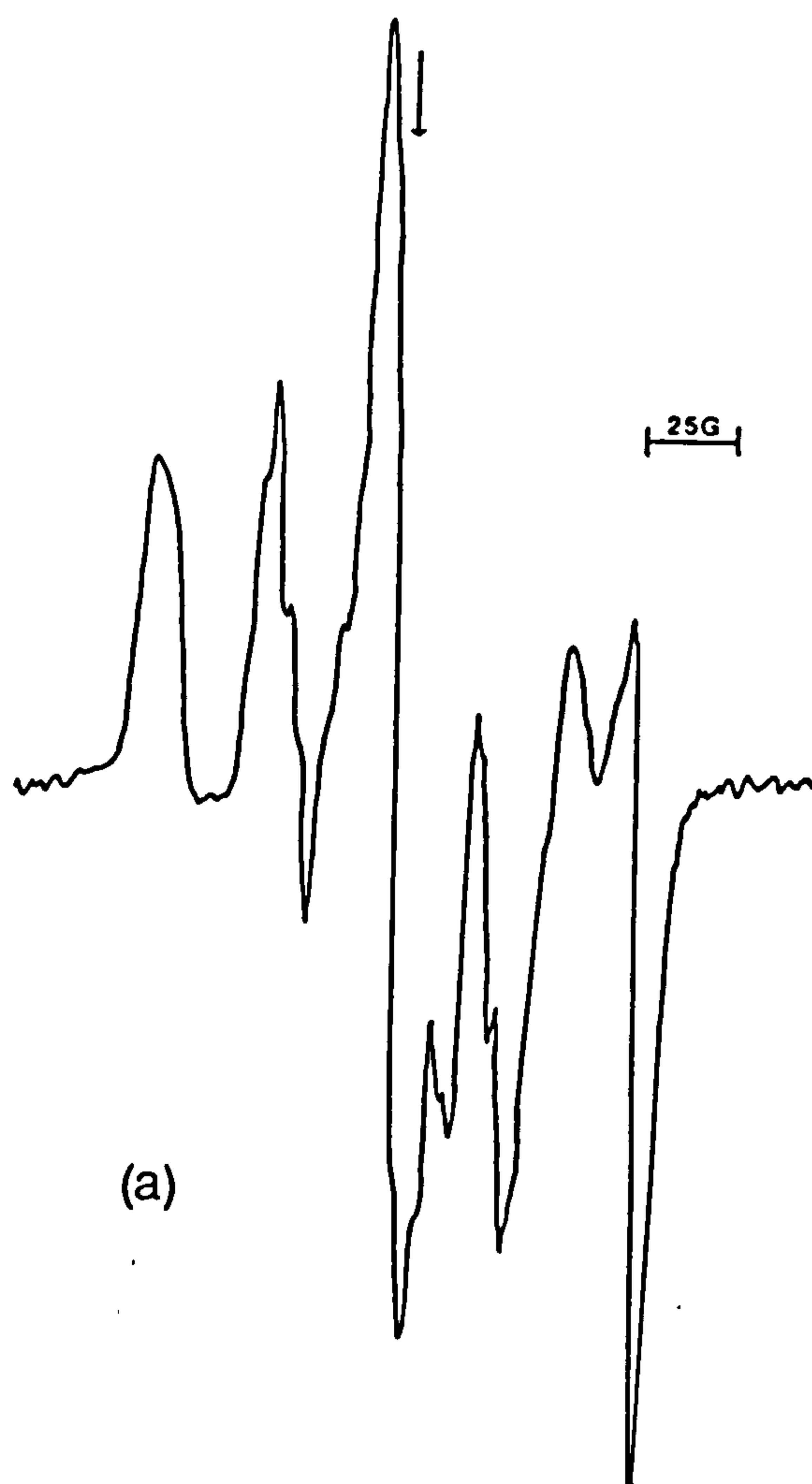
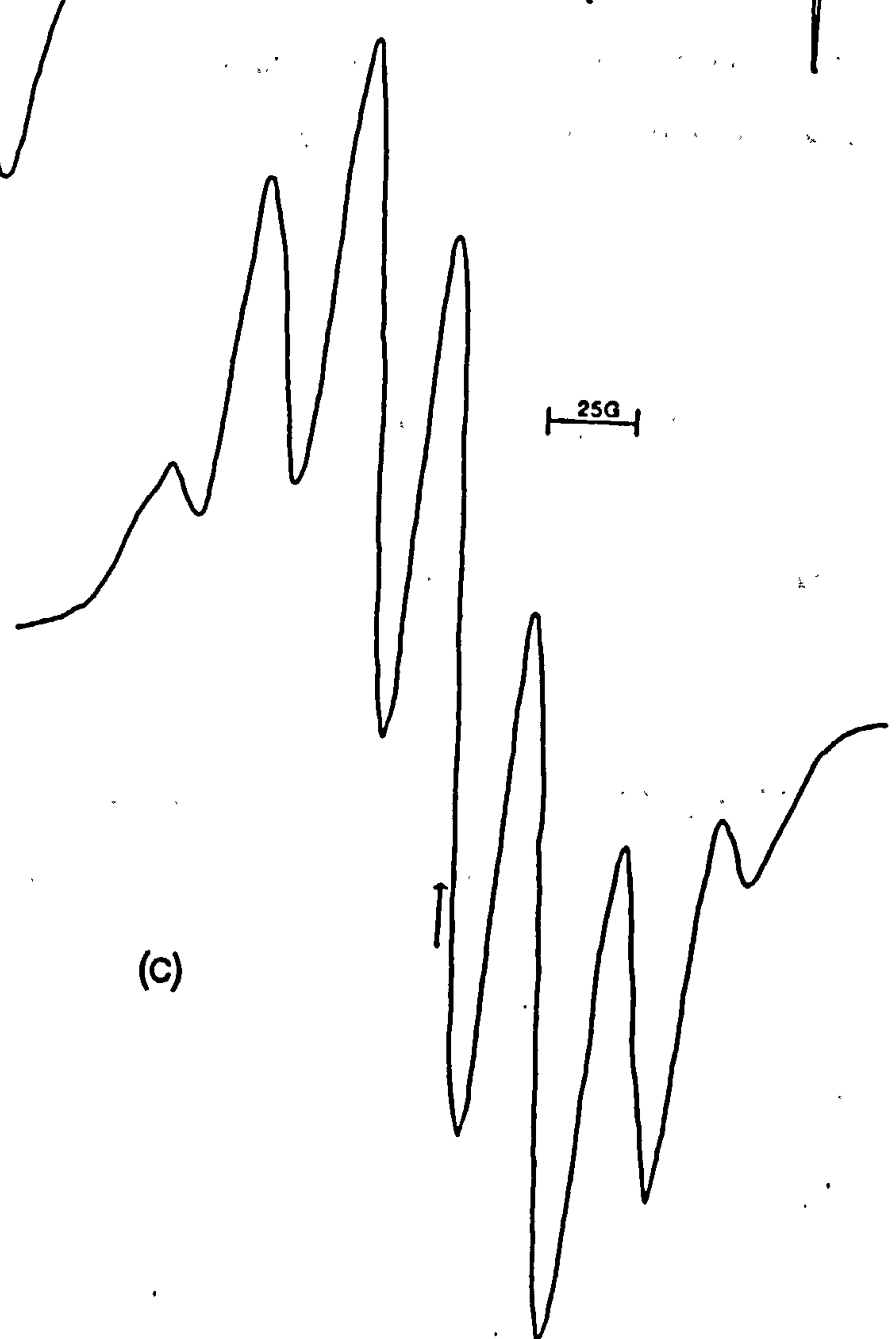
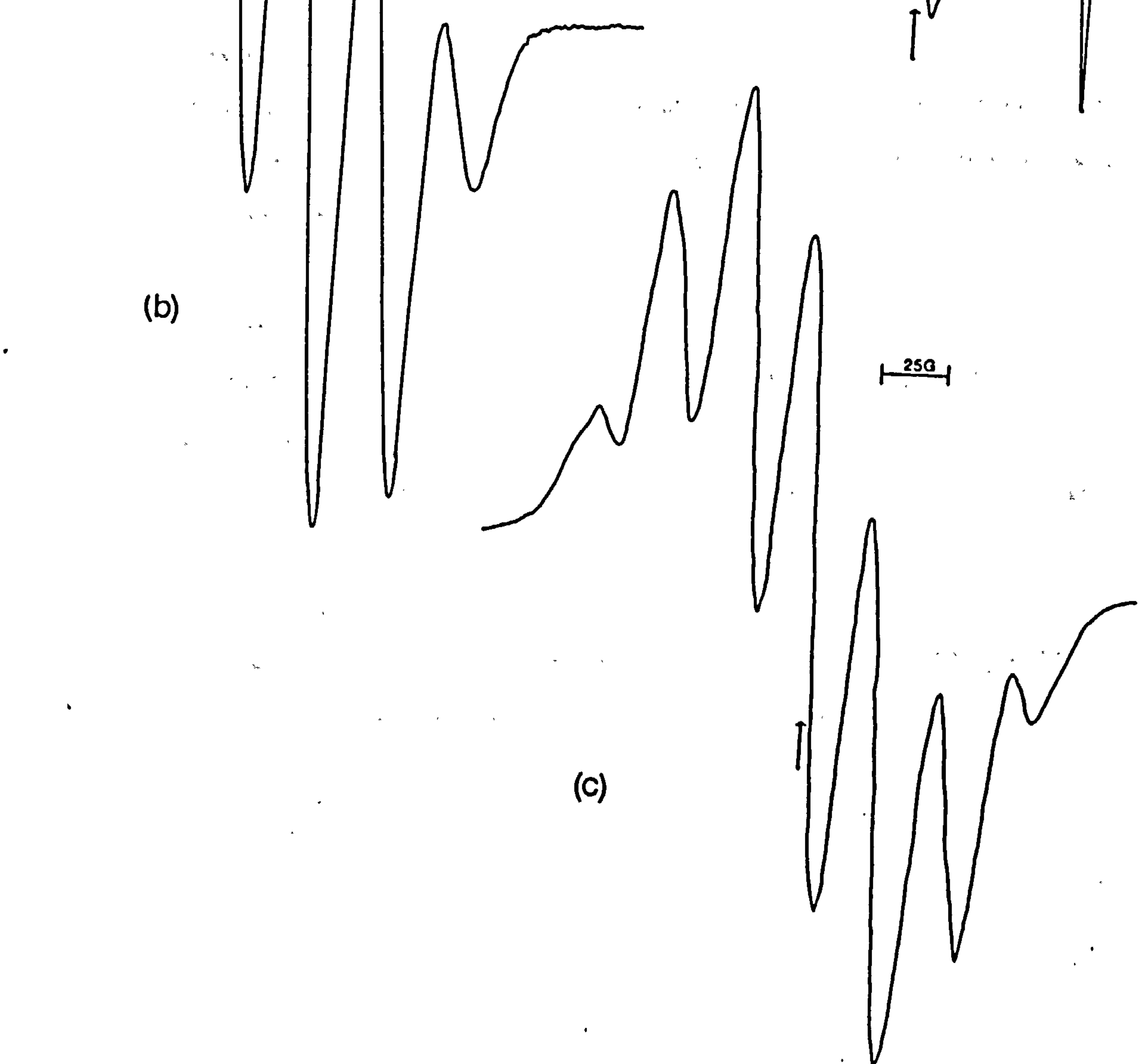
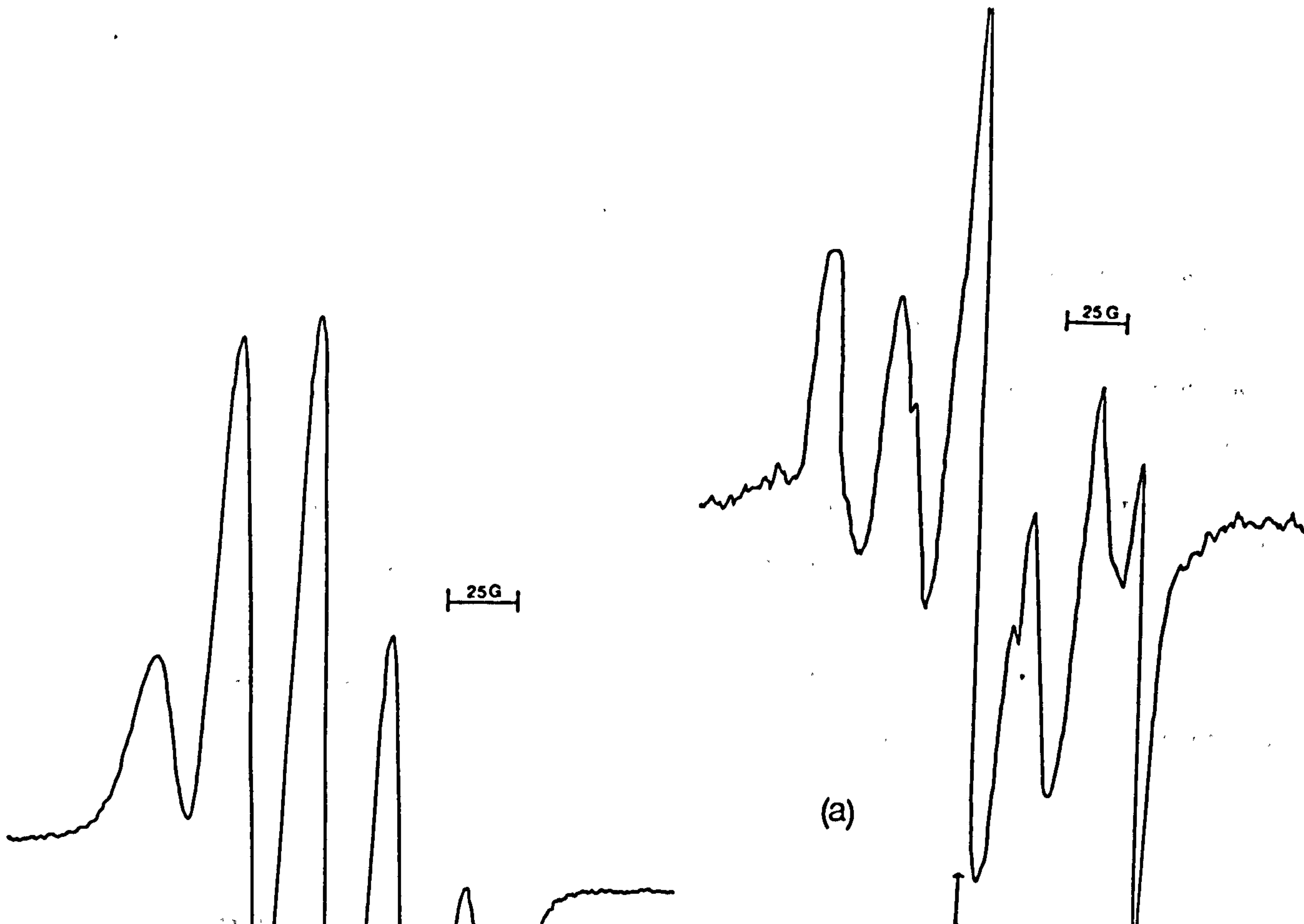


Figure 9.5 ESR spectra produced at 77 K on photolysis of  $\alpha$ -alanine in (a)  $\text{H}_2\text{O}$ , (b)  $\text{D}_2\text{O}$ , and (c)  $\text{Ce(IV)/H}_2\text{O}$ .





### $\beta$ -Alanine

A six-line spectrum was obtained in  $\text{H}_2\text{O}$  medium with  $a(\text{H})_{\text{av}} = 23 \text{ G}$  and  $g = 2.0031$ . The same spectrum was obtained in  $\text{D}_2\text{O}$ , see Figure 9.6(a) indicating that no coupling occurs to the N-H(D) protons. The spectrum is attributed to the radical  $\dot{\text{C}}\text{H}_2\text{CH}_2\text{NH}_3^+$  in which both  $\alpha$ -protons and one  $\beta$ -proton show  $a(\text{H}) = 23.0 \text{ G}$ , while the other  $\beta$ -proton shows  $a(\text{H}) = 46.0 \text{ G}$ , corresponding to a 'locked' conformation facilitating hyperconjugation with the semi-occupied orbital at  $\text{C}(1)^{203}$  as in  $\text{CH}_3\text{CH}_2\dot{\text{C}}\text{H}_2^{204}$  and other radicals of structure  $\text{XCH}_2\dot{\text{C}}\text{H}_2$ . A six-line spectrum was obtained using  $\text{Ce}(\text{ClO}_4)_4$  in  $\text{H}_2\text{O}$  with  $a(2\text{H})_{\alpha} = 23 \text{ G}$  and  $a(\text{H})_{\beta} = 23 \text{ G}$  while the other  $\beta$  proton shows  $a(\text{H}) = 46 \text{ G}$ , see Figure 9.6(b), identical to that produced with  $[\text{UO}_2]^{2+}$ .

### Valine

A broad poorly-resolved spectrum obtained in  $\text{H}_2\text{O}$  simplified in  $\text{D}_2\text{O}$  to a 1:2:1 triplet with  $a(\text{H}) = 24 \text{ G}$  and  $g = 2.0028$ , see Figure 9.7 which is assigned to  $\text{Me}_2\dot{\text{C}}\text{HCHND}_3^+$ .

### Glutamic Acid

A six-line spectrum was obtained in both  $\text{H}_2\text{O}$  and  $\text{D}_2\text{O}$ . In  $\text{H}_2\text{O}$  the spectrum has  $a(\text{H})_{\text{av}} = 23 \text{ G}$  and  $g = 2.0026$ , which is assigned to the radical  $\dot{\text{C}}\text{H}_2\text{CH}_2\text{CH}(\text{NH}_3^+)\text{CO}_2^-$ , the spectrum of which is shown in Figure 9.8.

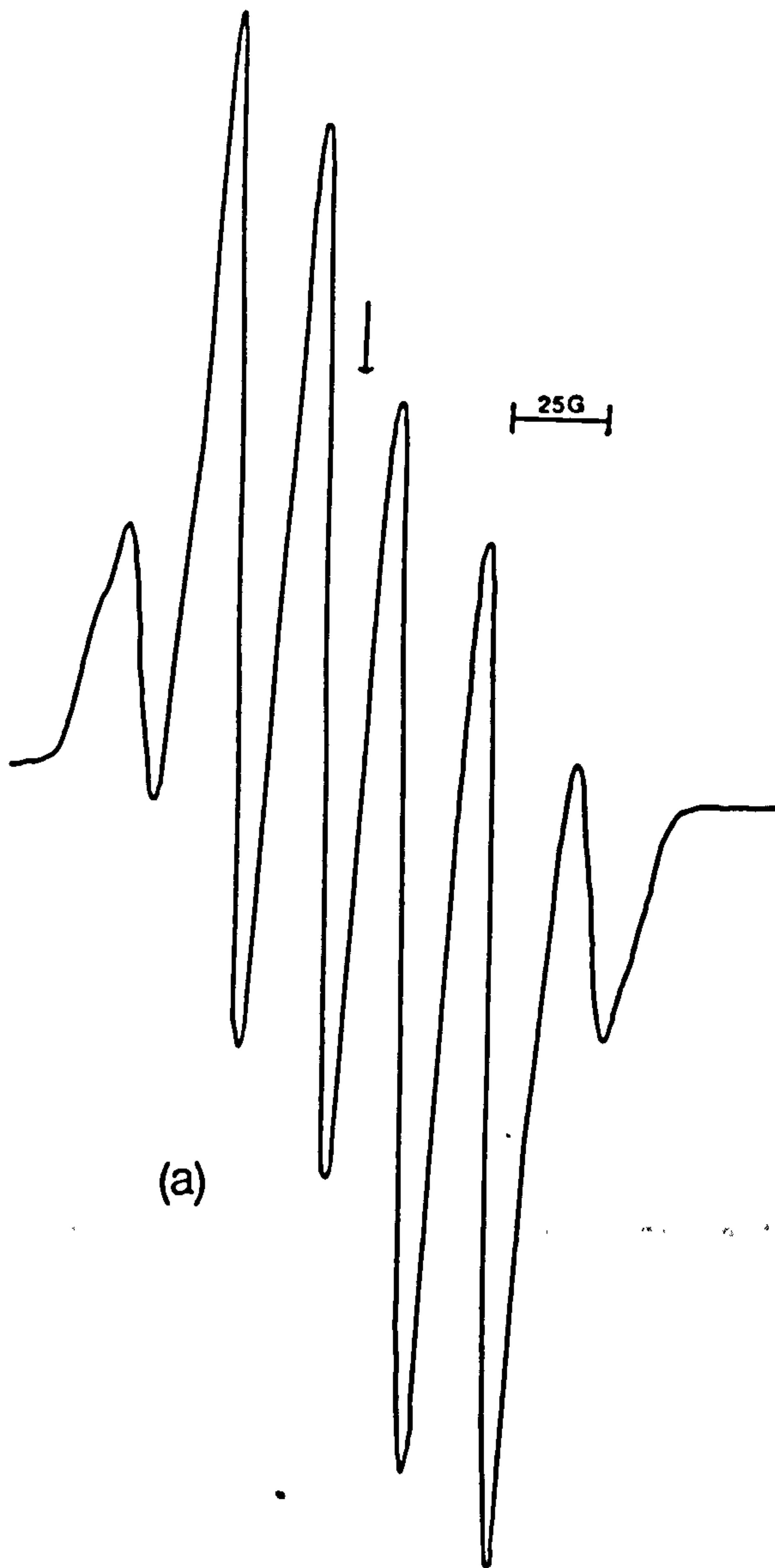
### Aspartic Acid

A five-line spectrum was found in  $\text{H}_2\text{O}$  and  $\text{D}_2\text{O}$  with  $a(\text{H})_{\text{av}} = 22 \text{ G}$ ,  $g = 2.0026$  which is assigned to  $\dot{\text{C}}\text{H}_2\text{CH}(\text{NH}_3^+)\text{CO}_2^-$ , see Figure 9.9.

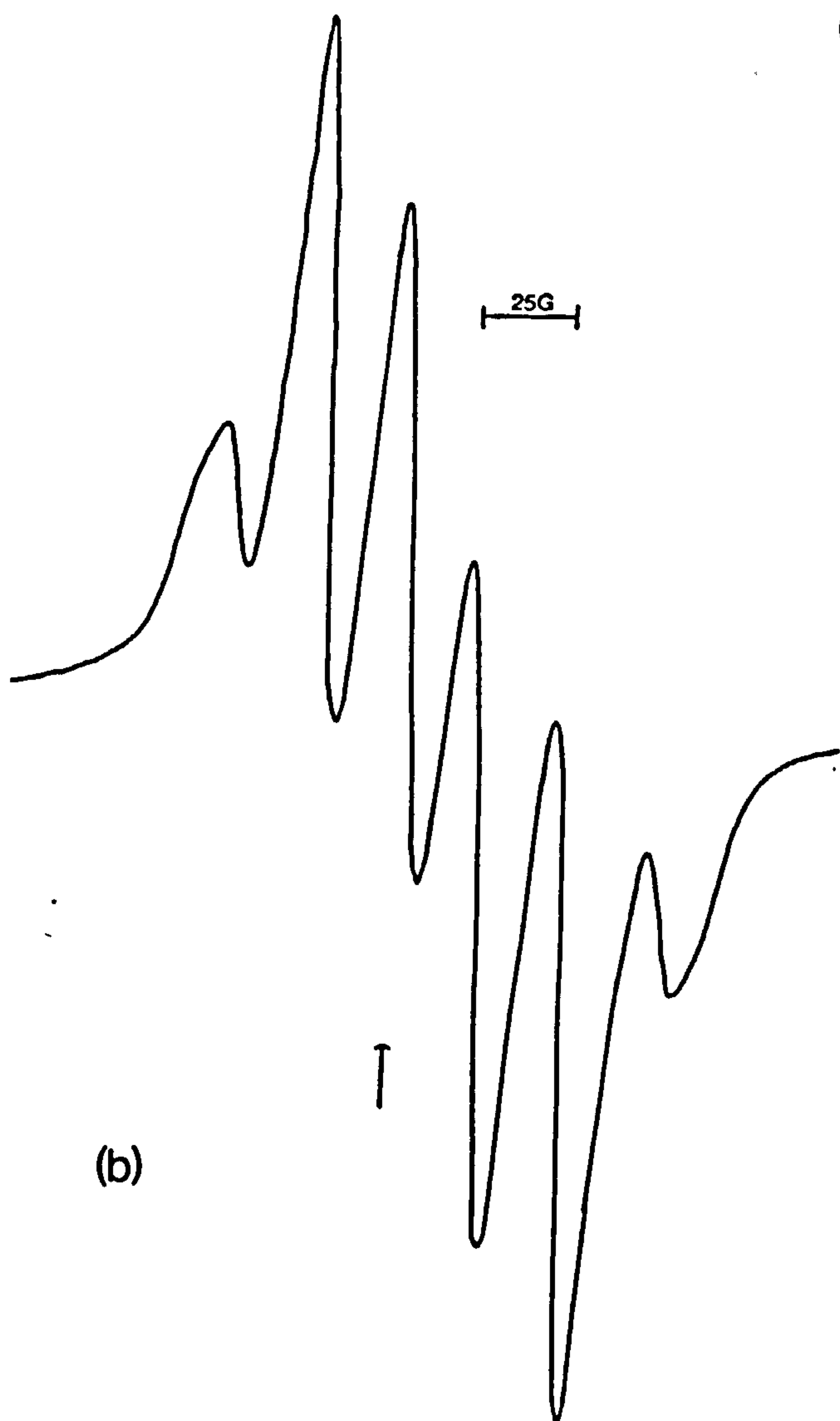
### Glutamine

A symmetrical weakly-resolved seven-line spectrum was produced in  $\text{H}_2\text{O}$

Figure 9.6 ESR spectra produced at 77 K on photolysis of  $\beta$ -alanine in (a)  $D_2O$  and (b)  $Ce(IV)/D_2O$ .



(a)



(b)

Figure 9.7      ESR spectra produced at 77 K on photolysis of valine in  
(a)  $\text{H}_2\text{O}$  and (b)  $\text{D}_2\text{O}$ .

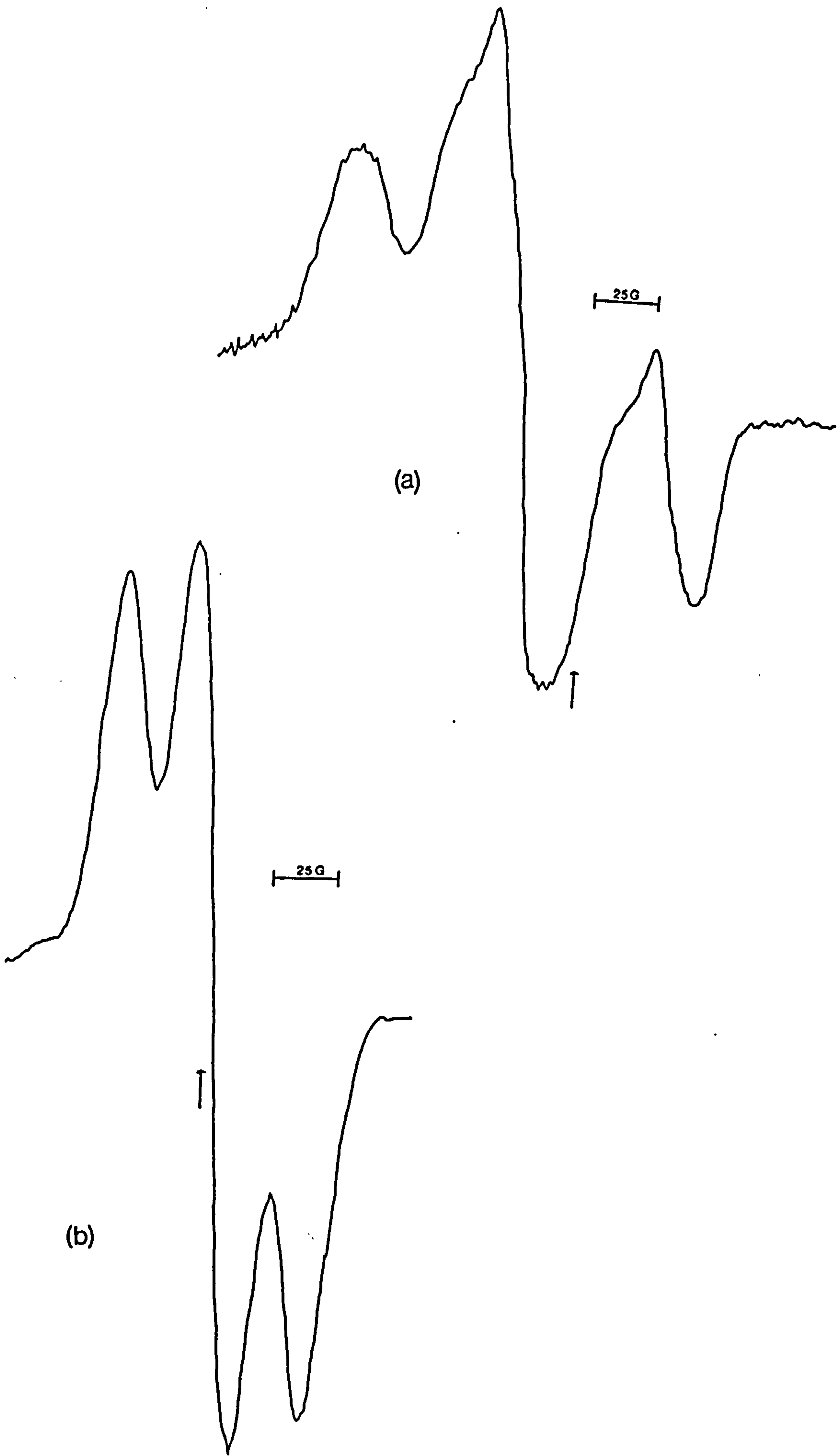


Figure 9.8

ESR spectrum produced at 77 K on photolysis of glutamic acid in H<sub>2</sub>O.

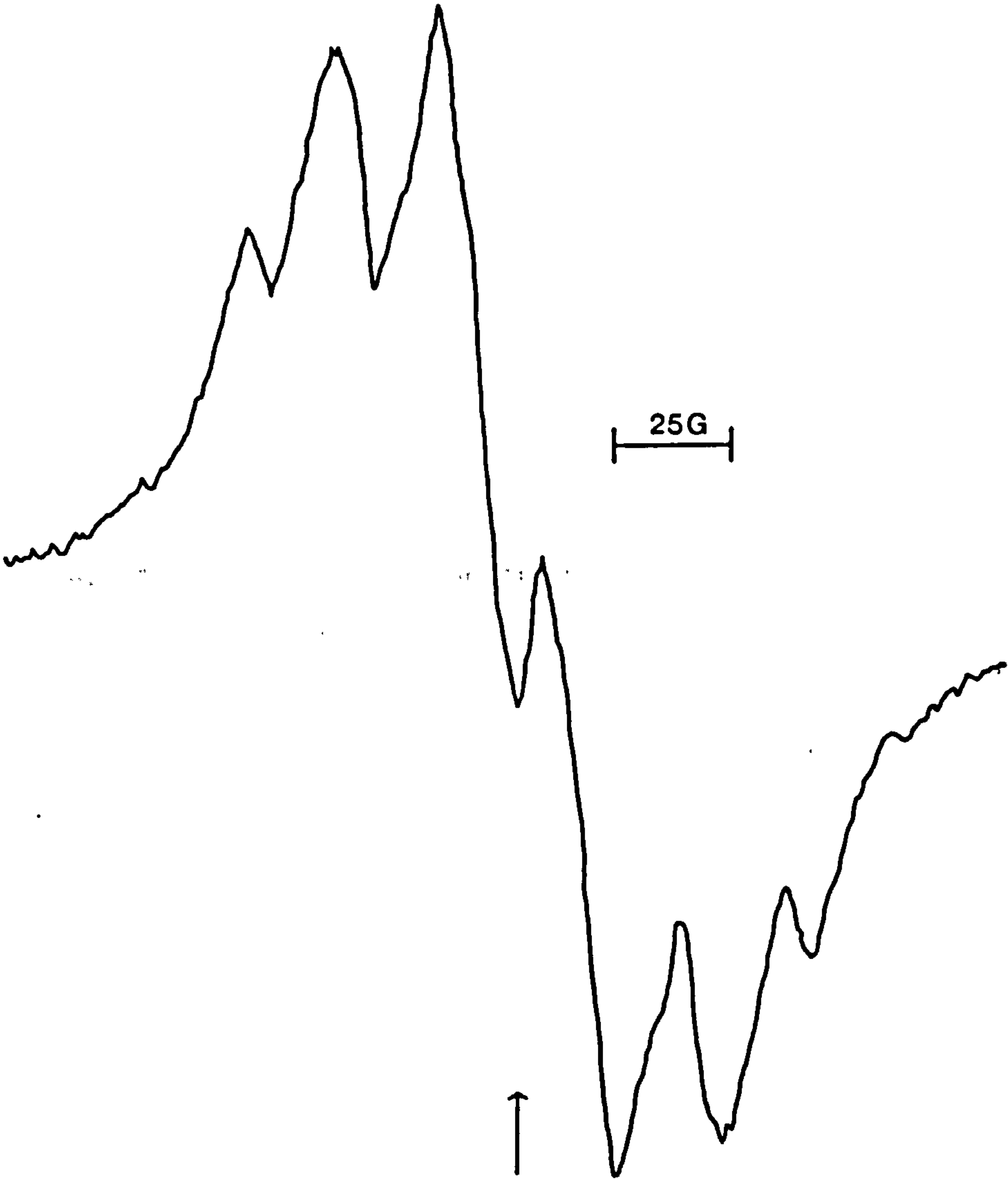
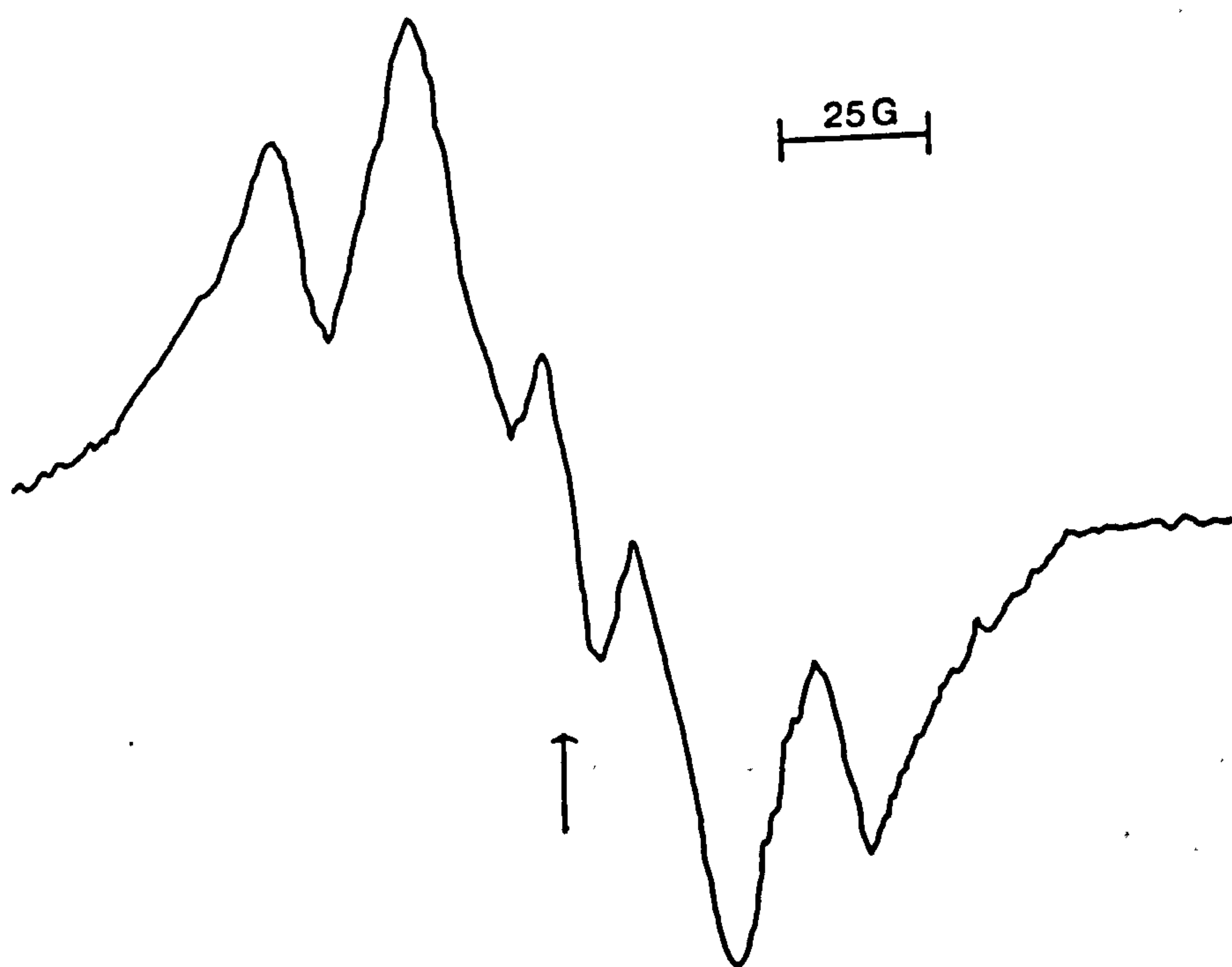




Figure 9.9 ESR spectrum produced at 77 K on photolysis of aspartic acid in H<sub>2</sub>O.



with  $a(H)_{av} = 26$  G and  $g = 2.00265$  which, in  $D_2O$ , yielded only five lines with  $a(2H) = 26$  G,  $(1H) = 52$  G. The radicals responsible are assigned to  $NH_2COCH_2CH_2\dot{C}H^+NH_3$  and  $NH_2COCH_2CH_2\dot{C}H^+ND_3$  and their spectra are shown in Figure 9.10.

### Asparagine

Again a poorly resolved seven-line spectrum in  $H_2O$ , see Figure 9.11(a), was reduced in  $D_2O$  to a basic broad triplet exhibiting some further structure, with  $a(2H) = 26$  G, which is shown in Figure 9.11(b). The most probable candidate species in  $H_2O$  and  $D_2O$  are  $NH_2COCH_2\dot{C}H^+NH_3$  and  $NH_2COCH_2\dot{C}H^+ND_3$  respectively.

### Methionine

An intense singlet was formed in  $H_2O$  and  $D_2O$  with  $g = 2.0125$  and  $\Delta H_{pp} = 33$  G, see Figure 9.12.

### Cysteine

A singlet featuring some sub-structure was formed in both  $H_2O$  and  $D_2O$  with  $g = 2.0105$  and  $\Delta H_{pp} = 32.5$  G, as shown in Figure 9.13.

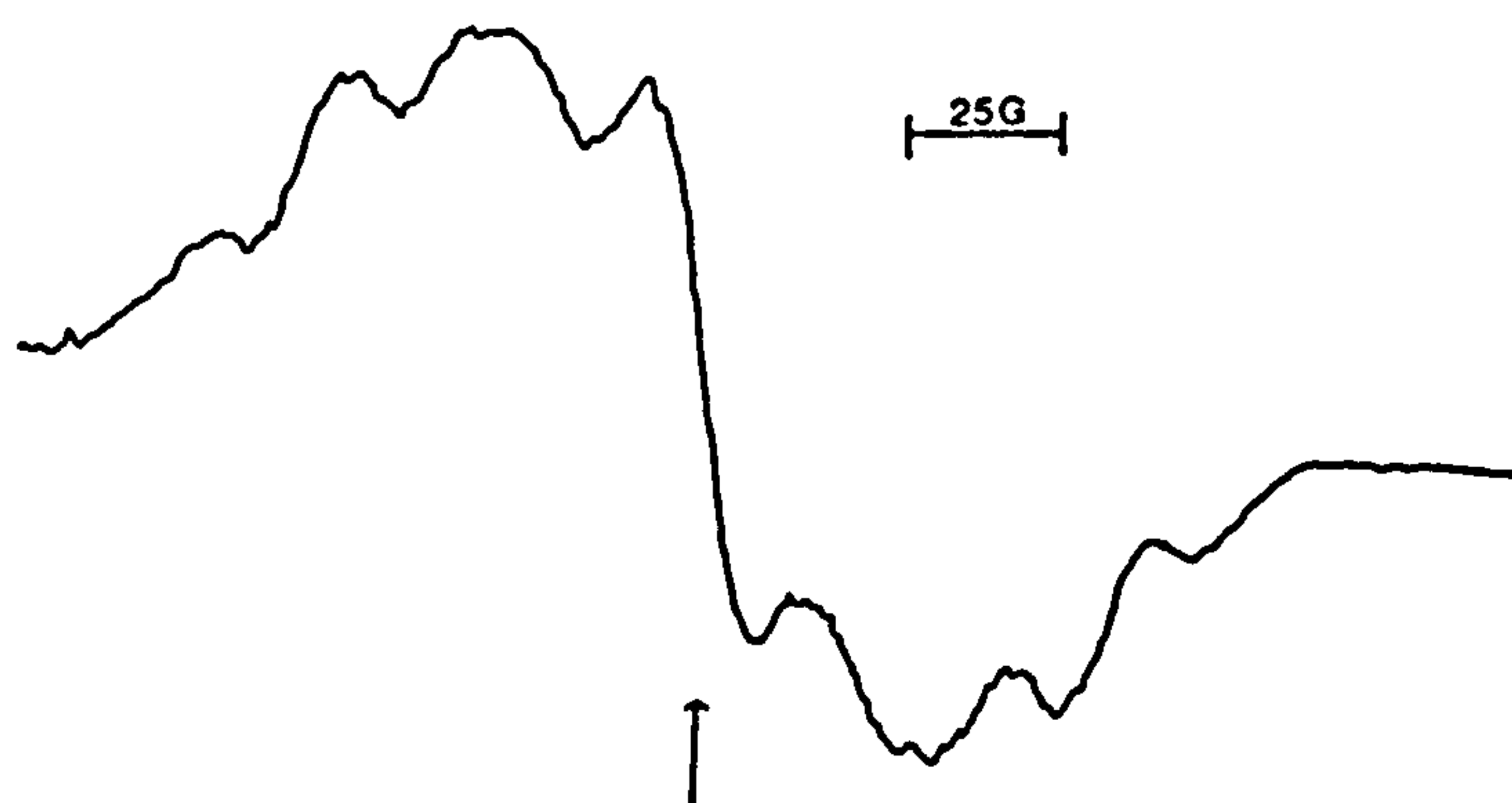
### Cystine

Again a singlet with some sub-structure was observed both in  $H_2O$  and  $D_2O$  with  $g = 2.0056$  and  $\Delta H_{pp} = 28$  G, depicted in Figure 9.14.

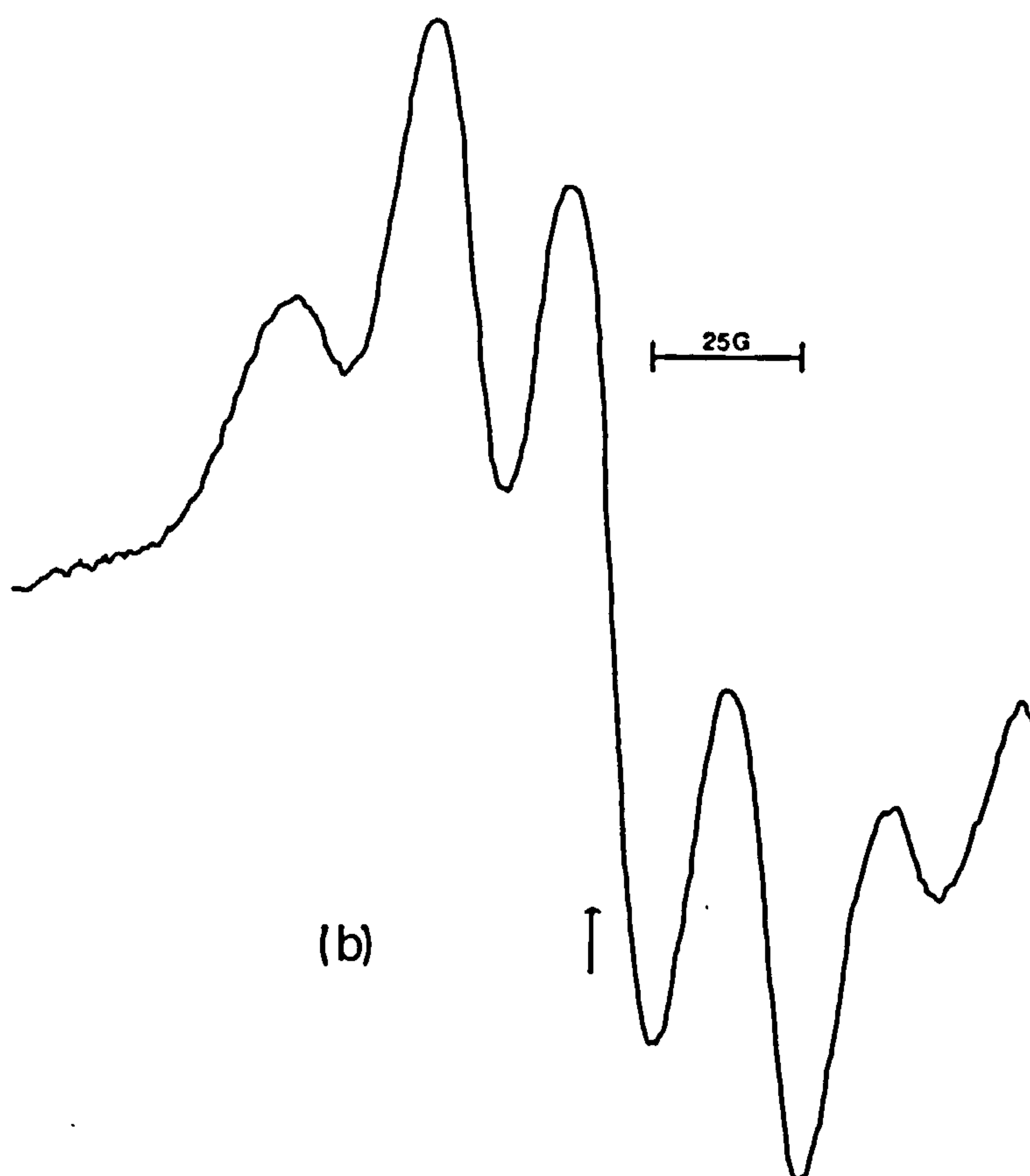
### Serine

A complex spectrum obtained in  $H_2O$  became a basic triplet in  $D_2O$  with  $a(2H) = 23.0$  G and  $g = 2.0056$ , see Figure 9.15, similar to that given by asparagine, and the most reasonable assignment is to the analogous radical, i.e. to  $DOCH_2-\dot{C}H^+ND_3$ .

Figure 9.10 ESR spectra produced at 77 K on photolysis of glutamine in (a)  $\text{H}_2\text{O}$  and (b)  $\text{D}_2\text{O}$ .



(a)



(b)

**Figure 9.11**      ESR spectra produced at 77 K on photolysis of asparagine  
in (a)  $\text{H}_2\text{O}$  and (b)  $\text{D}_2\text{O}$ .

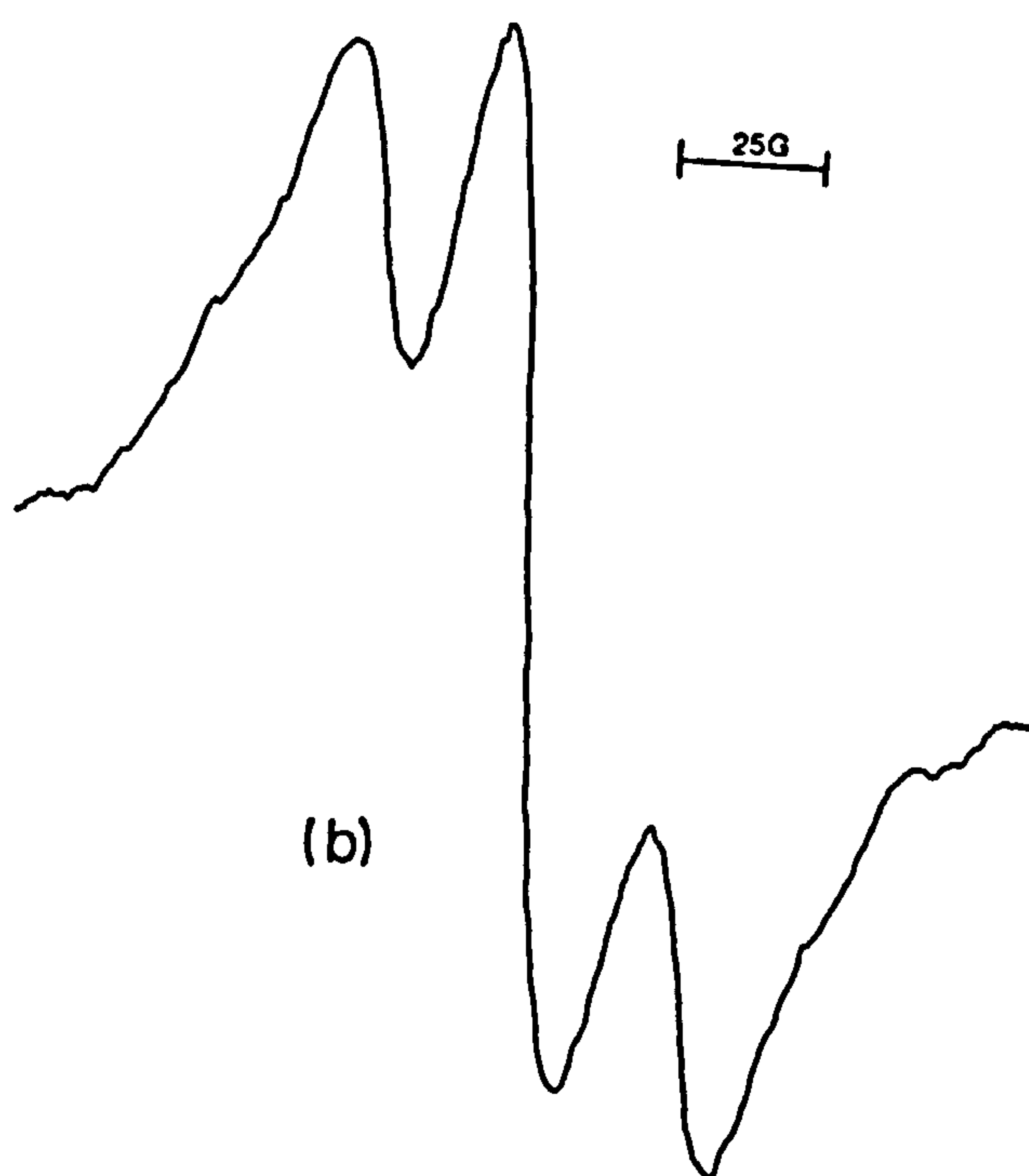
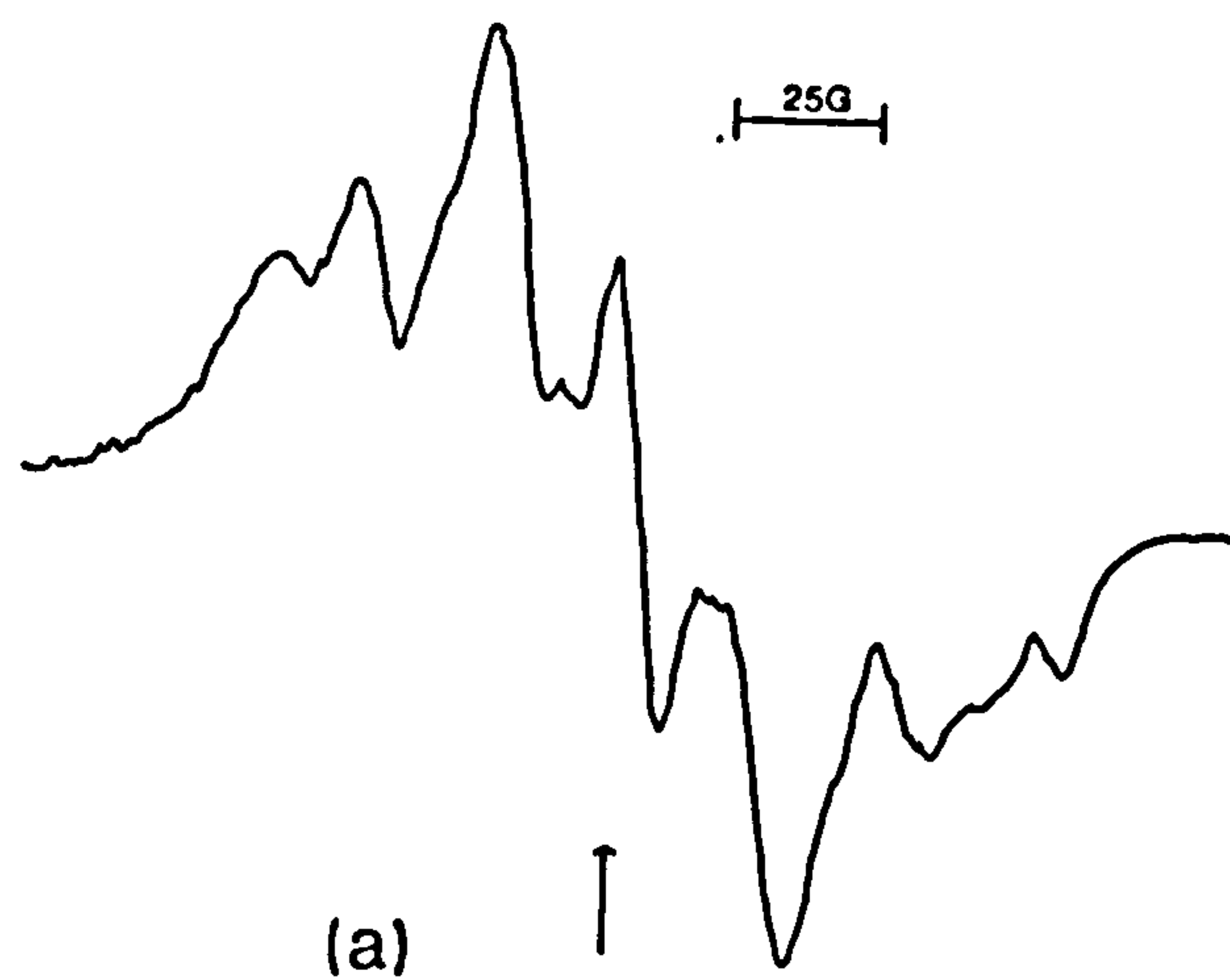




Figure 9.12      ESR spectrum produced at 77 K on photolysis of  
methionine in H<sub>2</sub>O

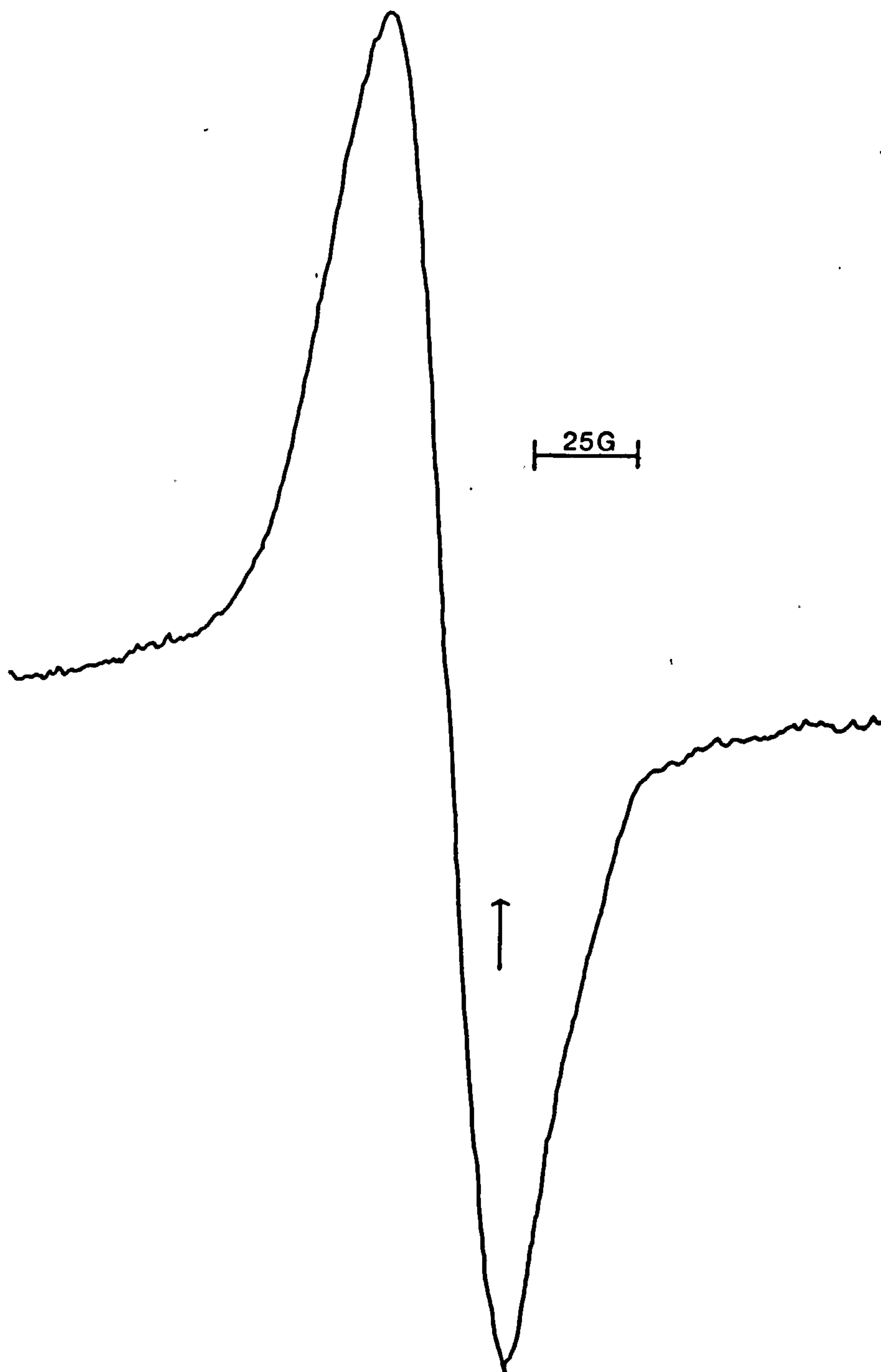


Figure 9.13      ESR spectrum produced at 77 K on photolysis of cysteine  
in H<sub>2</sub>O

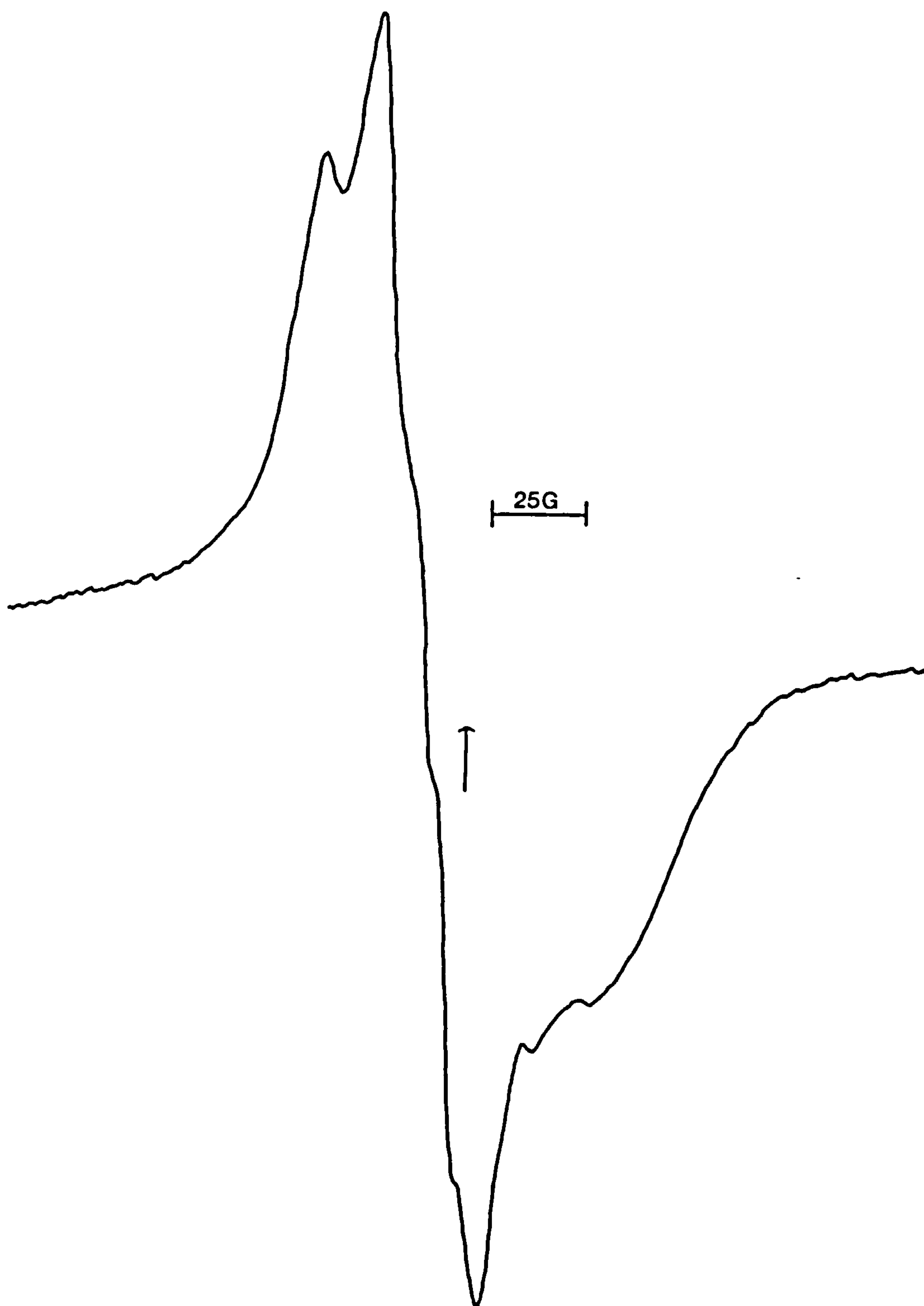


Figure 9.14

ESR spectrum produced at 77 K on photolysis of cystine  
in H<sub>2</sub>O

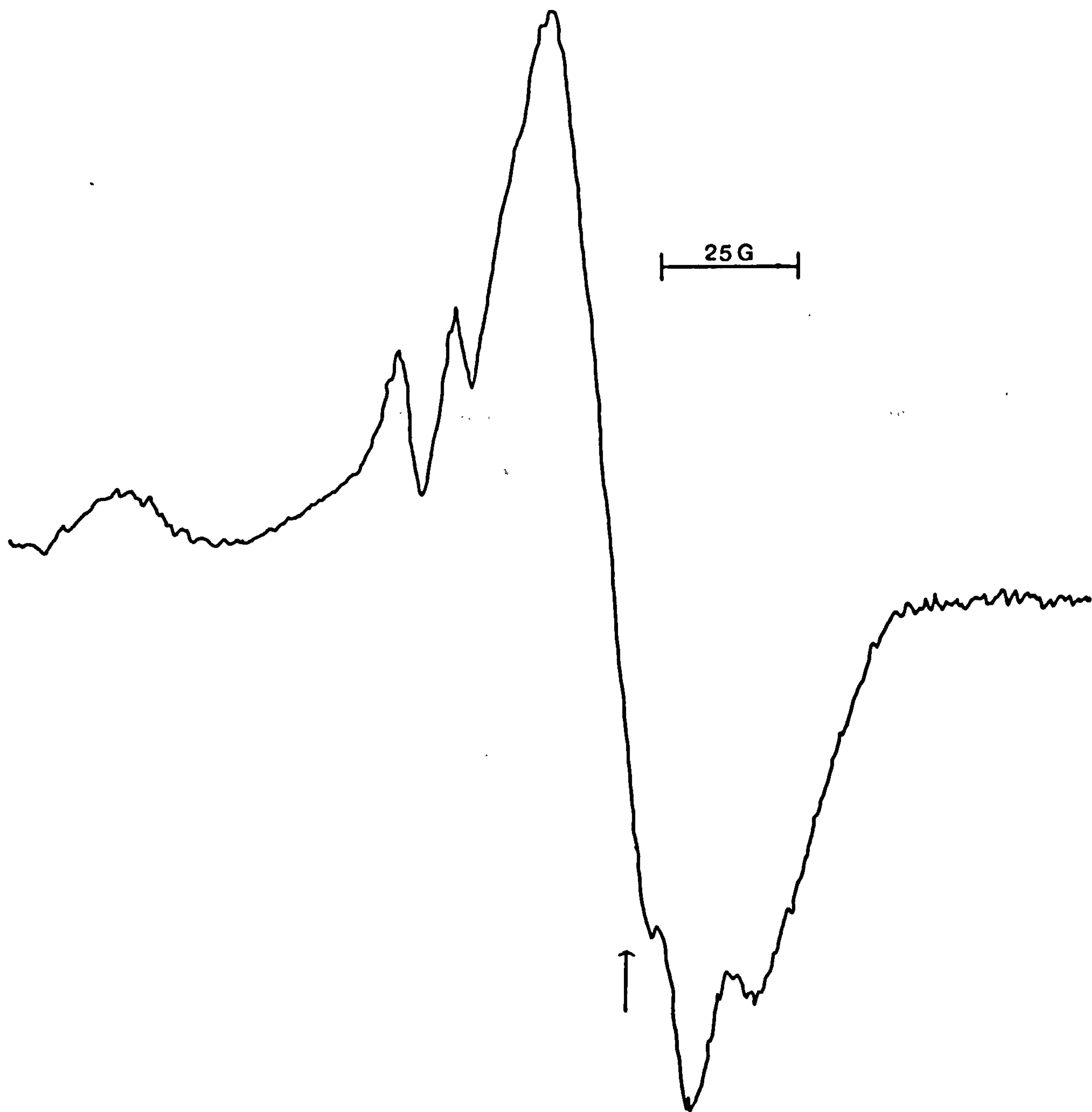
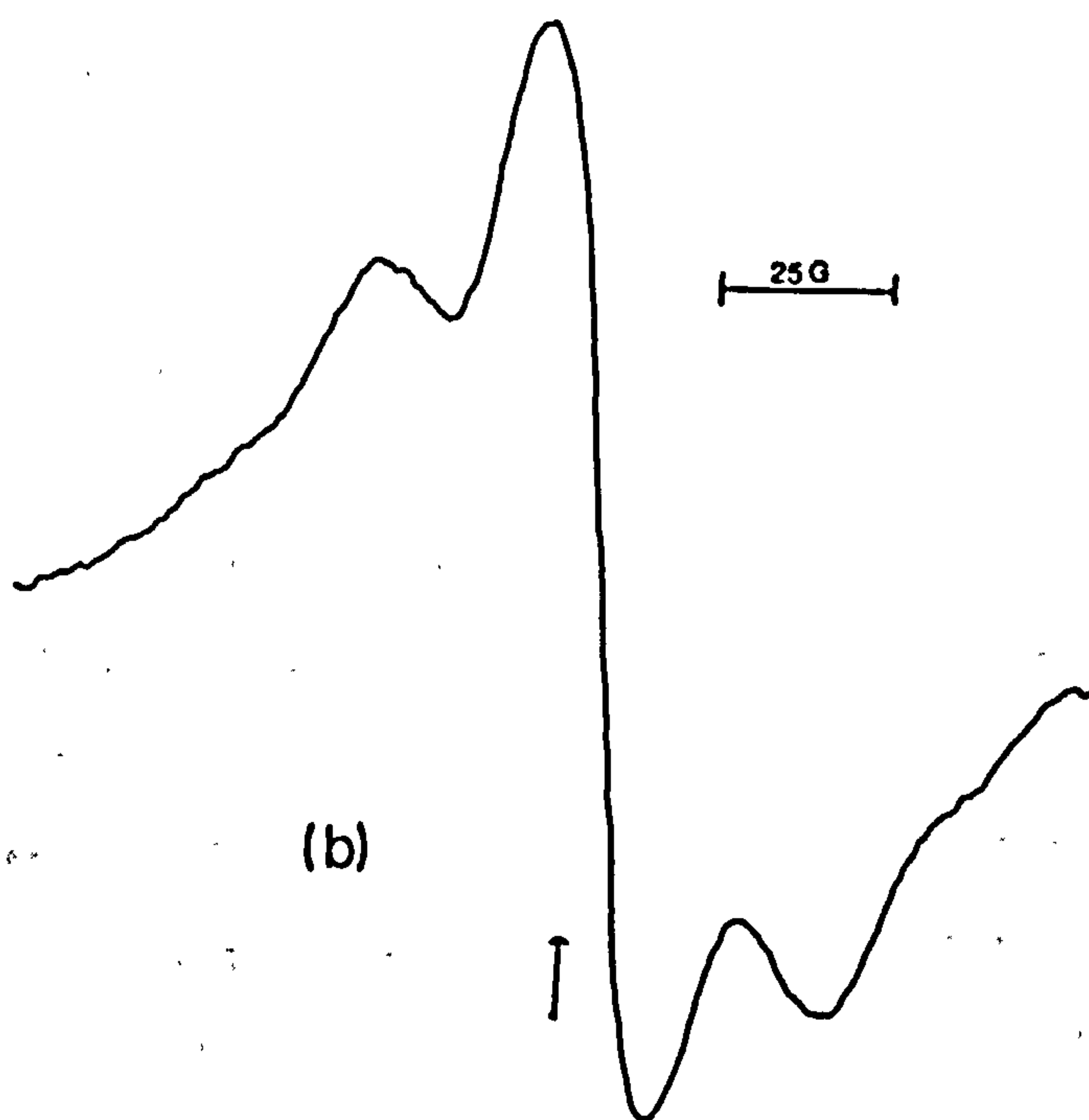
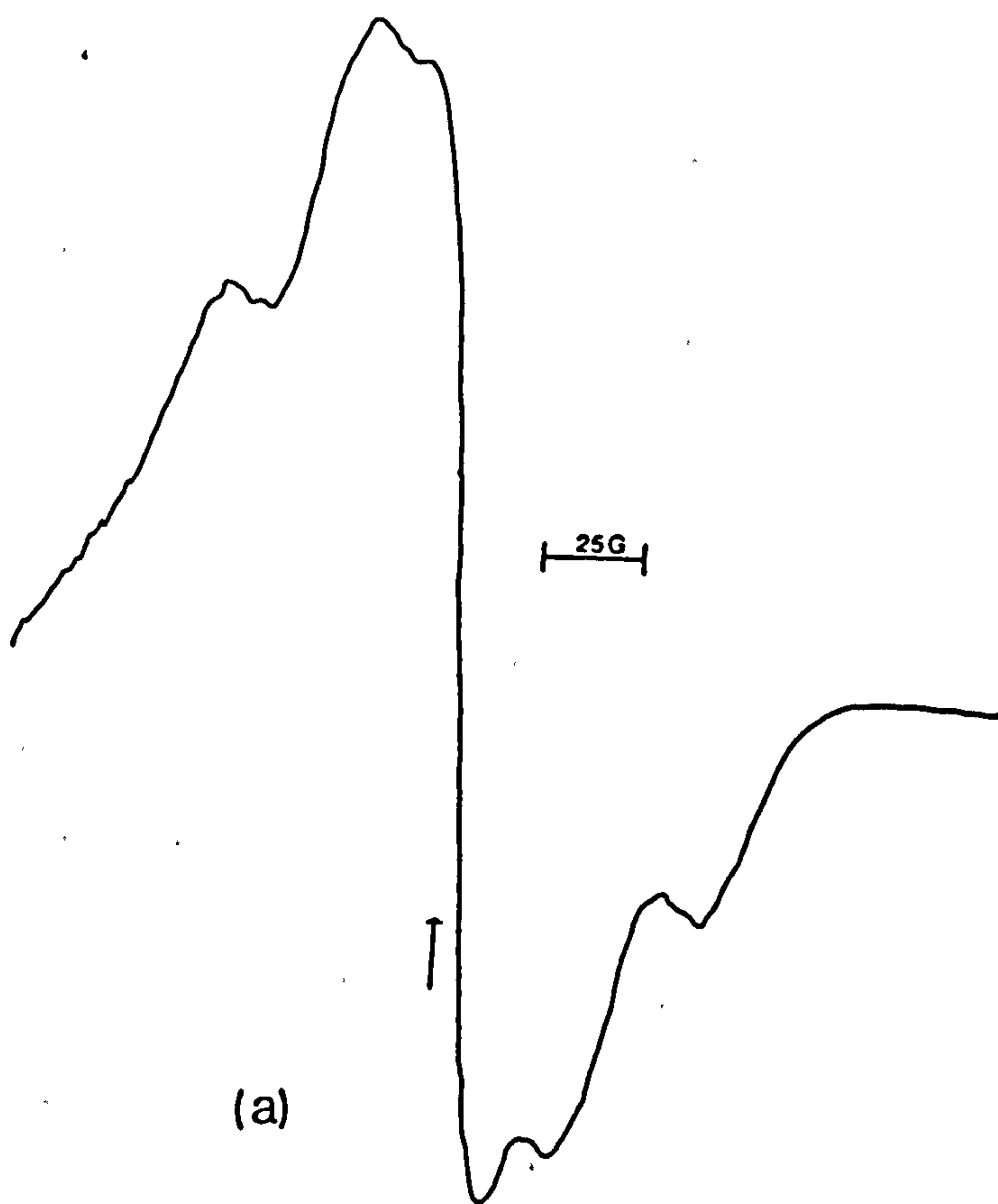


Figure 9.15 ESR spectra produced at 77 K on photolysis of serine in  
(a)  $\text{H}_2\text{O}$  and (b)  $\text{D}_2\text{O}$ .





### Iminodiacetic Acid

A complex spectrum obtained in  $\text{H}_2\text{O}$ , shown in Figure 9.16(a), reduced to a triplet in  $\text{D}_2\text{O}$  with  $a(\text{H}) = 25 \text{ G}$  and  $g = 2.0053$ , Figure 9.16(b) which is assigned to the radical  $\text{DN}(\text{CH}_2\text{CO}_2\text{H})\dot{\text{C}}\text{H}_2$ .

### 9.4 Discussion

Insertion of the value of  $\tau_0$ , obtained under the same conditions as that for  $K^{\text{SV}}$ , into the Stern-Volmer equation yielded values for  $k_2$  in good agreement with those obtained by laser flash photolysis. Thus, for phenylalanine  $K^{\text{SV}}$  was measured as  $1.90 \times 10^3 \text{ dm}^3 \text{ mol}^{-1}$ . Insertion of the lifetime for  $*[\text{UO}_2]^{2+}$  under the same conditions,  $\tau_0 = 2.85 \mu\text{s}$ , yielded a  $k_2$  value of  $6.65 \times 10^8$ , which compares well with  $7.92 \times 10^8$  obtained from lifetime quenching by phenylalanine.

Amino acids of the general structure  $\text{RCH}(\text{NH}_3^+)\text{CO}_2^-$  ( $\text{R} = \text{alkyl}$ ) have second-order quenching rate constants not exceeding  $6 \times 10^6 \text{ dm}^3 \text{ mol}^{-1} \text{ s}^{-1}$ . This indicates the inertness of these amino acids towards  $*[\text{UO}_2]^{2+}$  despite its highly oxidising character, with an estimated reduction potential of  $+2.60 \text{ V}^{205}$ . The quantum yields for U(IV) production are nearly, or exceed, 0.1 when  $\text{R}$  is a branched alkyl group as in valine, leucine and isoleucine.

ESR data for the photolysis of the amino acids,  $\text{RCH}(\text{NH}_3^+)\text{CO}_2^-$  in the presence of  $[\text{UO}_2]^{2+}$  at 77 K indicates that a decarboxylation of the amino acid is occurring, which leads to free radicals of the type  $\text{H}_3\text{N}^+\dot{\text{C}}\text{HR}$ . At liquid-nitrogen temperature, the spectra obtained in water are relatively complicated, due to anisotropic hyperfine interaction of protons with the unpaired electron; safer assignments of the radical

Table 9.4

Summary of ESR Data Relating to Radicals Produced at 77 K  
by Interaction of Amino Acids with Excited Uranyl Ion

Substrate	Medium	ESR Spectrum	Assignment
$\text{CH}_2(\text{NH}_3^+)\text{CO}_2^-$	$\text{H}_2\text{O}$	6 lines, 5H $a = 30 \text{ G}$	$\dot{\text{C}}\text{H}_2\text{NH}_3^+$
	$\text{D}_2\text{O}$	3 lines, 2H $a = 23.5 \text{ G}$	$\dot{\text{C}}\text{H}_2\text{ND}_3^+$
$\text{CH}_3\text{CH}(\text{NH}_3^+)\text{CO}_2^-$	$\text{D}_2\text{O}$	5 lines, 4H $a(\text{H})_{\text{av}} = 28 \text{ G}$	$\text{Me}\dot{\text{C}}\text{HND}_3^+$
$-\text{H}_3\text{N}^+\text{CH}_2\text{CH}_2\text{CO}_2^-$	$\text{H}_2\text{O}$	6 lines, 4H $a(\text{H})_{\alpha} = 23 \text{ G}$ $a(\text{H})_{\beta} = 46 \text{ G}$	$\dot{\text{C}}\text{H}_2\text{CH}_2\text{NH}_3^+$
	$\text{D}_2\text{O}$	6 lines, 4H	$\dot{\text{C}}\text{H}_2\text{CH}_2\text{ND}_3^+$
$\text{Me}_2\text{CHCH}(\text{NH}_3^+)\text{CO}_2^-$	$\text{H}_2\text{O}$	broad, poorly resolved	$\text{Me}_2\text{CH}\dot{\text{C}}\text{H}(\text{NH}_3^+)$
	$\text{D}_2\text{O}$	3 lines, 2H $a(\text{H}) = 24 \text{ G}$	$\text{Me}_2\text{CH}\dot{\text{C}}\text{H}(\text{ND}_3^+)$
$^-\text{O}_2\text{CCH}_2\text{CH}_2\text{CH}(\text{NH}_3^+)\text{CO}_2^-$	$\text{H}_2\text{O}$	6 lines, 4H $a(\text{H})_{\text{av}} = 23 \text{ G}$	$\dot{\text{C}}\text{H}_2\text{CH}_2\text{CH}(\text{NH}_3^+)\text{CO}_2^-$
	$\text{D}_2\text{O}$	6 lines	$\dot{\text{C}}\text{H}_2\text{CH}_2\text{CH}(\text{ND}_3^+)\text{CO}_2^-$

(contd.)

Table 9.4 (contd)

Substrate	Medium	ESR Spectrum	Assignment
${}^{-}\text{O}_2\text{CCH}_2\text{CH}(\overset{+}{\text{NH}}_3)\text{CO}_2^{-}$	$\text{H}_2\text{O}$	5 lines $a(\text{H})_{\text{av}} = 22 \text{ G}$	$\dot{\text{C}}\text{H}_2\text{CH}(\overset{+}{\text{NH}}_3)\text{CO}_2^{-}$
$\text{NH}_2\text{COCH}_2\text{CH}_2(\overset{+}{\text{NH}}_3)\text{CO}_2^{-}$	$\text{H}_2\text{O}$	7 lines, 6H $a(2\text{H}) = 26 \text{ G},$ $a(1\text{H}) = 52 \text{ G}$	$\text{NH}_2\text{COCH}_2\text{CH}_2\dot{\text{C}}\text{H}(\overset{+}{\text{NH}}_3)$
	$\text{D}_2\text{O}$	5 lines	$\text{NH}_2\text{COCH}_2\text{CH}_2\dot{\text{C}}\text{H}(\overset{+}{\text{ND}}_3)$
$\text{NH}_2\text{COCH}_2\text{CH}(\overset{+}{\text{NH}}_3)\text{CO}_2^{-}$	$\text{H}_2\text{O}$	7 lines, 6H	$\text{NH}_2\text{COCH}_2\dot{\text{C}}\text{H}(\overset{+}{\text{NH}}_3)$
	$\text{D}_2\text{O}$	3 lines $a(2\text{H}) = 26 \text{ G}$	$\text{NH}_2\text{COCH}_2\dot{\text{C}}\text{H}(\overset{+}{\text{ND}}_3)$
$\text{HOCH}_2\text{CH}(\overset{+}{\text{NH}}_3)\text{CO}_2^{-}$	$\text{D}_2\text{O}$	3 lines $a(2\text{H}) = 23 \text{ G}$	$\text{DOCH}_2\dot{\text{C}}\text{H}(\overset{+}{\text{ND}}_3)$
$\text{MeS}(\text{CH}_2)_2\text{CH}(\overset{+}{\text{NH}}_3)\text{CO}_2^{-}$	$\text{H}_2\text{O}/\text{D}_2\text{O}$	intense singlet $\Delta\text{Hpp} = 33 \text{ G}$	S-centred species
$\text{HSCH}_2\text{CH}(\overset{+}{\text{NH}}_3)\text{CO}_2^{-}$	$\text{H}_2\text{O}/\text{D}_2\text{O}$	singlet $\Delta\text{Hpp} = 32.5 \text{ G}$	
$[\text{SCH}_2\text{CH}(\overset{+}{\text{NH}}_3)\text{CO}_2^{-}]_2$	$\text{H}_2\text{O}/\text{D}_2\text{O}$	singlet $\Delta\text{Hpp} = 28 \text{ G}$	

(contd.)

Table 9.4 (contd)

Substrate	Medium	ESR Spectrum	Assignment
-----------	--------	--------------	------------

$\text{HN}(\text{CH}_2\text{CO}_2\text{H})_2$	$\text{D}_2\text{O}$	3 lines, $a(\text{H}) = 25 \text{ G}$	$\text{DN}(\text{CH}_2\text{CO}_2\text{D})\dot{\text{C}}\text{H}_2$
---	----------------------	--	---

Summary of ESR Data Relating to Radicals Produced at 77 K by Interaction of Amino Acids with Ce(IV)

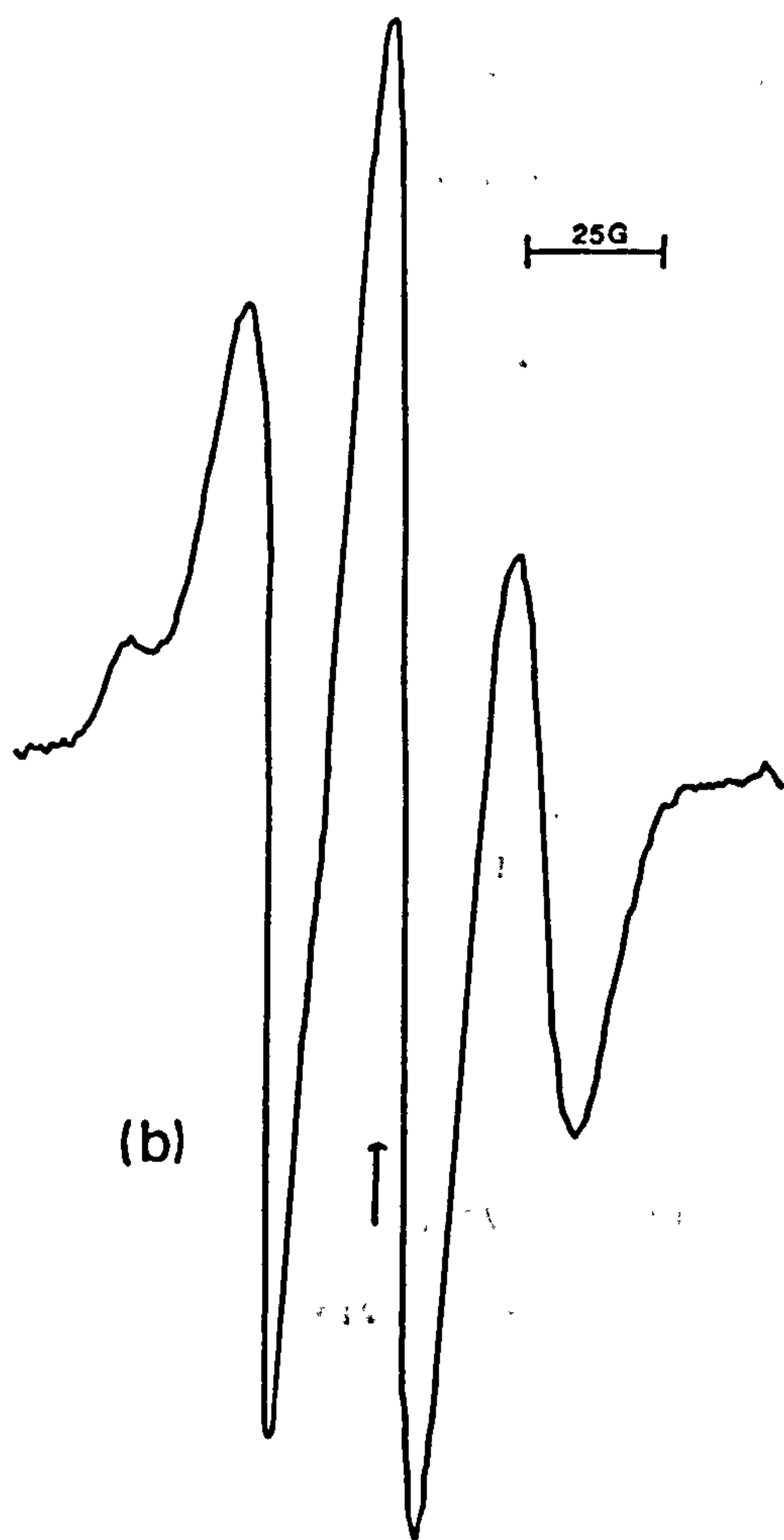
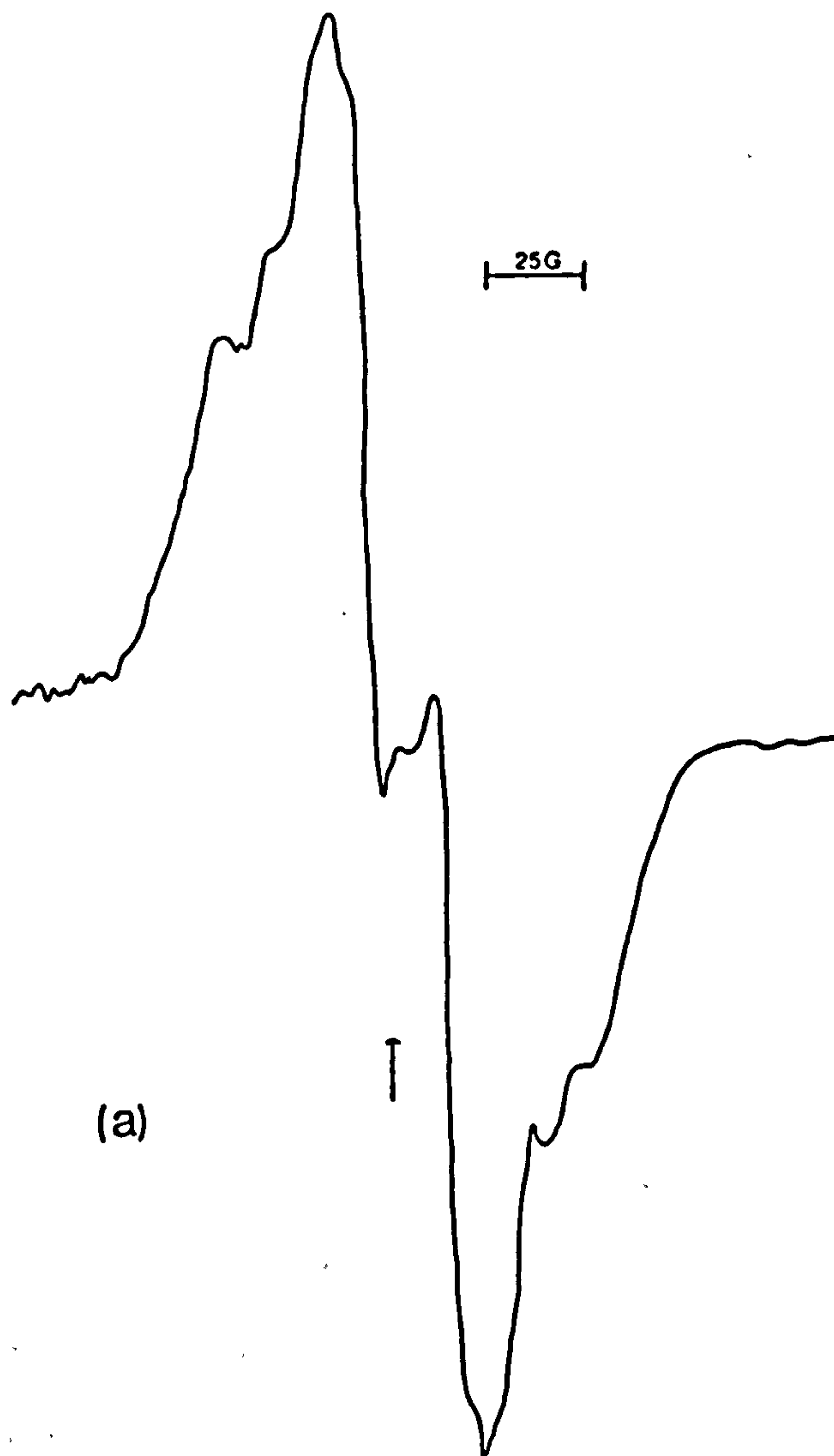
Substrate	Medium	ESR Spectrum	Assignment
-----------	--------	--------------	------------

$\text{CH}_2(\text{NH}_3^+)\text{CO}_2^-$	$\text{H}_2\text{O}$	6 lines, $a = 26 \text{ G}$	$\dot{\text{C}}\text{H}_2\text{NH}_3^+$
---	----------------------	--------------------------------	---

$\text{CH}_3\text{CH}(\text{NH}_3^+)\text{CO}_2^-$	$\text{H}_2\text{O}$	7 lines, $a(\text{H})_{\text{av}} = 27 \text{ G}$	$\text{CH}_3\dot{\text{C}}\text{H}(\text{NH}_3^+)$
--	----------------------	--	--

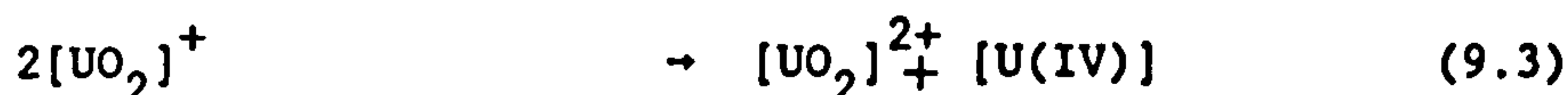
$\text{H}_3\text{N}^+\text{CH}_2\text{CH}_2\text{CO}_2^-$	$\text{H}_2\text{O}$	6 lines, $a(\text{H})\alpha = 23 \text{ G}$ $a(\text{H})\beta = 46 \text{ G}$	$\dot{\text{C}}\text{H}_2\text{CH}_2\text{NH}_3^+$
---	----------------------	---	--

Figure 9.16 ESR spectra produced at 77 K on photolysis of  
iminodiacetic acid (a)  $\text{H}_2\text{O}$  and (b)  $\text{D}_2\text{O}$

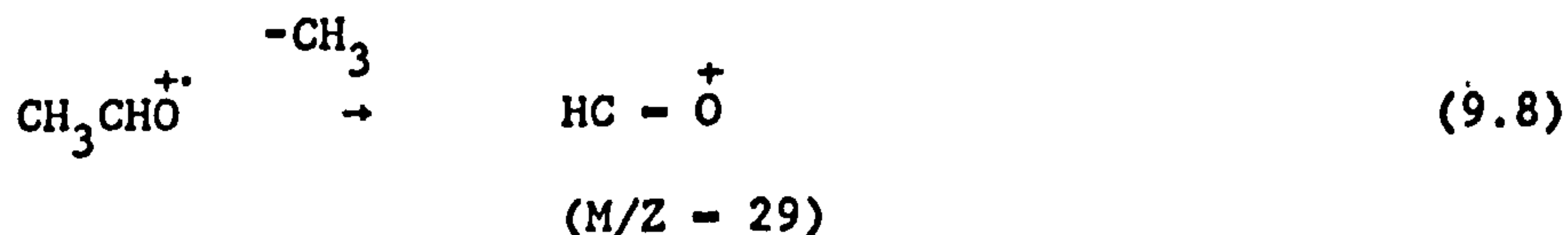
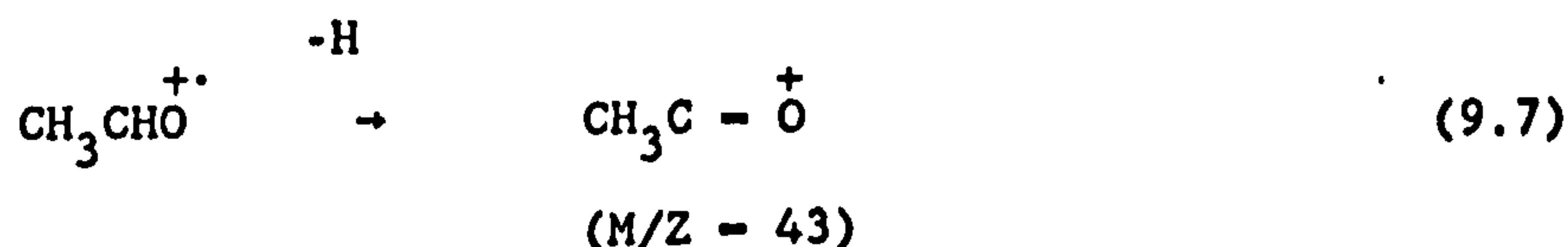
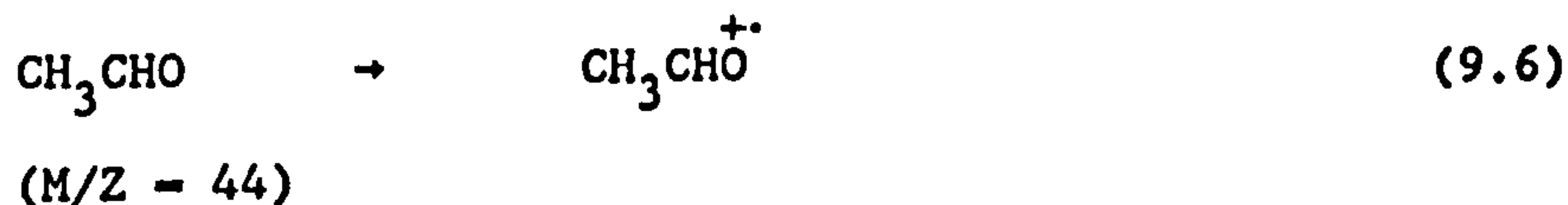




could be made by exchanging the amino protons with deuterium. The dicarboxylic amino acids, aspartic and glutamic acid, undergo a decarboxylation of the carboxylate group furthest removed from the protonated amino group. This is believed to be the ligating function of these amino acids<sup>148</sup>. The mechanism for the photochemical decomposition of the amino acids  $\text{RCH}(\text{NH}_3^+)\text{CO}_2^-$  is thought to be:



Support for the following mechanism has come from the detection of ethanal using GC/MS after prolonged photolysis of uranyl perchlorate in the presence of  $\alpha$ -alanine. Peaks at 44, 43 and 29 in the mass spectrum indicate the breakdown of ethanal



The values of  $\phi[\text{U(IV)}]$  as measured refer to all secondary processes leading to U(IV) after the primary photochemical act equation (9.1).

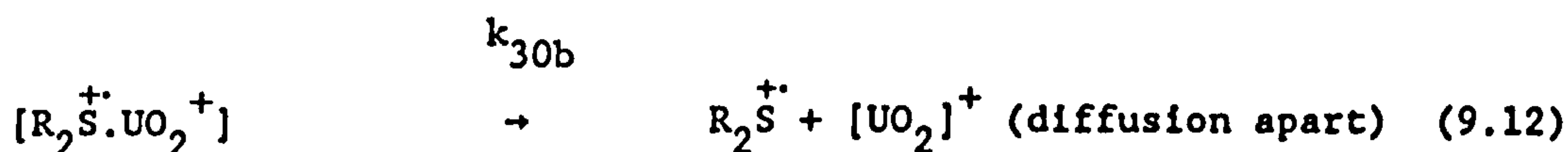
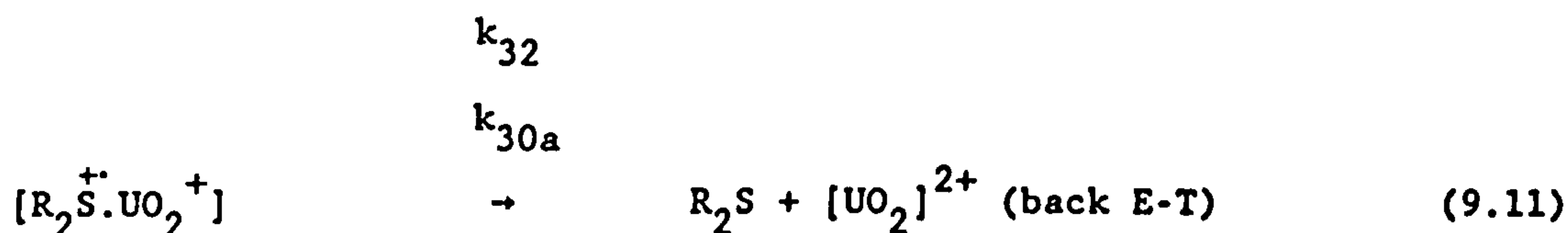
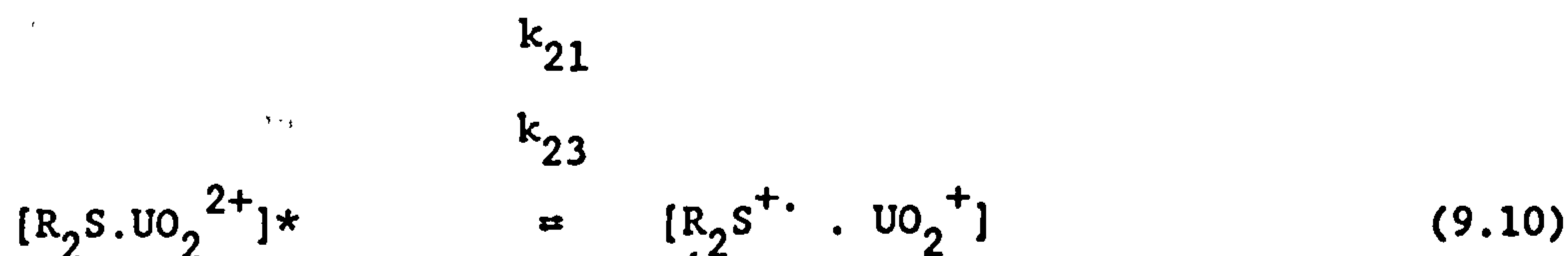
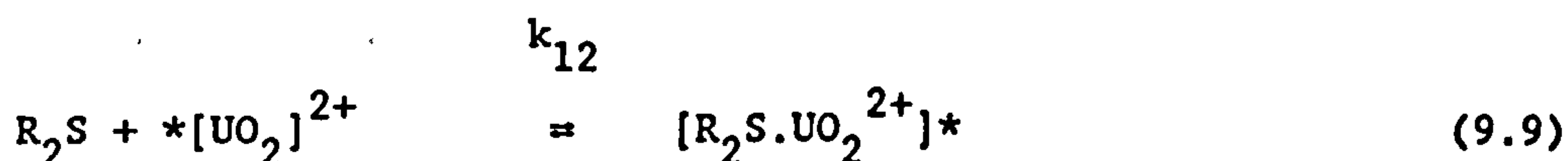
These will include the fast reduction of a second molecule of uranyl ion by the alkyl radical, equation (9.2) followed by the disproportionation, equation (9.3), and the subsequent attack on  $*[UO_2]^{2+}$  by the reactive aldehyde generated in equation (9.5); the ready photoreduction of  $*[UO_2]^{2+}$  by simple aldehydes has already been established<sup>206</sup>.

The aminopolycarboxylic acids, EDTA and CDTA give values of  $\phi [U(IV)]$  of just under 0.2, and also show a  $10^2$ -fold increase over the simple amino acids in their rate of quenching of  $*[UO_2]^{2+}$ . However, this reactivity must originate largely either in physical quenching processes, or in chemical quenching not leading to correspondingly large yields of separated radical-pairs.

The fast rates of quenching with amino acids bearing aromatic rings is associated with fast reversible exciplex formation between the  $\pi$ -system and the excited  $[U(VI)]$  species, as established for a series of substituted benzenes<sup>133</sup> and benzoic acids and alkenes<sup>134</sup>. Support for this view is indicated by the immeasurably small quantum yields for  $[U(IV)]$  formation and that no ESR signals were observable, even after prolonged photolysis of these amino acids in the presence of  $[UO_2]^{2+}$ .

The sulphur-containing amino acids display second-order kinetic quenching rate constants of between  $5.67 \times 10^8$  and  $1.29 \times 10^9 \text{ dm}^3 \text{ mol}^{-1} \text{ s}^{-1}$ , i.e. rather similar to those reported for simple thioethers and other sulphur compounds<sup>126</sup>, while, as with these simple compounds, the quantum yield of the redox process is very small. Thus, while the rate of interaction between  $*[UO_2]^{2+}$  and the thio-compounds is  $>10^2$ -fold faster than for the simple amino acids, the yield of redox products is ca. 10-fold lower.

The step  $k_{30a}$  in the Weller-type scheme, equation (9.11), evidently operates with high efficiency in these systems:



The production of sulphur-centred, rather than carbon-centred radicals from the thio compounds is strongly suggested by the line-shapes and g-tensors of the ESR spectra of the irradiated systems<sup>126,207</sup>, see Table 9.4.

A comparison of the absolute rate constants,  $k_2$  in Table 9.2, shows stronger quenchers when complexed with metal ions. The preferred mechanism here is one of energy-transfer from  $*[UO_2]^{2+}$  to the metal ion-amino acid complex, rather than electron transfer. This leads to photodecomposition of the complex yielding  $[Co(H_2O)_6]^{2+}$ , free ligand and ligand-derived products analogous to the pathway found during photosensitisation of  $[Co(acac)_3]$  using  $*[UO_2]^{2+}$ <sup>208</sup>.

Although in some respects  $*[UO_2]^{2+}$  behaves like  $[O - U(V) - \dot{O}]$ , i.e. a radical with its SOMO centred on an oxygen atom, such as triplet

benzophenone,  $\text{Ph}_2\dot{\text{C}}-\dot{\text{O}}$ , in its interaction with amino acids it behaves uniquely. Thus while triplet benzophenone, like  $*[\text{UO}_2]^{2+}$  reacts very slowly with glycine, and rapidly with EDTA, histidine, tryptophan, tyrosine and methionine<sup>164</sup>, the yields of redox species determined by flash photolysis are generally much higher for triplet benzophenone than for the excited uranyl ion, i.e. in equations (9.11) and (9.12),  $k_{30b} > k_{30a}$  for  $^3\text{Ph}_2\text{CO}$ .

## **Chapter 10**

### **Results**

#### **Physical and Chemical Quenching of Excited Uranyl Ion by Dialkyl Sulphides**

## 10.1 Introduction

A recent paper<sup>209</sup> has dealt with the photochemical reduction of uranyl ion by a series of dialkyl sulphides. The results presented in this paper are in disagreement both with a previous study of the photochemical reduction of  $[\text{UO}_2]^{2+}$  by di-n-butyl sulphide and other organosulphur compounds<sup>126</sup>, summarised in Table 10.1, and an analogous system employing the sulphur-containing amino acids, cysteine, cystine, and methionine as the photochemical reductants, see Chapter 9. The major points of disagreement are (i) the magnitudes of the quantum yields for  $[\text{U(IV)}]$  production, and (ii) the mechanism proposed for the photochemical oxidation of the dialkyl sulphides.

The work presented in this chapter constitutes a re-examination of the interaction of  $*[\text{UO}_2]^{2+}$  with a series of dialkyl sulphides,  $\text{R}_2\text{S}$  ( $\text{R} = \text{Me}$ ,  $\text{Et}$ ,  $^1\text{Pr}$ ,  $n\text{-Bu}$ ), in order to ascertain the source of the discrepancies.

Concentrating on point (i), the actinometric techniques of Sandhu et al.<sup>119</sup> differ from those of ourselves in that whereas the former group use a broad band of irradiation wavelengths, i.e. the output of a 125 W medium pressure Hg lamp filtered through pyrex (the reaction vessel), which is both polychromatic and more intense, we use the output of a current stabilised 200 W medium pressure Xe/Hg lamp filtered through a Balzer metal interference filter ( $\lambda_{\text{transmitted}} = 401 \pm 20 \text{ nm}$ ). Both groups use ferrioxalate actinometry. In order to test whether the origin of the discrepancy lies in the irradiation conditions,  $\text{R}_2\text{S}$  ( $\text{R} = \text{Et}$ ,  $n\text{-Bu}$ ) was photolysed under two very different radiation bandwidths, the results of which are shown in Table 10.2. The small variation in  $\phi[\text{U(IV)}]$ , despite the difference in irradiation bandwidth and uranium (VI) salt, shows that these factors are not the origin of the

Table 10.1      Quantum Yields for [U(IV)] Formation in the Photo-  
Oxidation of Dialkyl Sulphides (R<sub>2</sub>S)<sup>a</sup>:  
Comparison of Data from References 209 and 126

R <sub>2</sub> S	[R <sub>2</sub> S] M	IRRAD		Ref.
		Wavelength nm	ø[U(IV)]	
(C <sub>2</sub> H <sub>5</sub> ) <sub>2</sub> S	0.010	>300	0.20	209
(n-C <sub>3</sub> H <sub>7</sub> ) <sub>2</sub> S	0.010	>300	0.49	209
(n-C <sub>4</sub> H <sub>9</sub> ) <sub>2</sub> S	0.010	>300	0.69	209
(n-C <sub>4</sub> H <sub>9</sub> ) <sub>2</sub> S	0.200	401 ± 20	0.023	126
1,3-dithiane	0.100	401 ± 20	0.011	126
(CH <sub>2</sub> ) <sub>5</sub> S	0.200	401 ± 20	0.067	126
(CH <sub>2</sub> ) <sub>4</sub> S	0.200	401 ± 20	0.037	126

<sup>a</sup>Conditions: ref.209, [U(VI)] (as acetate) = 0.005 M, [H<sub>3</sub>O]<sup>+</sup> = 0.10 M,  
T = 30°C, ([U(VI)] = 0.0075 M for Et<sub>2</sub>S experiment);  
ref. 126, [U(VI)] (as nitrate) = 0.08 M, [HClO<sub>4</sub>] = 0.30 M,  
T = 21°C.



**Table 10.2**      **Quantum Yields for [U(IV)] Formation in the Photo-  
Oxidation of Dialkyl Sulphides (R<sub>2</sub>S):  
Effect of Irradiation Wavelength and Bandwidth**

R	[R <sub>2</sub> S] M	IRRAD	Ø[U(IV)]
		Wavelength nm	
(a) <u>Uranyl Acetate as Oxidant</u> <sup>a,b</sup>			
C <sub>2</sub> H <sub>5</sub>	0.01	401 ± 20	0.039 <sup>b,c</sup>
		>300	0.033 <sup>b,c</sup>
n-C <sub>4</sub> H <sub>9</sub>	0.01	401 ± 20	0.046 <sup>b,c</sup>
		>300	0.036 <sup>b,c</sup>
(b) <u>Uranyl Nitrate as Oxidant</u>			
n-C <sub>4</sub> H <sub>9</sub>	0.01	401 ± 20	0.051 <sup>b,d</sup>
	0.01	>300	0.043 <sup>b,d</sup>
	0.01	401 ± 20	0.019 <sup>c,e</sup>
n-C <sub>3</sub> H <sub>7</sub>	0.01	401 ± 20	0.0215 <sup>c,e</sup>
C <sub>2</sub> H <sub>5</sub>	0.01	401 ± 20	0.025 <sup>c,e</sup>

<sup>a</sup>Under the greater light intensity, the reaction mixture without R<sub>2</sub>S gave small yields of [U(IV)].

<sup>b</sup>[U(VI)] = 0.05 M, medium 3:4 v/v aqueous H<sub>2</sub>SO<sub>4</sub> (0.1 M) - acetone, T = 25°C.

<sup>c</sup>Actinometry with ferrioxalate.

<sup>d</sup>Actinometry by comparison with development of [U(IV)] in a uranyl sulphate (0.0648 M) - ethanol (1.5 M) mixture in aqueous H<sub>2</sub>SO<sub>4</sub> (3.00 M) with an independently determined quantum yield for [U(IV)] of 0.655.

<sup>e</sup>[U(VI)] = 0.08 M, medium 75%:25% MeCN-H<sub>2</sub>O (v/v), [HClO<sub>4</sub>] = 0.1 M, T = 20°C.

discrepancy, but rather there is simply a large difference between the results here and those of reference 209. It has also been noted that the photolysis of uranyl acetate in the absence of  $R_2S$  using 3:4 v/v aqueous  $H_2SO_4$  (0.1 M) - acetone as solvent, with broad band radiation ( $\lambda > 300$  nm), i.e. similar conditions to those used by Sandhu *et al.*, results in a small yield of  $[U(IV)]$ , see Figure 10.1, but this is not produced with normal simple zero-order kinetics (for high light absorbances). This process is associated with the photo-oxidation of the acetate ligands.

To test the question further, we made a comparison of our quantum yields for production of  $[U(IV)]$  from the dialkyl sulphides with those obtained during the photoreduction of ethanol, for which there is a generally agreed figure of ca. 0.6; thus Bell and Billings give  $0.603 \pm 0.037$  at  $25^\circ C$  for 476.5 nm argon ion laser irradiation<sup>115</sup>, Kireeva *et al.* give ca. 0.6 at  $20^\circ C$  for 410 nm radiation but 0.3 for polychromatic light<sup>210</sup>, Zheng *et al.* give a figure of  $0.69 \pm 0.03$  for 441.6 nm radiation using Cd/He laser light<sup>113</sup>. Our figures for  $\phi[U(IV)]$ , with  $\lambda_{irr} = 401$  nm and  $>300$  nm, with  $[EtOH] = 1.5$  M,  $[UO_2]^{2+} = 0.0648$  M,  $[H_2SO_4] = 3.0$  M and  $T = 25^\circ C$  are  $0.65(5) \pm 0.036$  and  $0.77(5) \pm 0.028$  respectively. As can be seen in Figure 10.2, the ratio of relative yields of  $[U(IV)]$  production for di-n-butyl sulphide and ethanol is 0.077:1, which implies a quantum yield for  $[U(IV)]$  in the case of di-n-butyl sulphide of 0.051, in good agreement with a figure of 0.046 given in Table 10.2, obtained using ferrioxalate actinometry. The analogous relative yields using pyrex-filtered light, see Figure 10.2, indicate  $\phi[U(IV)] = 0.043$ .

Figure 10.1      Development of absorbance of U(IV) at 648 nm during broad-band ( $\lambda > 300$  nm) photolysis of  $N_2$ -flushed acidic U(VI) solutions (0.05 M) containing ethanol (1.5 M) and di-n-butyl sulphide (0.01 M).

Media: ethanol experiment, aqueous  $H_2SO_4$  (3 M) containing uranyl sulphate; di-n-butyl sulphide experiment, 3:4 v/v aqueous  $H_2SO_4$  (0.1 M) - acetone containing uranyl acetate. Cells: 5 cm path length.

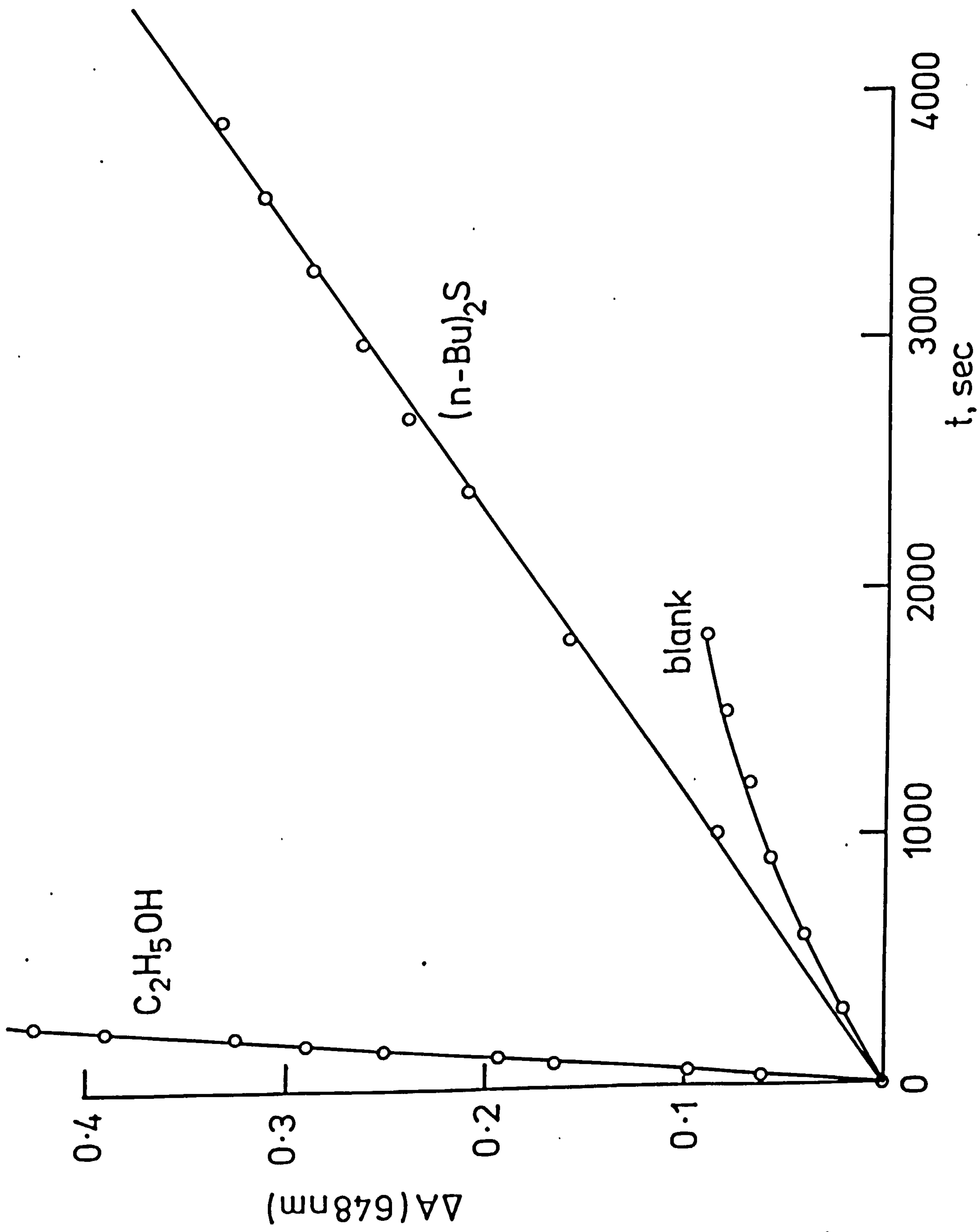
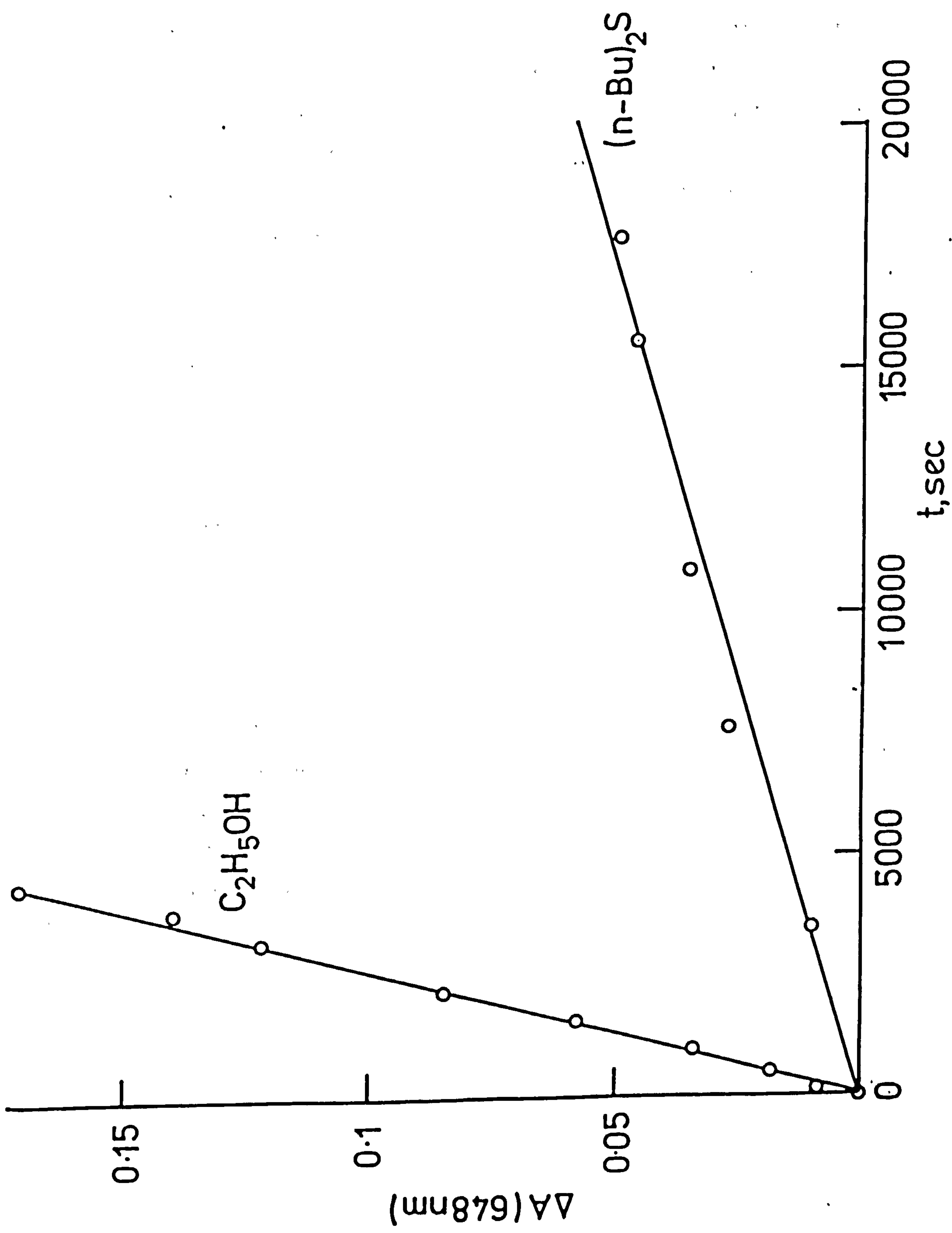


Figure 10.2      Development of absorbance of U(IV) at 648 nm during  
monochromatic ( $401 \pm 20$  nm) photolysis of  $N_2$ -flushed  
acidic U(VI) solutions (0.05 M) containing ethanol (1.5  
M) and di-n-butyl sulphide (0.01 M).

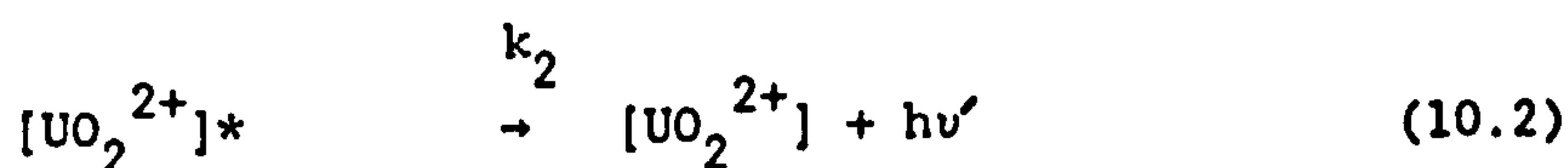
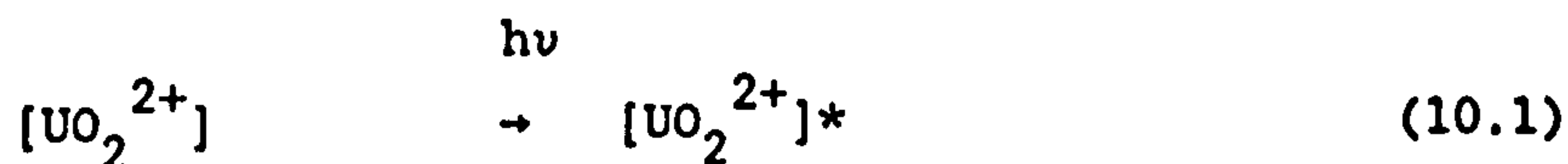
Media and cells are as for Figure 10.1.



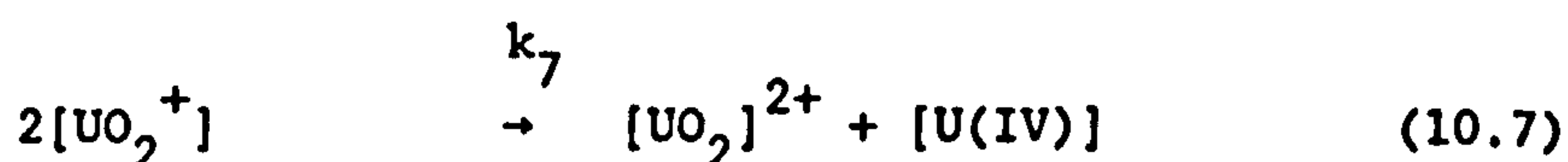
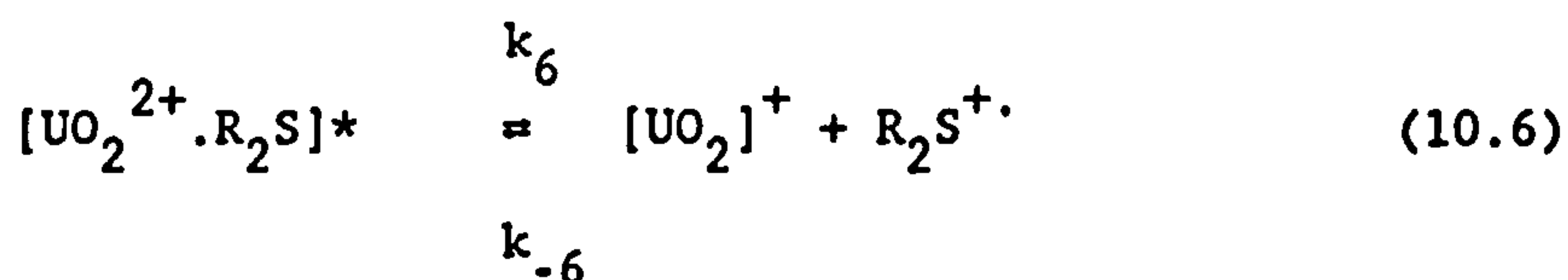
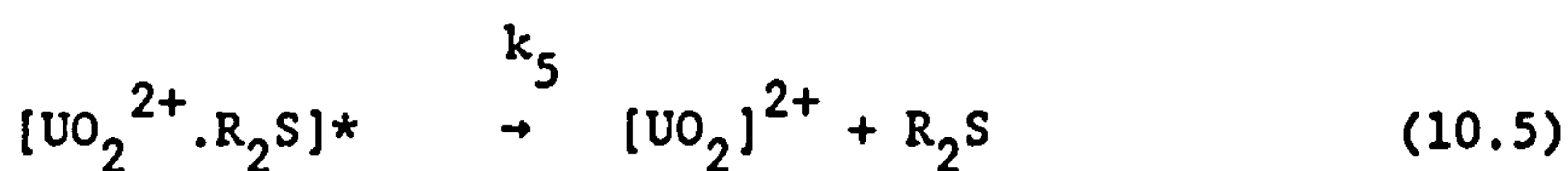
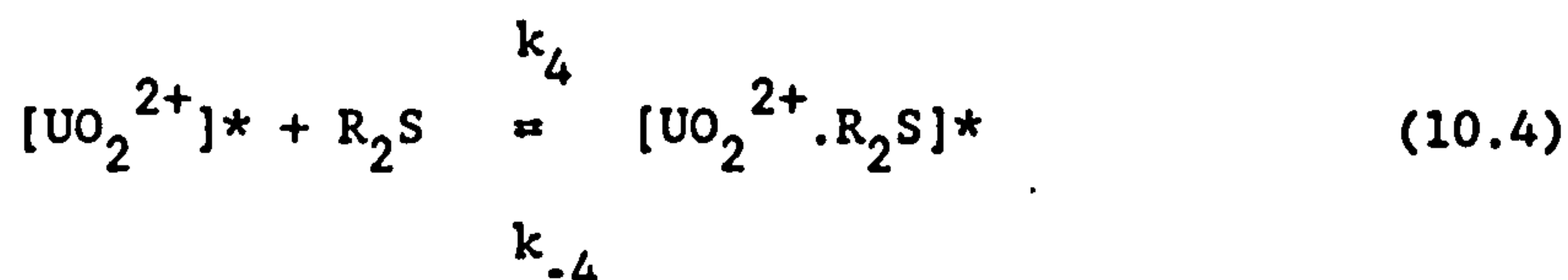
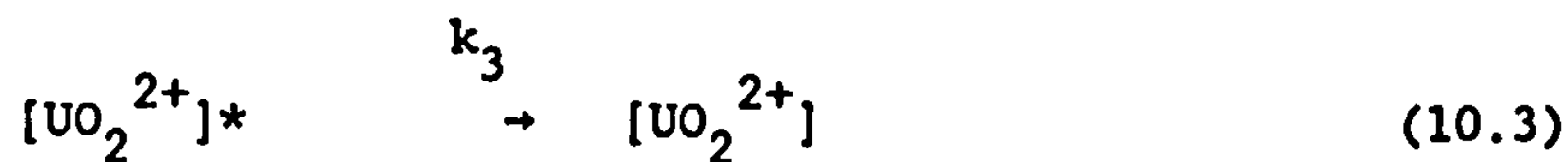
The use of ferrioxalate actinometry for "white light" irradiation is a doubtful procedure as the action spectra of the actinometer and the uranyl solutions need to match exactly. However, an approximate figure of 0.036 for n-Bu<sub>2</sub>S can be arrived at if we use a mean value of 1.20<sup>191</sup> for the quantum efficiency of the ferrioxalate actinometer. From the general consistency of the results, it can be concluded that, for n-Bu<sub>2</sub>S at least, the quantum yield reported by Sandhu, Kohli and Brar<sup>209</sup> is erroneously high.

The quantum yields for [U(IV)] formation for the other dialkyl sulphides investigated in reference 209 have also been measured and the results are summarised in Table 10.2. The values of  $\phi$ [U(IV)] for R = Et and n-Pr are similar to that for R = n-Bu, i.e. much lower than those reported in reference 209 of up to 0.23 and 0.58 for R = Et and n-Pr, respectively.

$\phi$ [U(IV)] for di-n-butyl sulphide, over a wide concentration range has also been measured, see Table 10.3. While  $\phi$ [U(IV)] increases with [n-Bu<sub>2</sub>S], the double reciprocal plot, shown in Figure 10.3, is non-linear. This contrasts with the plot given in reference 209 and is unusual for [U(VI)] photosystems where such linearity is common<sup>211</sup>. The simple kinetic scheme, equations (10-1) to (10-7):







normally operating in these systems does not hold for  $\text{R}_2\text{S}$ , and in particular, the normal practice of regarding step  $k_{-4}$  as negligible is probably incorrect in this case. By application of the steady-state approximation to equations (10.1 to 10.7), and assuming step (10.7) to be very fast, one can derive an expression for  $\emptyset[\text{U(IV)}]$ .

$$\emptyset[\text{UO}_2]^+ = \frac{k_6}{k_5 + k_6 + k_{-6}} \cdot \emptyset[\text{UO}_2^{2+} \cdot \text{R}_2\text{S}]^* \quad (10.8)$$

$$\emptyset[\text{UO}_2^{2+} \cdot \text{R}_2\text{S}]^* = \frac{(k_4 * [\text{UO}_2]^{2+} [\text{R}_2\text{S}])}{*[\text{UO}_2]^{2+} (k_4 [\text{R}_2\text{S}] + k_3 + k_2 + k_{-4} [\text{R}_2\text{S}])} \quad (10.9)$$

$$= \frac{k_4[R_2S]}{k_4[R_2S] + k_{-4}[R_2S] + k_2 + k_3} \quad (10.10)$$

$$\therefore \quad \phi[UO_2]^+ = \frac{k_6}{k_5 + k_6 + k_{-6}} \cdot \frac{k_4[R_2S]}{[R_2S](k_4 + k_{-4}) + k_2 + k_3} \quad (10.11)$$

$$\text{Since} \quad \phi[U(IV)] = \frac{\phi[UO_2]^+}{2}$$

$$\phi[U(IV)] = \frac{0.5 k_6}{k_5 + k_6 + k_{-6}} \cdot \frac{k_4[R_2S]}{[R_2S](k_4 + k_{-4}) + k_2 + k_3} \quad (10.12)$$

If  $k_{-6}$  can be neglected, then equation (10.12) can be simplified and rearranged to give:

$$\frac{1}{\phi[U(IV)]} = 2 + \frac{2k_5}{k_6} \cdot \frac{1 + (k_{-4}[R_2S] + k_2 + k_3)}{(k_4[R_2S])} \quad (10.13)$$

However, only if  $k_{-4}$  is set to zero does the plot of  $\phi[U(IV)]^{-1}$  vs  $[R_2S]^{-1}$  become linear.

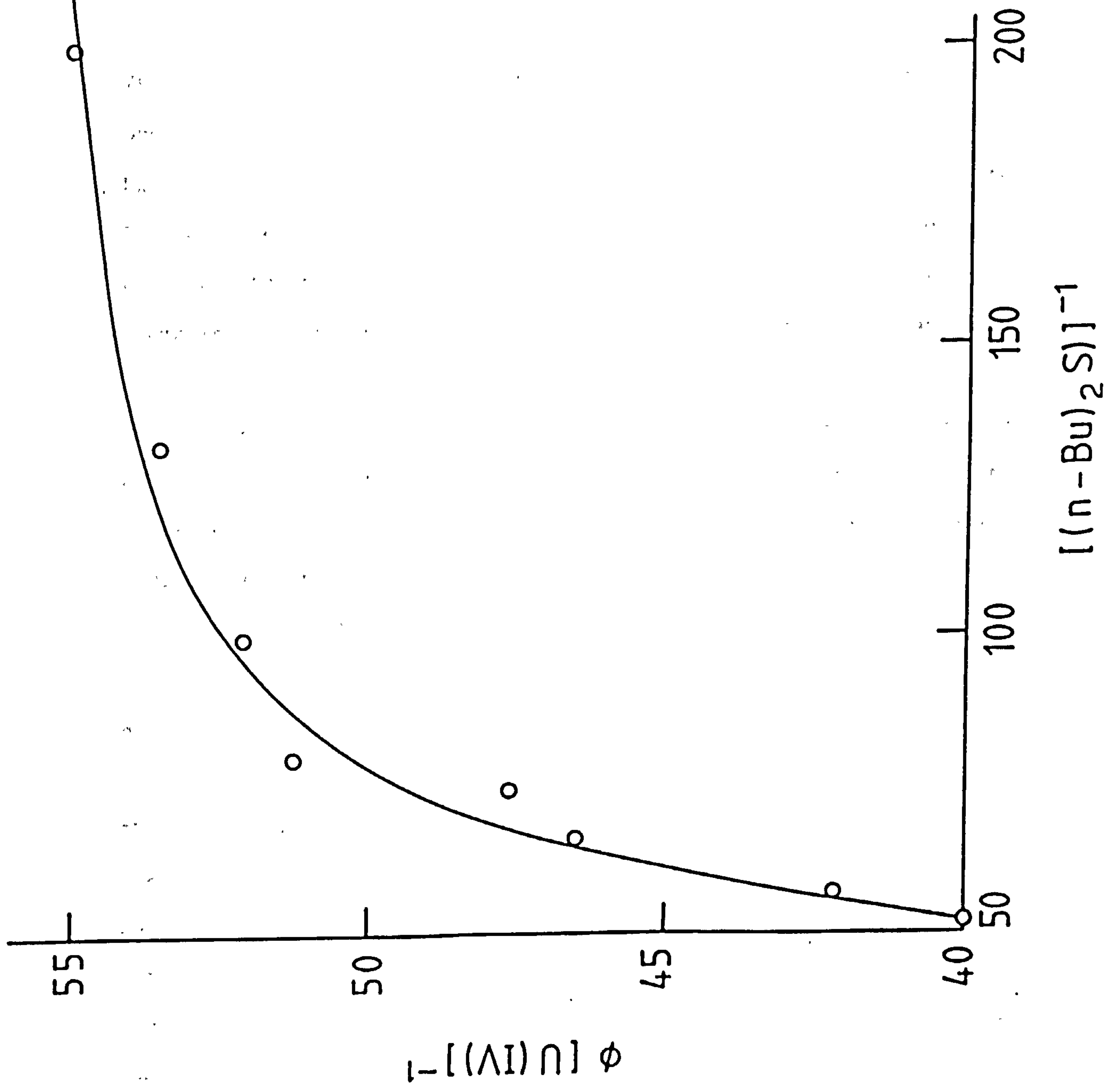
Another point refers to the "second-order rate constants" detailed in reference 209 (Tables 2 and 3). These are not true rate constants but appear to be derived from dividing the pseudo-first-order rate constants for appearance of  $[U(IV)]$  by the  $R_2S$  concentration. The Stern-Volmer constant for quenching of  $[U(VI)]^*$  as the acetate salt by di-n-propyl sulphide is given in reference 209 as  $780 \text{ M}^{-1}$ . The lifetime of  $[U(VI)]^*$ , as the acetate salt, as measured under the conditions adopted by Sandhu et al. is  $3.46 \mu\text{s}$ , which yields  $k_2$  for the second-order rate

Table 10.3      Quantum Yields for [U(IV)] Formation in the Photo-  
Oxidation of Di-n-butyl Sulphides: Effect of  
Substrate Concentration<sup>a</sup>

[n-Bu <sub>2</sub> S] M	ø[U(IV)]
<hr/>	
0.0050	0.0182
0.0075	0.0187
0.0100	0.0192
0.0125	0.0194
0.0133	0.0210
0.0150	0.0215
0.0175	0.0237
0.0190	0.0250
<hr/>	

<sup>a</sup>[UO<sub>2</sub>(NO<sub>3</sub>)<sub>2</sub>] = 0.08 M, [HClO<sub>4</sub>] = 0.1 M, solvent 75%:25% MeCN-H<sub>2</sub>O  
(v/v), λ = 401 ± 20 nm, T = 20°C

Figure 10.3      Double-reciprocal plot for the dependence of the quantum yield of U(IV) production upon concentration of di-n-butyl sulphide.



constants as  $0.225 \times 10^9 \text{ dm}^3 \text{ mol}^{-1} \text{ s}^{-1}$ , which accords roughly (bearing in mind the different [U(VI)] salts employed) with a figure of  $1.41 \pm 0.06 \times 10^9 \text{ dm}^3 \text{ mol}^{-1} \text{ s}^{-1}$  obtained directly from laser flash photolysis measurements for di-n-butyl sulphide made by using the nitrate salt (see below). It has no relation to the figure of  $1.240 \text{ M}^{-1} \text{ min}^{-1}$  given for di-n-propyl sulphide in Table 3 of reference 209.

The absolute quenching rate constants of excited [U(VI)] nitrate by  $\text{R}_2\text{S}$  (R = Me, Et, n-Pr, n-Bu) were obtained using 353 nm laser flash photolysis employing the most photoinert medium capable of dissolving  $\text{R}_2\text{S}$ , namely 75%:25% MeCN- $\text{H}_2\text{O}$  (v/v). A typical plot is shown in Figure 10.4 and the results are summarised in Table 10.4. The Stern-Volmer constants for quenching of  $*[\text{UO}_2]^{2+}$  by  $\text{R}_2\text{S}$  in the same medium are summarised in Table 10.5, while a typical plot is given in Figure 10.5.

The Stern-Volmer constants  $K^{\text{SV}}$  are equal to  $k_q \tau_0$  ( $k_q$  is the quenching constant and  $\tau_0$  is the lifetime of  $*[\text{UO}_2]^{2+}$  under the conditions of the experiment in the absence of quencher). For the solvent system MeCN- $\text{H}_2\text{O}$ ,  $\tau_0$  was determined as  $4.30 \mu\text{s}$ , and the resulting calculated values of  $k_q$  using the above relationship are given in Table 10.5. These calculated values of  $k_q$  uniformly exceed those measured by laser flash photolysis, indicating some contribution from static quenching.

The considerably lower values of  $K^{\text{SV}}$  given in reference 209 originate from two possible causes, i.e. shorter lifetimes  $\tau_0$  and lower kinetic quenching constants,  $k_2$ . The values of  $\tau_0$  for [U(VI)] acetate in 0.1 M sulphuric acid has been determined as  $3.46 \mu\text{s}$ , which implies a second-order quenching rate constant of  $0.225 \times 10^9 \text{ dm}^3 \text{ mol}^{-1} \text{ s}^{-1}$ , i.e. rather lower than the value in Table 10.5. Accordingly the  $K^{\text{SV}}$  value for the

Table 10.4      Absolute Second Order Constants for the Quenching of  
Uranyl Luminescence by Dialkyl Sulphides (R<sub>2</sub>S)<sup>a</sup> by  
Laser Flash Photolysis<sup>a</sup>

R	$10^{-9}k_2, \text{ dm}^3 \text{ mol}^{-1} \text{ s}^{-1}$
Me	4.11 ± 0.11
Et	1.68 ± 0.09
n-Pr	1.16 ± 0.03 <sup>b</sup>
n-Bu	0.956 ± 0.054

<sup>a</sup>[UO<sub>2</sub>(NO<sub>3</sub>)<sub>2</sub>] = 0.1 M, [HClO<sub>4</sub>] = 0.1 M, solvent 75%:25% MeCN-H<sub>2</sub>O

<sup>b</sup>Reference 126 gives  $(1.41 \pm 0.06) \times 10^9 \text{ dm}^3 \text{ mol}^{-1} \text{ s}^{-1}$  in acetone-water medium



Table 10.5      Stern-Volmer Constants for the Quenching of Uranyl  
Luminescence by Dialkyl Sulphides (R<sub>2</sub>S) Obtained  
by Using Fluorimetry<sup>a</sup>

R	$K^{sv}, M^{-1}$	$10^{-9}k_2^b, dm^3 mol^{-1} s^{-1}$
Me	$(3.72 \pm 0.13) \times 10^4$	8.65
Et	$(3.24 \pm 0.07) \times 10^{4c}$	7.53
n-Pr	$(1.105 \pm 0.11) \times 10^{4d}$	2.57
n-Bu	$(6.74 \pm 0.09) \times 10^3$	1.57

<sup>a</sup>[UO<sub>2</sub>(NO<sub>3</sub>)<sub>2</sub>] = 0.1 M, [HClO<sub>4</sub>] = 0.1 M, solvent 75%:25% MeCN-H<sub>2</sub>O,  $\lambda_{exc}$  = 410 ± 10 nm,  $\lambda_{em}$  = 510 ± 10 nm.

<sup>b</sup>Taking  $\tau_0$  = 4.30  $\mu s$

<sup>c</sup>Reference 209 gives  $1.367 \times 10^3 M^{-1}$  in acetone-water, which, taking  $\tau_0$  = 3.45  $\mu s$ , yields  $k_2 = 0.396 \times 10^9 dm^3 mol^{-1} s^{-1}$ .

<sup>d</sup>Reference 209 gives  $7.80 \times 10^2 M^{-1}$  in acetone-water, which, taking  $\tau_0$  = 3.46  $\mu s$ , yields  $k_2 = 0.225 \times 10^9 dm^3 mol^{-1} s^{-1}$ .

Figure 10.4      Dependence of reciprocal luminescence lifetime ( $k_1 - 1/\tau_1$ ) of uranyl ion upon the concentration of di-n-propyl sulphide.

$[\text{UO}_2(\text{NO}_3)_2] = 0.1 \text{ M}; [\text{HClO}_4] = 0.1 \text{ M}, \text{ solvent: } 75\%:25\% \text{ MeCN-H}_2\text{O}.$

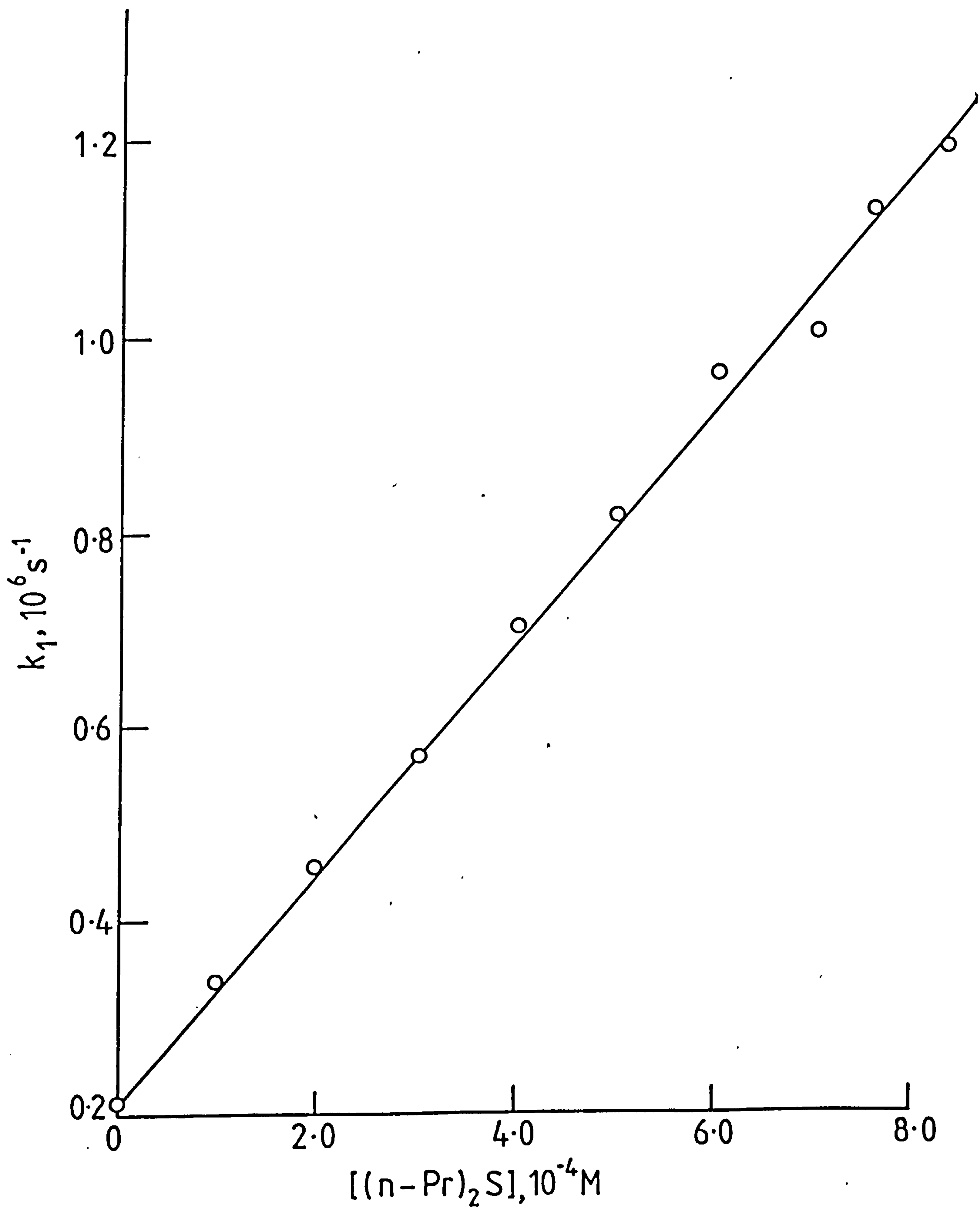
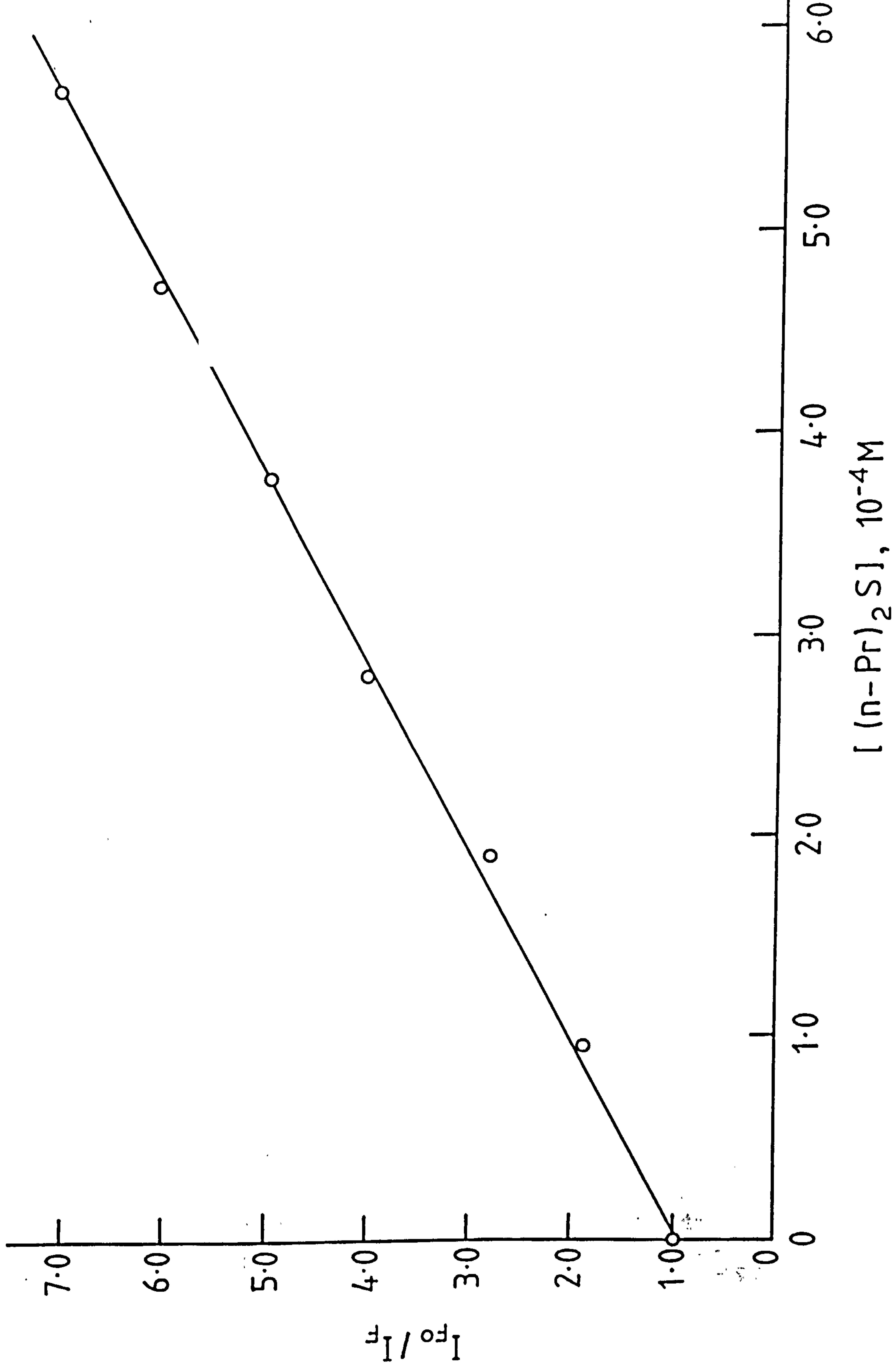


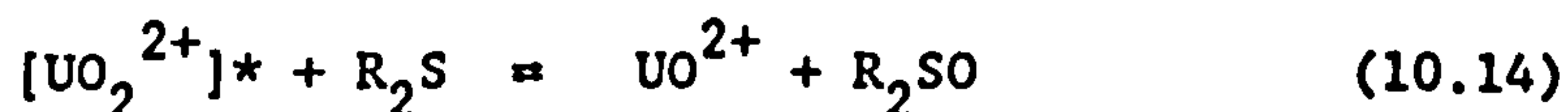
Figure 10.5 Stern-Volmer plot for the quenching of the luminescence intensity of uranyl ion by di-n-propyl sulphide.

$[\text{UO}_2(\text{NO}_3)_2] = 0.05 \text{ M}$ ;  $[\text{HClO}_4] = 0.1 \text{ M}$ ;  $\lambda_{\text{ex}} = 410 \pm 10$  nm;  $\lambda_{\text{em}} = 510 \pm 10$  nm, solvent: 75%:25% MeCN- $\text{H}_2\text{O}$ .



quenching of excited [U(VI)] acetate (0.02 M) in dilute H<sub>2</sub>SO<sub>4</sub> (0.1 M) in a water-acetone medium (3:4 v/v) by di-n-butyl sulphide has been measured as  $1402 \pm 20 \text{ M}^{-1}$ , in fair agreement with the figures for other R<sub>2</sub>S compounds given in reference 209, i.e. the use of acetate salt gives ca. factor of 5 reduction in K<sup>SV</sup> compared with the value for the nitrate salt. Finally, the absolute second-order quenching rate constants for the quenching of [U(VI)]\* in this same system has been measured as  $(3.10 \pm 0.53) \times 10^8 \text{ dm}^3 \text{ mol}^{-1} \text{ s}^{-1}$ , i.e. the excited [U(VI)] acetate is only one-third as reactive as excited nitrate salt (cf. Table 10.4).

Concentrating now on the photo-oxidation mechanisms, Sandhu *et al.*<sup>209</sup> propose an oxygen-atom transfer from uranyl ion to the dialkyl sulphide which results in the formation of sulphoxide.

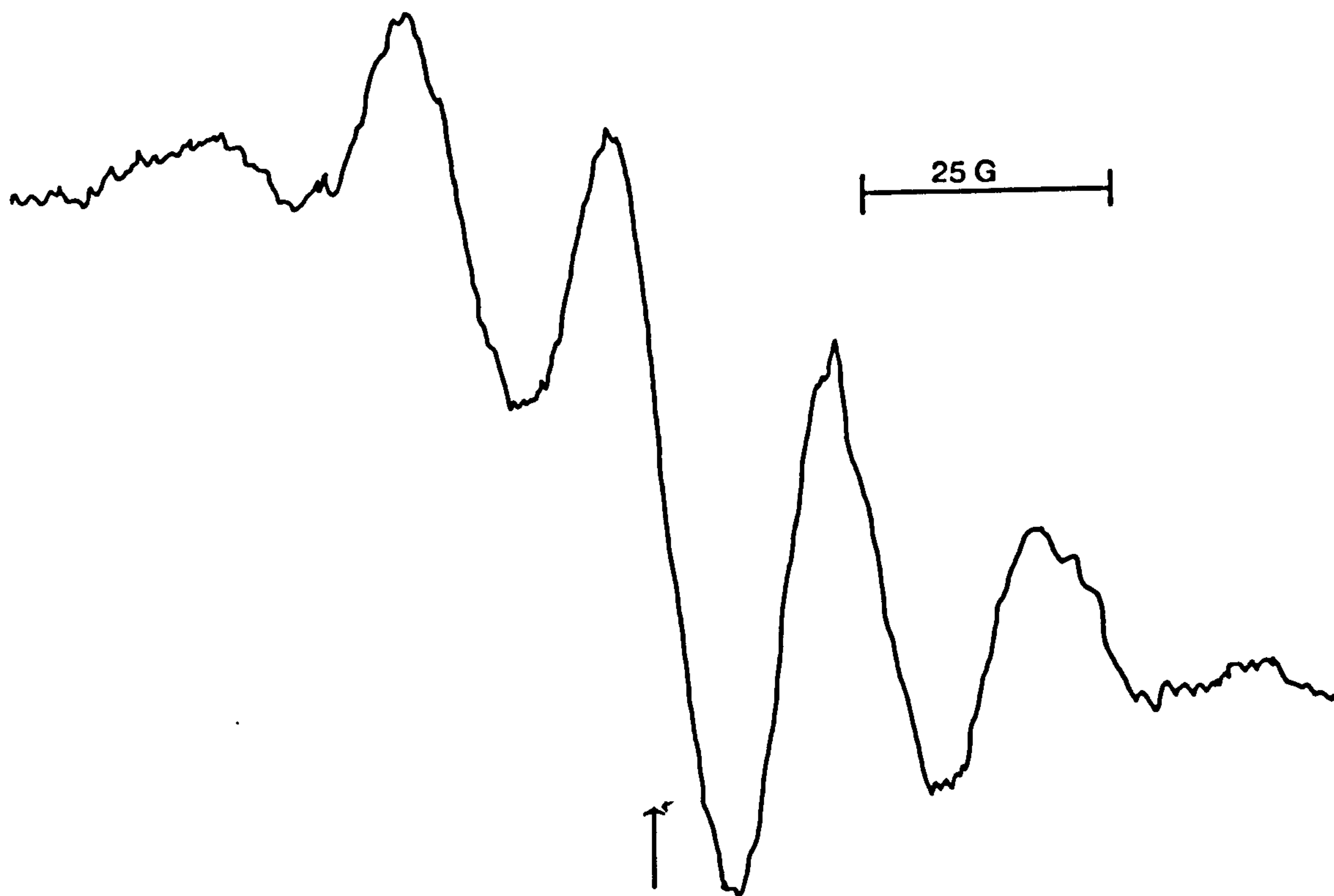


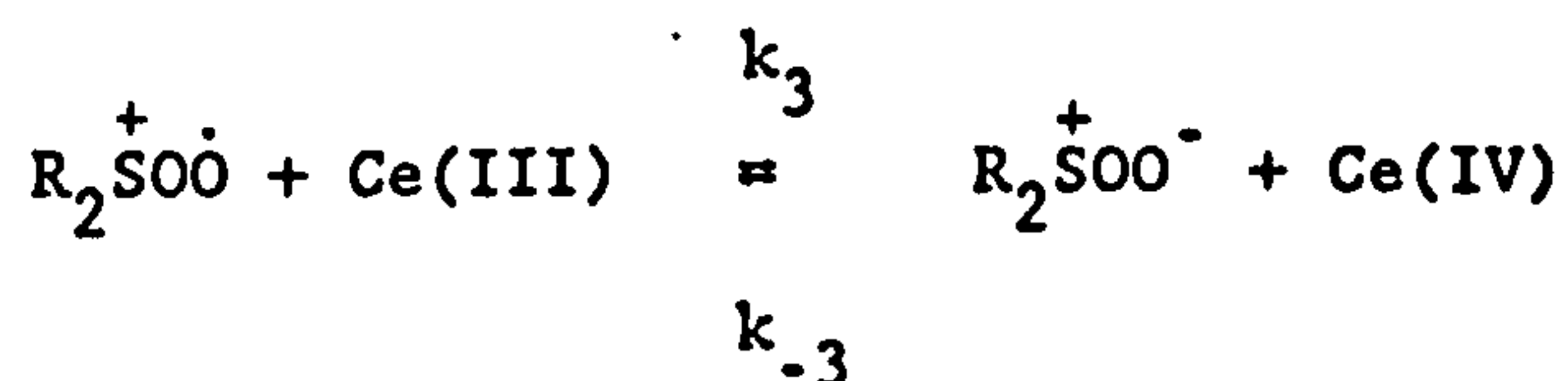
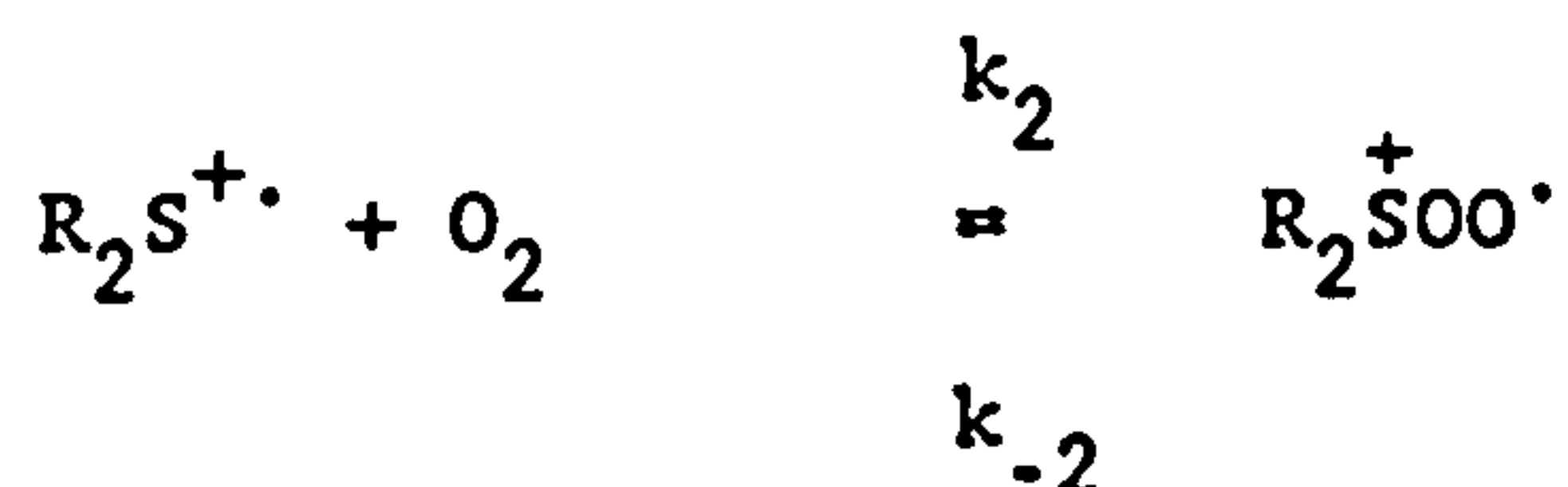
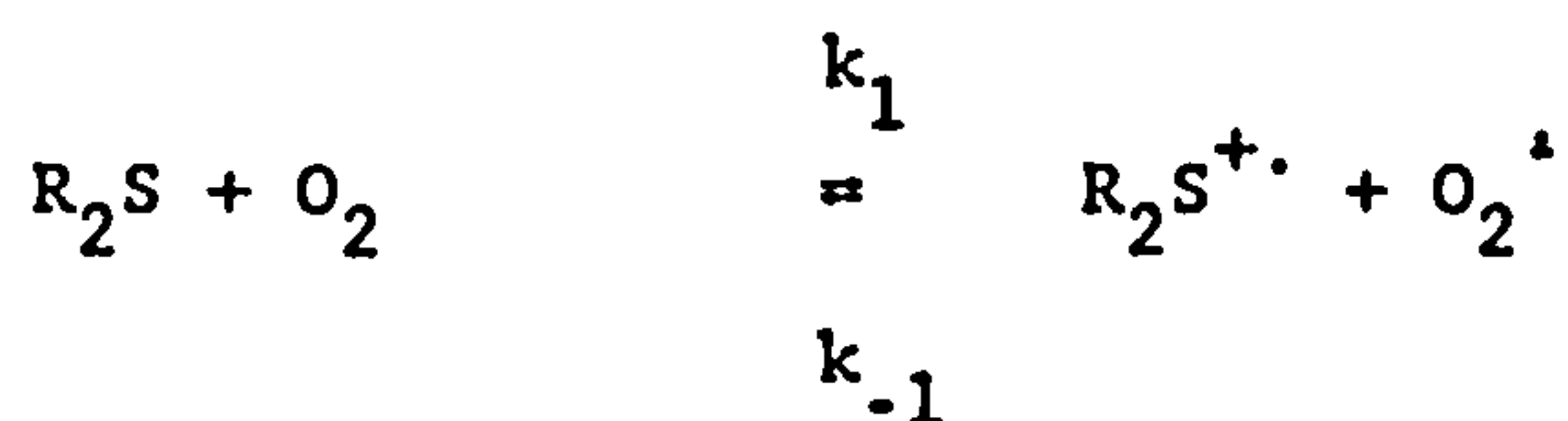
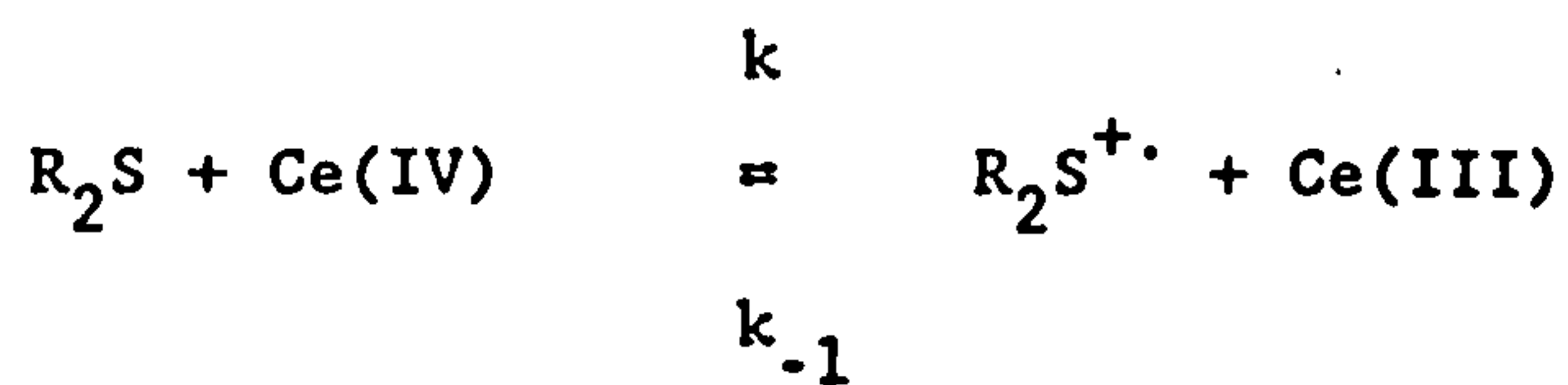
However, ESR measurements on the photolysis of [UO<sub>2</sub>]<sup>2+</sup> in the presence of organosulphur compounds, has been shown to result in the formation of a semi-oxidised substrate with a sulphur-centred singly occupied molecular orbital<sup>126,212</sup>, see chapter 9 Figures 9.12 and 9.13. The photolysis of uranyl perchlorate in the presence of diethyl sulphide results in a 5 line second derivative ESR spectrum, shown in Figure 10.6, with  $a(\text{H})_{\text{av}} = 21 \text{ G}$  and  $g = 2.0053$ . By comparison with spectral data both in solution and the solid state<sup>126,207</sup>, this radical is regarded as being (C<sub>2</sub>H<sub>5</sub>)<sub>2</sub>S<sup>+</sup>.

This radical mechanism accords with a recent study on the catalysed auto-oxidation of thioethers to sulphoxides by Ce(IV) salts<sup>213</sup>:

Figure 10.6      ESR spectrum (second derivative) produced at 77 K on  
photolysis of diethyl sulphide.







## 10.2 Concluding Remarks

Clearly there are some unusual features associated with the quenching of  $^*[\text{UO}_2]^{2+}$  by  $\text{R}_2\text{S}$ ; thus a large kinetic quenching rate constant, nearing the diffusion control limit of  $\text{ca. } 1.8 \times 10^{10} \text{ dm}^3 \text{ mol}^{-1} \text{ s}^{-1}$  is not matched by a large photoredox quantum yield. This implies that the vast majority of exciplexes  $[\text{UO}_2^{2+} \cdot \text{R}_2\text{S}]^*$  decay by nonchemical pathways, particularly those described by  $k_5$  and  $k_{-4}$ , reactions 10.5 and 10.4 respectively.

In summary, while the quantum yields for  $[\text{U(IV)}]$  production in reference 209 are erroneously high, we support values of  $K^{\text{SV}}$  given in reference 209. It has also been noted that there is a marked difference in kinetic reactivity towards  $\text{R}_2\text{S}$  between excited uranium (VI) nitrate and acetate.

## Chapter 11

### Results

#### A Study of the Photochemistry of Octacyanotungstate (IV) and (V) Ions

### 11.1 Introduction

The results presented in this Chapter on the photochemistry of  $[\text{W}(\text{CN})_8]^{4-}$  and  $[\text{W}(\text{CN})_8]^{3-}$  ions are divided into two parts. The first section re-examines the quantum yields of  $[\text{W}(\text{CN})_8]^{4-}$  formation produced during the photolysis of  $[\text{W}(\text{CN})_8]^{3-}$  ion in aqueous solution. The second section investigates and characterises a number of new W(V) species produced on photolysis of  $[\text{W}(\text{CN})_8]^{4-}$  and  $[\text{W}(\text{CN})_8]^{3-}$  in aqueous solution. ESR, UV-vis and IR spectroscopy are employed in the characterisation of these new tungsten-cyanide complexes.

### 11.2 Quantum yields of $[\text{W}(\text{CN})_8]^{4-}$ Formation in Aqueous Solution

Previously reported values of the quantum yield of  $[\text{W}(\text{CN})_8]^{4-}$  formation, produced during irradiation into the C-T band of aqueous  $[\text{W}(\text{CN})_8]^{3-}$ , are vastly different, the quoted figures being  $1.60^{171}$  and  $0.81^{176}$ . Measurement of the quantum yields under our experimental conditions produce values which are in close agreement with those obtained by Samotus *et al.*<sup>176</sup>.

Potassium octacyanotungstate (V) was photolysed in conventional aqueous buffer solutions which were prepared as follows: pH's 1.96, HCl + KCl; 4.00,  $\text{KHC}_8\text{H}_4\text{O}_4$  + HCl; 7.00,  $\text{KH}_2\text{PO}_4$  + KOH; 9.20,  $\text{Na}_2\text{B}_4\text{O}_7$  + KOH. In all quantum yield experiments, 0.01 M solutions of  $\text{K}_3[\text{W}(\text{CN})_8]$  were used after being bubbled with argon for 15 minutes. The freshly prepared solutions were photolysed in a 1 cm pathlength quartz cell with light from a 200 W medium pressure Xe/Hg lamp filtered through a 365 nm Balzer metal interference filter. To avoid secondary photolysis of the  $[\text{W}(\text{CN})_8]^{4-}$  formed irradiation times did not exceed 10 minutes. The formation of  $[\text{W}(\text{CN})_8]^{4-}$  with respect to time, depicted in Figure 11.1,

Figure 11.1      Development of absorbance of  $[\text{W}(\text{CN})_8]^{4-}$  at 430 nm during  
365 nm photolysis of  $\text{N}_2$ -flushed  $[\text{W}(\text{CN})_8]^{3-}$  solution  
(0.01 M) at pH 7.00.

was monitored spectrophotometrically at 430 nm ( $\epsilon_{430} = 106.5$  for  $[\text{W}(\text{CN})_8]^{4-}$  and  $\epsilon_{430} \approx 0$  for  $[\text{W}(\text{CN})_8]^{3-}$ . The increase in OD at 430 nm occurring upon photolysis of  $[\text{W}(\text{CN})_8]^{3-}$  was measured immediately after interrupting the exposure, and also after 1 hour storage in the dark to allow completion of any thermal reactions. Quantum yield calculations were performed using equation (7.3) in Chapter 7, and three quantum yields were measured at each pH value to obtain a mean figure.

### 11.3 Discussion

The quantum yield values for  $[\text{W}(\text{CN})_8]^{4-}$  formation over the pH range 1.96-9.20, are presented in Table 11.1. Examination of these figures reveals that the initial quantum yields,  $\phi_i$ , are virtually constant over the experimental pH range, and equal to a mean value of 0.770. For pH values of 7.00 and below no detectable dark reaction was observed; however, at pH 9.20 a thermal reaction was apparent, which was complete in ca. 1 hour, giving a final quantum yield,  $\phi_f$ , of 2.03, see Figure 11.2. The final quantum yields for alkaline solutions are greater than unity due to the secondary photolysis of alkaline  $[\text{W}(\text{CN})_8]^{4-}$ , reaction (11.1), and the thermal reaction of  $[\text{W}(\text{CN})_8]^{3-}$  with  $\text{CN}^-$  leading to the formation of  $[\text{W}(\text{CN})_8]^{4-}$ , reaction (11.2).

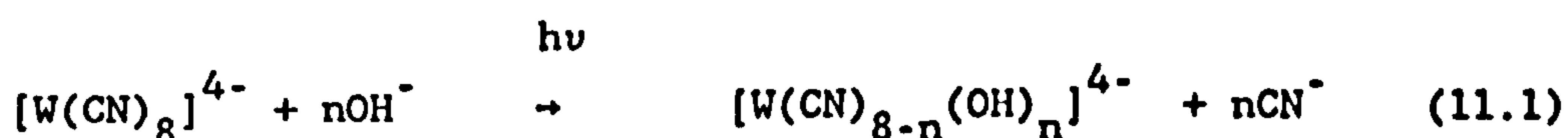


Table 11.1      Quantum Yields of  $[\text{W}(\text{CN})_8]^{4-}$  Formation as a  
Function of pH

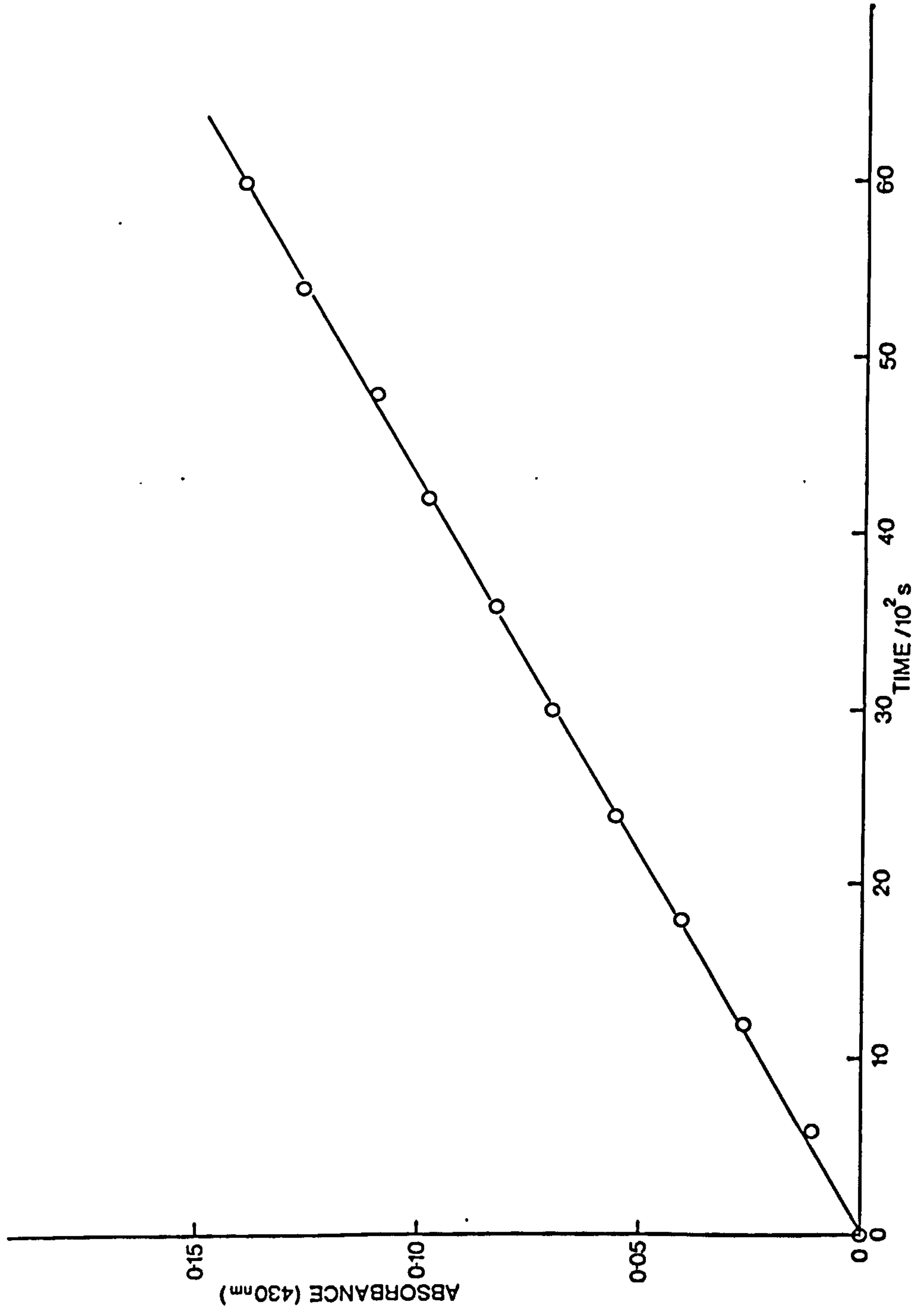
pH	$\phi_1$	$\phi_1$ (mean)
1.96	0.770, 0.770, 0.750	0.760
4.00	0.730, 0.730, 0.740	0.735
5.73 <sup>a</sup>	0.735, 0.740, 0.731	0.735
7.00	0.798, 0.810, 0.796	0.800
9.20	0.825, 0.830, 0.811	0.822

<sup>a</sup>Natural pH of aqueous  $[\text{W}(\text{CN})_8]^{3-}$  (0.01 M) solution.  
 $[\text{W}(\text{CN})_8]^{3-}$  = 0.01 M.  
 Formation of  $[\text{W}(\text{CN})_8]^{4-}$  monitored at 430 nm.  
 Solutions argon-bubbled for 15 minutes.  
 T = 20 ± 0.5°C.



Figure 11.2      Development of absorbance of  $[\text{W}(\text{CN})_8]^{4-}$  at 430 nm after storage in the dark for 1 hr, plotted against irradiation time.

$[\text{W}(\text{CN})_8]^{3-} = 0.01 \text{ M}$ , pH 9.2.



#### 11.4 Low Temperature UV-visible Spectra

The photolysis of  $K_3[W(CN)_8]$  (0.01 M) in a variety of solvents (aqueous 12 M LiCl, PVA, 1:1  $H_2O$ /glycerol, 1:1 MeOH/ $H_2O$ ), at 77 K using both pyrex- and 365 nm-filtered light from a 125 W Hg arc lamp, results in the initially colourless solid turning yellow-brown. A UV-visible spectrum at 77 K, of the photolysed solid results in a decrease of the absorption band due to  $[W(CN)_8]^{3-}$  at 358 nm, and in the development of a new band at ca. 410 nm, as shown in Figure 11.3. Warming up the photolysed solids to room temperature results in a dramatic change in the visible spectrum, which is dependent upon the composition of the surrounding medium. The results of these spectral changes are summarised in Table 11.2. The presence of oxygen in solution prior to photolysis at 77 K produced no significant changes in the UV-visible spectra, compared with the argon-flushed solutions.

The photolysis of  $K_4[W(CN)_8]$  at 77 K in identical solvents to those used above with  $K_3[W(CN)_8]$ , produced no change in the absorption spectrum. The warming up of the frozen solutions to 293 K also did not result in any spectral changes. It can be concluded from these results that the intermediate species trapped at 77 K, characterised by an absorption band at 410 nm, is not as a result of the formation of any photoproduct derived from  $[W(CN)_8]^{4-}$ .

#### 11.5 ESR Studies of the Photolysis of $[W(CN)_8]^{3-}$ Ion at 77 K

Irradiation of  $[W(CN)_8]^{3-}$  ions (0.01 M) in the c.t.t.m. band (355 nm) at 77 K induces a gradual decrease of the ESR absorption due to  $[W(CN)_8]^{3-}$  <sup>216</sup>, owing to the formation of diamagnetic W(IV), reaction (11.3):

Table 11.2      Photolysis of  $W(CN)_8^{3-}$  at 77 K-Absorption Spectra

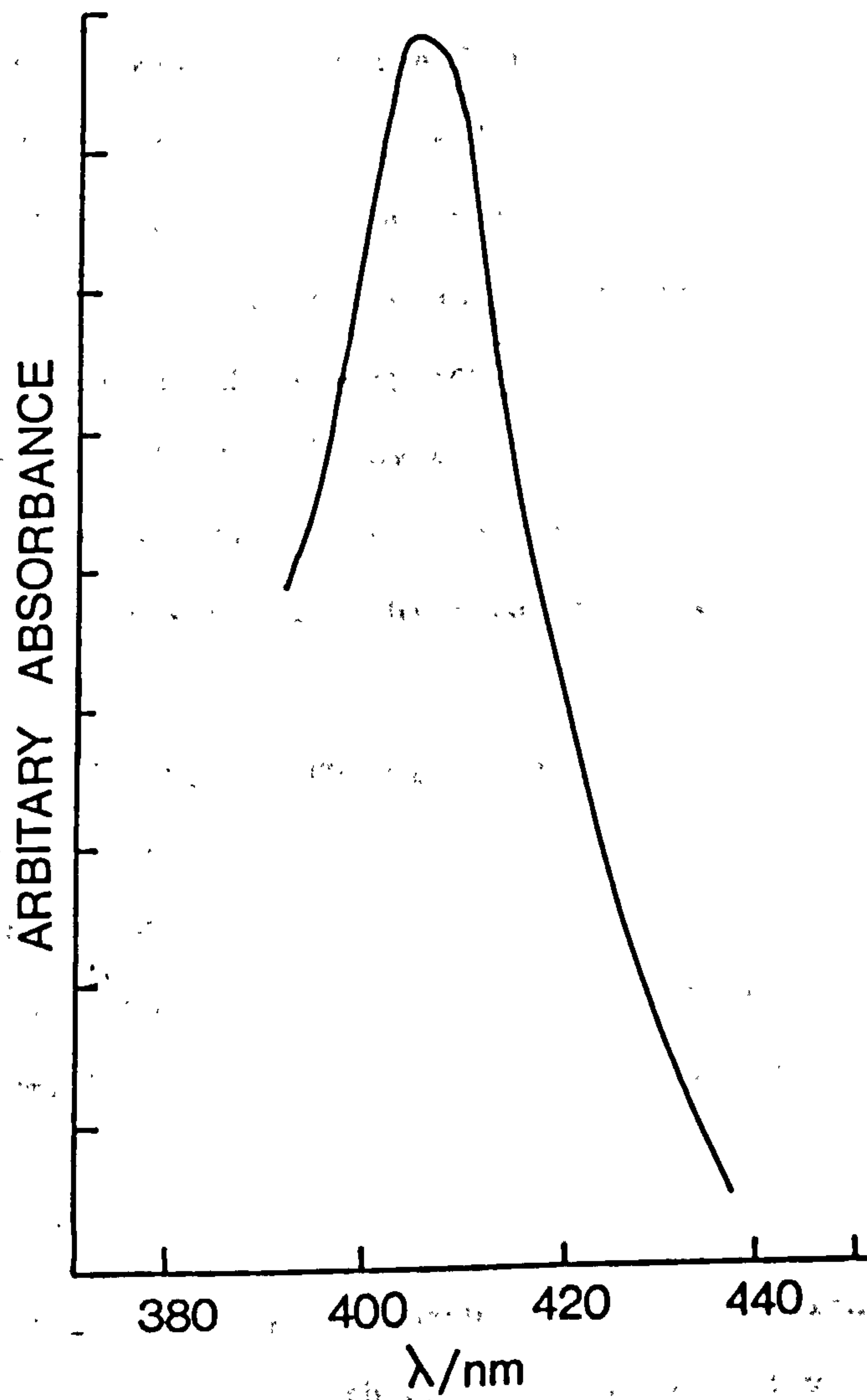
Matrix <sup>a</sup>	Conditions <sup>b</sup>	UV-vis Spectrum at 77 K	UV-vis Spectrum of solution after warming to room temperature <sup>c</sup>
Aqueous 12 M LiCl	$\lambda_{irr} > 300$ nm	Yellow-brown solid $\lambda = 410$ nm	Violet soln. $\lambda$ nm 241, 363, 445, 500, 570
1:1 MeOH/H <sub>2</sub> O	$\lambda_{irr} > 300$ nm	"      "	Magenta soln $\lambda$ 360, 510 (sh), 537
1:1 Glycerol/H <sub>2</sub> O	$\lambda_{irr} > 300$ nm	"      "	Magenta soln $\lambda$ 537, 570 (sh)
PVA	$\lambda_{irr}$ 330-390 nm	Yellow-brown film $\lambda$ nm = 410 (sh) 520 nm (vw)	Brown-magenta film $\lambda$ nm 510, 570 Film dissolved in H <sub>2</sub> O to give magenta soln. $\lambda$ nm 535, 570 (sh)

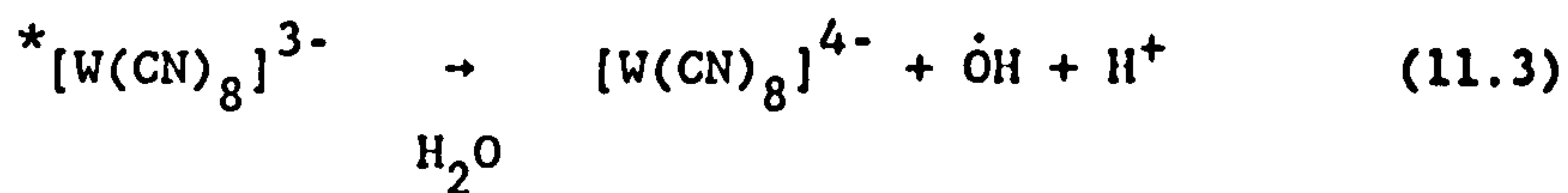
<sup>a</sup>Ar bubbled for 15 mins prior to photolysis at 77 K

<sup>b</sup> $[W(CN)_8]^{3-} = 0.01$  M

<sup>c</sup>Warmed to 293 K under a nitrogen atmosphere.

Figure 11.3      Absorption spectrum of  $[\text{W}(\text{CN})_8]^{3-}$  in 12 M aqueous LiCl  
at 77 K, photolysed  $\lambda > 300$  nm.





This coincides with the formation of new paramagnetic photoproducts containing W(V), principally of the same origin despite the wide variation in the character of the solvent medium, see Table 11.3.

When  $[W(CN)_8]^{3-}$  was ca. one-third destroyed, it was found that there was ca. 10% conversion into the form of an axially symmetric species, denoted species I, with  $g_1 = 1.917-1.919$  and  $g_{11} = 2.012-2.017$ , e.g. Figure 11.4 for a solution in 1:1  $H_2O$ /glycerol. After warming to the melting point of the solid and recooling to 77 K there was a sudden decrease in the ESR absorption due to  $[W(CN)_8]^{3-}$ , probably due to reduction to  $[W(CN)_8]^{4-}$  by a solvent-derived radical. Two new species (denoted II and III) were also formed at the same time. Species II is completely anisotropic, while for species III only  $g_1$  was resolved.

#### 11.5.1 ESR Study of Photolysis of $[W(CN)_8]^{3-}$ Ions at Room Temperature

The results for the photolysis of  $[W(CN)_8]^{3-}$  in solution at room temperature are summarised in Table 11.4. Photolysis of  $[W(CN)_8]^{3-}$  in either aqueous (pH = 2.0) or aqueous-methanol solution (1:1), results in the formation of a single W(V) photoproduct with  $\langle g \rangle = 1.9456$  and 1.9426 respectively.

Freezing the photolysed aqueous-methanol solution to 77 K results in an anisotropic spectrum with  $g_1 = 2.0241$ ,  $g_2 = 1.955$  and  $g_3 = 1.9141$ . These results are suggestive of the presence of species II.





Table 11.4      Summary of ESR Data for the Photolysis of  $[\text{W}(\text{CN})_8]^{3-}$  ions at 293 K

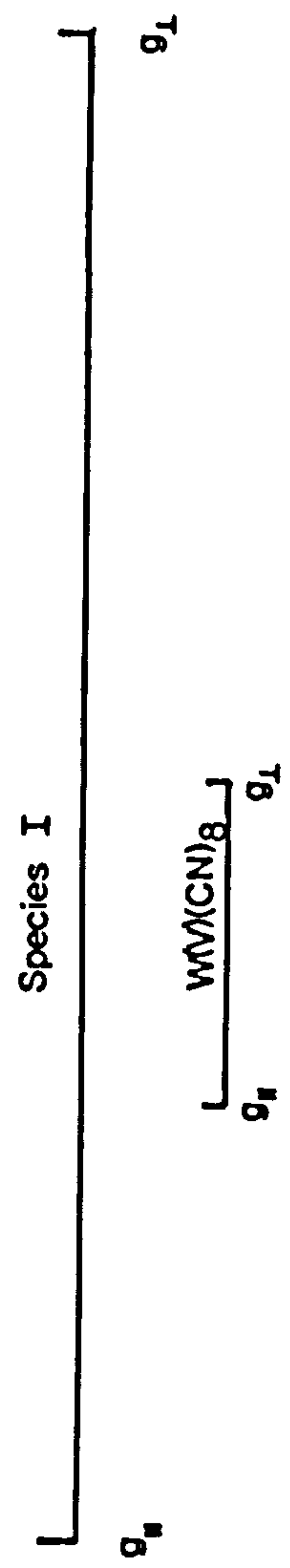
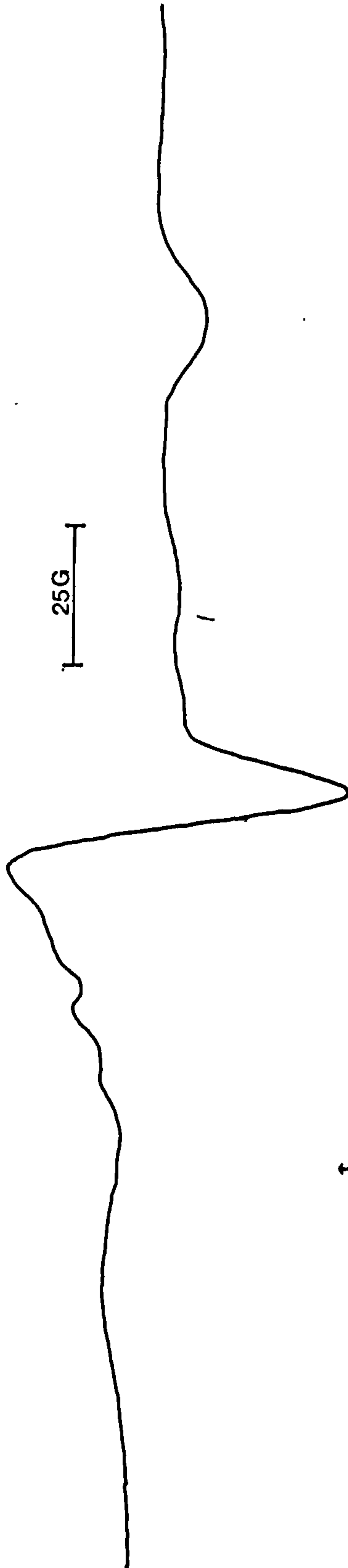
Solvent	Conditions	$[\text{W}(\text{CN})_8]^{3-}$	Species II	Frozen to 77 K
$\text{H}_2\text{O}$	unphotolysed	$\langle g \rangle - 1.9705$ $\langle A \rangle - 54.5 \text{ G}$		
$\text{H}_2\text{O}$	$\lambda_{\text{irr}} 365 \text{ nm}$ $\text{pH} - 2.0$	$\langle g \rangle - 1.9705$ $\langle A \rangle - 54.4 \text{ G}$	$\langle g \rangle - 1.9456$ $\langle A \rangle - 59 \text{ G}$	
1:1 $\text{H}_2\text{O}/\text{MeOH}$	$\lambda_{\text{irr}} 365 \text{ nm}$	$\langle g \rangle - 1.9667$ $\langle A \rangle - 56 \text{ G}$	$\langle g \rangle - 1.9426$	$g_3 - 2.0241$ $g_2 - 1.9547$ $g_1 - 1.9278$
PVA	$\lambda_{\text{irr}} 365 \text{ nm}$	$\langle g \rangle - 1.9703^\dagger$		
5:1 $\text{MeCN}/\text{Benzene}$	$\lambda_{\text{irr}} 365 \text{ nm}$ $(\text{Ph}_4)_4[\text{W}(\text{CN})_8]$ $+ \text{ND}^a$	$\langle g \rangle - 1.9705$	$\langle g \rangle - 1.9466^\ddagger$	

<sup>a</sup>Nitrosodurene

<sup>†</sup>No W(V) Photoproducts detected

<sup>‡</sup>Spin-adduct detected:  $a(\text{N}) - 9.59 \text{ G}$

Figure 11.4      ESR spectrum produced on photolysis of  $[\text{W}(\text{CN})_8]^{3-}$  at 77  
K in 1:1  $\text{H}_2\text{O}$ /glycerol.

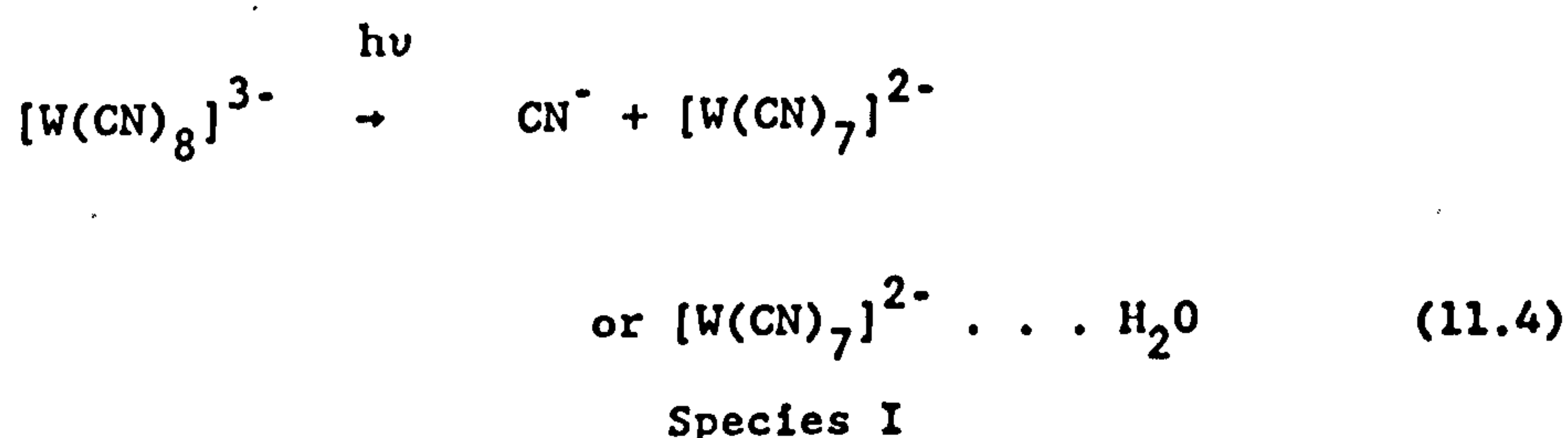


However, photolysis of  $[\text{W}(\text{CN})_8]^{3-}$  in PVA at 293 K results in a steady decrease of the W(V) signal with no other paramagnetic photoproducts being observed.

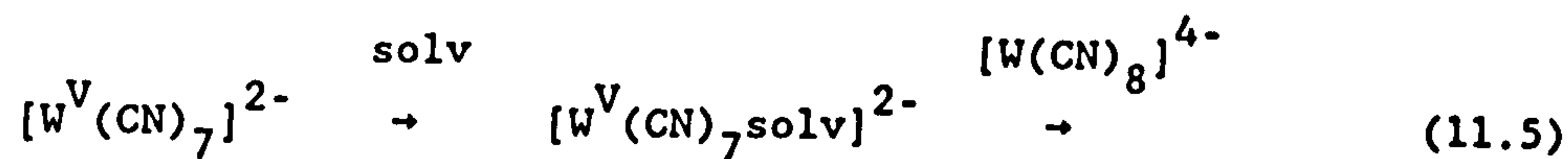
#### 11.5.2 Assignments for Species I-III

The photolysis of  $[\text{W}(\text{CN})_8]^{3-}$  ion at 77 K in a wide variety of solvents leads primarily to species I which is axially symmetric with  $g_{av} = 1.948-1.951$ . On warming and refreezing to 77 K, this is converted into species II and III displaying full anisotropy with  $g_{av} = 1.961-1.965$  and  $g_{\perp} = 1.889-1.895$  respectively.

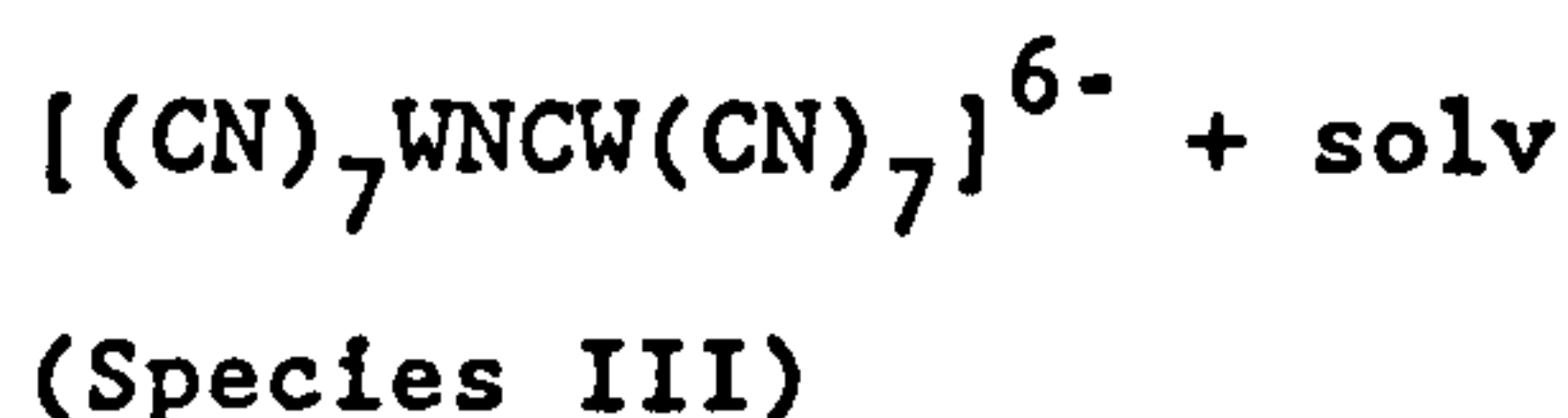
The initial photochemical act, not referring to any photoredox process leading to diamagnetic W(IV), is that of photodissociation to yield species I either as the coordinatively unsaturated  $[\text{W}(\text{CN})_7]^{2-}$ , or such a species undergoing interaction with the water matrix, equation (11.4):



The warming-recooling experiment leads to species II with a slightly higher average g-tensor, which is associated with the eight-coordinate species  $[\text{W}(\text{CN})_7(\text{H}_2\text{O})]^{2-}$ , which has been tentatively assigned previously with  $g_{av} = 1.943^{174}$ . Species III, with its reduced  $g_{\perp}$  is regarded as a cyanide-bridged dimer  $[(\text{CN})_7\text{WNCW}(\text{CN})_7]^{6-}$ , analogous to the dimer,  $[(\text{CN})_7\text{MoNCMo}(\text{CN})_7]^{6-}$  seen in the photolysis of  $[\text{Mo}(\text{CN})_8]^{3-}$  in methanol/ $\text{CH}_2\text{Cl}_2$  solution at 293 K<sup>214</sup>. The tungsten dimer may be formed via equation (11.5):



Initial product	product formed
at 77 K	on warming
(Species I)	(Species II)



An alternative route to the dimer should be:



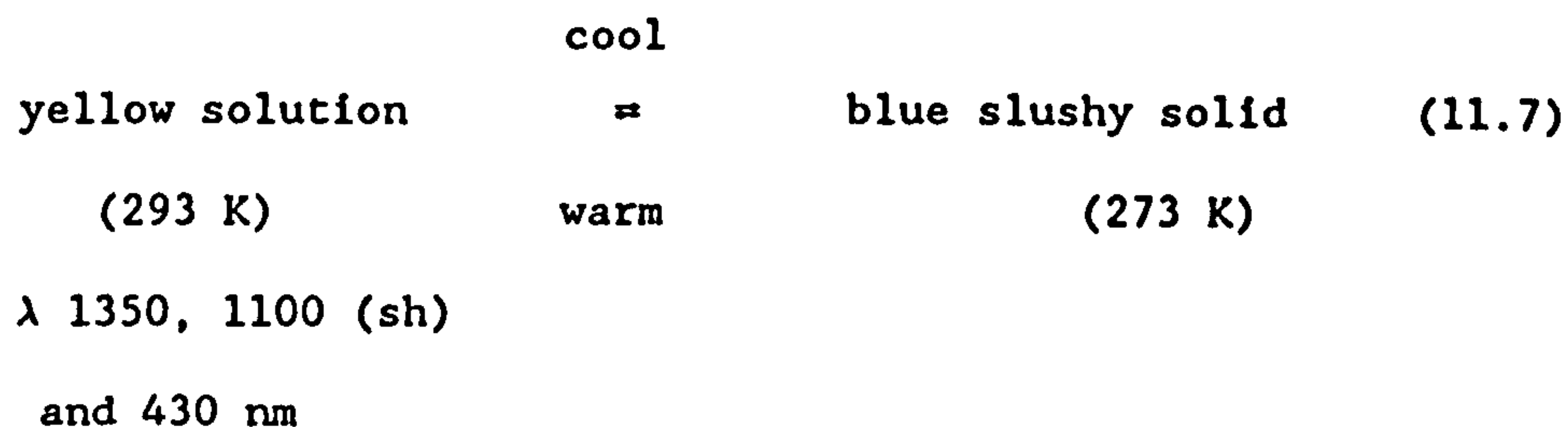
In order to explore the possibility of this reaction, the photolysis of  $[W(CN)_8]^{4-}$  was studied as well, the results of which are summarised in Table 11.5. Photolysis (365 nm) of  $K_4[W(CN)_8]$  (0.01 M) at 0°C (pH = 2.0) results in the production of a 'red solution',  $\lambda_{\text{max}}$  510 nm of  $[W(CN)_7H_2O]^{3-}$  ion<sup>184</sup>. This solution was weakly paramagnetic with absorptions due to  $[W(CN)_8]^{3-}$  and  $[W^V(CN)_7H_2O]^{2-}$  (species II); the mechanisms of these minor oxidation pathways remain obscure. After standing overnight the 'red solution' became yellow (to give the so-called 'yellow solution'), with species II converting into species III the mixed valence dimer ( $g = 1.9466$ ).

In addition, this 'yellow solution' showed remarkable reversible colour changes on cooling, equation (11.7):

Table 11.5      Photolysis of  $K_4[W(CN)_8]$  Ions in Solution

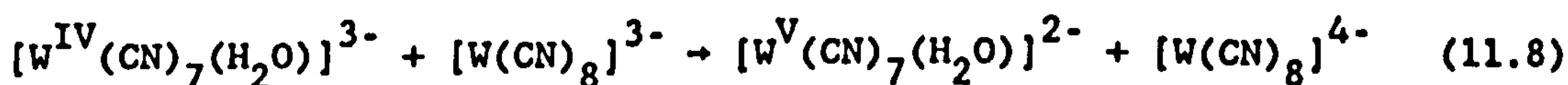
Sample	Species I	Species II	Species III
<hr/>			
'Red solution'	<g> - 1.9705 <A> - 54.4 G	<g> - 1.9450	
'Red solution'	<g> - 1.9705		<g> - 1.9466
+ $K_3[W(CN)_8]$	<A> - 54.4 G		<A> - 56 G
'Yellow solution'	<g> - 1.9705 <A> - 54.5 G		<g> - 1.9466 <A> - 56 G
<hr/>			





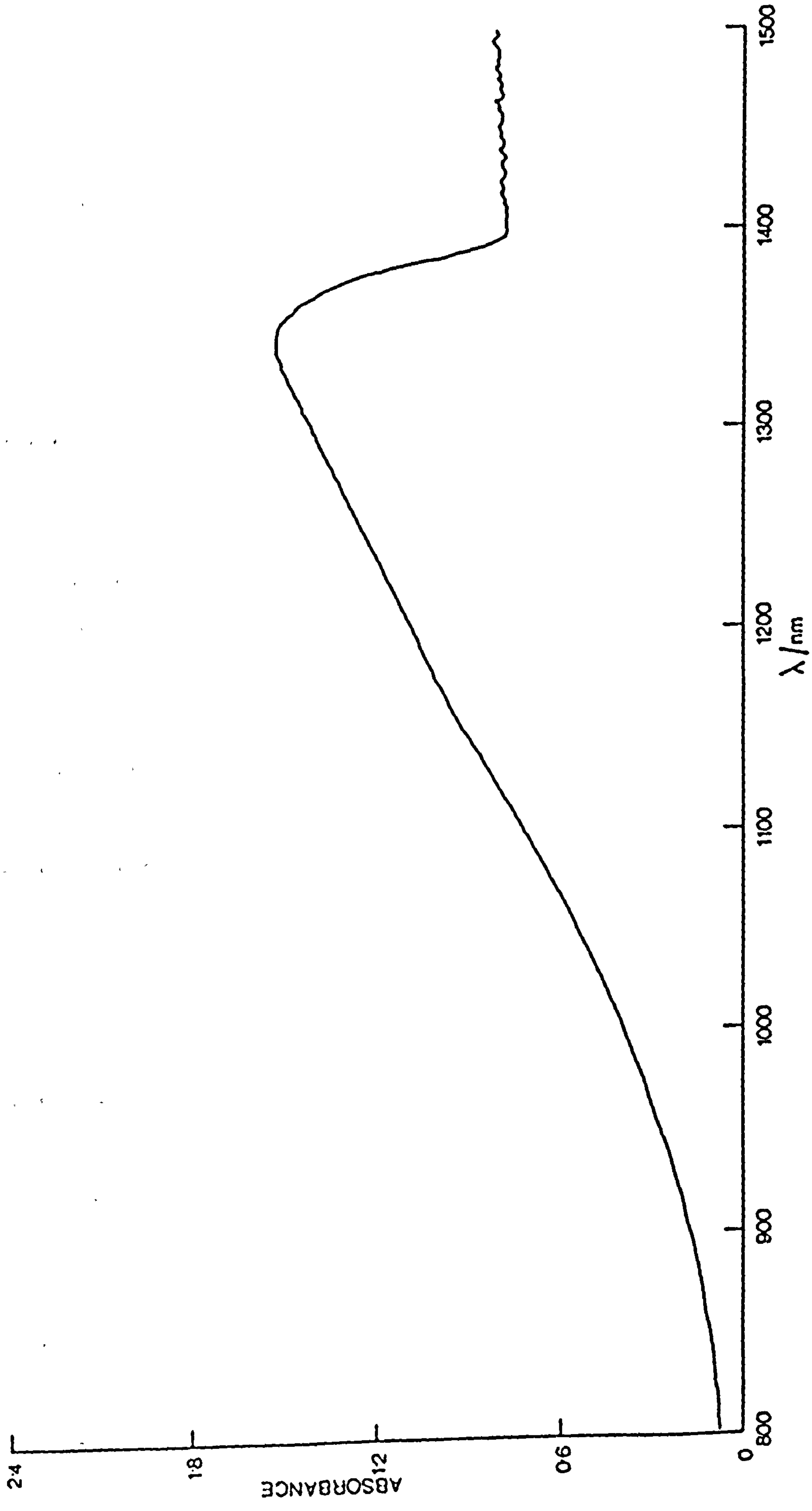
The observation in the 'yellow solution' of an intense near-IR band is consistent with the assignment of species III to the mixed-valence dimer. An absorption band detected at ca. 1200 nm after the photolysis of  $H_4[W(CN)_8]$  in aqueous solution has also been assigned to  $[(CN)_7WNCW(CN)_7]^{6-}$ <sup>177</sup>. The position of intervalence transfer (IT) absorption bands of mixed valence dimers have been shown to be dependent upon the dielectric properties of the solvent, the redox asymmetry of the two metal centres, and the type of ligand available in the first coordination sphere of the donor site of the mixed-valence system<sup>215</sup>. IT bands are very broad compared with normal CT bands and usually occur in the red to near-IR region of the spectrum.

This assignment is supported by the fact that addition of  $[W(CN)_8]^{3-}$  to the 'red solution' results in an instant change to the 'yellow solution' and the steady increase of the near-IR band in the dark, see Figure 11.5, producing a solution with  $g = 1.9466$ . However, the oxidation of  $[W^{IV}(CN)_7(H_2O)]^{3-}$  to  $[W^V(CN)_7(H_2O)]^{2-}$  by  $[W(CN)_8]^{3-}$ , equation (11.8) cannot be excluded as a possible pathway



The reaction between  $[W(CN)_7(H_2O)]^{2-}$  and  $[W(CN)_8]^{4-}$  may then occur rapidly to form the dimer, therefore precluding the detection of  $[W^V(CN)_7(H_2O)]^{2-}$ .

Figure 11.5      Electronic spectrum obtained on photolysis of  $k_4[W(CN)_8]$  (0.005 M) in aqueous solution at pH 2.0 at 273 K using a 439 nm Balzer filter, followed by addition of an equimolar aliquot of  $k_3[W(CN)_8]$ . Path length = 1.0 cm.



The intensification of the near-IR band on cooling may be responsible for the colour change, the band being temperature-dependent, rather than to a perturbation of an equilibrium between 'yellow' and 'blue' species.

The strongest evidence for the existence of  $[\text{W}(\text{CN})_7]^{2-}$  comes from the photolysis of  $(\text{Ph}_4\text{P})_4[\text{W}(\text{CN})_8]$  in MeCN-benzene mixture (5:1 v/v) in the presence of nitrosodurene, when a spin-trap product was observed with  $a(^{14}\text{N}) = 9.59 \text{ G}$  which is attributed to  $\text{Ar-N(O)} - \text{W}(\text{CN})_7^{2-}$  by analogy with its Mo counterpart<sup>214</sup>. The absorption band seen at 410 nm in the low temperature photolysis of the  $[\text{W}(\text{CN})_8]^{3-}$  ion, produced a slightly blue shifted but essentially similar absorption spectrum compared with that obtained upon laser flash photolysis of  $[\text{W}(\text{CN})_8]^{3-}$  in aqueous solution, see Figure 11.6. The 410 nm band may be tentatively associated with either species I or II, namely  $[\text{W}(\text{CN})_7]^{2-}$  or  $[\text{W}(\text{CN})_7(\text{H}_2\text{O})]^{2-}$ , respectively, rather than  $\{[\text{W}^{\text{IV}}(\text{CN})_7(\text{CN})]^{3-}\text{M}^+\}$  as previously reported<sup>178</sup>.

## 11.6 Photolysis of $\text{K}_3[\text{W}(\text{CN})_8]$ in KBr Discs and PVA Film

### 11.6.1 Analysis of Photoproducts using IR Spectroscopy at 293 and 12 K

The photolysis of  $\text{K}_3[\text{W}(\text{CN})_8]$  in a KBr disc or PVA film, both at 293 and 12 K, using pyrex- or 365 nm-filtered light results in a gradual change in colour of the film or disc to red-brown. This colour change is associated with a number of interesting changes in the IR spectrum, the main area of interest being the cyanide stretching region (ca.  $2100 \text{ cm}^{-1}$ ). Figure 11.7 displays the IR spectrum obtained during photolysis of  $\text{K}_3[\text{W}(\text{CN})_8]$  in a KBr disc, (identical results are also obtained in PVA film), and Table 11.6 displays the IR absorption bands in  $\text{cm}^{-1}$ .

Table 11.6      Summary of IR Spectrum in the Cyanide Stretching  
Region of Photolysed  $K_3[W(CN)_8]$  in KBr Disc

$K_3[W(CN)_8]$			Photolysed $K_3[W(CN)_8]$		
Frequency/ $cm^{-1}$	Strength	Assignment	Frequency/ $cm^{-1}$	Strength	Assignment
2166	m		2110	vs/b	$[W(CN)_7]^{2-}$
2157	vs	$\nu(C\equiv N)$	2220	m/b	or
2151	vs				$[(CN)_7WNCW(CN)_7]^{6-}$
2145	m				+ $[W(CN)_8]^{4-}$

Abbreviations used:

s, strong; m, medium; w, weak; v, very; b, broad

Figure 11.6      Comparison of (a) transient absorption spectrum obtained on laser flash photolysis of an aqueous solution of  $[\text{W}(\text{CN})_8]^{3-}$  with (b) absorption spectrum of  $[\text{W}(\text{CN})_8]^{3-}$  in 12 M aqueous LiCl at 77 K photolysed  $\lambda > 300$  nm.

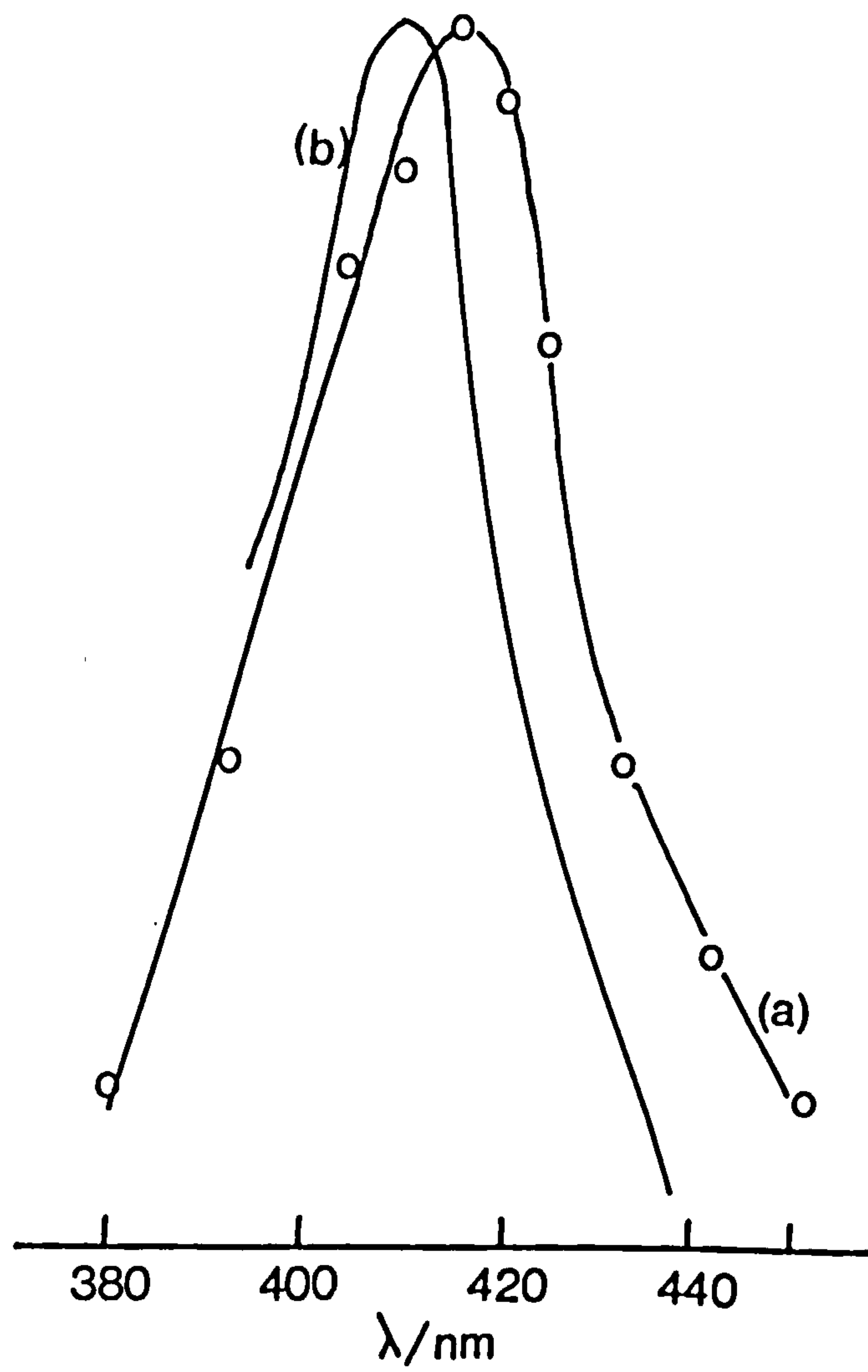
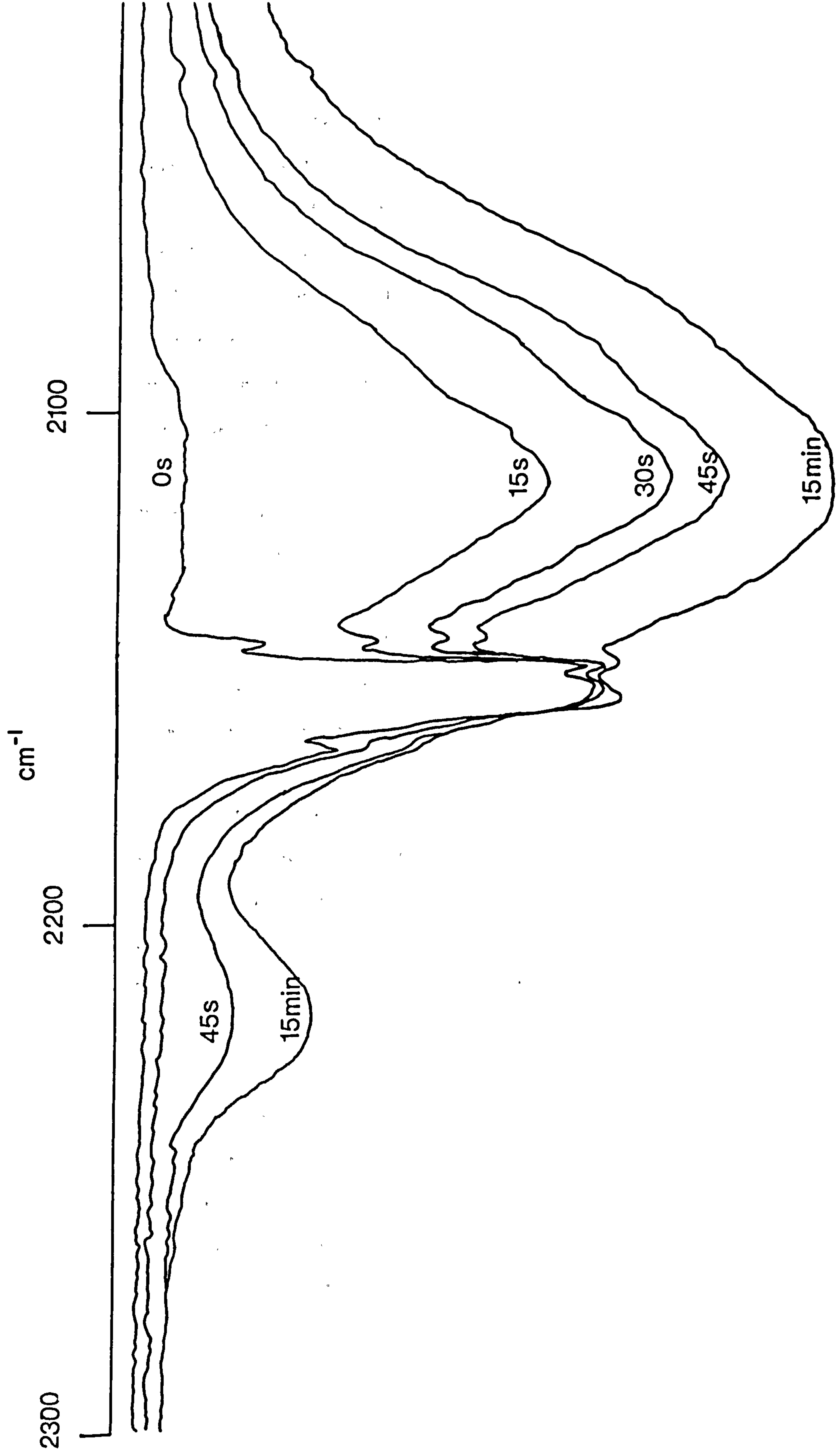




Figure 11.7      IR spectrum (KBr disc) in cyanide stretching region of  
photolysed  $\text{K}_3[\text{W}(\text{CN})_8]$ .



as can be seen from the IR spectrum, photolysis results in very broad, unresolved bands appearing at ca. 2110, and 2220  $\text{cm}^{-1}$ , with the extinction coefficient for the 2110  $\text{cm}^{-1}$  band exceeding that of the cyanide stretching bands of  $\text{K}_3[\text{W}(\text{CN})_8]$ . Dilution of the  $\text{K}_3[\text{W}(\text{CN})_8]$  disc with KBr and running the IR spectrum at higher resolutions and slower scan speeds does not resolve any vibrational structure in the broad IR bands. Deoxygenation of the film or disc prior to photolysis produced identical spectra to the non-deoxygenated variety.

Photolysis of  $\text{K}_4[\text{W}(\text{CN})_8]$  in a KBr disc for over 1 hour with broad band radiation (300-600 nm) produced very little change in the IR spectrum.

#### 11.6.2 Assignment of IR Changes

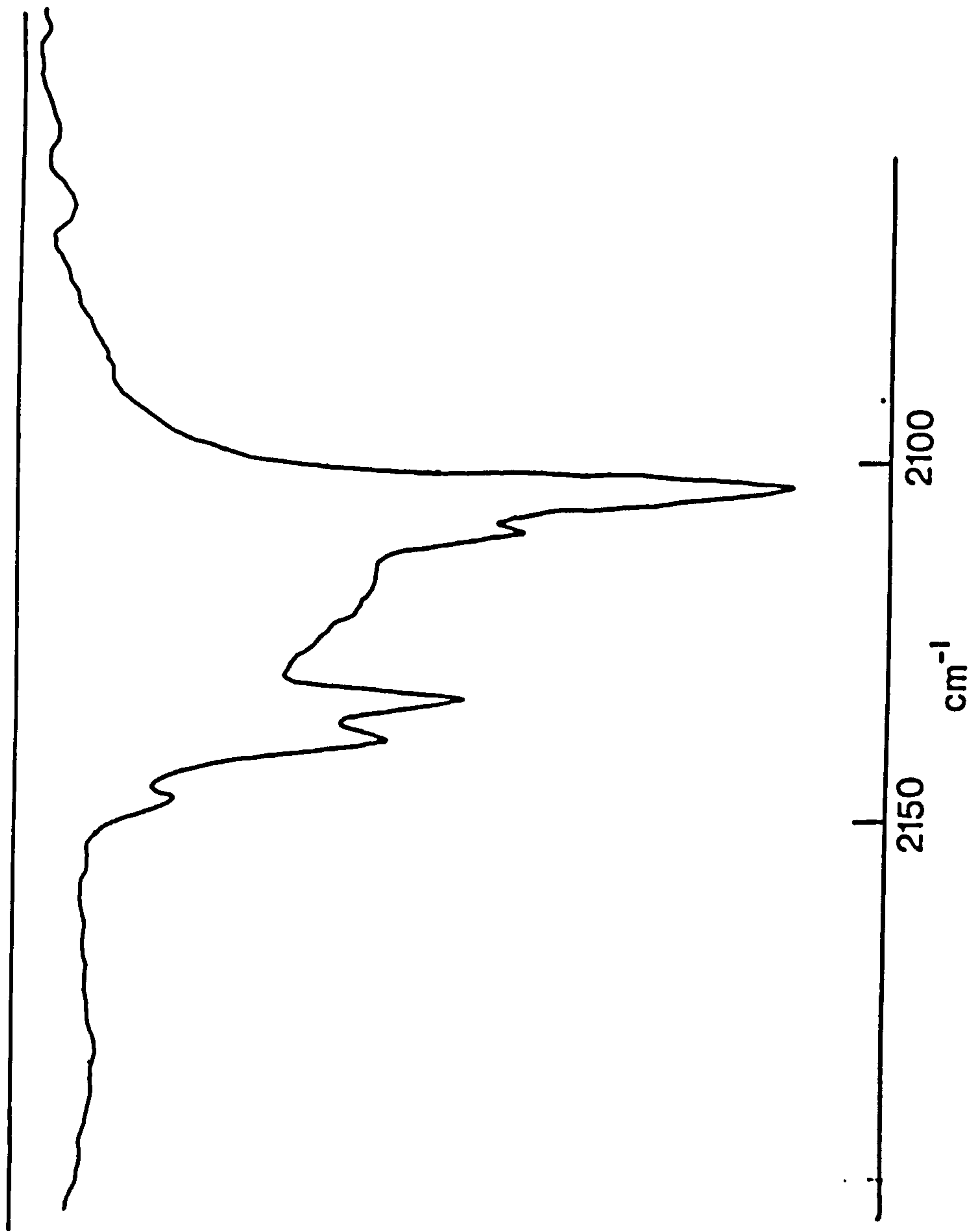
Photolysis of  $\text{K}_3[\text{W}(\text{CN})_8]$  in a KBr disc or PVA film may result in the formation of more than one photoproduct. The appearance of the IR spectrum is independent of temperature and the nature of the surrounding matrix. The appearance of the new IR bands are not the result of any direct photolysis product obtained from  $\text{K}_4[\text{W}(\text{CN})_8]$ , which may have been formed via a photo-redox process from  $\text{K}_3[\text{W}(\text{CN})_8]$ . Comparison of the IR spectra of  $\text{K}_4[\text{W}(\text{CN})_8]$ , see Figure 11.8 and Table 11.7, with photolysed  $\text{K}_3[\text{W}(\text{CN})_8]$ , reveals that the new bands are not wholly as a result of the formation of  $\text{K}_4[\text{W}(\text{CN})_8]$ .

The extremely broad nature of the product IR bands strongly suggests that the symmetry of the photoproduct has been greatly reduced, compared with the symmetry of  $\text{K}_3[\text{W}(\text{CN})_8]$ . This would facilitate a large number of metal-cyanide stretching bands covering a wide energy range. Possible explanations for these results are (a) the photoproduct is  $[\text{W}(\text{CN})_7]^{2-}$  and/or (b) a mixed valence bridge dimer  $[(\text{CN})_7\text{W}^{\text{IV}}\text{NCW}^{\text{V}}(\text{CN})_7]^{6-}$ . Evidence

Table 11.7      Summary of IR Spectrum in Cyanide Stretching Region  
of  $K_4[W(CN)_8]$  in KBr Disc

Frequency/(cm <sup>-1</sup> )	Strength <sup>a</sup>	Assignment
2146	vw	
2138	m	
2133	m	$\nu$ (C = N)
2108	m	
2104	vs	

Figure 11.8 IR spectrum (KBr disc) in cyanide stretching region of  $K_3[W(CN)_8]$ .



for the formation of a dimer arises from a previously reported 1:1 uranyl- $[\text{Mo}(\text{CN})_8]^{4-}$  dimer<sup>215</sup> in which the sharp CN stretching bands characteristic of the anion are replaced by a broad envelope centred on  $2140\text{ cm}^{-1}$ . Addition of uranyl nitrate to  $\text{K}_4[\text{W}(\text{CN})_8]$  in solution in a 1:1 molar ratio results in the formation of a red-brown precipitate of  $\text{K}_2[(\text{CN})_7\text{W}^{\text{IV}}\text{NC UO}_2]\cdot n\text{H}_2\text{O}$ . An IR spectrum of this complex reveals absorption bands very similar in shape and position to that obtained during the photolysis of  $\text{K}_3[\text{W}(\text{CN})_8]$  in a KBr disc.

In matrices both of PVA film and KBr disc, no accompanying new bands attributable to free  $\text{CN}^-$  (about  $2080\text{ cm}^{-1}$ ) were observed. However, this band would have been very weak because its extinction coefficient is at least ten-fold smaller than that of the parent compound.

### 11.7 Summary

The photo-irradiation of  $[\text{W}(\text{CN})_8]^{3-}$  is accompanied by a variety of intriguing spectroscopic changes. While the main end-product is  $[\text{W}(\text{CN})_8]^{4-}$ , other materials have been observed<sup>174</sup> and assignments given, although some revision of these is currently being undertaken.

Intermediate stages have been revealed in laser flash photolysis and IR matrix experiments, and tentative suggestions have been made as to their nature.

ESR spectroscopy has revealed a series of W(V) species which are formed in parallel with the photoredox pathway. It seems very likely that the initial species is some kind of heptacyanotungsten complex which subsequently leads to a dimer with an intense intervalence C-T band.



### 11.8 Suggestions for Further Work

So many intermediates have been noted from the IR, UV-visible and ESR spectra that one needs to place some of the assignments on a firmer footing. Isolation of crystalline materials may be possible in some instances, enabling x-ray crystal structure determination and, subsequently, unequivocal assignments of IR frequencies and g-tensors. Fast-atom bombardment (FAB) mass spectrometry offers the possibility of molecular mass determination and an insight into molecular structure where only microcrystalline or amorphous solids can be isolated. Indeed, as the final stages of this thesis were being written, Dr. B. Sieklucka had shown in our laboratory that well-resolved mass spectra can be obtained by positive-ion FAB mass spectrometry of certain model compounds such as  $K_3[W(CN)_8]$ ,  $K_4[W(CN)_8]$  and  $K_3[Fe(CN)_6]$ .

**Appendix I**

**References**

1. C. K. Jørgensen, Prog. Inorg. Chem., 1962, 4, 73.
2. Y. Tanabe and S. Sugano, J. Phys. Soc. Jpn., 1954, 2, 753.
3. V. Balzani and V. Carassiti, 'Photochemistry of Coordination Compounds', Academic Press, London, 1970.
4. J. G. Calvert and J. N. Pitts. 'Photochemistry', Wiley, New York, 1962.
5. B. N. Figgis, 'Introduction to Ligand Fields'. Wiley-Interscience, New York, 1966.
6. H. H. Schmidtke, Z. Phys. Chem., 1963, 38, 170.
7. C. K. Jørgensen, Adv. Chem. Phys., 1965, 8, 47.
8. C. K. Jørgensen, 'Orbitals in Atoms and Molecules', Academic Press, London, 1962.
9. W. S. Fiffe, J. Chem. Phys., 1962, 37, 1894.
10. L. J. Heidt and M. E. Smith, J. Am. Chem. Soc., 1948, 70, 2476.
11. M. Linhard and M. Weigel, Z. Anorg. Allg. Chem., 1951, 266, 73.
12. M. Kasha, Faraday Discuss. Chem. Soc., 1950, 2, 14.
13. J. N. Demas and G. A. Crosby, J. Am. Chem. Soc., 1970, 92, 7262.
14. J. Bjerrum, A. W. Adamson, and O. Bostrup; Acta Chem. Scand., 1956, 10, 329.
15. A. W. Adamson and P. D. Fleischauer, 'Concepts of Inorganic Photochemistry', Wiley-Interscience, London, 1975.
16. D. F. Nelson and M. D. Sturge, Phys. Rev., 1965, A137, 1117.
17. K. K. Chatterjee and L. S. Forster, Spectrochim. Acta, 1964, 20, 1603.

18. H. L. Schläfer, H. Gausmann, and H. Witzke, J. Chem. Phys., 1967, 46, 1423.
19. G. B. Porter and H. L. Schläfer, Z. Physik. Chem., 1963, 37, 109.
20. M. Mingardi and G. B. Porter, J. Chem. Phys., 1971, 54, 2247.
21. D. M. Klassen and G. A. Crosby, J. Chem. Phys., 1968, 48, 1853.
22. T. J. Kemp., Prog. React. Kinet., 1980, 10, 301.
23. J. N. Demas, 'Excited State Lifetime Measurements', Academic Press, New York, 1983.
24. 'Creation and Detection of the Excited State', Ed., W. R. Wane, Dekker, New York, 1976.
25. C. A. Parker, 'Photoluminescence of Solutions', Elsevier, Amsterdam, 1968.
26. J. N. Demas and A. W. Adamson, J. Am. Chem. Soc., 1973, 95, 5159.
27. D. G. Taylor and J. N. Demas, J. Chem. Phys., 1979, 71, 1032.
28. J. Jortner, S. A. Rice, and R. M. Hochstrasser, Adv. Photochem., 1969, 7, 149.
29. B. Henry and M. Kasha, Ann. Rev. Phys. Chem., 1968, 19, 161.
30. R. Englman and J. Jortner, Mol. Phys., 1970, 18, 145.
31. B. Barnett and R. Englman, J. Lumin., 1970, 3, 55.
32. G. W. Robinson and R. P. Frosch, J. Chem. Phys., 1962, 37, 1962.
33. J. P. Byrne, E. F. McCoy, and I. G. Ross, Aust. J. Chem., 1965, 18, 1589.
34. T. R. Thomas, R. J. Watts, and G. A. Crosby, J. Chem. Phys., 1973, 59, 2123.

35. F. D. Carnassei and L. S. Forster, J. Chem. Phys., 1969, 50, 2603.
36. D. S. McClure, Solid State Physics, 1959, 9, 399.
37. V. Balzani, F. Bolletta, M. T. Gandolfi, and M. Maestri, Top. Curr. Chem., 1978, 75, 1.
38. D. Rehm and A. Weller, Isr. J. Chem., 1970, 8, 259.
39. R. A. Marcus, J. Chem. Phys., 1965, 43, 679.  
R. A. Marcus, J. Chem. Phys., 1965, 43, 2654.
40. R. A. Marcus, Discuss. Faraday Soc., 1968, 45, 7.
41. K. Sandros, Acta Chem. Scand., 1964, 18, 2355.
42. D. L. Dexter, J. Chem. Phys., 1953, 21, 838.
43. J. Chem. Ed., 1983, 60, 785-887.
44. P. C. Ford, D. Wink, and J. Dibenedetto, J. Prog. Chem., 1983, 30, 213.
45. J. R. Morton, J. W. Rowlands, and D. H. Whiffen, Nat. Phys. Lab. Circular, No. BPR 13.
46. D. H. Whiffen, J. Chim. Physique, 1964, 61, 1589.
47. A. Carrington, Quart. Rev., 1963, 17, 67.
48. H. M. McConnell and D. B. Chesnut, J. Chem. Phys., 1958, 31, 1688.
49. S. I. Weissman, J. Chem. Phys., 1956, 25, 890.
50. H. S. Jarnett, J. Chem. Phys., 1956, 26, 1289.
51. R. Bersohn, J. Chem. Phys., 1956, 25, 1066.
52. A. D. McLachlan, Mol. Phys., 1958, 1, 233.
53. S. P. McGlynn and J. K. Smith, J. Mol. Spectrosc., 1961, 6, 164.
54. J. E. Fleming and H. Lynton, Chem. Ind., 1960, 1415.
55. R. L. Belford, J. Chem. Phys., 1961, 34, 318.
56. R. L. Belford and G. Belford, J. Chem. Phys., 1961, 34, 1330.

57. S. P. McGlynn, J. K. Smith, and W. C. Neely, J. Chem. Phys., 1961, 35, 105.
58. C. A. Coulson and G. R. Lester, J. Chem. Soc., 1956, 3650.
59. M. Boring, J. H. Wood, and J. M. Moscowitz, J. Chem. Phys., 1975, 63, 638.
60. C. Y. Yang, K. H. Johnson, and J. A. Horsley, J. Chem. Phys., 1978, 68, 1001.
61. J. T. Bell and R. E. Biggers, J. Mol. Spectrosc., 1965, 18, 247.
62. N. Sevchenko and Analele Stunt, Univ. Al. I Cuza Iasi, 1961, 2, 121.
63. P. Brint and A. J. McCaffery, Mol. Phys., 1973, 25, 311.
64. J. T. Bell and R. E. Biggers, J. Mol. Spectrosc., 1967, 22, 262.
65. J. T. Bell and R. E. Biggers, J. Mol. Spectrosc., 1968, 25, 312.
66. L. V. Volod'ko, A. I. Komyak, and L. E. Sleptsov, Optics and Spectroscopy, 1967, 23, 397.
67. C. Görller-Walrand and L. G. Vanquickenborne, J. Chem. Phys., 1971, 54, 4178.
68. C. Görller-Walrand and L. G. Vanquickenborne, J. Chem. Phys., 1972, 57, 1436.
69. C. Görller-Walrand and S. Dejaegere, J. Chim. Phys. Phys.-Chim. Biol., 1972, 69, 726.
70. C. Görller-Walrand and S. Dejaegere, Spectrochim. Acta, Part A, 1972, 28, 257.
71. J. C. Barnes and P. Day, J. Chem. Soc., 1964, 3886.
72. L. J. Heidt, G. W. Tregay, and F. A. Middleton, J. Phys. Chem., 1970, 74, 1876.



73. I. M. Kopashova, G. N. Larkin, and D. S. Umreiko, *Opt. Spectroskopiya*, 1973, 35, 244.
74. R. J. Hill, T. J. Kemp, D. M. Allen, and A. Cox. *J. Chem. Soc. Faraday, Trans. I.*, 1974, 70, 847.
75. P. Benson, A. Cox, T. J. Kemp, and Q. Sultana, *Chem. Phys. Lett.*, 1975, 35, 195.
76. D. D. Pant and H. B. Tripathi, *J. Lumin.*, 1974, 8, 492.
77. G. I. Sergeeva, A. K. Chibisov, A. V. Karyakin, L. V. Levshin, A. A. Nemodruk, and B. F. Myasoedov. *High Energy Chem.*, 1974, 8, 30.
78. V. N. Korobeinikova, V. P. Kazakov, and Yu. N. Chuvilin, *Dokl. Akad. Nauk. SSSR.*, 1973, 213, 884.
79. A. M. Bonch-Bruevich, E. N. Kalitlevskaya, and G. O. Karapetyan. *Opt. Spektroskopiya*, 1969, 27, 795.
80. J. L. Kropp, *J. Chem. Phys.*, 1967, 46, 843.
81. R. Matsushima, H. Fujimori, and S. Sakuraba, *J. Chem. Soc., Faraday Trans. I*, 1974, 70, 1702.
82. H. D. Burrows, S. J. Formoshino, M. da'Graça Miguel, and F. P. Coelko, *J. Chem. Soc., Faraday Trans. I*, 1976, 72, 163.
83. M. D. Marcantonatos and M. Deschaux, *Chem. Phys. Lett.*, 1981, 80, 327.
84. M. Deschaux and M. D. Marcantonatos, *J. Inorg. Nucl. Chem.*, 1981, 43, 2915.
85. Y. Yokoyama, M. Moriyasu, and S. Ikeda, *J. Inorg. Nucl. Chem.*, 1974, 36, 385.
86. M. Moriyasu, Y. Yokoyama, and S. Ikeda, *J. Inorg. Nucl. Chem.*, 1977, 39, 2205.
87. O. Traverso, R. Rossi, L. Magon, A. Cinquantini, and T. J. Kemp. *J. Chem. Soc., Dalton Trans.*, 1978, 569.



88. H. D. Burrows, J. Phys. Chem., 1982, 86, 1043.
89. S. Sostero, O. Traverso, P. D. Bernardo, and T. J. Kemp, J. Chem. Soc., Dalton Trans., 1979, 658.
90. D. Rehorek, A. Rehorek, M. Ackermann, P. Thomas, H. Henning, and H. Sautereau, J. Signalaufzeichnungsmaterialien, 1981, 2, 291.
91. M. Moriyasu, Y. Yokoyama, and I. Ikeda, Bunseki Kagaku, 1975, 24, 257.
92. I. K. Skutov and D. S. Umreiko, Zh. Prikl. Spektrosk, 1972, 17, 1027.
93. R. G. Bulgakov, V. P. Kazakov, and S. V. Lotnik, Khim. Vysokikh Energ., 1975, 2, 555.
94. H. D. Burrows and J. D. Pedrosa de Jesus, J. Photochem., 1976, 5, 265.
95. E. Schneider, Z. Phys. Chem., 1935, 28, 311.
96. M. D. Mercantonatos, Inorg. Chim. Acta., 1977, 24, L37.
97. E. Rabinowitch and R. L. Belford, 'Spectroscopy and Photochemistry of Uranyl Compounds', Pergamon Press, Oxford, 1964.
98. J. J. McBrady and R. Livingston, J. Phys. Chem., 1946, 50, 176.
99. D. Patnaik and B. Sahoo, Curr. Sci. [India].., 1959, 27, 292.
100. A. G. Brits, R. Van Eldik, and J. A. Van den Berg, Inorg. Chim. Acta., 1980, 39, 47.
101. G. E. Heckler, A. E. Taylor, C. Jensen, D. Percival, R. Jensen, and P. Fung, J. Phys. Chem., 1963, 67, 1.
102. B. Claudel, M. Fève, J. P. Puaux, and H. Sautereau, Compt. Rend. C., 1975, 280, 169.

103. D. Greatorex, R. J. Hill, T. J. Kemp, and T. J. Stone, *J. Chem. Soc., Faraday Trans. I.*, 1972, 68, 2059.
104. D. Greatorex, R. J. Hill, T. J. Kemp, and T. J. Stone, *J. Chem. Soc., Faraday Trans. I.*, 1974, 70, 216.
105. E. Bauer, *Helv. Chim. Acta.*, 1936, 19, 234.
106. S. Sakuraba and R. Matsushima, *Bull. Chem. Soc. Jpn.*, 1970, 43, 1950.
107. H. D. Burrows, D. Greatorex, and T. J. Kemp, *J. Am. Chem. Soc.*, 1971, 93, 2539.
108. T. J. Kemp and L. J. A. Martins, *J. Chem. Soc. Perkin Trans. II*, 1980, 1708.
109. R. Venkataraman and S. B. Rao, *Indian J. Chem.*, 1971, 9, 500.
110. S. K. Bhattacharyya and S. Gulvady, *J. Indian Chem. Soc.*, 1952, 29, 649.
111. S. K. Bhattacharyya and S. Gulvady, *J. Indian Chem. Soc.*, 1952, 29, 659.
112. S. Gulvady and S. K. Bhattacharyya, *J. Indian Chem. Soc.*, 1952, 29, 731.
113. Qi-Ke Zheng, Hai-Rong Zhang, and Fu-Xing Tan, *Tzu Jan Tsa Chih*, 1979, 2, 406.
114. J. T. Bell and R. S. Buxton, *J. Inorg. Nucl. Chem.*, 1974, 36, 1575.
115. J. T. Bell and M. R. Billings, *J. Inorg. Nucl. Chem.*, 1975, 37, 2529.
116. A. Ledwith, P. J. Russel, and L. H. Sutcliffe, *Proc. R. Soc. London*, 1973, A332, 151.
117. P. Gray and A. Williams, *Chem. Rev.*, 1959, 59, 239.
118. T. Harazono, S. Sato, and H. Fukutomi, *Bull. Chem. Soc. Jpn.*, 1984, 57, 768.

119. A. S. Brar, R. Chander, and S. S. Sandhu, *Indian J. Chem.*, 1979, 17A, 554.
120. A. S. Brar, A. S. Sarpal, and S. S. Sandhu, *Indian J. Chem.*, 1980, A19, 413.
121. S. S. Sandhu, M. S. Sidhu, and A. S. Brar, *J. Indian Chem. Soc.*, 1982, 59, 173.
122. A. S. Brar, S. S. Sandhu, and A. S. Sarpal, *Indian J. Chem.*, 1978, A16, 587.
123. A. S. Brar, S. S. Sandhu, and A. S. Sarpal, *Indian J. Chem.*, 1979, A18, 19.
124. A. S. Brar, A. S. Sarpal, and S. S. Sandhu, *Indian J. Chem.*, 1980, A19, 902.
125. K. R. Butter and T. J. Kemp, *J. Chem. Soc., Dalton Trans.*, 1984, 923.
126. H. B. Ambroz, K. R. Butter, and T. J. Kemp, *Faraday Discuss. Chem. Soc.*, 1984, 78, paper 4.
127. K. Venkatarao and M. Santappa, *Curr. Sci. India*, 1965, 33, 709.
128. K. Venkatarao and M. Santappa, *Z. Phys. Chem.*, 1967, 54, 101.
129. G. N. Kireeva and V. I. Savel'eva, *Radiokhimiya*, 1972, 14, 401.
130. K. Venkatarao and M. Santappa, *J. Polym. Sci., Polym. Chem. Ed.*, 1970, 8, 1785.
131. K. Venkatarao and M. Santappa, *Indian J. Chem.*, 1967, 5, 304.
132. T. Sato, S. Yoshie, T. Imamura, K. Hasegawa, M. Miyahara, S. Yamamura, and O. Ito, *Bull. Chem. Soc. Jpn.*, 1977, 50, 2714.
133. S. Sakurana and R. Matsushima, *J. Am. Chem. Soc.*, 1971, 93, 7143.

134. M. Ahmad, A. Cox, T. J. Kemp, and Q. Sultana, J. Chem. Soc., Perkin Trans. II., 1975, 1867.
135. A. Bismondo, U. Casellato, S. Sitran, and R. Graziani, Inorg. Chem. Acta, 1985, 110, 205.
136. A. Bismondo, L. Rizzo, P. Di Bernado, and P. L. Zanonato, J. Chem. Soc., Dalton Trans, (submitted for publication).
137. A. Bismondo, L. Rizzo, and G. Tomat, Inorg. Chim. Acta., 1983, 74, 21.
138. V. V. Ramanujam, K. Rengaray, and B. Suasankar, Bull. Chem. Soc. Jpn., 1979, 52, 2713.
139. P. Prasad, H. L. Yadav, S. Singh, P. C. Yadov, and K. L. Yadava, J. Electrochem. Soc. India, 1983, 32, 377.
140. V. G. Dongre and D. G. Dhuley, Curr. Sci., 1980, 49, 305.
141. G. M. Sergeev and I. A. Korshunov, Radiokhimiya, 1973, 15, 621.
142. N. C. Li, Brother E. Doody, and J. M. White, J. Am. Chem. Soc., 1958, 80, 5901.
143. O. Farooq, A. U. Anees, A. Naseer, and S. M. F. Rakman, J. Electrochem. Chem. Interfacial Electrochem, 1970, 24, 464.
144. R. N. Shckelokov, I. M. Orlova, and G. V. Podnesbesnova. Russ. J. Inorg. Chem. (Engl. Transl.), 1974, 19, 744.
145. G. M. Sergeev and I. A. Korshunov, Radiokhimiya, 1974, 16, 787.
146. M. Nourmand and N. Meissami, J. Chem. Soc., Dalton Trans., 1983, 1529.
147. R. Raghavan and M. Santappa, J. Inorg. Nucl. Chem., 1973, 35, 3363.
148. I. Feldman and L. Koval, Inorg. Chem., 1963, 2, 145.

149. H. Wieczorek and H. Kozlowski, *Inorg. Nucl. Chem. Lett.*, 1980,  
16, 401.
150. D. N. Shelke and D. V. Jahagirdar, *Indian J. Chem.*, 1978,  
16A, 60.
151. R. N. Shchelokov, Yu N. Mikhaulov, G. M. Lobanova, A. S.  
Karsishchova, I. M. Orlova, N. B. Generalova, and G. V.  
Podnesbesnova, *Russ. J. Inorg. Chem. (Engl. Transl.)*, 1982,  
27, 1324.
152. K. Kabur-ud-Din and A. Iqrar, *Monatsh. Chem.*, 1978,  
109, 1343.
153. P. C. Rauat and C. M. Gupta, *Chem. Abs. No. 83(2): 17658g*.
154. K. Rangaraj and V. V. Ramanujam, *J. Inorg. Nucl. Chem.*, 1977,  
39, 489.
155. A. Marzotto, L. Garbin, and F. Braga, *J. Inorg. Biochem*, 1979,  
10, 257.
156. R. S. Saxena and G. L. Shurma, *J. Electrochem. Soc. India*,  
1981, 30, 148.
157. M. Delcanale, R. Marchelli, A. Maniglia, A. Dossena, and G.  
Casnati, *Angew. Chem.*, 1983, 95, 562.
158. P. Smith, W. M. Fox, D. J. McGinty, and R. D. Stevens, *Can. J.*  
*Chem.*, 1970, 48, 480.
159. H. R. Falle, F. S. Dainton, and G. A. Salmon, *J. Chem. Soc.*,  
*Faraday Trans. II*, 1976, 12, 2001.
160. A. L. Poznyak, G. A. Shagisultanova, and S. I. Arzhankov,  
*Biofizika*, 1970, 15, 20.
161. A. L. Poznyak, S. I. Arzhankov, and G. A. Shagisultanova,  
*Biofizika*, 1974, 19, 233.
162. R. Poupko, I. Rosenthal, and D. Elad, *Photochem. Photobiol.*,  
1973, 17, 395.



163. A. K. Bansal, S. Goyal, and R. D. Dubey, *Acta. Ciencia India Chem.*, 1983, 90, 215.
164. By. Sudhindra, N. Bhattacharyya, and P. K. Das, *J. Chem. Soc., Faraday Trans. II*, 1984, 80, 1107.
165. M. V. Encinas, E. A. Lissi, and A. F. Olea. *Photochem. Photobiol.*, 1985, 42, 347.
166. E. König, *Theoret. Chim. Acta.*, 1962, 1, 23.
167. E. L. Goodenow and C. S. Garner, *J. Am. Chem. Soc.*, 1955, 77, 5268.
168. R. J. Campion, N. Purdie, and N. Sutin, *Inorg. Chem.*, 1964, 3, 1091.
169. O. Collenberg, *Z. Phys. Chem.*, 1924, 109, 353.
170. J. R. Perumareddi, A. D. Liehr, and A. W. Adamson, *J. Am. Chem. Soc.*, 1963, 85, 249.
171. V. Carassiti and V. Balzani, *Ann. Chim. (Rome)*, 1961, 51, 518.  
V. Carassiti and V. Balzani, *Ann. Chim. (Rome)*, 1961, 51, 533.
172. L. Moggi, F. Bolletta, V. Balzani, and F. Scandola, *J. Inorg. Nucl. Chem.*, 1966, 28, 2589.
173. D. Rehorek, E. G. Janzen, and H. J. Stronks, *Z. Chem.*, 1982, 22, 64.
174. B. Sieklucka, A. Samotus, S. Sostero, and O. Traverso, *Inorg. Chim. Acta*, 1984, 86, L51.
175. A. Samotus, *Adv. Mol. Relax. Processes*, 1973, 5, 121.
176. B. Sieklucka, A. Kanas, and A. Samotus, *Transition Met. Chem.*, 1982, 7, 131.
177. A. Samotus, *Roczniki Chemii.*, 1973, 47, 251.

178. K. R. Butter, T. J. Kemp, B. Sieklucka, and A. Samotus, J. Chem. Soc., Dalton Trans., 1986, 1217.
179. W. L. Waltz and A. W. Adamson, J. Phys. Chem., 1969, 73, 4250.
180. A. Vogler, W. Lasse, and H. Kunkely, J. Chem. Soc., Chem. Commun., 1979, 187.
181. P. Thomas, C. Saidi, and H. Henning, Inorg. Chim. Acta, 1984, 82, L11.
182. R. P. Mitra, B. K. Sharma, and H. Mohan, Can. J. Chem., 1969, 47, 2317.
183. G. W. Gray and J. T. Spence, Inorg. Chem., 1971, 10, 2751.
184. A. Samotus and B. Siekluka, J. Inorg. Nucl. Chem., 1978, 40, 315.
185. B. Siekluka and A. Samotus, J. Inorg. Nucl. Chem., 1980, 42, 1003.
186. M. Dudek and A. Samotus, Transition Met. Chem., 1985, 10, 271.
187. A. W. Adamson, W. L. Waltz, E. Zinato, D. W. Watts, P. D. Fleischauer, and R. D. Lindholm, Chem. Rev., 1968, 68, 541.
188. J. J. Alexander and H. B. Gray, Coord. Chem. Rev., 1967, 2, 29.
189. A. Marchay and F. Wasgestian, Inorg. Chim. Acta, 1985, 102, L13.
190. R. G. W. Norrish and G. Porter, Nature, 1949, 164, 658.
191. C. G. Hatchard and C. A. Parker, Proc. R. Soc., London, Ser. A, 1956, 235, 518.
192. J. G. Leipoldt, L. D. C. Bok, and P. J. Cilliers, Z. Anorg. Allg. Chem., 1974, 407, 350.
193. A. W. Parker, Ph.D. Thesis, University of Warwick, 1986.



194. R. H. Buchi and R. O. Ragsdale, *Inorg. Synth.*, 1972, 13, 202.
195. M. Mori, M. Shibata, E. Kyuno, and M. Kanaya, *Bull. Chem. Soc. Jpn.*, 1961, 34, 1837.
196. F. P. Dwyer, E. C. Gyarfas, and D. P. Mellor, *J. Phys. Chem.*, 1955, 296.
197. A. Samotus, *Roczniki Chemii.*, 1973, 47, 265.
198. M. Moriyasu, Y. Yokoyama, and S. Ikeda, *J. Inorg. Nucl. Chem.*, 1977, 39, 2199.
199. F. R. Hartley, C. Burgess, and R. M. Alcock, 'Solution Equilibria', John Wiley and Sons, New York, 1980.
200. C. K. Jørgensen, *Rev. Chim. Minérale*, 1977, 14, 127.
201. L. J. Heidt, *J. Am. Chem. Soc.*, 1954, 76, 5962.
202. D. Greatorex and T. J. Kemp, *Trans. Faraday Soc.*, 1971, 67, 576.
203. J. R. Morton, *Chem. Rev.*, 1964, 64, 453.
204. P. B. Ayscough and C. Thomson, *Trans. Faraday Soc.*, 1962, 58, 1477.
205. C. K. Jørgensen and R. Reisfeld, *J. Electrochem. Soc.*, 1983, 130, 681.
206. R. M. Haas and K. H. Gayer, *Z. Anorg. Allg. Chem.*, 1969, 102, 367.
207. D. N. R. Rao, M. C. R. Symons, and B. W. Wren, *J. Chem. Soc., Perkin Trans. II*, 1984, 1681.
208. H. Y. Al-Saigh and T. J. Kemp, *J. Chem. Soc., Perkin Trans. II*, 1983, 615.
209. S. S. Sandhu, K. B. Kohli, and A. S. Brar, *Inorg. Chem.*, 1984, 23, 3609.
210. G. N. Kireeva, V. I. Savel'eva, I. D. Sokolova, and B. N. Gromov, *Russ. J. Phys. Chem. (Engl. Transl.)*, 1972, 46, 531.

211. H. D. Burrows and T. J. Kemp, Chem. Soc. Rev., 1974, 3, 139.
212. H. B. Ambroz and T. J. Kemp, J. Chem. Res. Synop., 1985, 290.
213. D. P. Riley and P. E. Correa, J. Chem. Soc. Chem. Commun., 1986, 1097.
214. D. Rehorek, J. Salvetter, A. Hantschmann, H. Henning, Z. Stasicka, and A. Chodkowska, Inorg. Chim. Acta, 1979, 37, L471.
215. H. Henning, A. Rehorek, D. Rehorek, and P. Thomas, Inorg. Chim. Acta, 1984, 86, 41.
216. R. A. Pribus and R. D. Archer, Inorg. Chem., 1974, 13, 2556.